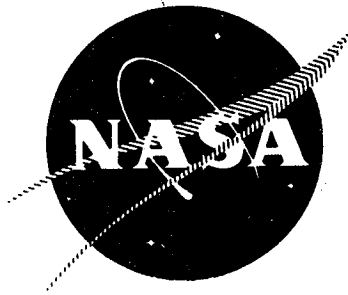


N73-18493

NASA CR-120815
R-8806



FINAL REPORT
STUDY OF BLADE CLEARANCE EFFECTS
ON CENTRIFUGAL PUMPS

by
R. K. Hoshide and C. E. Nielson



ROCKETDYNE
A DIVISION OF NORTH AMERICAN ROCKWELL CORPORATION

prepared for
NATIONAL AERONAUTICS AND SPACE ADMINISTRATION

NASA-Lewis Research Center
Contract NAS3-13311



NOTICE

This report was prepared as an account of Government-sponsored work. Neither the United States, nor the National Aeronautics and Space Administration (NASA), nor any person acting on behalf of NASA:

- A. Makes any warranty of representation, expressed or implied, with respect to the accuracy, completeness, or usefulness of the information contained in this report, or that the use of any information, apparatus, method, or process disclosed in this report may not infringe privately-owned rights; or
- B. Assumes any liabilities with respect to the use of, or for damages resulting from the use of, any information, apparatus, method or process disclosed in this report.

As used above, "person acting on behalf of NASA" includes any employee or contractor of NASA, or employee of such contractor, to the extent that such employee or contractor of NASA or employee of such contractor prepares, disseminates, or provides access to any information pursuant to his employment or contract with NASA, or his employment with such contractor.

Requests for copies of this report should be referred to

National Aeronautics and Space Administration
Scientific and Technical Information Facility
P.O. Box 33
College Park, Md. 20740

1. Report No. NASA CR-120815		2. Government Accession No.		3. Recipient's Catalog No.	
4. Title and Subtitle STUDY OF BLADE CLEARANCE EFFECTS ON CENTRIFUGAL PUMPS (FINAL REPORT)				5. Report Date November 1972	
				6. Performing Organization Code	
7. Author(s) R. K. Hoshide and C. E. Nielson				8. Performing Organization Report No. R-8806	
9. Performing Organization Name and Address Rocketdyne, a division of North American Rockwell Canoga Park, California 91304				10. Work Unit No.	
				11. Contract or Grant No. NAS3-13311	
12. Sponsoring Agency Name and Address National Aeronautics and Space Administration Washington, D.C. 20546				13. Type of Report and Period Covered Contractor Report	
				14. Sponsoring Agency Code	
15. Supplementary Notes Project Manager, Dean D. Scheer, NASA-Lewis Research Center, Cleveland, Ohio					
16. Abstract A program of analysis, design, fabrication, and testing has been conducted to develop and experimentally verify analytical models to predict the effects of impeller blade clearance on centrifugal pumps. The effect of tip clearance on pump efficiency, and the relationship between the head coefficient and torque loss with tip clearance was established. Analysis were performed to determine the cost variation in design, manufacture, and test that would occur between unshrouded and shrouded impellers. An impeller, representative of typical rocket engine impellers, was modified by removing its front shroud to permit variation of its blade clearances. It was tested in water with special instrumentation to provide measurements of blade surface pressures during operation. Pump performance data were obtained from tests at various impeller tip clearances. Blade pressure data were obtained at the nominal tip clearance. Comparisons of predicted and measured data are given.					
17. Key Words (Suggested by Author(s)) Shrouded Impellers Unshrouded Impellers Tip Clearance Centrifugal Pumps			18. Distribution Statement Unclassified - unlimited		
19. Security Classif. (of this report) Unclassified		20. Security Classif. (of this page) Unclassified		21. No. of Pages 223	22. Price*

* For sale by the National Technical Information Service, Springfield, Virginia 22151

FOREWORD

This report presents a summary of the work conducted under Contract NAS3-13311, "Study of Blade Clearance Effects on Centrifugal Pumps," by Rocketdyne, a Division of North American Rockwell Corporation, Mr. H. G. Diem, Program Manager. The contract was sponsored by the Lewis Research Center of the National Aeronautics and Space Administration, Cleveland, Ohio, and was administered under the technical direction of the Chemical Rocket Division with Mr. D. D. Scheer, Project Manager. This report covers the period from 2 July 1969 to 30 September 1971.

Special recognition is hereby extended to the following Rocketdyne personnel who contributed in large measure to the successful completion of the contract effort: Mr. F. C. Catterfeld, who was responsible for the mechanical design of the pump test assembly; Mr. L. J. Frederick, who was responsible for the instrumentation of the test impeller, and for the buildup of the pump test assembly.

CONTENTS

Foreword	ii
Abstract	v
Introduction	3
Technical Program	5
Task A: Literature Survey	5
Task B: Performance Analysis Formulation	6
Task C: Impeller Clearance and Cost Analysis	28
Task D: Test Rig and Instrumentation Design	39
Task E: Fabrication	55
Task F: Test and Data Correlation	69
Concluding Remarks	139
Prediction of Blade Loading and Impeller Velocity Distribution	139
Prediction of Tip Clearance Effect on Torque, Head, and Efficiency	139
Clearance and Cost Analysis	140
General	140
<u>Appendix A</u>	
Literature Survey Summary	141
<u>Appendix B</u>	
Method of Computing Velocity Distributions on Arbitrarily Shaped Blades in Incompressible Flow	147
<u>Appendix C</u>	
Parts Requirements List for AP70-126 Test Installation	191
<u>Appendix D</u>	
References	195
<u>Appendix E</u>	
Bibliography List	197
<u>Appendix F</u>	
Distribution List (Contract NAS3-13311)	201

ABSTRACT

A program of analysis, design, fabrication, and testing has been conducted to develop and experimentally verify analytical models to predict the effects of impeller blade clearance on centrifugal pumps. The effect of tip clearance on pump efficiency, and the relationship between the head coefficient and torque loss with tip clearance was established. Analysis were performed to determine the cost variation in design, manufacture, and test that would occur between unshrouded and shrouded impellers. An impeller, representative of typical rocket engine impellers, was modified by removing its front shroud to permit variation of its blade clearances. It was tested in water with special instrumentation to provide measurements of blade surface pressures during operation. Pump performance data were obtained from tests at various impeller tip clearances. Blade pressure data were obtained at the nominal tip clearance. Comparisons of predicted and measured data are given.

ILLUSTRATIONS

1. Flow Mechanism Causing Clearance Vortex	7
2. Three-Dimensional Secondary-Flow Patterns	8
3. Potential Flow Into a Slot	10
4. Potential Flow Into a Corner	11
5. Cross Section of Impeller Passage	12
6. Tip Leakage Flow With Boundary Layer	15
7. Blade Pressure Rise Due to Boundary Layer Scraping	17
8. Torque Loss Due to Momentum Loss in the Tip Clearance Leakage Flow	21
9. Meridional View of Impeller	22
10. Head Shift Due to Tip Clearance Leakage Flow Increase	23
11. Head Loss Due to Tip Clearance at Design Flow	24
12. Meridional View of Impeller	25
13. LO ₂ Pump Configuration Layouts	29
14. Unshrouded LO ₂ Impeller Stress Investigation	30
15. Volute Section for S = 0.003 Inch Maximum	32
16. Scanivalve Test Setup Schematic	40
17. Modification to Scanivalve Rotating Valve	42
18. J-2 Oxidizer Pump Impeller Front Shroud Removed	43
19. Impeller Clearance Effect Preliminary Layout	44
20. Pump Inlet Assembly Clearance Effect Study	45
21. Volute Assembly Clearance Effect Study	47
22. Stackup Assembly Layout.	51
23. Shrouded and Unshrouded J-2S Oxidizer Impellers	56
24. Impeller Pressure Tube Installation (Suction Side)	57
25. Impeller Pressure Tube Installation (Pressure Side)	58
26. Rear View of Impeller Showing Epoxyed Pressure Tubes (20 Each)	59
27. Pump Inlet Assembly	60
28. Slip-Ring Assembly	61
29. Scanivalve Assembly	63
30. Impeller Pressure Tubes Protruding Through Aft End of Main Shaft	64
31. Sealed Aft End of Main Shaft	65
32. Assembled Aft End of Pump Assembly	66
33. Inducer and Impeller Installed on Drive Shaft	67
34. Inlet View of Pump Assembly	68
35. Schematic of the Pump Calibration Facility	70
36. Installed Pump Test Assembly	71
37. Pump Test Assembly in the Pump Calibration Facility	72
38. Typical Scanivalve Blade Pressure Data	75
39. Blade Static Tip Streamline Pressures	77
40. Blade Static Mean Streamline Pressures	78
41. Blade Static Tip Streamline Pressures for Open Impeller	79
42. Blade Static Mean Streamline Pressures for Open Impeller	80
43. Wall Tap Static Pressures for Open Impeller	81
44. Modified J-2 Oxidizer Pump Wall Tap Static Pressures for Open-Faced Impeller	82
45. Modified J-2 Oxidizer Pump Wall Tap Static Pressures for Open-Faced Impeller	83
46. Wall Tap Static Pressures for Open Impeller	84

47.	Modified J-2 Oxidizer Pump Wall Tap Static Pressures for Open-Faced Impeller	85
48.	Modified J-2 Oxidizer Pump Wall Tap Static Pressures for Open-Faced Impeller	86
49.	Modified J-2 Oxidizer Pump Wall Tap Static Pressures for Open-Faced Impeller	87
50.	Modified J-2 Oxidizer Pump Wall Tap Static Pressure for Open-Faced Impeller	88
51.	Modified J-2 Oxidizer Pump Wall Tap Static Pressures for Open-Faced Impeller	89
52.	Modified J-2 Oxidizer Pump Wall Tap Static Pressures for Open-Faced Impeller	90
53.	Modified J-2 Oxidizer Pump Wall Tap Static Pressures for Open-Faced Impeller	91
54.	Modified J-2 Oxidizer Pump Suction Performance	92
55.	Modified J-2 Oxidizer Pump Suction Performance	93
56.	Modified J-2 Oxidizer Pump Suction Performance	94
57.	Modified J-2 Oxidizer Pump Suction Performance	95
58.	Modified J-2 Oxidizer Pump Suction Performance (Open-Faced Impeller)	97
59.	Modified J-2 Oxidizer Pump Suction Performance (Open-Faced Impeller)	98
60.	Modified J-2 Oxidizer Pump Suction Performance (Open-Faced Impeller)	99
61.	Modified J-2 Oxidizer Pump Suction Performance (Open-Faced Impeller)	100
62.	Modified J-2 Oxidizer Pump Tip Clearance Effect on Performance	101
63.	Modified J-2 Oxidizer Pump Tip Clearance Effect on Performance	102
64.	J-2 Oxidizer Impeller Comparison of Calculated Blade Loading Distribution to Measured	104
65.	Modified J-2 Oxidizer Pump Suction Performance for Shrouded and Open-Faced Impellers	106
66.	Modified J-2 Oxidizer Pump Suction Performance for Shrouded and Open-Faced Impellers Operating With Same Inducer	107
67.	Modified J-2 Oxidizer Pump Tip Clearance Effect on Performance	108
68.	Modified J-2 Oxidizer Pump Tip Clearance Effect on Performance	109
69.	Modified J-2 Oxidizer Pump Tip Clearance Effect on Head Rise	110
70.	Modified J-2 Oxidizer Pump Tip Clearance Effect on Head Rise	111
71.	Modified J-2 Oxidizer Pump Tip Clearance Effect on Pump Efficiency	112
72.	Modified J-2 Oxidizer Pump Tip Clearance Effect on Pump Efficiency	113
73.	Modified J-2 Oxidizer Pump Tip Clearance Effects on Pump Performance (Summary)	115
74.	Modified J-2 Oxidizer Pump Tip Clearance Effects on Pump Performance (Summary)	116
75.	S-4 Oxidizer Pump Performance Comparison Shrouded and Open-Faced Impellers	117
76.	S-4 Oxidizer Impeller Meridional View for Calculation of Blade Loading	118
77.	S-4 Oxidizer Impeller Blade Angle Distribution	119
78.	S-4 Oxidizer Impeller Calculated Blade Loading at Impeller Tip	120

79.	Hydraulic Performance of RI-15 Model Impellers ASME Paper No. 64-WA/FE-17	121
80.	Wood's Impeller RI-15 Meridional View for Calculation of Blade Loading	122
81.	RI-15 Model Impeller Blade Angle Distribution	123
82.	Wood's Impeller RI-15 Calculated Blade Loading at Impeller Tip	124
83.	J-2 Oxidizer Pump Impeller Front Shroud Removed	126
84.	J-2 Modified Oxidizer Impeller (Front Shroud Removed) Blade Angle Distribution	127
85.	J-2 Oxidizer Impeller Calculated Blade Loading at Impeller Tip	128
86.	S-4 Oxidizer Pump Tip Clearance Effects on Pump Performance (Summary)	129
87.	Wood's RI-15 Pump Tip Clearance Effects on Pump Performance (Summary)	130
88.	Head Change Due to Tip Clearance Based on Flow Change Using Blade Loading	131
89.	Head Loss Due to Tip Clearance at Design Flow	133
90.	Head Loss Due to Tip Clearance at Design Flow	134
91.	Head Change Due to Tip Clearance Leakage and Increased Impeller Flow.	135
92.	Torque Loss Due to Momentum Loss in the Tip Clearance Leakage Flow	137

TABLES

1.	Manufacturing and Material Cost Estimates for Shrouded LO ₂ Pump Assembly	33
2.	Manufacturing and Material Cost Estimates for Unshrouded LO ₂ Pump Assembly	33
3.	Cost Analysis Breakdown for Components of Shrouded LO ₂ Pump Assembly	35
4.	Cost Analysis Breakdown for Components of Unshrouded LO ₂ Pump Assembly	37
5.	Instrumentation List	53
6.	Test Program Log	74



SUMMARY

The study of blade clearance effects on centrifugal pumps was undertaken to evaluate the effects of impeller clearance on pump performance and cost. The study consisted of: (1) a literature survey to establish current state of the art, (2) formulation of analytical models to predict performance effects, (3) analysis of impeller clearance and cost effects, (4) design and fabrication of a test impeller and test rig, (5) a test program in which pump performance and blade pressures were measured and compared with predictions.

The test rig and instrumentation were designed with provisions for measurement of blade surface pressure and variation of blade tip clearances. The impeller was tested in a closed water loop, and the resultant data were compared with values predicted by the analytical models. Minor refinements were made to the program as a result of the correlation.

A computer program was used to calculate impeller blade relative velocity. The relative velocities allow the calculation of the static pressure differential across the impeller blade. A comparison of the measured impeller blade loading with the calculated data indicated that the calculated data were greater than the measured value. The loading distribution was of good accuracy, but the measurement of blade loading was curtailed due to failure of the test device. The minimum blade loading data obtained did not permit the correlation of the model at various other speeds. The data did indicate that the slip factors in the impeller program may not be of a proper magnitude and, therefore, resulted in greater levels of calculated blade loading than that measured.

A method was developed to predict the pump head loss due to tip clearance increase. The data correlated with the model and indicated that the prediction gave good results over a flow interval about the design point or point of maximum efficiency. The method, however, was not as accurate at high and low values of flow. The torque change that occurred in the pump due to impeller tip variation was analyzed and a model was developed predicting the energy loss through the tip clearance gap due to leakage. The prediction was based on the blade loading at the impeller tip and calculated the energy loss due to tip clearance leakage flow.

INTRODUCTION

In the design of impellers for rocket engine turbopumps, hydrodynamic performance can be predicted from empirical data for shrouded or unshrouded impellers with small blade clearances. The lack of information on blade pressure loading and performance as a function of tip clearance presents problems to the designer. Consequently, the impeller mechanical design is usually based on several approximations, with liberal safety factors applied. This approach results in relatively heavy impellers with undesirably thick blades. Also, because of the uncertainty of the effects of unshrouded impeller tip clearance on pump performance, close clearances are required or larger clearances are permitted with a degradation in pump performance. Shrouded impellers may be used, but these impellers have lower stress limits and may be more difficult to fabricate.

The purpose of this program is to evaluate the effects of centrifugal pump impeller clearances on rocket engine pump performance and cost. The initial task of this program consisted of conducting a literature survey of the effects of tip clearance on the performance of centrifugal and axial-flow pumps (and compressors). The results of the survey were used as a basis for formulating an analytical model to predict the effects of tip clearance on centrifugal pump performance. Analyses were performed to determine the probable range of impeller clearance that would be used in an unshrouded centrifugal pump, and cost variation in design, manufacture, and test that would occur between unshrouded and shrouded impellers. An unshrouded centrifugal J-2 oxidizer pump was tested in water to determine the magnitude of performance degradation caused by an increase in impeller tip clearance. The use of the J-2 oxidizer pump permitted a basic comparison to be made between shrouded and unshrouded impeller performances, as well as a comprehensive study of impeller clearance on performance. Also, experimental data were obtained which were used for correlating the results of the analytical models and to refine the model. This final report covers all the work performed under the contract.

TECHNICAL PROGRAM

This technical program to investigate analytically and experimentally, impeller clearance effects on centrifugal pumps is discussed herein. The combined analytical and experimental effort was divided into the following six tasks:

- A. Literature Survey
- B. Performance Analysis Formulation
- C. Impeller Clearance and Cost Analyses
- D. Test Rig and Instrumentation Design
- E. Fabrication
- F. Test and Data Correlation

TASK A: LITERATURE SURVEY

A literature survey was conducted to determine the current state of the art on the effects of tip clearance on the performance of centrifugal and axial-flow pumps and compressors. The Rocketdyne Technical Information Center compiled bibliographies from the North American Rockwell Technical Information Processing System, the National Aeronautics and Space Administration accessions, and the Defense Documentation Center. Approximately 3500 bibliographies from these indices were reviewed. From this list, 330 reports were ordered and reviewed. Selected applicable summaries are presented in Appendix A along with a bibliography list of pertinent reports, papers, and books. Applicable reports were utilized to formulate theories for predicting the effects of tip clearance on pump performance.

TASK B: PERFORMANCE ANALYSIS FORMULATION

A study of the literature indicated that many changes in flow patterns occur as a tip clearance varies in a centrifugal impeller.

Of major concern in this study was that the mathematical model developed for the performance analysis formulation would not be so complex and cumbersome as to limit its usefulness to the designer. As a result, the effort involved formulation of a model from which a performance prediction could be made for a broad range of centrifugal impellers. Several methods of developing a model are presented to give the designer a better insight into the mechanics of the problems involved.

The basic performance parameters of concern when formulating a model of this type are torque or power, head, and efficiency. These are interrelated, however, since the change in efficiency due to tip clearance is related to the change in impeller head and power. The tip clearance torque loss is a wasted energy and directly affects the efficiency. Similarly, the reduction in head additionally indicates an efficiency penalty. Torque and head effects can be derived independently and used to predict efficiency loss due to tip clearance. Head and torque are also related since the blade loading across an impeller blade is directly proportional to the torque.

Flow Patterns in the Centrifugal Impeller

The complex nature of the flow structure in the centrifugal impeller with tip clearance makes it necessary to construct simplified models from which an analysis can be formulated. A study of the literature dealing with flow in turbomachines with open-face rotors indicates that a combination of three major effects are associated with tip clearance. Figure 1 presents a sketch of a cross section of blade passage and shows these effects to be (1) secondary flow due to pressure gradients across the flow passages, (2) leakage of the flow past the tip clearance because of pressure differential across the blade tip, and (3) the boundary layer "scraping" effect caused by the blades moving relative to the wall boundary layer and scraping up fluid from it. In pumps and compressors, the leading surface of the blade in relation to its tangential velocity is the pressure surface. Conversely, the trailing surface of the blade is the suction surface. Within an impeller passage, the pressure gradient from pressure to suction surface sets up the secondary flow pattern as shown and, across the blade tip, instigates the tip leakage flow. The fluid vortex is created by both the clearance flow and the boundary layer scraping. Both these phenomena are additive, and tests indicate they may develop into a single loss core per passage (Ref. 1 through 3), or several depending upon the relative strength of both. The position of the core is dependent upon the blade velocity relative to the wall, tip clearance, and wall boundary layer thickness. Several methods have been advanced for the calculation of these effects for axial turbomachinery, and cascade data have been obtained (Ref. 2, 4, and 5).

Expanding the two-dimensional concept of the flow mechanism to a simplified three-dimensional analysis gave a flow pattern approximating that shown in Fig. 2. Included are the boundary layer scraping, tip leakage, and secondary flows coupled to

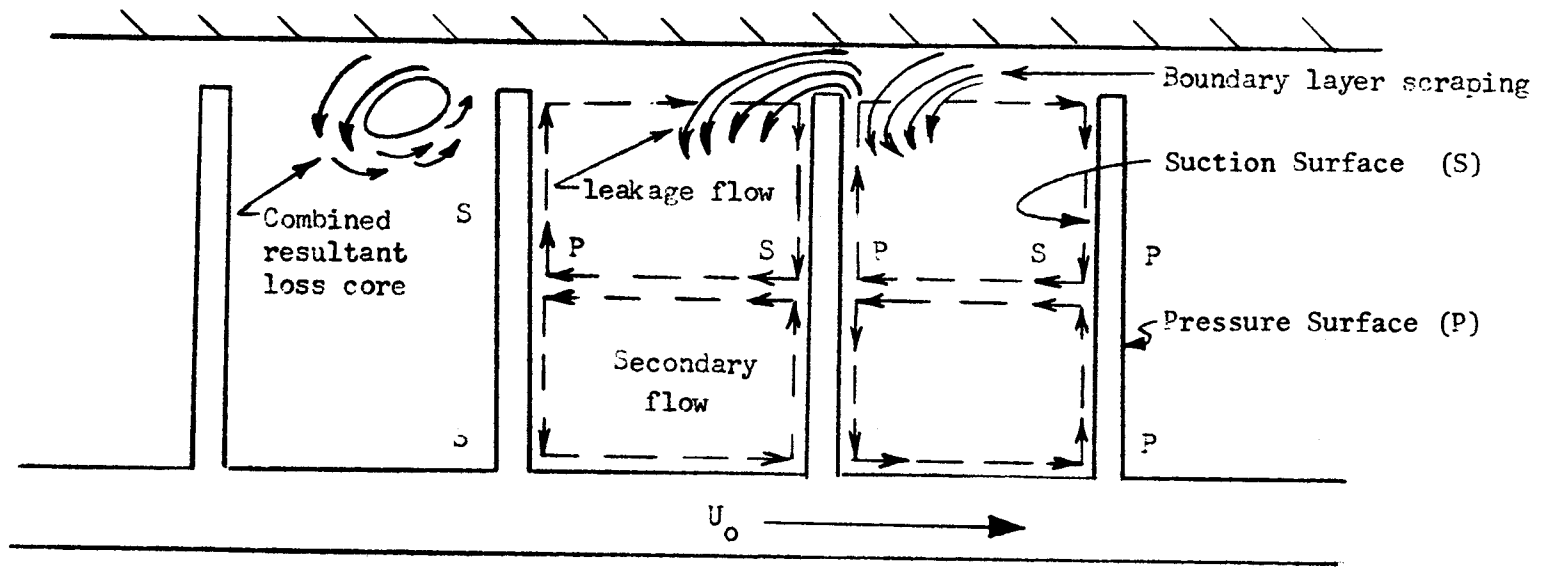


Figure 1. Flow Mechanism Causing Clearance Vortex

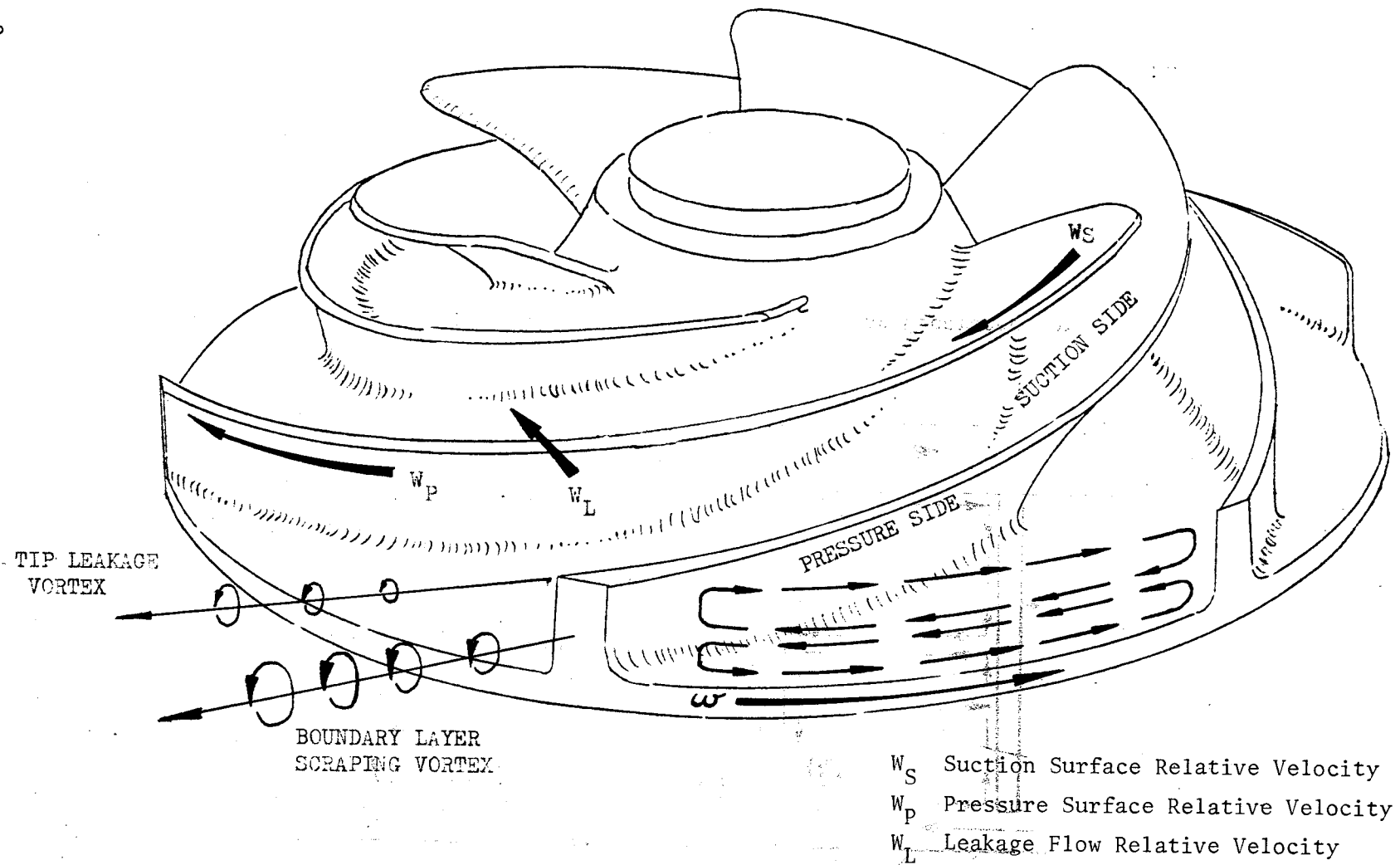


Figure 2. Three-Dimensional Secondary-Flow Patterns

a rotation of the impeller. It is apparent that boundary layer effects are varying degrees and dependent upon impeller rotational speed, housing curvature, flow-rate, blade number, etc. Hamrick (Ref. 3) found that the adiabatic efficiency of an impeller tested in air was maximum at a clearance greater than the minimum clearance tested. He explained this by indicating the scraping effect was possibly predominant for this lightly loaded blade causing higher losses than when the boundary layer scraping and the blade pressure differential at the greater clearance matched, allowing the blades to maintain the blade pressure differential without a pressure surface boundary layer buildup. At the smaller clearance, the pressure face of the blade indicated a boundary layer buildup which could not be bled to the suction surface because of the scraping effect. An exact method of calculation of these effects currently does not exist and test data must be relied upon to aid in the development of models to predict these effects.

Preliminary Investigations

Potential Flow Solution for Spanwise Pressure Distribution. Some of the earliest work done on tip clearance studies was accomplished by Rains (Ref. 6) for axial-flow machines. In his work he developed a potential flow solution for flow into a slot. This allowed him to determine that the perfect fluid model (when compared with his test data) was accurate for determining the spanwise pressure gradient for flow into a clearance. His data also indicated that, for the large Reynolds numbers existent in turbomachinery, and with the ratios of tip clearance to blade thickness commonly used (>0.07), the viscous force effect on stationary blading can be neglected without large errors. Figure 3 presents the potential flow model of flow through a slot and its attendant pressure gradient (Ref. 6).

A continuation of Rains' study indicated that with rotation, the boundary layer scraping effect on blade spanwise pressure was of sufficient magnitude to modify the pressure field significantly. Visual observations of a rotating disk past a blade indicated two regions of flow in the tip clearance: one being the boundary layer flow close to the disk and the other where the tip flow was influenced by the free stream flow. The mathematical analogy to the boundary layer scraping was simulated by the potential flow into a corner (Fig. 4). The spanwise increase in pressure was presented as well as the model. The superposition of the slot flow and the scraping flow were then made to determine a net torque increase on N rotor blades. For axial turbomachinery, the total force change can be applied at the tip of near-constant radius; however, the radial machine must take into account the effect of radius change over the blade chord as well as the effect of boundary layer dependency on radius. This makes the procedure much more complex for radial machines but, with considerable effort, it could possibly be developed further. The solution of this approach may prove satisfactory for determining torque change due to spanwise pressure variations caused by tip clearance leakage and boundary layer scraping.

Methods of Deriving Torque Change Due to Tip Clearance. Several general approaches can be utilized to determine the torque change due to tip clearance. As a result, several approaches are discussed here which were studied during the model formulation task period. The torque is described generally as the force moment created by the pressure loading along the blade. In a centrifugal impeller, the spanwise

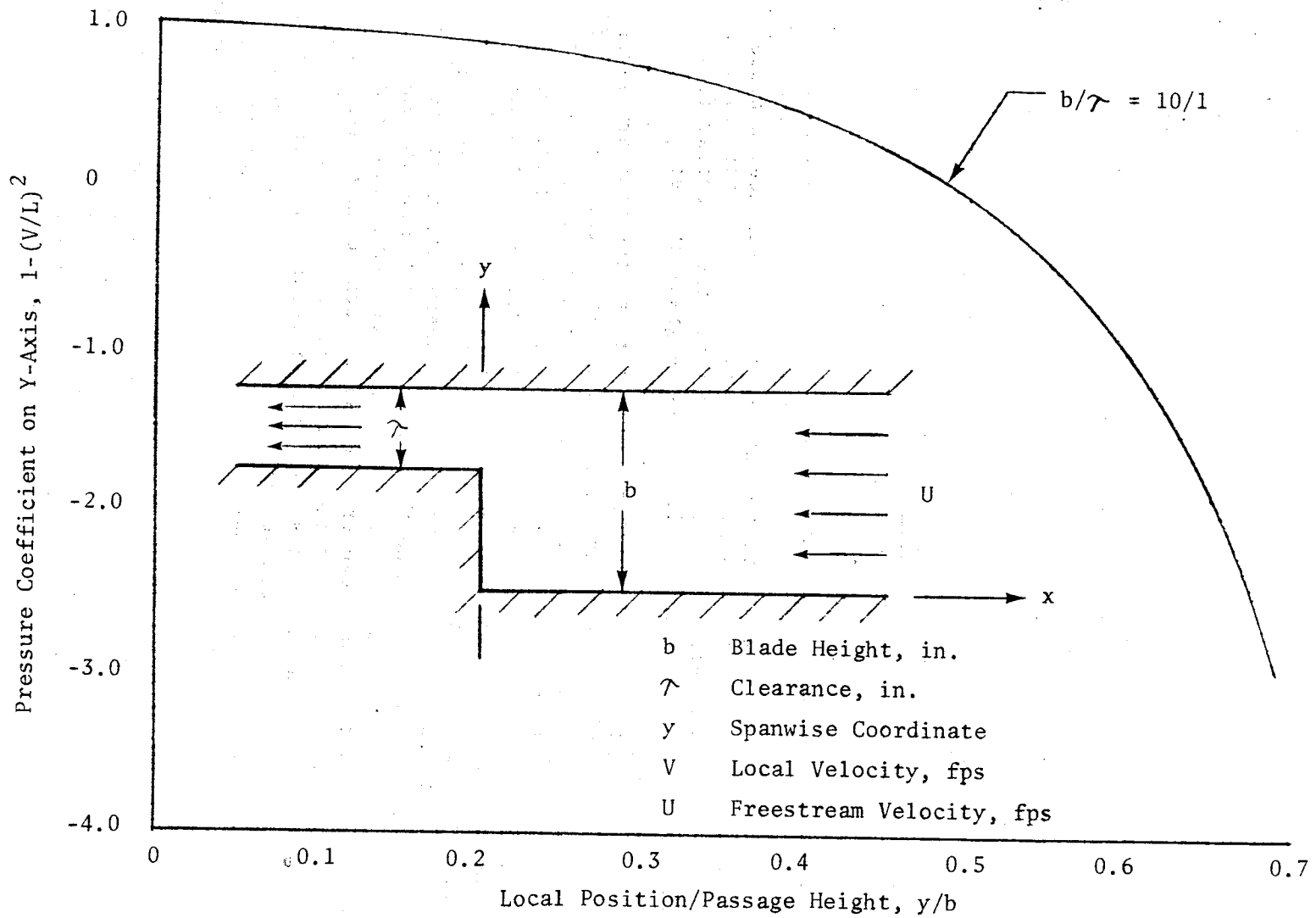


Figure 3. Potential Flow Into a Slot

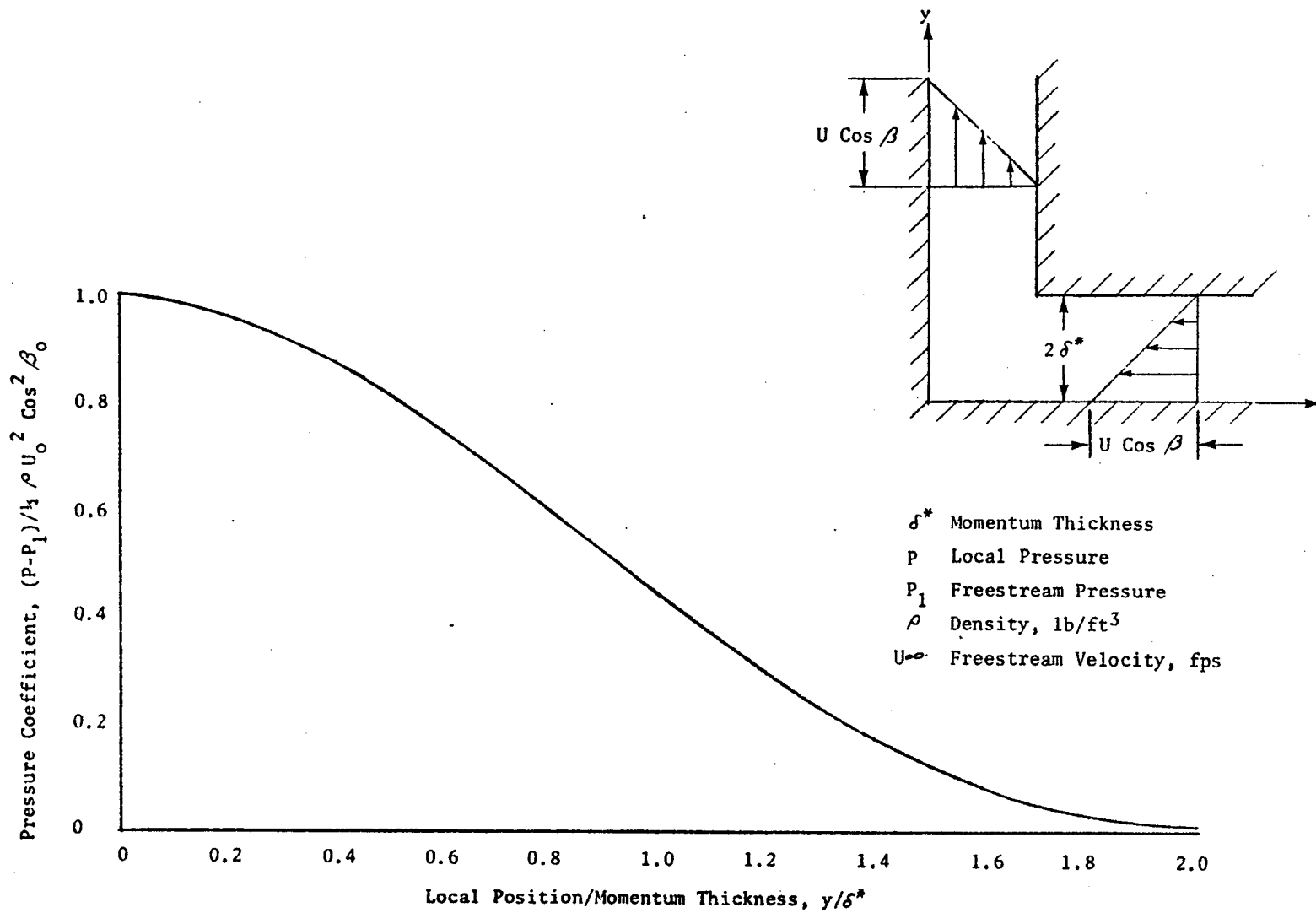


Figure 4. Potential Flow Into a Corner

pressure gradient as well as the radial variation in pressure must be accounted for. Present methods for the prediction of blade loading do not account for the spanwise effects caused by tip clearance flow. This requires that the spanwise pressure distribution be developed more fully, which was not considered to be within the scope of the present effort. The models presently developed to determine the blade torque utilize an average pressure loading distributed spanwise over the blade. The relative effects of this assumption can be studied when comparing the model to test data.

Torque by Use of a Control Volume. If we assume steady incompressible frictionless flow, a force balance may be developed for the control volume of the blade passage of a radial machine as shown below. At any station, the torque on the machine can be equated to the pressure force exerted on the blade normal to the area times the radius r , as shown by Fig. 5.

$$T = \int (P_p - P_s) r (b - \lambda) dr$$

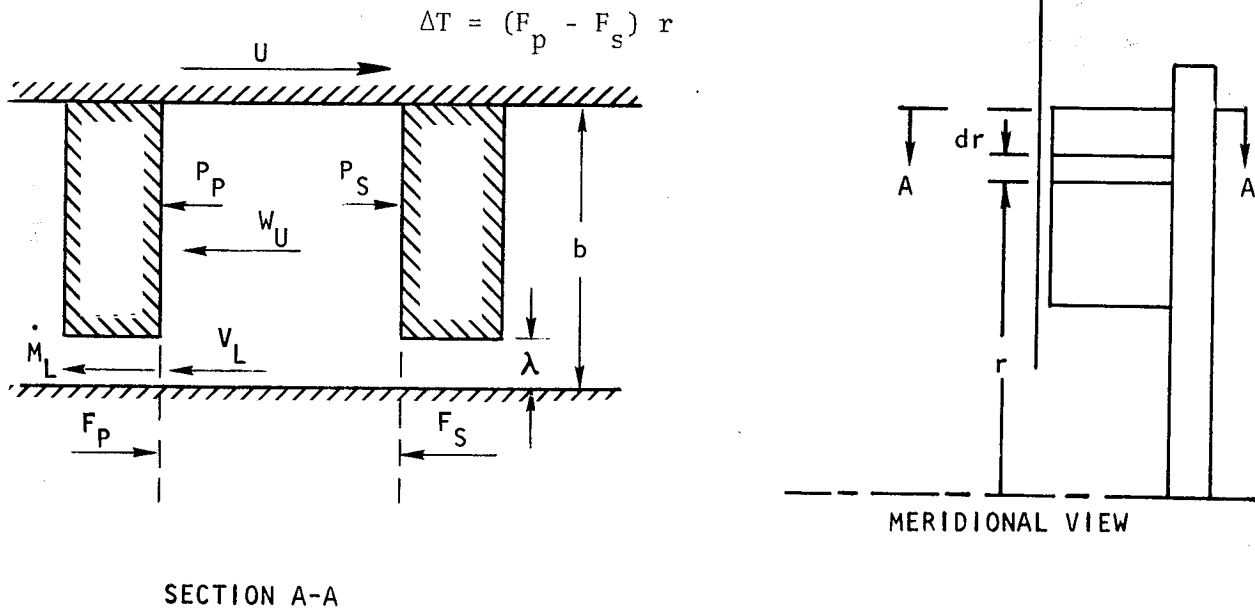


Figure 5. Cross Section of Impeller Passage

That torque translates a force to the fluid which can be found by force balance to be

$$\int (P_p - P_s) r (b) dr = (\dot{m}_T W_U + \dot{m}_L (W_U - V_L)) r$$

where \dot{m}_T = total mass flowrate of the fluid, and \dot{m}_L = leakage mass flowrate.

W_U is the relative tangential velocity of the fluid within the control volume, and V_L is the leakage velocity relative to the blade. The mass flowrates can be expressed in terms of velocities and areas so that

$$\dot{m}_T = \rho A_T W_U; \dot{m}_L = \rho A_L V_L$$

where $A_T = (b-\lambda) dr$ and $A_L = \lambda dr$, with ρ being mass density

or

$$\dot{m}_T = \rho W_U (b-\lambda) dr; \dot{m}_L = \rho V_L \lambda dr$$

This gives, then,

$$dT = \rho W_U^2 (b-\lambda) r dr + \rho V_L \lambda (W_U - V_L) r dr$$

The first term, then, is the torque directly affecting the blades, as can be seen by letting λ go to zero. This gives the ideal torque at zero clearance. The second term is the torque caused by the tip clearance, which is a torque loss assuming the kinetic energy in the leakage velocity is lost in the tip clearance vortex.

$$dT_{\text{loss}} = \rho V_L \lambda (W_U - V_L) r dr$$

Assuming the leakage velocity is caused by the blade pressure differential from pressure to suction side,

$$V_L = K \sqrt{2g \frac{\Delta P}{\gamma}}$$

where K is an equivalent orifice coefficient and γ is the specific weight. Similarly, the relative tangential velocity W_U can be expressed as a function of radius and other independent variables. Using a slip correction factor (X_M) to aid in the definition

$$W_U = U - C_U = U - \frac{1}{X_M} \left(U - \frac{C_M}{\tan \beta_B} \right)$$

where C_U is the absolute tangential velocity, C_M is the absolute meridional velocity, β_B = the blade angle which is dependent on the radius.

The development of W_U as a function of radius may be extended as shown or may be defined at the convenience of the designer. Using the above approach with the assumption that the meridional velocity remained constant throughout the impeller, an expression was obtained for the relative tangential velocity.

$$W_U^2 = \frac{\omega^2}{X_M^2 (\alpha + \zeta_r)} \left[(X_M^2 - 1) (\alpha + \zeta_r) r^2 + 2(X_M - 1) (\alpha + \zeta_r) \phi_t r_t r + \phi_t^2 r_t^2 \right]$$

where ω is the rotative speed in radians/second, and $(\alpha + \zeta_r) = \tan \beta_B$ through the blade passage. The subscript t refers to the reference tip of the impeller in the flow coefficient ϕ_t and the radius r_t .

The pressure differential across the blade (ΔP) presented above was also fitted to a polynomial of second order such that

$$\Delta P = \Delta P_{\max} (A + Br + Cr^2)$$

These parameters were substituted into the torque loss equation, and the equation was integrated over the interval from the inlet radius to discharge radius along the blade tip. This expression was developed for the J-2 (Mark 15) oxidizer pump. The results indicated a torque loss occurring at the tip clearance which was so excessive as to be unrealistic. The simplifying assumptions such as the approximations of the slip correction factor, and blade angle variation may have been too general. This approach, however, should not be entirely discarded, as further development may result in a better model.

Method of Determining Energy Loss in the Tip Clearance With Boundary Layer. The effect of the boundary layer is difficult to assess in the centrifugal impeller operating with a tip clearance, due to the complex three-dimensional effects. There are two distinct and separate cases which should be examined when the boundary layer is taken into account in the analysis of tip clearance flow. The first case is that of a large boundary layer such that the boundary layer thickness δ is larger than the tip clearance λ or $\delta/\lambda > 1$. This was the case where boundary layer scraping takes place, adding a component to the vortex or loss core caused by impeller tip leakage, as previously discussed. The second case where boundary layer should be accounted for is where the boundary layer was large enough to affect the velocity distribution of the tip clearance flow due to blade pressure differential. Let the kinetic energy of the tip clearance flow be assumed as totally lost due to its downstream dissipation within the tip vortex core. The kinetic energy within an incremental flow area will be defined as

$$\Delta E = \dot{w} V_L^2 / 2g$$

Where \dot{w} is the tip leakage weight flow, with V_L being the tip leakage velocity as shown in Fig. 6. The weight flow can be shown to be

$$\dot{w} = \rho g V_L dy dr$$

if y is the spanwise distance above the housing. The velocity U is the housing velocity relative to the blade.

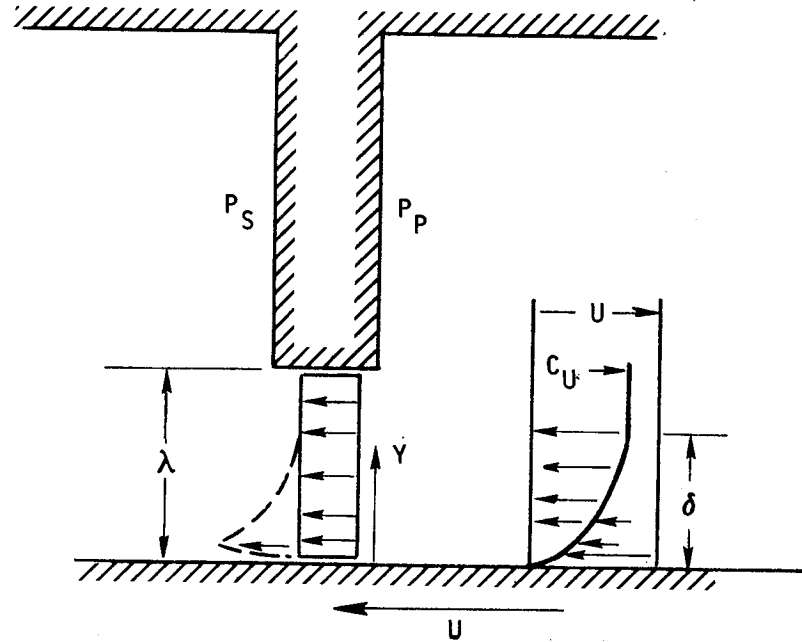


Figure 6. Tip Leakage Flow With Boundary Layer

The leakage velocity profile-due to blade pressure differential will be assumed to be independent of the spanwise component y , and will be expressed as a function of pressure differential

$$V_P = K \sqrt{2 \frac{\Delta P}{\rho}}$$

The velocity distribution will be expressed as

$$V_B = U - C_U \left(\frac{y}{\delta} \right)^{1/N}$$

where N is an integer value. The net leakage velocity is then

$$V_L = V_P + V_B = K \sqrt{2 \frac{\Delta P}{\rho}} + U - C_U \left(\frac{y}{\delta} \right)^{1/N}$$

and the net energy loss in the leakage fluid is

$$\Delta E = \frac{P}{2} \int_0^\lambda \int_{r_1}^{r_t} \left(K \sqrt{2 \frac{\Delta P}{\rho}} + U - C_U \left(\frac{y}{\delta} \right)^{1/N} \right)^3 dy dr$$

Letting the absolute fluid velocity C_U be defined by a slip function ξ

$$C_U = \frac{U}{\xi} = \frac{\omega r}{\xi}$$

with ω being the angular velocity,

$$\Delta E = \frac{\rho}{2} \int_0^\lambda \int_{r_1}^{r_t} \left(K \sqrt{2 \frac{\Delta P}{\rho}} + \omega r \left(1 - \frac{1}{\xi} \left(\frac{y}{\delta} \right)^{1/N} \right) \right)^3 dy dr$$

The equation is solved by integration of the expanded function, assuming ΔP independent of y and the boundary layer buildup not dependent upon the radius. This latter assumption may be valid since the fluid velocity C_U increases in proportion to the boundary layer growth length between blades. The first integration results in the following:

$$\begin{aligned} \Delta E = \frac{\rho \lambda}{2} \int_{r_0}^{r_t} \left[K^3 \left(2 \frac{\Delta P}{\rho} \right)^{3/2} + 4K^2 \frac{\Delta P}{\rho} \omega r \left(1 - \frac{1}{\xi} \left(\frac{\lambda}{\delta} \right)^{1/N} \frac{N+1}{N} \right) + \right. \\ \left. 2K \sqrt{2 \frac{\Delta P}{\rho}} \omega^2 r^2 \left(1 - \frac{2}{\xi} \frac{N}{N+1} \left(\frac{\lambda}{\delta} \right)^{1/N} + \frac{1}{\xi} \frac{N}{N+2} \left(\frac{\lambda}{\delta} \right)^{2/N} \right) + \right. \\ \left. \omega^3 r^3 \left(1 - \frac{2}{\xi} \left(\frac{\lambda}{\delta} \right)^{1/N} \frac{N}{N+1} + \frac{2}{\xi^2} \left(\frac{\lambda}{\delta} \right)^{2/N} \frac{N}{N+2} - \frac{1}{\xi^3} \left(\frac{\lambda}{\delta} \right)^{3/N} \frac{N}{N+3} \right) \right] dr \end{aligned}$$

The final integration can be accomplished by numerical methods. The differential pressure P is defined by the polynomial,

$$\Delta P = \Delta P_{\max} (A + Br + Cr^2 + \dots)$$

The results are then tied to the boundary layer thickness δ , which has not been developed. The boundary layer thickness would depend upon the blade spacing and relative rotational effects since the blade tends to destroy the boundary layer as it passes past a point on the housing.

Method of Determining Blade Loading Increase Due to Blade Scraping of the Boundary Layer. The boundary layer affects the blade spanwise pressure distribution at the blade tip for the case where the boundary layer thickness δ is greater than the clearance λ ($\delta > \lambda$). This is due to the relative boundary layer velocity

impinging on the blade tip. The velocity relative to the blade goes from W_U at the point where $y/\delta = 1$ to the value of $C_U (\lambda/\delta)^{1/N} + W_U$ at the point where $y/\delta = \lambda/\delta$ (Fig. 7).

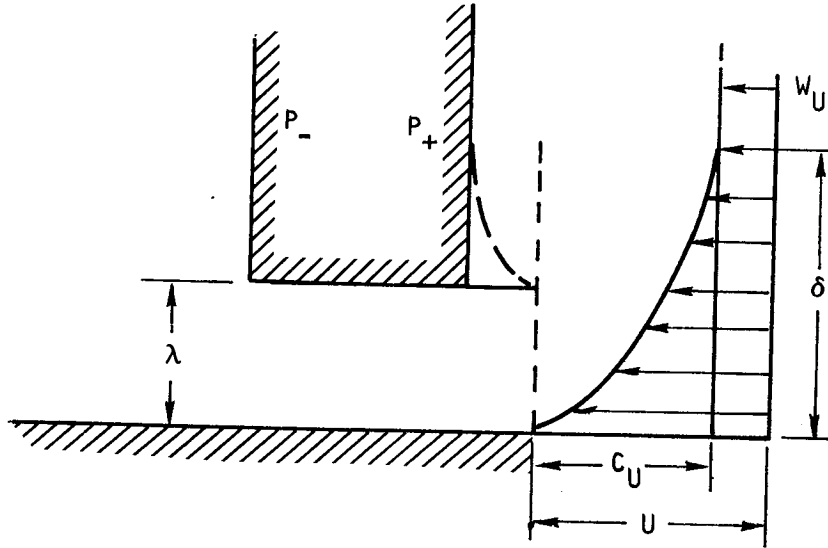


Figure 7. Blade Pressure Rise Due to Boundary Layer Scraping

The pressure rise then is due to the added velocity component $C_U (y/\delta)^{1/N}$ over the blade tip. Letting the pressure variation

$$P_y = \frac{1}{2g} \left[\left(W_U + C_U \left(\frac{y}{\delta} \right)^{1/N} \right)^2 - W_U^2 \right]$$

so that

$$P_y = \frac{1}{2g} \left[C_U^2 \left(\frac{y}{\delta} \right)^{2/N} + 2 C_U W_U \left(\frac{y}{\delta} \right)^{1/N} \right]$$

the pressure then is integrated over the blade spanwise interval of influence of $y = \lambda$ to δ and the meridional distance along the blade m at a radius r to determine the torque caused by the increased blade load. This, then, gives

$$\Delta T = \int_{\lambda}^{\delta} \int_{m_0}^{m_T} P_y r dy dm$$

or

$$\Delta T = \frac{\delta}{2g} \int_{\lambda/\delta}^1 \int_{m_0}^{m_T} \left(C_U^2 \left(\frac{y}{\delta} \right)^{2/N} + 2 C_U W_U \left(\frac{y}{\delta} \right)^{1/N} \right) r \, d\left(\frac{y}{\delta} \right) dm$$

Substituting for $W_U = U - C_U$ and $C_U = U/\xi = \omega r/\xi$; $W_U = \omega r (1 - 1/\xi)$

$$\Delta T = \frac{\delta \omega^2}{2g} \int_{\lambda/\delta}^1 \int_{m_0}^{m_T} \left(\frac{1}{\xi^2} \left(\frac{y}{\delta} \right)^{2/N} + \frac{2}{\xi} \left(1 - \frac{1}{\xi} \right) \left(\frac{y}{\delta} \right)^{1/N} \right) r^3 \, d\left(\frac{y}{\delta} \right) dm$$

Since y is not dependent on the radius r

$$\Delta T = \frac{\delta \omega^2}{2g} \int_{m_0}^{m_T} \left[\frac{1}{\xi^2} \left(\frac{y}{\delta} \right)^{(N+2)/N} \frac{N}{N+2} + \left(\frac{2}{\xi} - \frac{2}{\xi^2} \right) \left(\frac{y}{\delta} \right)^{(N+1)/N} \frac{N}{N+1} \right] \Big|_{\lambda/\delta}^1 r^3 dm$$

$$\Delta T = \frac{\delta \omega^2}{2g} \int_{m_0}^{m_T} \left[\frac{1}{\xi^2} \left(\frac{N}{N+2} \right) \left(1 - \left(\frac{\lambda}{\delta} \right)^{(N+2)/N} \right) + \frac{2}{\xi} \left(\frac{N}{N+1} \right) \left(1 - \frac{1}{\xi} \right) \left(1 - \left(\frac{\lambda}{\delta} \right)^{N+1/N} \right) \right] r^3 dm$$

This represents the additional torque added to the blade due to boundary layer scraping. The radius of the blade tip r for a given impeller can be stated as a function of the meridional length of the blade and can be integrated. This is assuming that the boundary layer is considered independent of the radius, which is not necessarily valid at this point, as stated in the previous section. Under this assumption, however, and assuming the radius as a function of the meridional length, $r = a + bm$

$$\Delta T = \frac{K}{4b} \left[(a + bm)^4 \right]_{m=0}^{m=m_T}$$

where

$$K = \frac{\delta \omega^2}{2g} \left[\frac{1}{\xi^2} \left(\frac{N}{N+2} \right) \left(1 - \left(\frac{\lambda}{\delta} \right)^{N+2/N} \right) + \frac{2}{\xi} \left(\frac{N}{N+1} \right) \left(1 - \frac{1}{\xi} \right) \left(1 - \left(\frac{\lambda}{\delta} \right)^{N+1/N} \right) \right]$$

Model Formulation to Determine Torque and Head Change Due to Tip Clearance

Torque Loss Due to Leakage Momentum. A loss in torque can be calculated by the momentum force caused by the leakage mass flowrate \dot{m}_L moving through the clearance space λ at a velocity V_L , or

$$\Delta F = \dot{m}_L V_L$$

If the mass flowrate is determined by continuity $\dot{m}_L = \rho \lambda V_L dr$ for the incremental area λdr , the incremental torque is then

$$dt_L = \rho \lambda V_L^2 r dr$$

If the leakage velocity is defined as the blade loading ΔP by use of an orifice equation

$$V_L = K \sqrt{2 \frac{\Delta P}{\rho}},$$

$$T_L = 2K^2 \lambda \int \Delta P r dr$$

The differential blade pressure ΔP can be formed by the blade loading program of Appendix B, and can be expressed as a function of radius in polynomial form.

$$\Delta P = \Delta P_{\max} (A + Br + Cr^2 + \dots)$$

The resultant integral was given as

$$T_L = 2K^2 \lambda \int_{r_1}^{r_t} \Delta P_{\max} (A + Br + Cr^2 + \dots) r dr$$

and this was readily solved to yield

$$T_L = 2K^2 \lambda \Delta P_{\max} \left(\frac{A}{2} (r_t^2 - r_1^2) + \frac{B}{3} (r_t^3 - r_1^3) + \frac{C}{4} (r_t^4 - r_1^4) + \dots \right)$$

By the assumption that the spanwise pressure gradient was negligible and that the blade pressure differential can be expressed as an average across the span, the blade torque can be found. This was done by integrating the blade loading across the area bdr . The span of the blade b is variable, but should be expressible as a function of radius r .

The assumption of a constant meridional velocity throughout the impeller gives the relation

$$b = \frac{b_t r_t}{r}$$

This leads to blade torque equation

$$T_B = b_t r_t \int_{r_1}^{r_t} \Delta P dr$$

Expressing the pressure as before and integrating the solution for torque is

$$T_B = b_t r_t \Delta P_{MAX} \left(A(r_t - r_1) + \frac{B}{2} (r_t^2 - r_1^2) + \frac{C}{3} (r_t^3 - r_1^3) + \dots \right)$$

The leakage clearance tends to reduce the blading torque by movement of fluid across the clearance space.

$$T_T = T_B - T_L$$

Referencing the blading torque T_B as the torque expended by the machine at zero clearance, the ratio of the torque developed by the blade with clearance T_C to that with zero clearance T_O is

$$\frac{T_C}{T_O} = 1 - \frac{T_L}{T_B}$$

The resultant equation is then

$$\frac{T_C}{T_O} = 1 - \frac{2K^2\lambda}{b} \left[\frac{\left(\frac{A}{2r_t^2} \left(1 - \left(\frac{r_1}{r_t} \right)^2 \right) + \frac{B}{3r_t} \left(1 - \left(\frac{r_1}{r_t} \right)^3 \right) + \frac{C}{4} \left(1 - \left(\frac{r_1}{r_t} \right)^4 \right) + \dots \right)}{\left(\frac{A}{r_t} \left(1 - \frac{r_1}{r_t} \right) + \frac{B}{2r_t} \left(1 - \left(\frac{r_1}{r_t} \right)^2 \right) + \frac{C}{3} \left(1 - \left(\frac{r_1}{r_t} \right)^3 \right) + \dots \right)} \right]$$

The equation was solved for the Mark 4 oxidizer impeller as a test case for polynomial curve fits of the pressure from order 2 to 4 with the same results within 4 percent. The major factor here, however, was that the defining polynomial of the blade pressure differential must be accurate over the interval r_1 to r_t . For additional checks of the equation, an impeller tested and reported, by Wood, et.al. (Ref. 7) was checked and found to agree well with the model. The comparison of test data with the model is presented in Fig. 8.

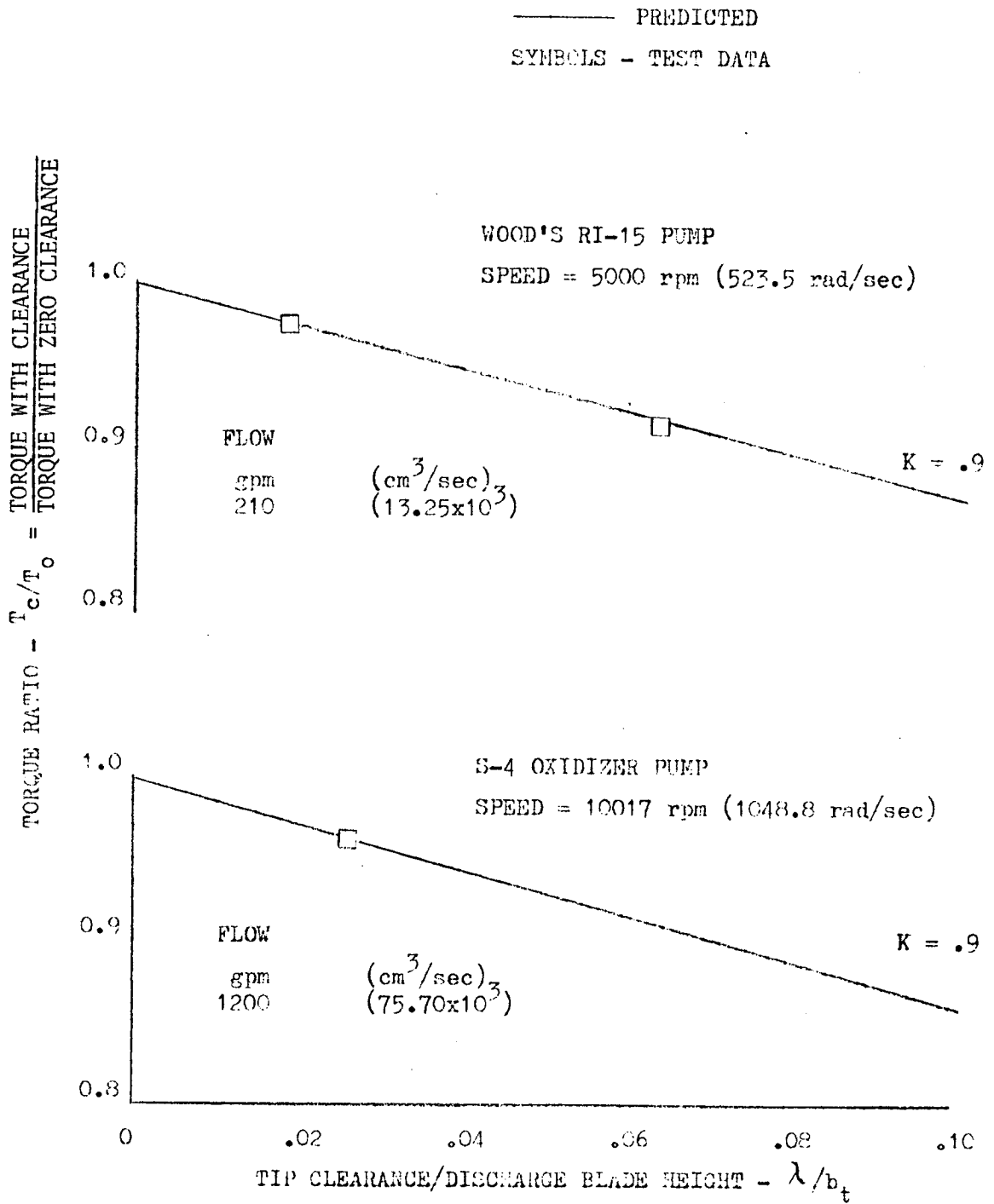


Figure 8. Torque Loss Due to Momentum Loss in the Tip Clearance Leakage Flow

Pump Head Rise as Affected by Impeller Tip Clearance Flow Based Upon Impeller Head Coefficient. The impeller head-flow characteristic is set by the impeller design geometry, namely blade angle distribution, radius ratio, solidity, etc. The delivered flow from a pump is not necessarily the same as that found flowing through the impeller. This is caused by the recirculation of the leakage flow around the impeller. With shrouded impellers, it is in the form of seal leakage and, with open-faced impellers, it is caused by the tip clearance flow recirculation. For small shrouded impellers or impellers with relatively large tip clearances, this recirculation flow becomes very large and must be taken into account by the designer during the analysis and design. The flow causes the impeller to operate at a flow different than delivered and will result in a shift in the head-flow performance.

The leakage flow is a function of the clearance area, the pump pressure rise, and the blockage. The delivered throughflow of an impeller is $Q_D = C_M A = C_M 2\pi r_A b_A$, where b_A is the average blade height and r_A is the average radius (Fig. 9). The leakage flow is then $V_L (2\pi r_A) \lambda_A$. Taking the ratio of flows,

$$\frac{Q_L}{Q_D} = \frac{V_L (2\pi r_A) \lambda_A}{C_M (2\pi r_A) b_A} = \frac{V_L \lambda_A}{C_M b_A}$$

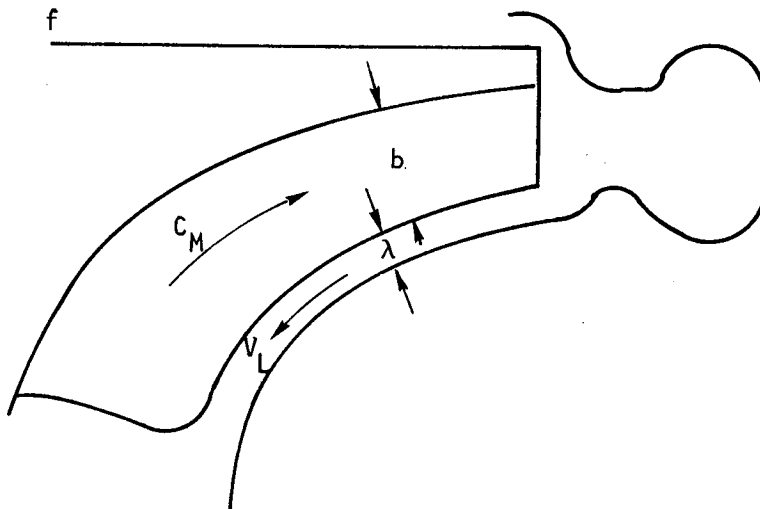


Figure 9. Meridional View of Impeller

The leakage velocity V_L can be expressed as

$$V_L = K \sqrt{2g\Delta H}$$

where the impeller head rise

$$\Delta H = \psi_D \frac{U_t^2}{g}$$

with ψ_D being the pump delivered head coefficient and U_t the impeller tip velocity, then

$$V_L = KU_t \sqrt{2\psi_D}$$

Defining the impeller flow coefficient $\phi_D = C_M/U_t$, we have

$$\frac{Q_L}{Q_D} = \frac{K \sqrt{2\psi_D}}{\phi_D} \frac{\lambda}{b_A}$$

with subscripts D and L defining delivered and leakage flow, respectively. The leakage flow Q_L adds to the design flow Q_D to determine the true impeller flow Q_T , or

$$\frac{\phi_T}{\phi_D} = \frac{Q_T}{Q_D} = \frac{Q_L + Q_D}{Q_D} = 1 + \frac{K \sqrt{2\psi_D}}{\phi_D} \frac{\lambda}{b_A}$$

If a pump head-flow characteristic is known, the impeller head coefficient ψ may be represented as a linear function of the flow coefficient so that $\psi = A+B\phi$ or $\psi_D = A+B\phi_D$, where B is the slope of the head-flow curve. This can be used on most pumps for fairly large intervals of flow with sufficient accuracy (Fig. 10). The resultant head coefficient with leakage flow added to impeller throughflow is then $\psi_C = A + B\phi_D \phi_T/\phi_D$ so

$$\psi_C = A+B \left(\phi_D + K \sqrt{2\psi_D} \frac{\lambda}{b_A} \right)$$

Now, since $A = \psi_D - B\phi_D$,

$$\psi_C = \psi_D + \frac{B\lambda K}{b_A} \sqrt{2\psi_D}$$

Since the zero clearance head coefficient ψ_o equals the delivered head coefficient ψ_D , the ratio of the head coefficients is

$$\frac{\psi_C}{\psi_o} = 1 + \frac{B\lambda K}{b_A} \sqrt{\frac{2}{\psi_D}}$$

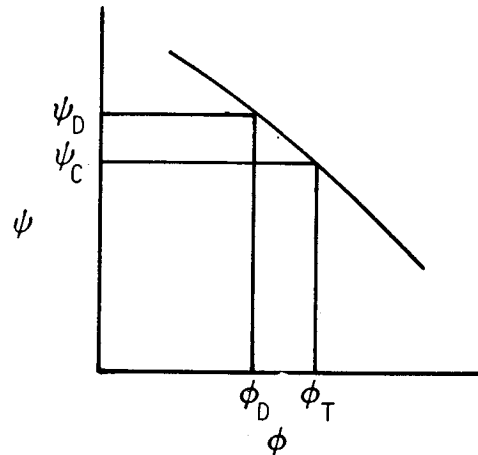


Figure 10. Head Shift Due to Tip Clearance Leakage Flow Increase

The test data of two pumps were used to test the validity of the above equation. The results are presented in Fig. 11. The results showed good agreement. The orifice factor K, determined from the test data, varies from 0.74 for the S-4 oxidizer pump to 0.702 for Woods (Ref. 7) test pump. The correlation of this parameter may be dependent upon a function such as the eye-to-tip radius ratios which were 0.65 and 0.59 for the respective pumps, or for the head coefficients which were 0.449 and 0.302, respectively. This method does indicate a possible method for determination of the head reduction due to a tip clearance increase.

$$\frac{\psi_c}{\psi_o} = 1 + \frac{\beta K \lambda}{b_A} \sqrt{\frac{2}{\psi_D}}$$

	SPEED		FLOWRATE	
	PUMP	RPM (rad/sec)	GPM (cm ³ /sec)	(cm ³ /sec)
○	S-4	10017 (1048.8)	1200	(75.70x10 ³)
□	RI-15	5000 (523.5)	210	(13.25x10 ³)
—	PREDICTED		K = .71	

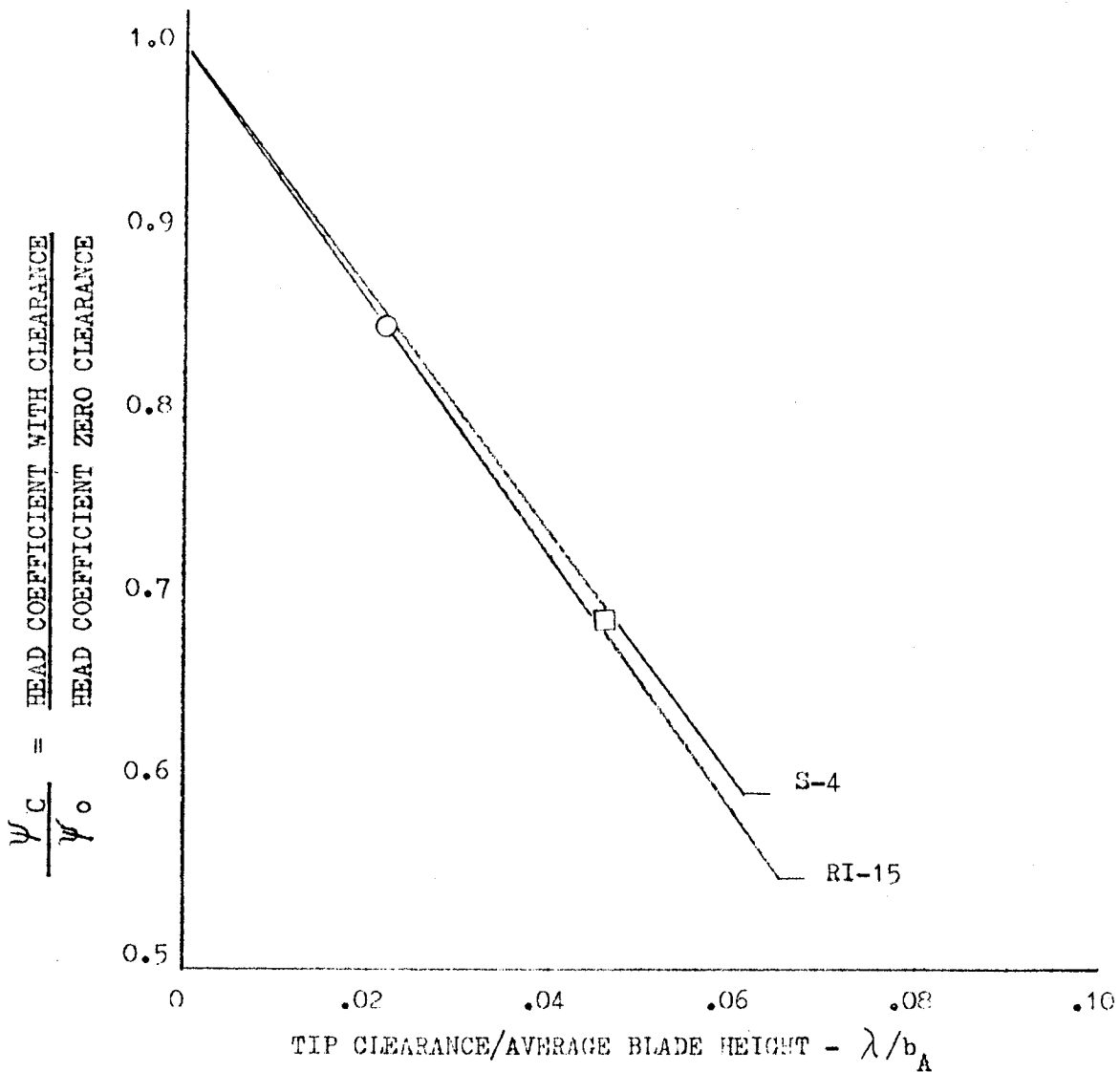


Figure 11. Head Loss Due to Tip Clearance at Design Flow

Pump Head Rise as Affected by Impeller Tip Clearance Flow Based Upon Impeller Blade Loading. In the previous section, the impeller tip leakage flow was described as a function of the total head rise of the pump. This method has merit because the individual blade loading determines the resultant pump head rise. It is then of interest to approach the tip leakage flow from the point of determining a leakage through a space (λ) resulting from a blade pressure differential (ΔP) and integrated over the meridional length of the blade tip (Fig. 12).

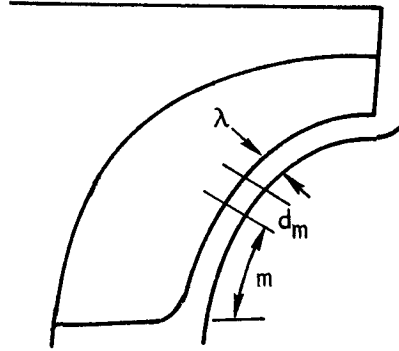


Figure 12. Meridional View of Impeller

Defining a leakage flow across the blade tip as being a function of meridional increment dm , the clearance λ , and the leakage velocity defined by the blade loading, we have

$$Q_L = V_L A = K \sqrt{2\Delta P/\rho} \lambda dm$$

Blade loading ΔP can be defined as a function of m in polynomial form $\Delta P = \Delta P_{\max} (A+Bm+Cm^2+\dots)$ or $= \Delta P_{\max} (M)$, so that

$$Q_L = K\lambda \sqrt{\frac{2}{\rho} \Delta P_{\max}} \int_0^{m_T} \sqrt{M} dm$$

$$M' = \int_0^{m_T} \sqrt{A+Bm+Cm^2} dm = \int_0^{m_T} \sqrt{M} dm$$

The solution of the integral is available and the results can be represented as a dimensionless form factor M' , so that

$$Q_L = K\lambda \sqrt{\Delta P_{\max}} \sqrt{2/\rho} M'$$

The form factor represents the distribution of the blade loading in the above equation. The delivered flow, $Q_D = \phi_D U_t 2\pi r_t b_t$.

The ratio of the leakage flow to delivered flow becomes

$$\frac{Q_L}{Q_D} = \frac{K\lambda \sqrt{\Delta P_{\max}} \sqrt{2/\rho} M'}{(\phi_D U) 2\pi r_t b_t} = \frac{\phi_L}{\phi_D}$$

Leakage flow adds to the delivered flow to determine the true impeller flow Q_T for a given clearance

$$\frac{Q_T}{Q_D} = \frac{Q_L + Q_D}{Q_D} = 1 + \frac{K\lambda \sqrt{\Delta P_{\max}} \sqrt{2/\rho} M'}{(\phi_D U) 2\pi r_t b_t}$$

If $\psi_C = A+B(\phi_L + \phi_D)$ and $\psi_D = A+B\phi_D$

$$\psi_C = A+B \left(1 + \frac{K\lambda \sqrt{\Delta P_{\max}} \sqrt{2/\rho} M'}{\phi_D U_t 2\pi r_t b_t} \right) \phi_D$$

or, with ψ_D being or zero clearance reference head coefficient ψ_0 ,

$$\frac{\psi_C}{\psi_0} = 1 + \frac{B\phi_D}{\psi_D} \left(\frac{K\lambda \sqrt{\Delta P_{\max}} \sqrt{2/\rho} M'}{2\pi\phi_D U_t r_t b_t} \right)$$

Where B is the slope of the reference head flow coefficient curve, b_t , r_t , and U_t is the impeller tip blade height, radius, and tangential velocity, respectively.

Efficiency Correlation With the Head and Power Change Due to Tip Clearance. The pump efficiency that is of interest to this application is the overall efficiency, which is defined as the energy increase of the delivered flow divided by the power input to the pump. The models presently formulated were developed to predict the effective torque or power change required due to tip clearance, and the head or energy level reduction due to tip clearance effect. The combination of a torque and head prediction models can then result in a prediction of efficiency.

If the reference efficiency is defined as

$$\eta_0 = \frac{\gamma Q_0 H_0}{\text{BHP}_0}$$

where γ is the specific weight, and the efficiency at a tip clearance is

$$\eta_C = \frac{\gamma Q_C H_C}{\text{BHP}_C}$$

When the comparison is made at the same delivered flowrate, the ratio of efficiencies can be found as

$$\frac{\eta_0}{\eta_C} = \frac{H_0}{H_C} \frac{BHP_C}{BHP_0}$$

or for comparable pump speeds

$$\frac{\eta_0}{\eta_C} = \frac{H_0}{H_C} \frac{T_C}{T_0}$$

where the torque and head ratios are given by the models developed. This approach was developed to predict the efficiency ratio and was used in the data correlation.

TASK C: IMPELLER CLEARANCE AND COST ANALYSIS

The hydrodynamic analysis and mechanical design of a liquid oxygen pump were completed for the following nominal operating conditions:

Flow, gpm (m^3/s)	=	5000 (0.3155)
Head, feet (m)	=	3100 (944.88)
NPSH, feet (m)	=	30 (9.144)

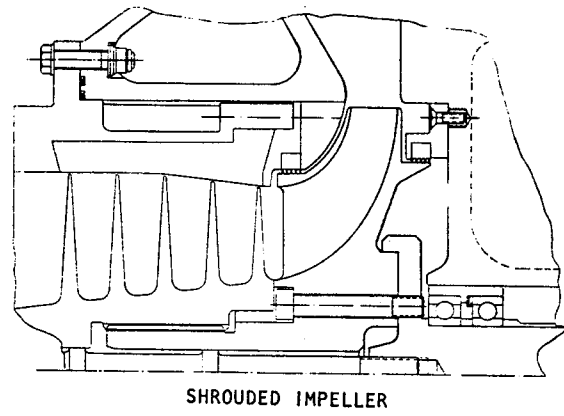
The design used state-of-the-art practice in both the hydrodynamic and mechanical design areas, and was sufficiently complete for obtaining impeller clearance and cost analysis. Two impeller configurations (shrouded and unshrouded) of the basic design were priced and found to be approximately the same.

Hydrodynamic Design

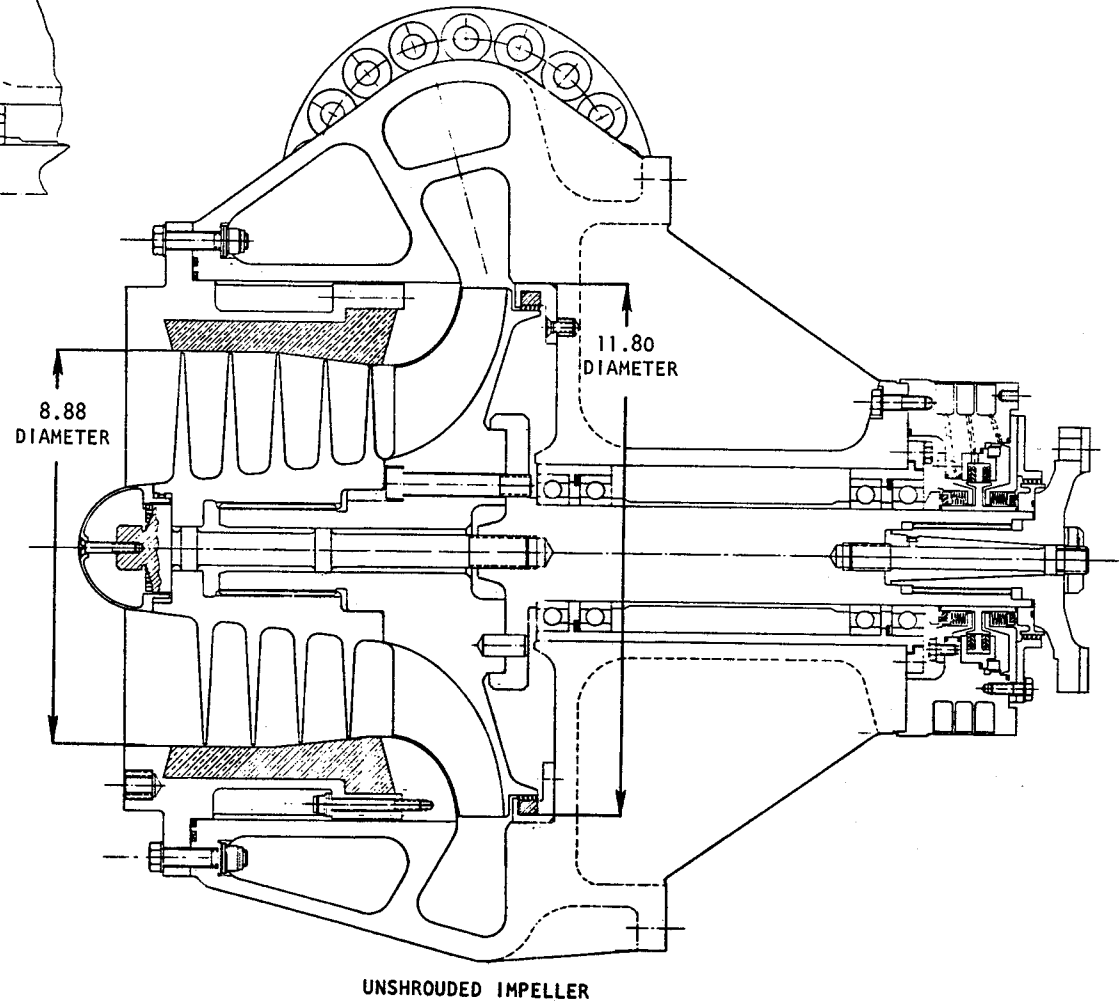
To meet the nominal operating conditions (see above), the pump utilizes a high suction specific speed inducer followed by a centrifugal impeller. Shrouded and unshrouded impeller configurations were designed and are shown in Fig. 13. Current state of the art permits a suction specific speed of 45,000 to be obtained by the inducer; therefore, a pump speed of 8150 rpm (853.5 rad/s) was selected. The inducer hub was tapered while the outside diameter was cylindrical for half the axial length, then tapered to a decreased diameter. The high suction specific speed used requires low inducer inlet velocities and large inlet diameters. The inducer has an inlet flow coefficient of approximately 0.095 and a head coefficient of approximately 0.12. Tapering of the inducer outside diameter at the discharge resulted in a better impeller eye-to-tip diameter ratio and increased turning radius for the impeller. The impeller was approximately 11.8 inches (0.30 m) in diameter, with an impeller discharge flow coefficient of 0.11. Five full and five partial vanes were used with a discharge blade angle of 32 degrees (0.557 rad) from tangential. A scroll collector was designed to provide minimum radial loads on the pump bearings. Also, a conical diffuser was used to ensure high pump efficiency. The axial thrust was controlled by the wear ring on the impeller rear shroud.

Stress Analysis

The stress analysis of the LO₂ pump design is summarized in Fig. 14. Both the deflected and undeflected positions of the volute inner walls relative to the impeller are shown. The deflections calculated are due to pressure loads within the volute and to centrifugal loads on the impeller. The differential thermal contractions of the parts were not included because the parts were assumed to be made of the same material (Tens-50) and were of uniform temperature. The operating pressures and design parameters are also noted in Fig. 14. The volute design as shown was not desirable for the unshrouded impeller application because of the relatively large axial deflection of the volute front wall from the impeller blade tip (approximately 0.010 inch (0.0254 cm)).

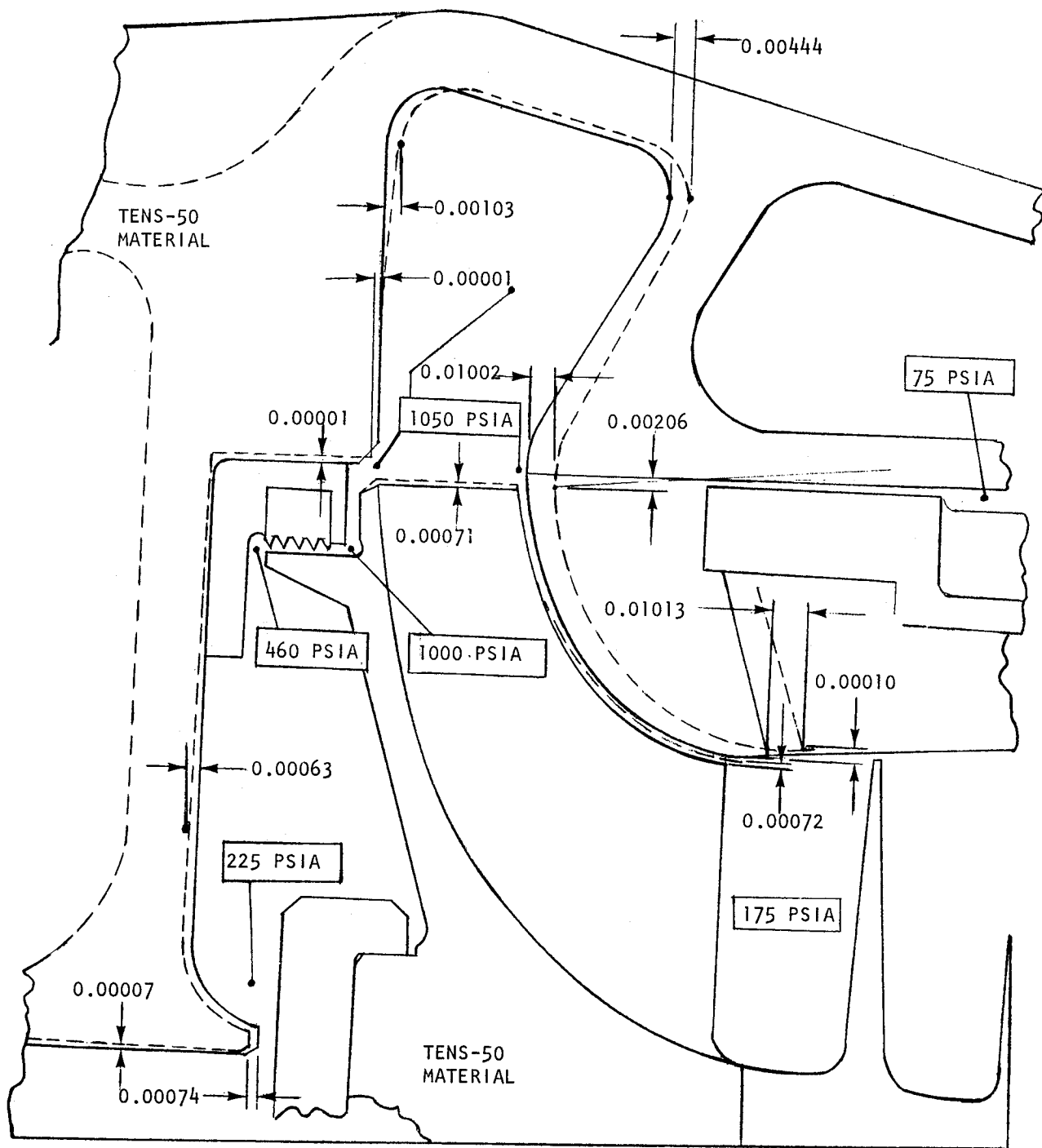


SHROUDED IMPELLER



UNSHROUDED IMPELLER

Figure 13. LO₂ Pump Configuration Layouts



LO_2
 $Q = 5000 \text{ gpm}$ $NPSH = 30 \text{ feet}$
 $H = 3100 \text{ feet}$ $N = 8150 \text{ rpm}$
 $Pd = 1510 \pm 50 \text{ psi}$

Figure 14. Unshrouded LO_2 Impeller Stress Investigation

The design was modified to reduce the axial deflection of the volute front wall from the impeller blade tip. By increasing the thickness of the volute walls and structural members, a 0.003-inch (0.00762 cm) maximum relative axial deflection of the volute front wall with respect to the impeller blade tip was obtained. This stress analysis investigation indicated that the volute front wall, with its box-shaped structural ring section, must be increased in stiffness by about 45 percent. A sketch of the new section superimposed on the original section is shown in Fig. 15. This figure shows the approximate radial increase of 0.75 inch (1.905 cm) in OD of the box-shaped structure and a smaller cored section.

Clearance Analysis

For a given pump design, the hardware and manufacturing costs should be lower if increased tip clearance is permitted. However, in actual practice the unshrouded impeller pump designs are generally manufactured with small blade tip and housing clearances to maintain efficiency. To obtain the desired close clearance, profiles are machined on a pattern from which the impeller and housing contours are then duplicated. The design impeller tip clearance at assembly is then obtained by the use of shims. To maintain impeller tip clearance during pump operation, axial and radial thrust, thermal and pressure deflections, mechanical dynamics of the pump rotor, and shaft deflections due to cavitation-induced radial loads are some of the important factors that must be considered in a proper design. Increased clearances or changes in pump design may be required to allow for all these design factors.

If the engine system is found to be less efficient and a larger (or more efficient) pump drive system is required, the net effect of the large drive system on engine performance should be determined. This net effect could be related through engine thrust and specific impulse (I_s) of the vehicle and, in turn, to the vehicle payload. Some representative exchange factors for a gas generator cycle engine with an LO_2 pump in the same general class as the one under study (J-2 LO_2 pump) are given below:

1. An increase of 1.0 percent (for example, from 80.0 to 81.0 percent) in LO_2 pump efficiency yields a +0.92-percent change in engine thrust.
2. An increase of 1.0 percent (for example, from 80.0 to 81.0 percent) in LO_2 pump efficiency yields a +0.082-second change in engine I_s .
3. An increase of 1.0 percent in LO_2 pump efficiency for the six J-2 engines on the S-II and S-IVB stages of the Saturn V will change the payload by about 315 pounds.

Cost Analysis

The liquid oxygen pump design cost analysis was completed by Rocketdyne Manufacturing Planning. Two configurations (shrouded and unshrouded impellers) of the basic design were priced on the basis of one end item. Tables 1 and 2 list the manufacturing and material cost estimates for both the shrouded and unshrouded LO_2

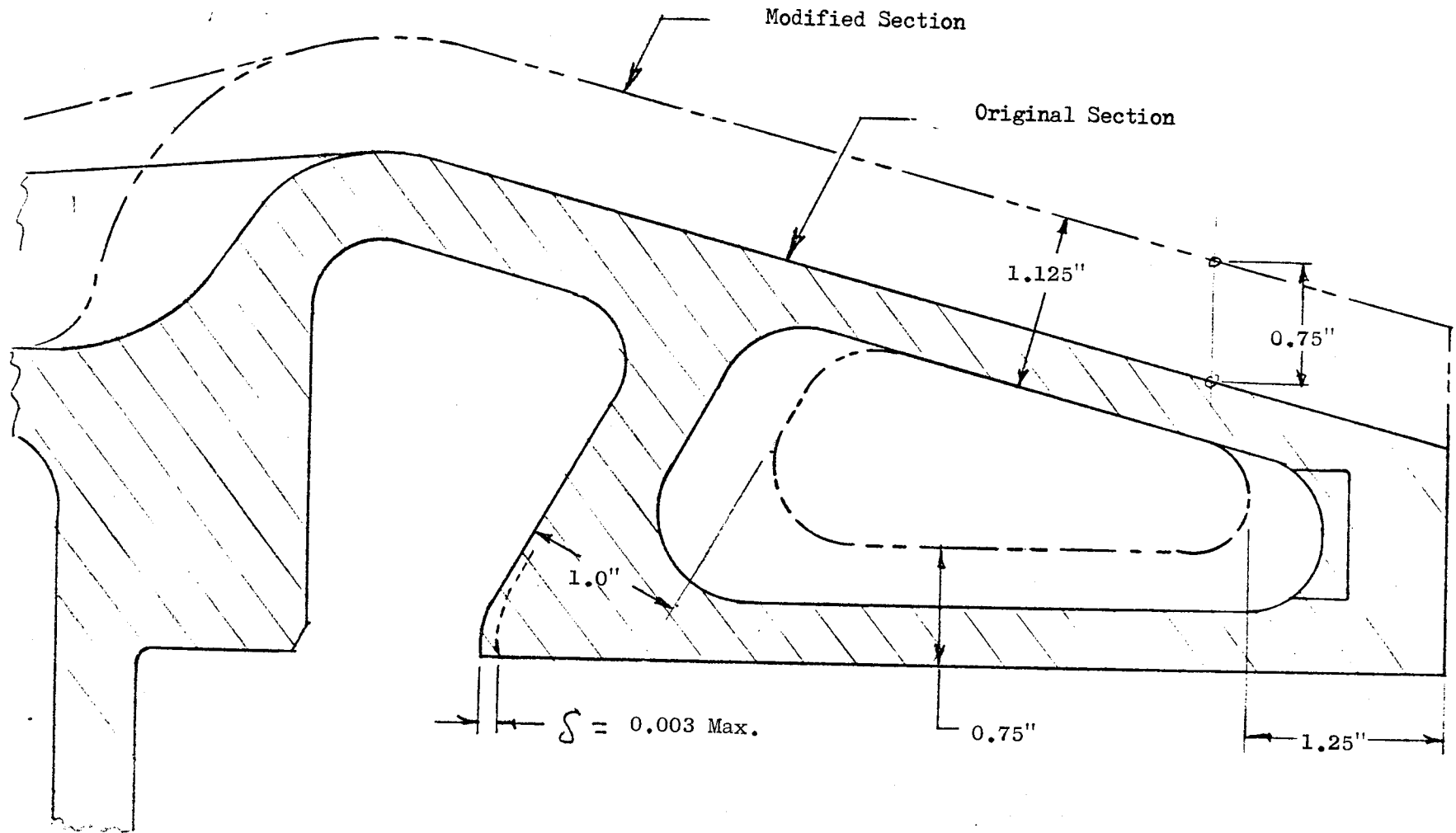


Figure 15. Volute Section for $S = 0.003$ Inch Maximum

TABLE 1. MANUFACTURING AND MATERIAL COST ESTIMATES
FOR SHROUDED LO₂ PUMP ASSEMBLY

	<u>Labor Hours</u>	<u>Material Dollars</u>
Manufacturing		
Fabrication	2324	
Tooling		
Basic	510	
Maintenance	186	
Tool Engineer	<u>50</u>	
Subtotal Tooling	746	1,670
Manufacturing Services		
Manufacturing Support	220	
Manufacturing Engineer	<u>245</u>	
Subtotal Manufacturing Services	465	
Material		
Nonproductive		1,670
Productive		12,305
Vendor Tooling		<u>33,150</u>
Total	3535	47,125

TABLE 2. MANUFACTURING AND MATERIAL COST ESTIMATES
FOR UNSHROUDED LO₂ PUMP ASSEMBLY

	<u>Labor Hours</u>	<u>Material Dollars</u>
Manufacturing		
Fabrication	2366	
Tooling		
Basic	510	
Maintenance	189	
Tool Engineer	<u>50</u>	
Subtotal Tooling	749	1,678
Manufacturing Services		
Manufacturing Support	--	
Manufacturing Engineer	<u>--</u>	
Subtotal Manufacturing Services	473	
Material		
Nonproductive		1,678
Productive		12,067
Vendor Tooling		<u>33,150</u>
Total	3588	46,895

pumps, respectively. Tables 3 and 4 list the cost analysis breakdown for the various pump component parts for both the shrouded and unshrouded pumps, respectively. The cost analysis included fabrication, tooling, inspection, and assembly (under clean room conditions). The cost of the unshrouded and shrouded impeller configurations was found to be approximately the same (\approx \$50,000).

The cost of the modified (thickened) volute increased the cost of the pump only a small amount (only the cost of the additional material required) and, therefore, did not affect the overall pump costs.

TABLE 3. COST ANALYSIS BREAKDOWN FOR COMPONENTS OF SHROUDED
LO₂ PUMP ASSEMBLY

Part Number and Part Name		Quantity	Total Fabrication Hours	Material Dollars	Vendor Tooling Dollars
AP70-126-3	Spinner	1	40	7	
-5	Shaft	1	46	54	
-7	Inducer	1	461	1110	
-9	Liner	1	28	634	
-15	Housing	1	125	263	
-33	Volute	1	202	1600	20,000
-39S	Spacer	1	45	15	
-43S	Impeller	1	107	150	12,000
-45	Pin	1	5	2	
-47	Shaft	1	126	371	
-49S	Seal	1	13	4	
-53S	Seal	1	15	111	
-55S	Retainer	1	33	14	
-59	Retainer	1	29	23	
-65	Spacer	1	24	36	
-67	Shaft	1	32	7	
-69	Retainer	1	33	39	
-73	Spacer	2	14	27	
-75	Plate	1	21	35	
-77	Ring	1	28	238	
-105	Washer	1	4	4	
-113	Aft Curvic Coupling	1	139	259	
-115	Aft Mating Ring	1	48	238	
-117	Seal	1	45	43	
-123	Retainer	1	18	35	
-125	Sleeve	1	41	475	
-127	Seal Housing	1	28	35	
-135	Cover	3	16	9	
-137	Manifold Housing	1	40	137	
-137A	Manifold Housing Assembly	1	116	--	
-149	Manifold Tubing	3	16	--	
-165S	Seal	1	14	111	
-167S	Seal	1	42	134	

TABLE 3. (Concluded)

Part Number and Part Name		Quantity	Total Fabrication Hours	Material Dollars	Vendor Tooling Dollars
AP70-126-	Pump Assembly	1	330	--	
-17	Seal	1	PP*	250	75
-19	Seal	1		275	75
-57	Bearing	4		23	
-63	Spring	2		500	
-85	Seal	1		1500	500
-87	Seal	2		112	
-89	Seal	2		68	
-93	Seal	1		80	
-95	Seal	1		85	
-103	Seal	1		38	
-107	Nut	1		4	
-119	Seal	1		1500	500
-129	Spring	1		250	
-133	Seal Assembly	4	PP*	1400	
Total Shrouded Pump Assembly		1	2,324	12,305	33,150

*Purchased Part

TABLE 4. COST ANALYSIS BREAKDOWN FOR COMPONENTS OF UNSHROUDED
LO₂ PUMP ASSEMBLY

Part Number and Part Name		Quantity	Total Fabrication Hours	Material Dollars	Vendor Tooling Dollars
AP70-126-3	Spinner	1	40	7	
-5	Shaft	1	46	54	
-7	Inducer	1	461	1110	
-9	Liner	1	28	634	
-15	Housing	1	125	263	
-15A	Housing Assembly	1	8	--	
-33A	Volute	1	202	1600	20,000
-39	Spacer	1	47	22	
-43	Impeller	1	135	150	12,000
-45	Pin	1	5	2	
-47	Main Shaft	1	126	371	
-49	Seal, Cover	1	15	4	
-53	Seal	1	16	111	
-55	Retainer	1	33	14	
-59	Retainer	1	29	23	
-65	Spacer	1	24	36	
-67	Shaft	1	32	7	
-69	Retainer	1	33	39	
-73	Spacer	2	14	27	
-75	Plate	1	21	35	
-77	Ring	1	28	238	
-105	Washer	1	4	4	
-113	Aft Curvic Coupling	1	139	259	
-115	Aft Mating Ring	1	48	238	
-117	Seal	1	45	43	
-123	Retainer	1	18	35	
-125	Sleeve	1	41	475	
-127	Seal Housing	1	28	35	
-135	Cover	3	18	9	
-137	Manifold Housing	1	40	137	
-137A	Manifold Housing Assembly	1	116	--	
-149	Manifold Tubing	3	16	--	
	Pump Assembly	1	385	--	

TABLE 4. (Concluded)

Part Number and Part Name		Quantity	Total Fabrication Hours	Material Dollars	Vendor Tooling Dollars
AP70-126-17	Seal	1	PP*	250	75
-19	Seal	1	↓	275	75
-57	Bearing	4	↓	23	
-63	Spring	2	↓	500	
-85	Seal	1	↓	1500	500
-87	Seal	2	↓	112	
-89	Seal	2	↓	68	
-93	Seal	1	↓	80	
-95	Seal	1	↓	85	
-103	Seal	1	↓	38	
-107	Nut	1	↓	4	
-119	Seal	1	↓	1500	500
-129	Spring	1	↓	250	
-133	Seal Assembly	4	PP*	1400	
Total Unshrouded Pump Assembly			2366	12,067	33,150

*Purchased Part

TASK D: TEST RIG AND INSTRUMENTATION DESIGN

The test rig and instrumentation design using an existing J-2 oxidizer pump was completed. Detailed analysis and design of all new and modified components necessary to test the pump at the Pump Calibration Facility were completed. The design layout included removal of the impeller front shroud, and incorporating a pressure scanning valve located in the pump shaft. Static pressure taps were located at various stations along the impeller blades to obtain blade loading data. A schematic of the "Scanivalve" test setup is shown in Fig. 16. The instrumentation design also incorporated provision for measuring wall static pressures and all parameters required to obtain the overall performance of the test pump.

Test Rig Design

A standard J-2 oxidizer pump and test adaptor was modified to obtain the pressure differential across the impeller tip at various stations along the vanes. Two approaches were considered and were as follows:

1. Use of a pressure scanning valve (Scanivalve Company, San Diego, California) located in the impeller shaft
2. Use of miniature transducers mounted on the impeller blades or in the impeller back shroud

The Scanivalve system was selected over the miniature transducers for obtaining the blade pressure data. The successful results using the Scanivalve system under NASA contract NAS3-11216 "Study of Inducer Load and Stress", and the need for increasing the number of measurements led to the Scanivalve selection.

Scanivalve Design. A standard model 48-J Scanivalve was selected and modified to meet the test conditions and program requirements. The modifications were as follows:

1. Use of stabilized O-ring sets to prevent implosion of the sensing seals
2. Installation of a 400-cycle drive motor with the required gear-train drive
3. Installation of a Statham pressure transducer
4. Purge port machined into the rotating valve

Because of the increased operating and purge pressures of up to 500 psi (413.7 N/cm^2), the rotating valve seals were modified by use of internal collars to prevent implosion of the O-rings. The use of a 400-cycle drive motor (Model JMC-115-400) permitted the Scanivalve to be rotated up to 6000 rpm (628.4 rad/sec). The gear-train drive permitted the valve to scan at the desired 1 rpm (0.1047 rad/sec). The Statham pressure transducer (Model PA 208TC-IM-350) was installed in the Scanivalve to measure the selected blade pressures from the pressure-sensing tubes.

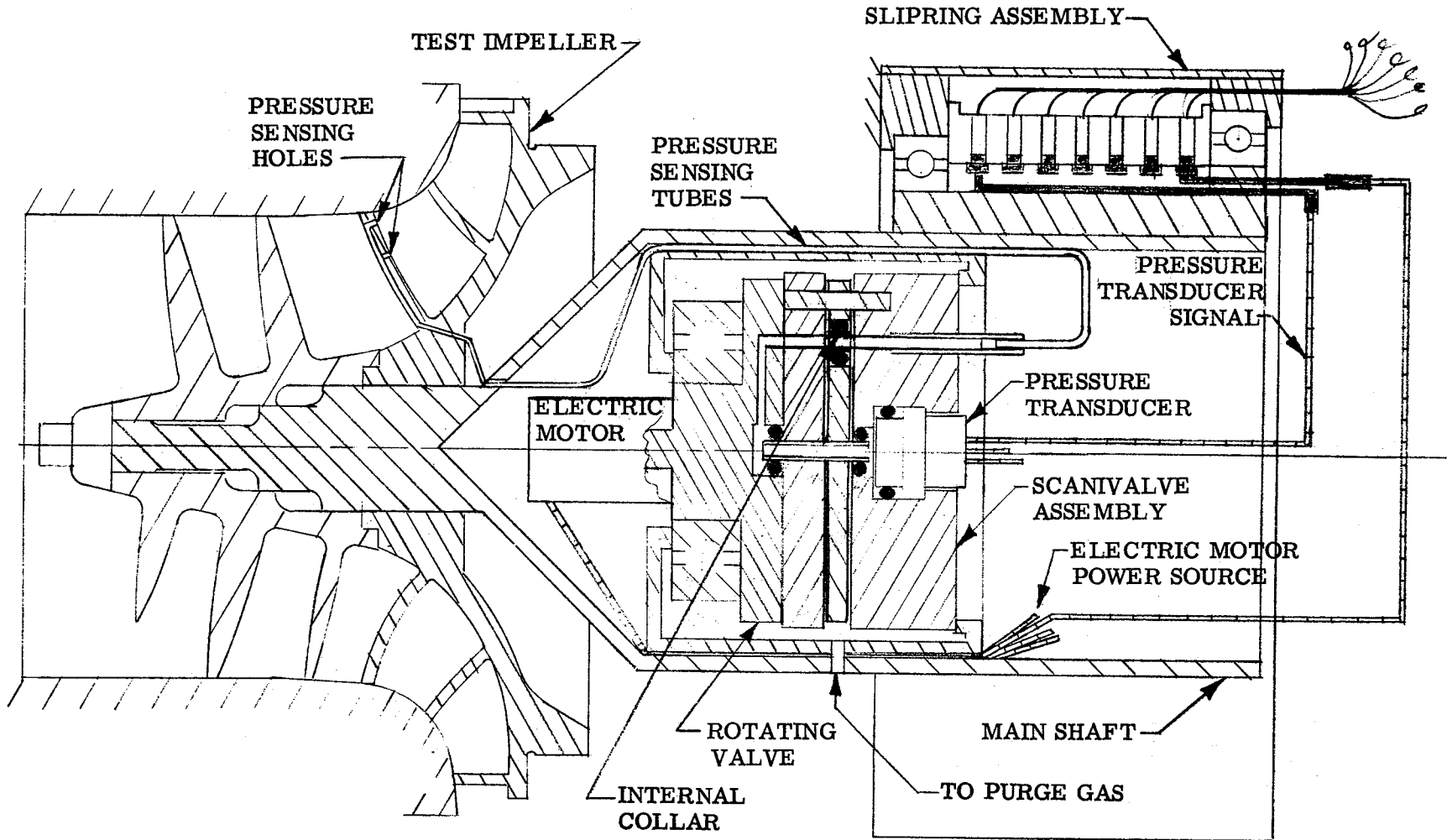


Figure 16. Scanivalve Test Setup Schematic

Blade pressure measurements selected included five locations each on both the suction and pressure surfaces along two of the tip and mean streamlines. These 20 pressure taps were connected to 0.040-inch (0.1016 cm) tubing which, in turn, were connected to the Scanivalve. To ensure that the tubing contained GN₂ only prior to pressure measurement, the Scanivalve rotating valve was modified to permit purging (Fig. 17). The purge port was located to permit tube purging when the pressure transducer measured a blank tap. When the Scanivalve obtained a blade pressure measurement, a blank tap was purged. With this Scanivalve purge sequence, purged GN₂ did not pass through the impeller passages when the blade pressure measurement was being recorded.

Impeller Modification. Both the J-2 oxidizer impeller (P/N 456293) and the J-2S oxidizer impeller (P/N 460422) were stress analyzed to determine the allowable speed when the front shrouds were removed. The allowable operating speeds were reduced primarily due to increased vane pressure bending stresses. The results showed that the J-2S impeller permitted higher operating speeds compared to the J-2 impeller because of increased material properties. The allowable operating speeds for the shroudless impellers for minimum and typical material properties and vane thicknesses are summarized below:

	<u>Minimum Material/ Minimum Vane</u>	<u>Typical Material/ Typical Vane</u>
J-2 impeller allowable rpm (rad/sec)	5090 (533.1)	5640 (590.7)
J-2S impeller allowable rpm (rad/sec)	6750 (706.9)	7300 (764.6)

From these results, the unshrouded J-2S impeller was selected for use in the J-2 oxidizer pump. The locations of the pressure taps on the impeller vanes were obtained and are shown in Fig. 18.

Design Layout. The mechanical and instrumentation design layout is shown in Fig. 19 and consists of the following elements:

1. Modified J-2 oxidizer pump
2. Modified J-2 oxidizer pump test adaptor
3. Quill shaft with shear neck
4. Torquemeter
5. Mount assembly

Detailed layouts prescribing the static pressure taps along the impeller front and rear housings profile were selected. Locations are shown in Fig. 20 and 21. These impeller front taps were located at the same radii as the impeller blade tip pressure taps (Fig. 18).

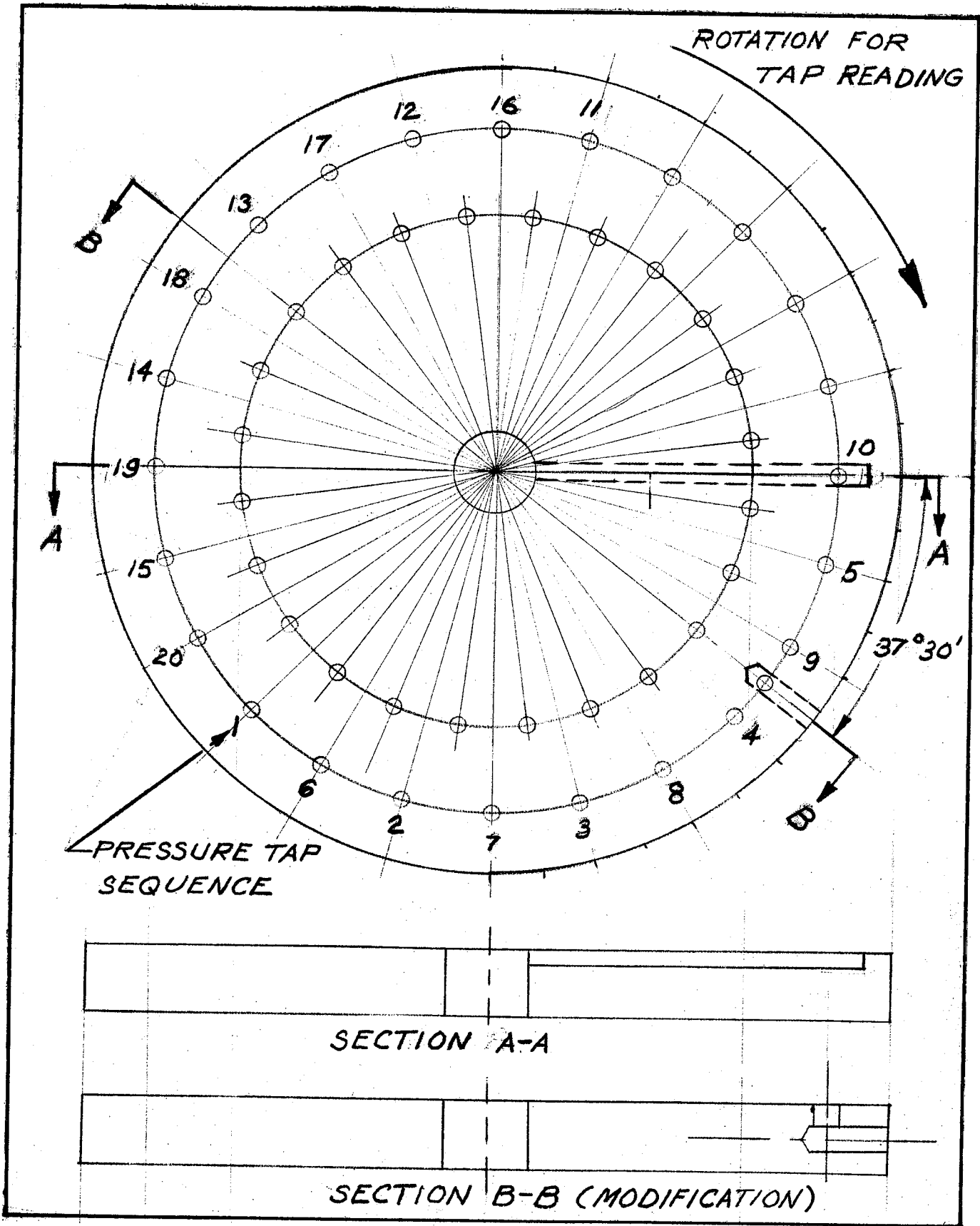


Figure 17. Modification to Scanivalve Rotating Valve

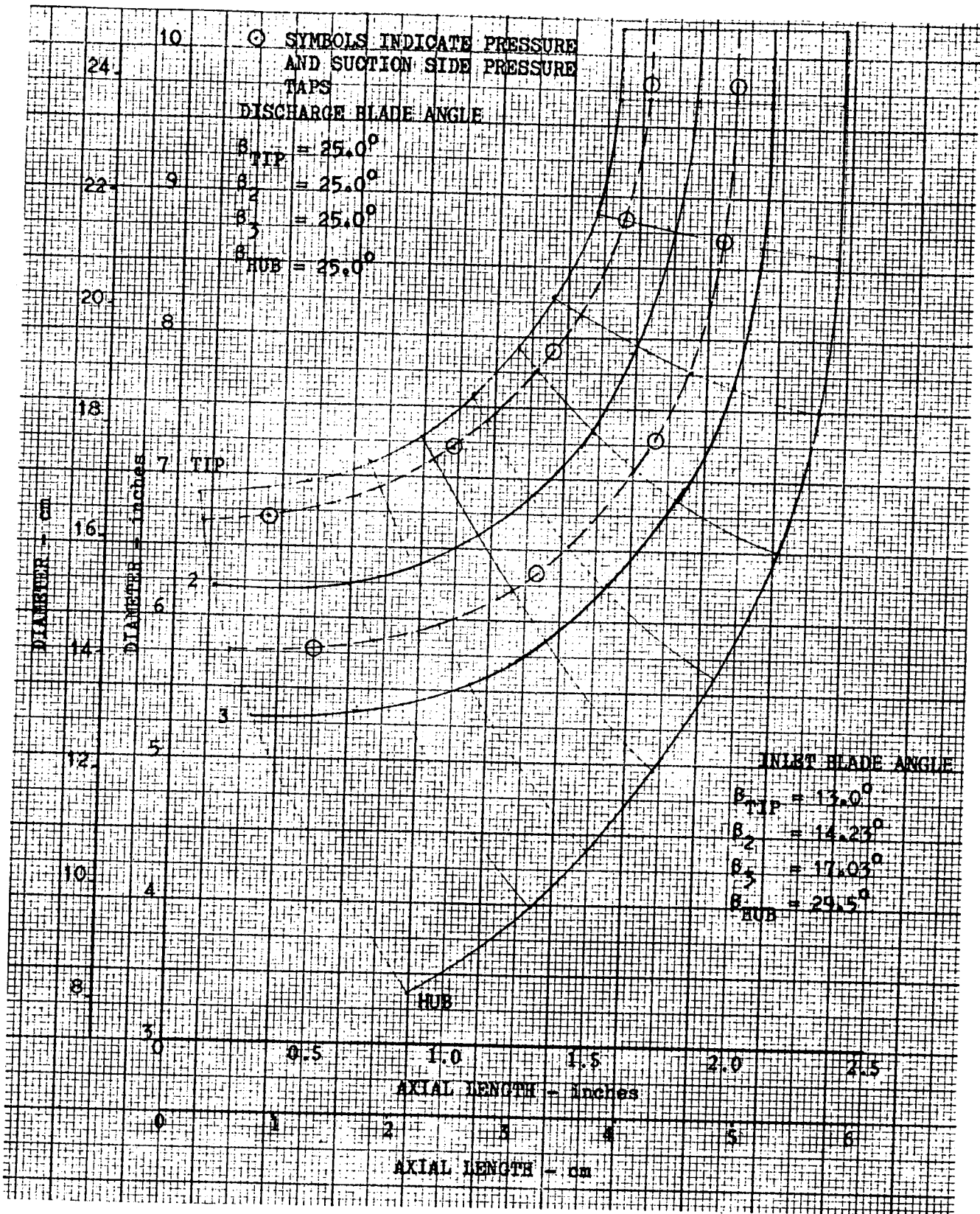


Figure 18. J-2 Oxidizer Pump Impeller Front Shroud Removed.

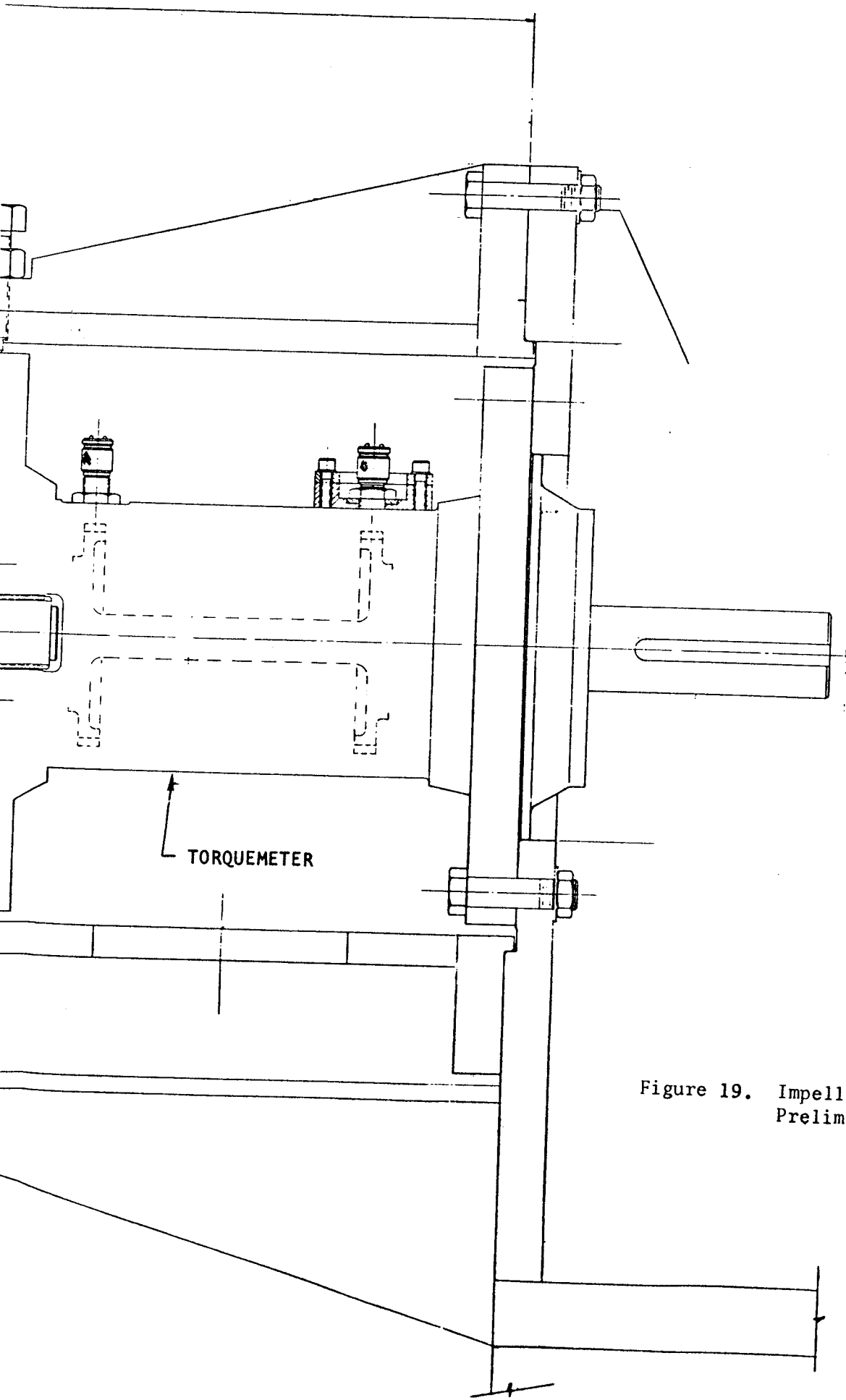
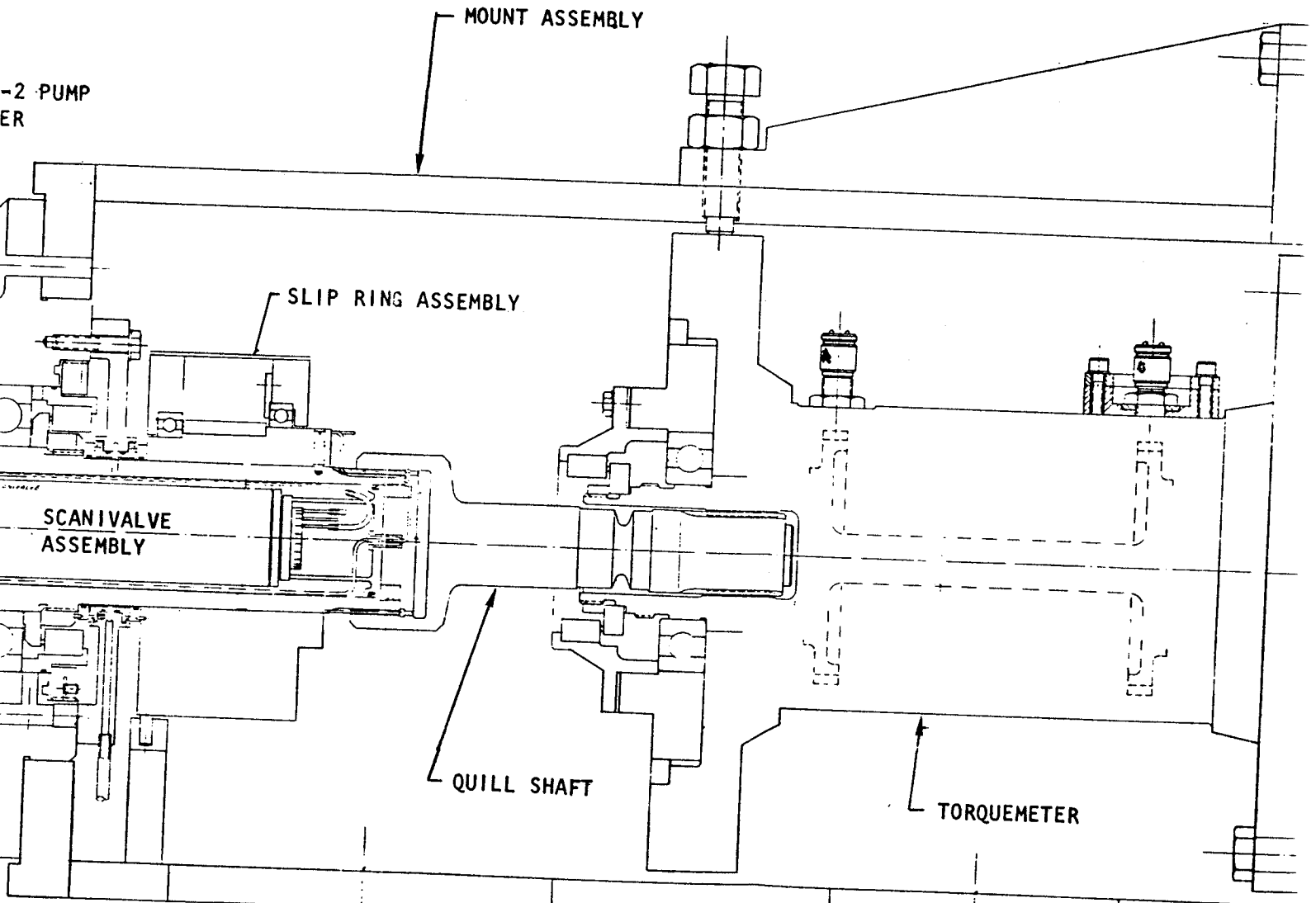
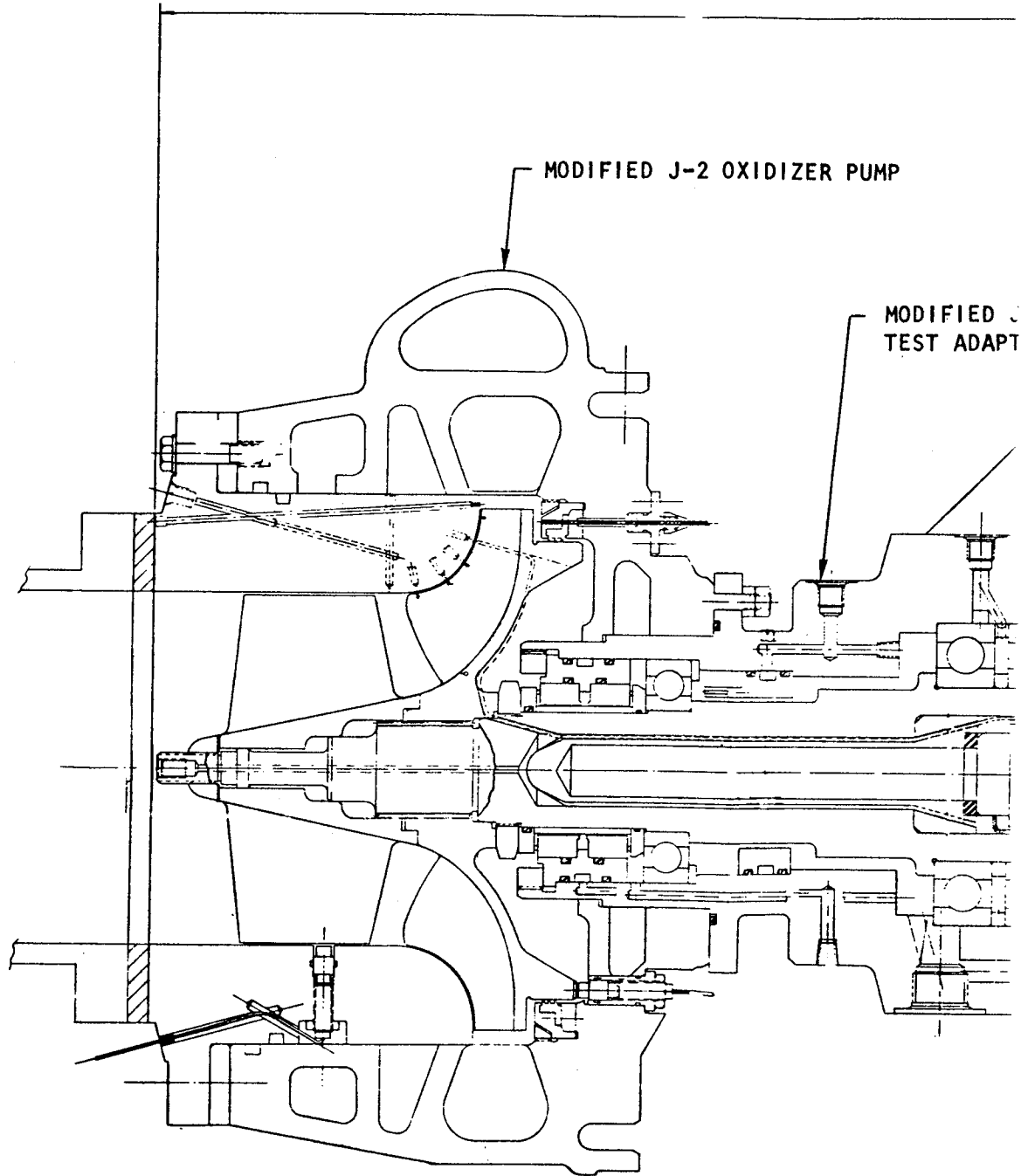


Figure 19. Impeller Clearance Effect
Preliminary Layout

FOLDOUT FRAME 1



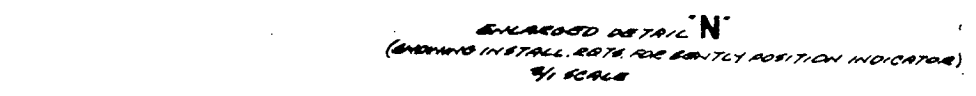
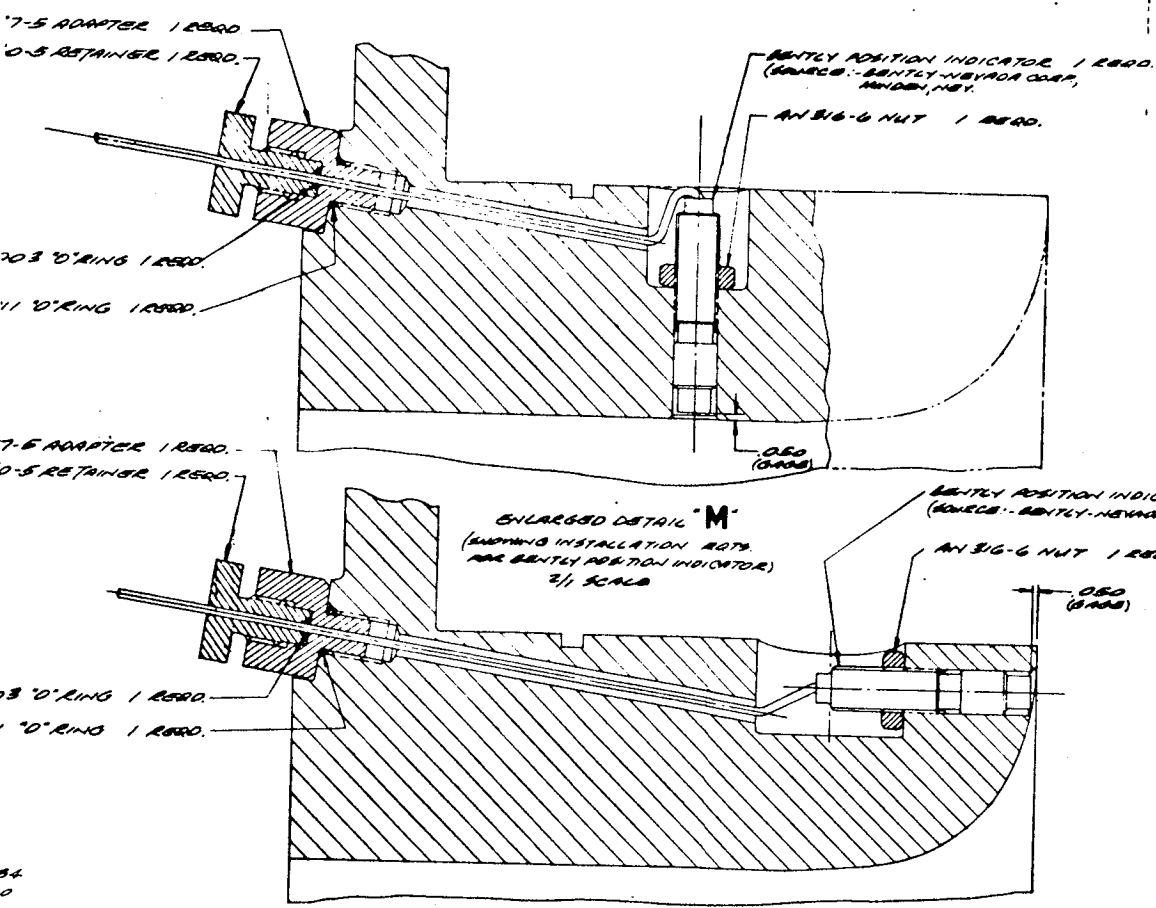




1
2
3
4
5
6
7
8
9
10
11
12
13
14
15
16
17
18
19
20
21
22
23
24
25
26
27
28
29
30
31
32
33
34
35
36
37
38
39
40
41
42
43
44
45
46
47
48
49
50
51
52
53
54
55
56
57
58
59
60
61
62
63
64
65
66
67
68
69
70
71
72
73
74
75
76
77
78
79
80
81
82
83
84
85
86
87
88
89
90
91
92
93
94
95
96
97
98
99
100



REVISIONS		DATE	APPROV.
NO.	DATE	DESCRIPTION	
1		REVISED MACHINING CALLOUT FOR KINLEYS INSERTS IN PLACES	
2		IMPACT ON EXISTING PART	
3		RECORD CHANGE	
4		NOW SHOP PRACTICE	
5		PARTS MADE ON	



(GIVEN BELOW)

126-30-1
126-30-2
126-30-3
126-30-4
126-30-5
126-30-6
126-30-7
126-30-8
126-30-9

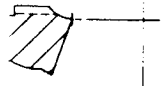
- ① SOURCE:--NEWTON INSERT CO., LOS ANGELES, CALIF.
 - ② FILE CONTAINS UNIFORMITY BETWEEN ALL TABULATED COORDINATES.
 - 15. TOLERANCES ON:--ANGLES 20°30', DECIMALS .XX ±0.3-.XXX ±0.10
 - 16. ALL SURFACES
 - 17. MATE:--6061-T6 DO NOT USE HARD POLISHING, SAE. 99-A-367, ALLOY 6061
 - 18. FLASH HARD ANODIZED IN CONFORMANCE WITH LB0125-103 TYPE II (RADIO-9-010) COATING THICKNESS .0001-.0002 ALL SURFACES.
 - 11. DIMENSIONS APPLY AT 68°F.
 - ③ IDENTIFY AND LOCATIONS--008
 - ④ ANGULAR TOLERANCES NOT ACCUMULATIVE
 - ⑤ SOURCE OF AN PLUG IS 158 CANAM, WESTBORO, MASS.
 - ⑥ AN. 1567 DIA., .150 DEEP, C&K 90°X. 150 DIA. DRILL 1/8 (125), 1.500 DEEP. INSTALL 156001 AN PLUG AND BACHE-003 1.2500. (2 PLCS. TOTAL REQ.)
 - ⑦ AN. 1567 DIA., .150 DEEP, C&K 90°X. 150 DIA. DRILL 1/8 (125), 1.800 DEEP. INSTALL 156001 AN PLUG AND BACHE-003 1.2500. (2 PLCS. TOTAL REQ.)
 - ⑧ AN. 1567 DIA., .150 DEEP, C&K 90°X. 150 DIA. DRILL 1/8 (125), 1.850 DEEP. INSTALL 156001 AN PLUG AND BACHE-003 1.2500. (2 PLCS. TOTAL REQ.)
 - ⑨ AN. 750 DIA., .050 DEEP, .030 FILLET R. DRILL 1/4 (125) 5.560 DEEP FROM S.F. MACHINING SURF ARE H5 JS649-S ARE 1/4 TURNS.
 - ⑩ AN. 750 DIA., .060 DEEP, .030 FILLET R. DRILL 1/4 (125) 5.170 DEEP FROM S.F. MACHINING SURF ARE H5 JS649-S ARE 1/4 TURNS.
 - ⑪ AN. 750 DIA., .060 DEEP, .030 FILLET R. DRILL 1/4 (125) 4.780 DEEP FROM S.F. MACHINING SURF ARE H5 JS649-S ARE 1/4 TURNS. 1. MACHINING ARE R.010S-.002.
- NOTE:--UNLESS OTHERWISE SPECIFIED

Figure 20. Pump Inlet Assembly Clearance Effect Study

R#70-126-41 GUIDE 1.25 RD.

530
RESTRICTION

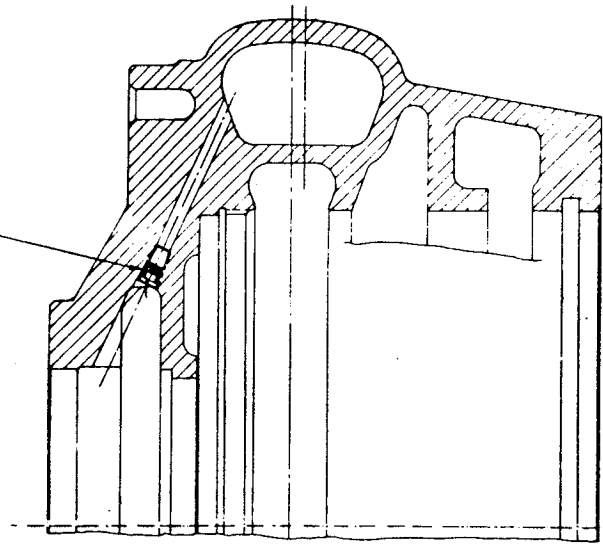
3/4



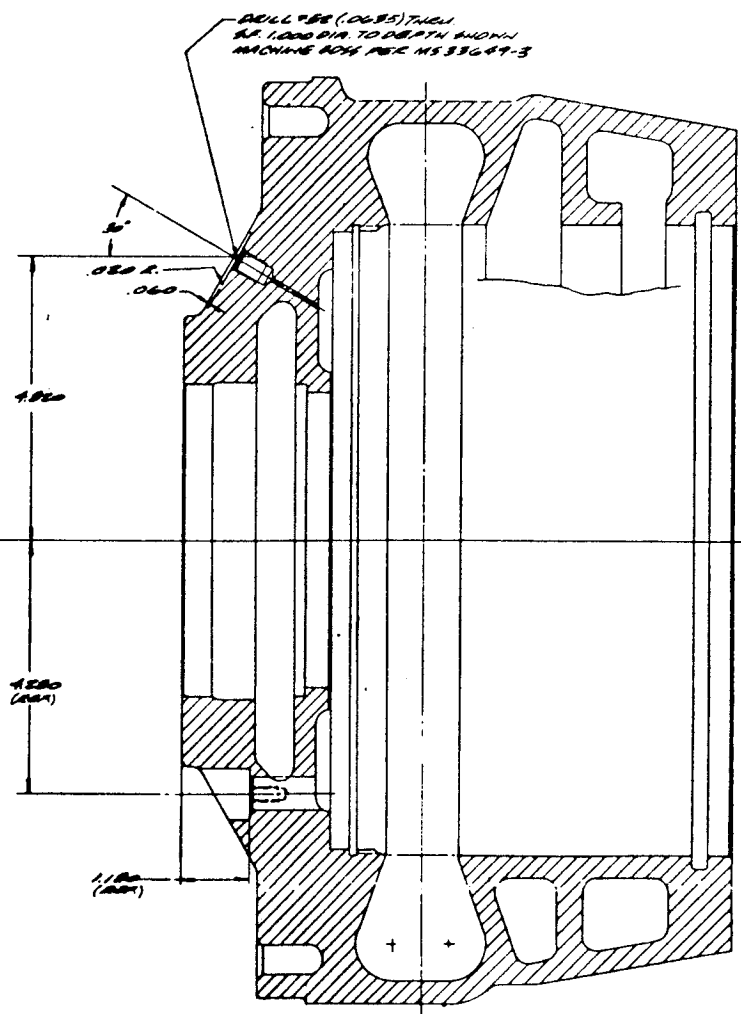
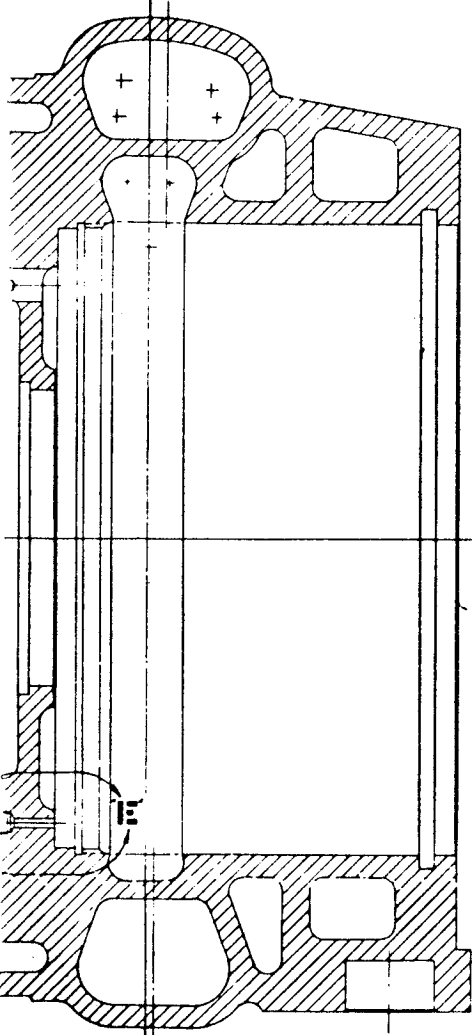
1/2
R#70-126-41 GUIDE

AN9SEDE PLUG 1.25 RD.

SECTION F-F
(DIM 578.16)



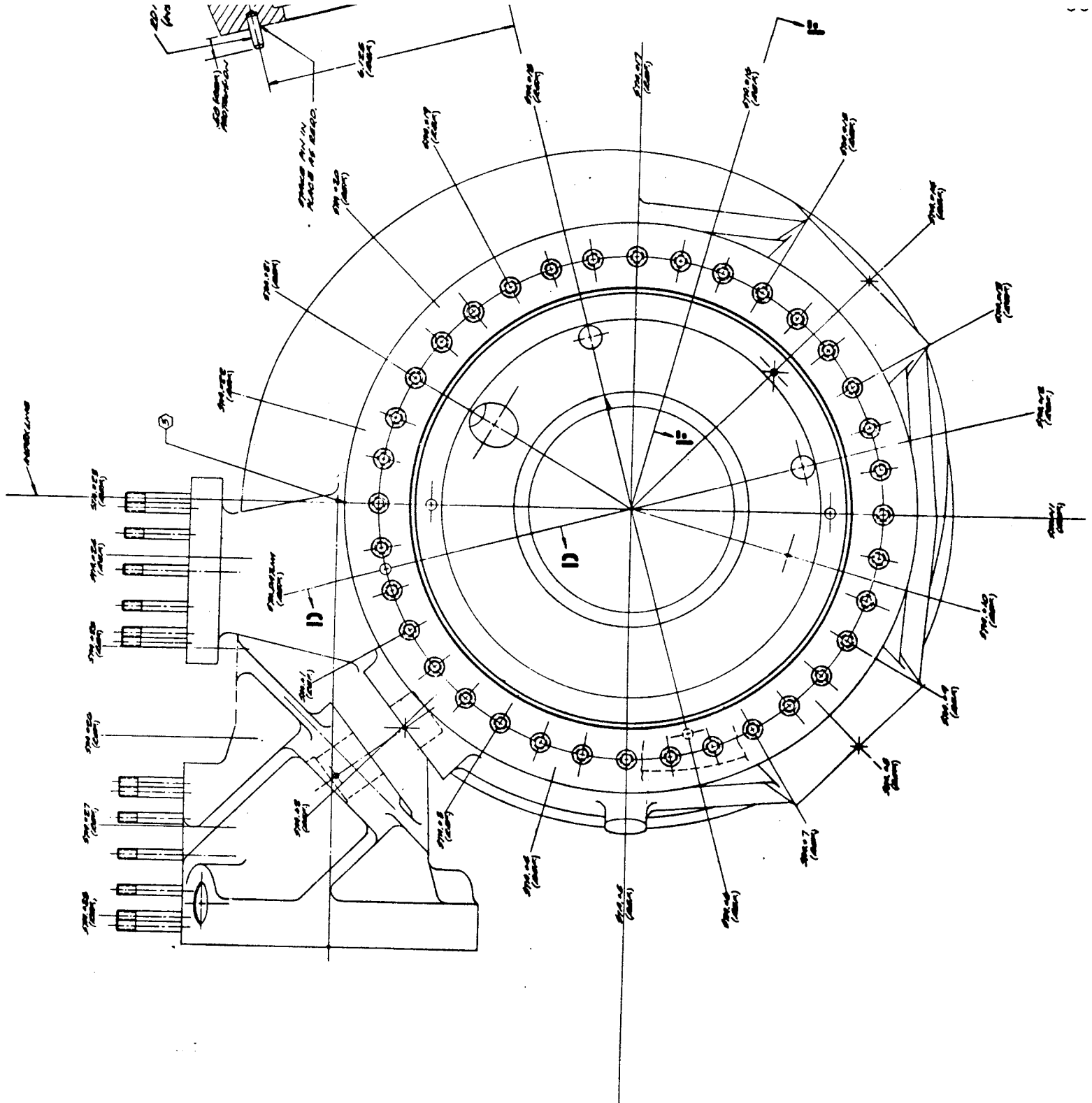
DILL #88 (.0035) TAPER
SR 1.000 DIA. TO DEPTH SHOWN
MACHINE SHOP SPEC MS 33649-3



SECTION B-B
(DIM 578.16 (MAX) & 578.16 (MIN) DIM)

SECTION C-C
(DIM 578.16 (MAX) & 578.16 (MIN) DIM)

FOLDOUT FRAME 3



FOLDOUT FRAME 4

100-111111

REVISIONS			
NO.	DATE	DESCRIPTION	APPROVED
		1. NEW OR REWORKED 2. CHANGE OR REWORKED 3. PARTS MADE ON	
		3. RECORD CHANGE 4. NEW SHOP PRACTICE 5. PARTS MADE ON	
A		1. ADDED 64C F-F 64C F-F ON EXISTING PART	

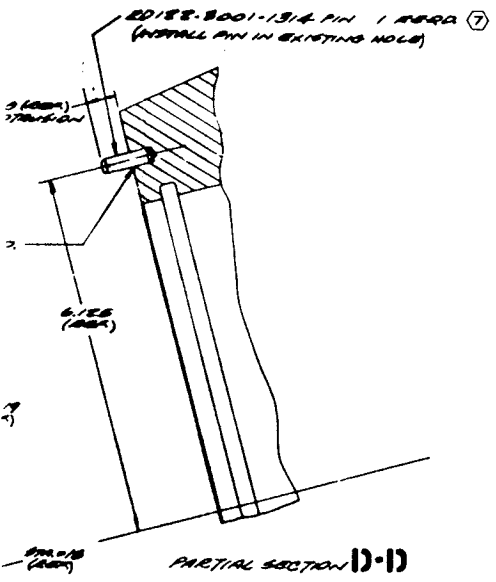


Figure 21. Volute Assembly Clearance Effect Study

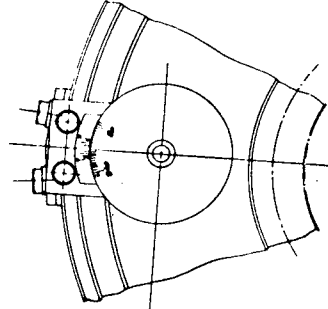
- ① KINGS...NORTON INSERT CO. LOS ANGELES, CALIF.
- ② BALL END (1.50 O.D. X .75 LONG) MAY BE SUBSTITUTED.
- ③ ALL SURFACES .001
- ④ TOLERANCES ON ANGLES 10:30, DECIMALS .XX .03, .XXX .010.
- ⑤ DIMENSIONS APPLY AT 66°F.
- ⑥ IDENTIFY ALL RADII R-008.
- ⑦ NAME FROM PART 5/1 6663480 (TO BE FURNISHED BY SNOWBERAND)
- ⑧ REFER TO DWG # 458161 AND OTHER DATA.
- ⑨ APPROVING ALL RADII R-008
- UNLESS OTHERWISE SPECIFIED

All detailed drawings were completed. The stackup assembly drawing (Fig. 22) was completed to verify the assembly and mechanical design of the component parts. The parts requirements list is also shown in Appendix C.

Instrumentation Requirements. Instrumentation was designed to obtain all pertinent experimental data required to correlate with and refine the analytical model. These measurements included wall static pressures, blade static pressures at various stations along the vanes, and the various pump parameters necessary to obtain the overall pump performance. The instrumentation list is shown on Table 5.

M1048B/Bolt 2
 MS 3522B-40 WASHER 2
 AP70-120-40 CLAMP 1
 AP70-120-47 BRACKET 1
 M104708 Bolt 2
 MS 3522B-39 WASHER 2
 CLAMP 2
 C-ROD 2

ATTACHMENT SUPPLIED BY ENGINEERING



AP70-120-48 ROD/TEE 1
 MS 3522B-018 W/ING 1
 AP70-120-42 BRACKET 1
 MS 3522B-010 W/ING 1

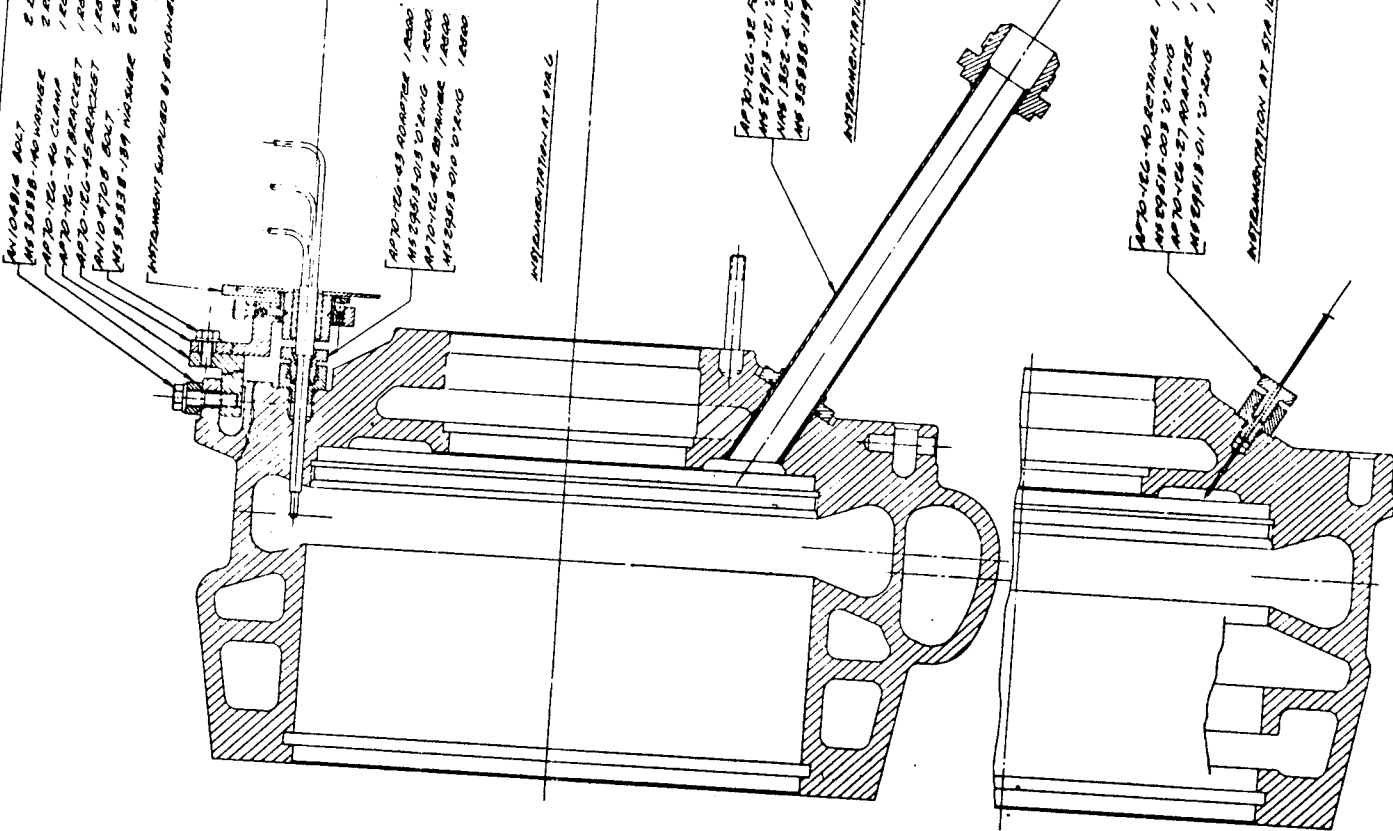
ATTACHMENT SUPPLIED BY ENGINEERING

AP70-120-32 RANGE/ANY/DI 1
 MS 3522B-121 W/ING 1
 MS 3522B-4-1C BOLT 2
 MS 3522B-129 WASHER 2

ATTACHMENT SUPPLIED BY ENGINEERING

AP70-120-40 RETAINER 1
 MS 3522B-003 W/ING 1
 AP70-120-27 BRACKET 1
 MS 3522B-011 W/ING 1

ATTACHMENT SUPPLIED BY ENGINEERING



FOLDOUT FRAME /



- AN104818 BOLT 2.0000
- MS 35338-140 WASHER 2.0000
- AP70-126-40 CLAMP 1.0000
- AP70-126-47 BRACKET 1.0000
- AP70-126-45 BRACKET 1.0000
- AN104708 BOLT 2.0000
- MS 35338-139 WASHER 2.0000

INSTRUMENTATION SUPPLIED BY ENGINEERING

- AP70-126-53 ADAPTER 1.0000
- MS 29518-013 O-RING 1.0000
- AP70-126-42 RETAINER 1.0000
- MS 29518-010 O-RING 1.0000

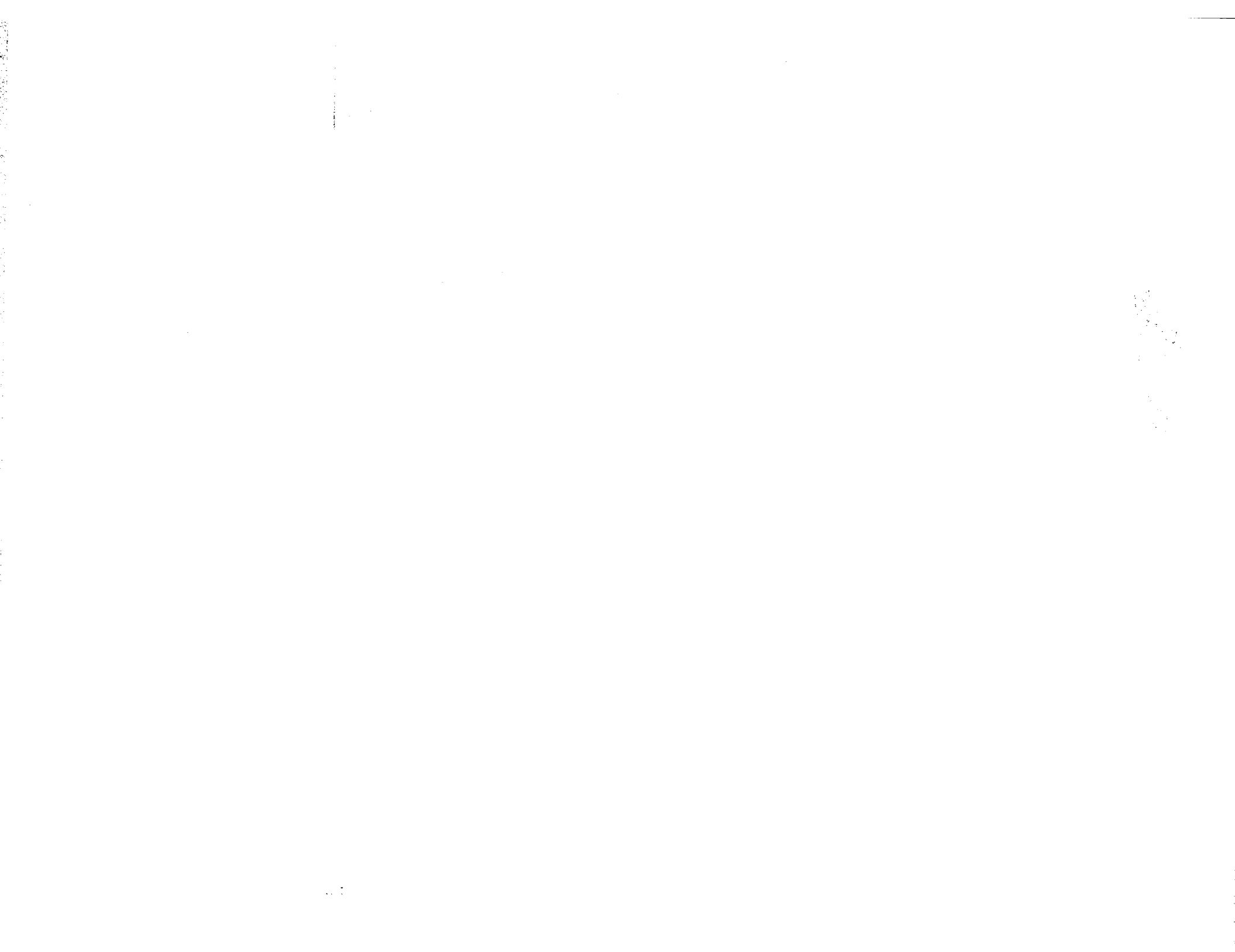
INSTRUMENTATION AT STA 6

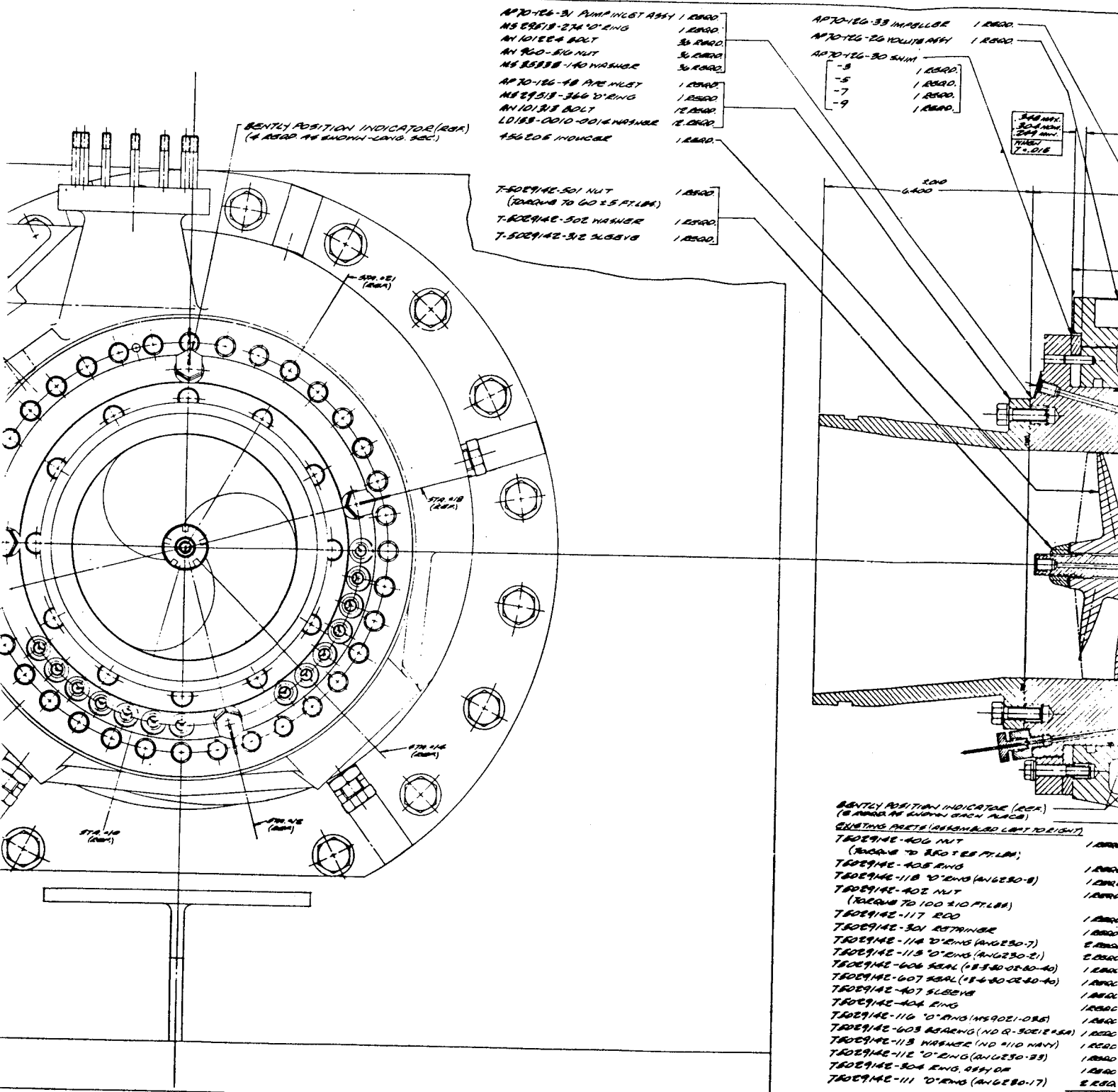
- AP70-126-32 FLANGE, ANY OF 1.0000
- MS 29518-121 O-RING 1.0000
- MS 1352-4-12 BOLT 2.0000
- MS 35338-139 WASHER 2.0000

INSTRUMENTATION AT STA 21

- AP70-126-40 RETAINER 1.0000
- MS 29518-003 O-RING 1.0000
- AP70-126-27 ADAPTER 1.0000
- MS 29518-011 O-RING 1.0000

INSTRUMENTATION AT STA 10



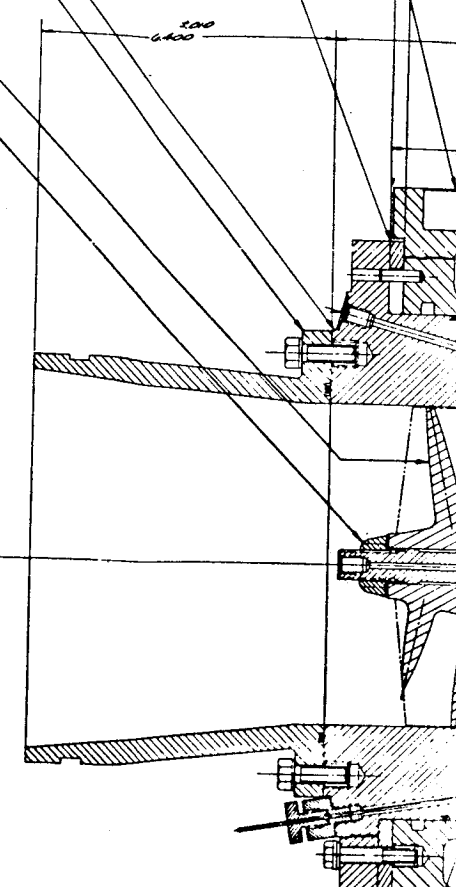


- AP70-126-21 PUMP INLET ASSY 1 EA000
- MS 2813-274 0" RING 1 EA000
- AN 10124-BOLT 3 EA000
- AN 160-510 NUT 3 EA000
- MS 25338-140 WASHER 3 EA000
- AP70-126-18 PIP INLET 1 EA000
- MS 29313-366 0" RING 1 EA000
- AN 10131-BOLT 12 EA000
- LD 188-0010-0014 WASHER 12 EA000
- 456205 INDOOR 1 EA000

- T-802914E-501 NUT 1 EA000
- (TORQUE TO 60 ± 5 FT LBS)
- T-802914E-502 WASHER 1 EA000
- T-802914E-503 SLEEVES 1 EA000

- AP70-126-33 IMPELLOR 1 EA000
- AP70-126-22 IMPELLOR ASSY 1 EA000
- AP70-126-30 SHIM
- 8 1 EA000
- 5 1 EA000
- 7 1 EA000
- 9 1 EA000

3/4" MAX.
2 1/4" MIN.
7 ± 0.18



- BENTLY POSITION INDICATOR (R&R)
- (8 AREA AT EACH CORNER)
- CLUTCHING PLATE (ASSEMBLED LEFT TO RIGHT)
- T802914E-406 NUT 1 EA000
- (TORQUE TO 80 FT LBS)
- T802914E-405 RING 1 EA000
- T802914E-118 0" RING (ANGLE 30-8) 1 EA000
- T802914E-402 NUT 1 EA000
- (TORQUE TO 100 ± 10 FT LBS)
- T802914E-117 ROD 1 EA000
- T802914E-301 RESTRAINER 1 EA000
- T802914E-116 0" RING (ANGLE 30-7) 2 EA000
- T802914E-115 0" RING (ANGLE 30-2) 2 EA000
- T802914E-606 SEAL (18-540 05-60-40) 1 EA000
- T802914E-607 SEAL (18-540 05-60-40) 1 EA000
- T802914E-407 SLEEVES 1 EA000
- T802914E-404 RING 1 EA000
- T802914E-116 0" RING (MS 9021-026) 1 EA000
- T802914E-603 ASSEMBLY (NO Q-30212 USA) 1 EA000
- T802914E-113 WASHER (NO 910 NAVY) 1 EA000
- T802914E-112 0" RING (ANGLE 30-13) 1 EA000
- T802914E-306 RING ASSY OR 1 EA000
- T802914E-111 0" RING (ANGLE 30-17) 2 EA000

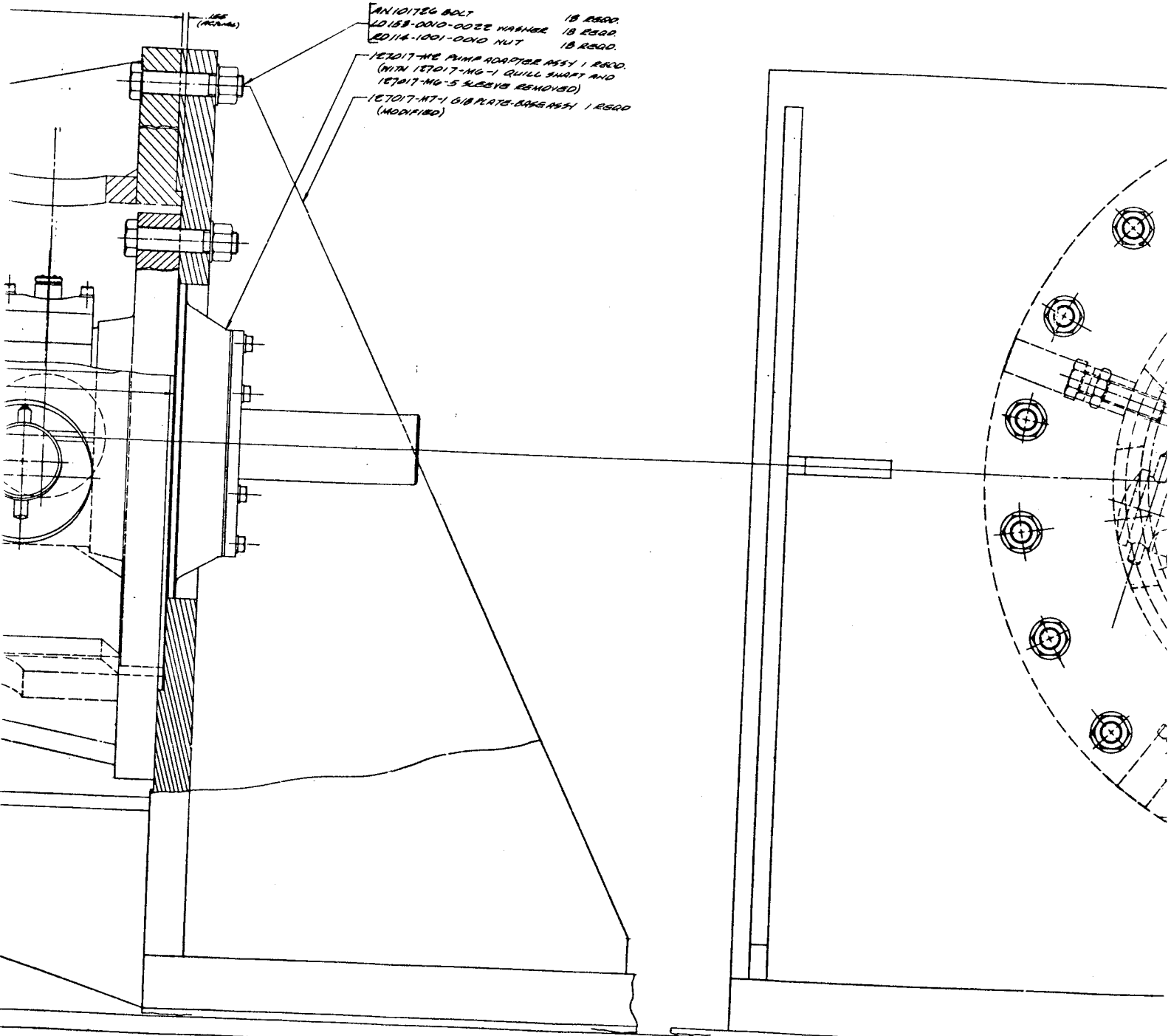
100

100

100



- 18Y 1 R500
- 1 R500
- 18Y 1 R500
- 6 R500
- 6 R500
- 1 R500



FOLDOUT FRAME 5

1000

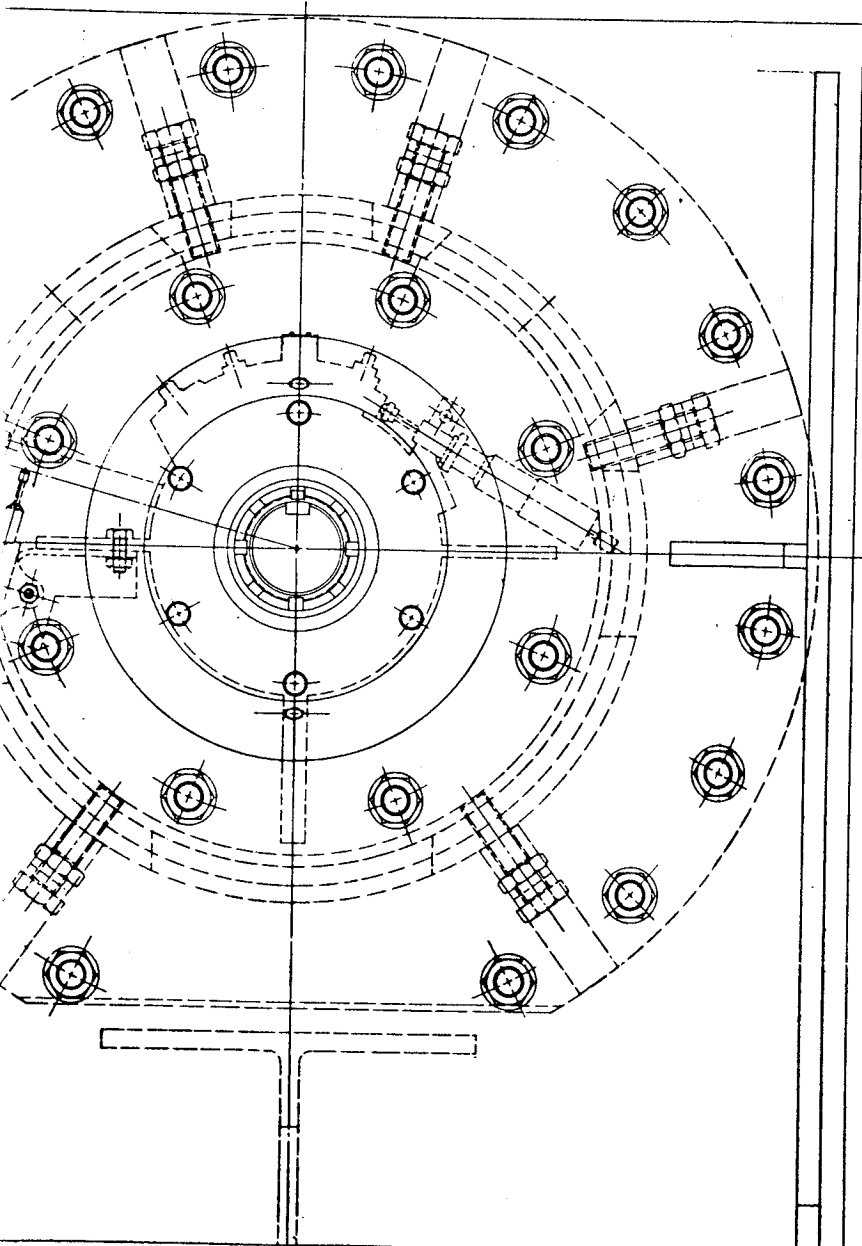


Figure 22. Stackup Assembly Layout

TABLE 5. INSTRUMENTATION LIST

	Range	Readout
<u>Pressure, psig (N/cm²)</u>		
P _{S1} , Inducer Inlet	-15 to +35 (-10.3 to 24.1)	DIGR
P _{S2} , Inducer Discharge	0 to 150 (0 to 103.4)	↓
P _{S3} , Impeller Intermediate, Station 1	0 to 200 (0 to 137.9)	
P _{S4} , Impeller Intermediate, Station 2	0 to 200 (0 to 137.9)	
P _{S5} , Impeller Intermediate, Station 3	0 to 300 (0 to 206.8)	
P _{S6} , Impeller Intermediate, Station 4	0 to 300 (0 to 206.8)	
P _{S7} , Impeller Intermediate, Station 5	0 to 400 (0 to 275.8)	Brusch
P _{S8} , Impeller Discharge, Front No. 1	0 to 500 (0 to 344.7)	↓
P _{S9} , Impeller Discharge, Front No. 2	0 to 500 (0 to 344.7)	
P _{S10} , Impeller Discharge, Back	0 to 500 (0 to 344.7)	
P _{S11} , Volute Discharge	0 to 500 (0 to 344.7)	
ΔP, Pump ΔP (P _{S11} - P _{S1})	0 to 500 (0 to 344.7)	DIGR
P _{S12} , Cavity	0 to 150 (0 to 103.4)	Brusch
P _S Scanivalve	0 to 500 (0 to 344.7)	↓
P _{t14} , Probe Total	0 to 500 (0 to 344.7)	Gage
ΔP ₁₃ , Probe Static ΔP	-100 to 100 (-68.9 to 68.9)	↓
<u>Temperature, F (K)</u>		
T ₁ , Inlet Water	40 to 140 (277.6 to 333.2)	Brown
T _t , Tank Water	40 to 140 (277.6 to 333.2)	Monitor
T _B , Bearing Discharge Oil	50 to 150 (283.2 to 338.7)	Brusch
<u>Flow, gpm (cm²/s)</u>		
Q ₁ , Inlet Water	0 to 2500 (0 to 15,770)	Brown
Q ₂ , Inlet Water	0 to 2500 (0 to 15,770)	EPUT
<u>Speed, rpm (rad/sec)</u>		
N ₁ , Pump	3976-5038 (416 -527)	EPUT
<u>Torque, in-lb (cm-N)</u>		
τ, Pump	0 to 15,000 (0 to 169,477)	Brown

TABLE 5. (Concluded)

<u>Impeller Movement, inches (cm)</u>	Range	Readout
D ₁ , Bently Radial (Inducer)	0.050 nominal (0.127) ↓	Monitor ↓
D ₂ , Bently Radial (Inducer)		
D ₃ , Bently Axial (Impeller Front)		
D ₄ , Bently Axial (Impeller Front)		
D ₅ , Bently Axial (Impeller Back)		
D ₆ , Bently Axial (Impeller Back)		

TASK E: FABRICATION

Fabrication included all effort necessary to modify and instrument the J-2 oxidizer pump and test rig defined in Task D. A J-2S impeller casting (CP/N 460422-3) was ordered and modified by removal of its front shroud. The Scanivalve system was installed, and all required parts were fabricated or purchased. The blade pressure taps and pressure-sensing tubes were installed to the Scanivalve assembly. Required drive, instrumentation, and mounting elements were fabricated and all components were assembled.

Impeller Fabrication

The fabrication of the impeller was divided into two steps. The first step was machining the drive spline, rear labyrinth seal, mounting pilots, clamping surfaces, and the final contour after removal of the shroud. The second step was positioning of the instrumentation blade pressure holes on the suction and pressure surfaces, and routing the pressure-sensing tubing from the blades through the impeller hub and main shaft to the Scanivalve.

Machining of the drive spline, mounting pilots and clamping surfaces were completed. The front shroud was removed using a pattern that followed the blade tip contour. The blade tips were handworked and the tip fillets removed. The blade surfaces were then shot-peened and the rear labyrinth seal surface machined. Figure 23 shows the unshrouded impeller and a typical production shrouded J-2 oxidizer impeller.

Preliminary tube installation and bending evaluation tests were completed using aluminum U-channels. Type 321 annealed CRES tubing of 0.040-inch (0.1016 cm) OD with 0.005-inch (0.0127 cm) wall thickness was selected from the results of these tests. Machining of the holes and channels for the pressure tubes were completed followed by dynamic balancing.

The 20 pressure tubes for recording blade pressures were installed and attached into the holes and channels in the impeller blades with epoxy (EpoxyLite 211). EpoxyLite 211 was selected because of the highly successful results obtained with this epoxy under the Mark 10 (F-1) impeller strain gage test program.

Figures 24 through 26 show the pressure tube installation on the blade suction side, blade pressure side, and rear shroud of the test impeller, respectively. The epoxy on both the suction and pressure surfaces of the instrumented impeller was faired to provide smooth hydrodynamic flow surfaces.

Other Components

The pump inlet assembly was machined with one set of static pressure taps installed. The part was hard-flash anodized and is shown in Fig. 27.

One Fabricast slip-ring assembly (Fig. 28), type 1274 was purchased with eight low-noise slip rings (four brushes per ring) for 5000 rpm (523.5 rad/s) service. This slip-ring assembly was used to transmit blade pressure data, and power to the Scanivalve electric motor.

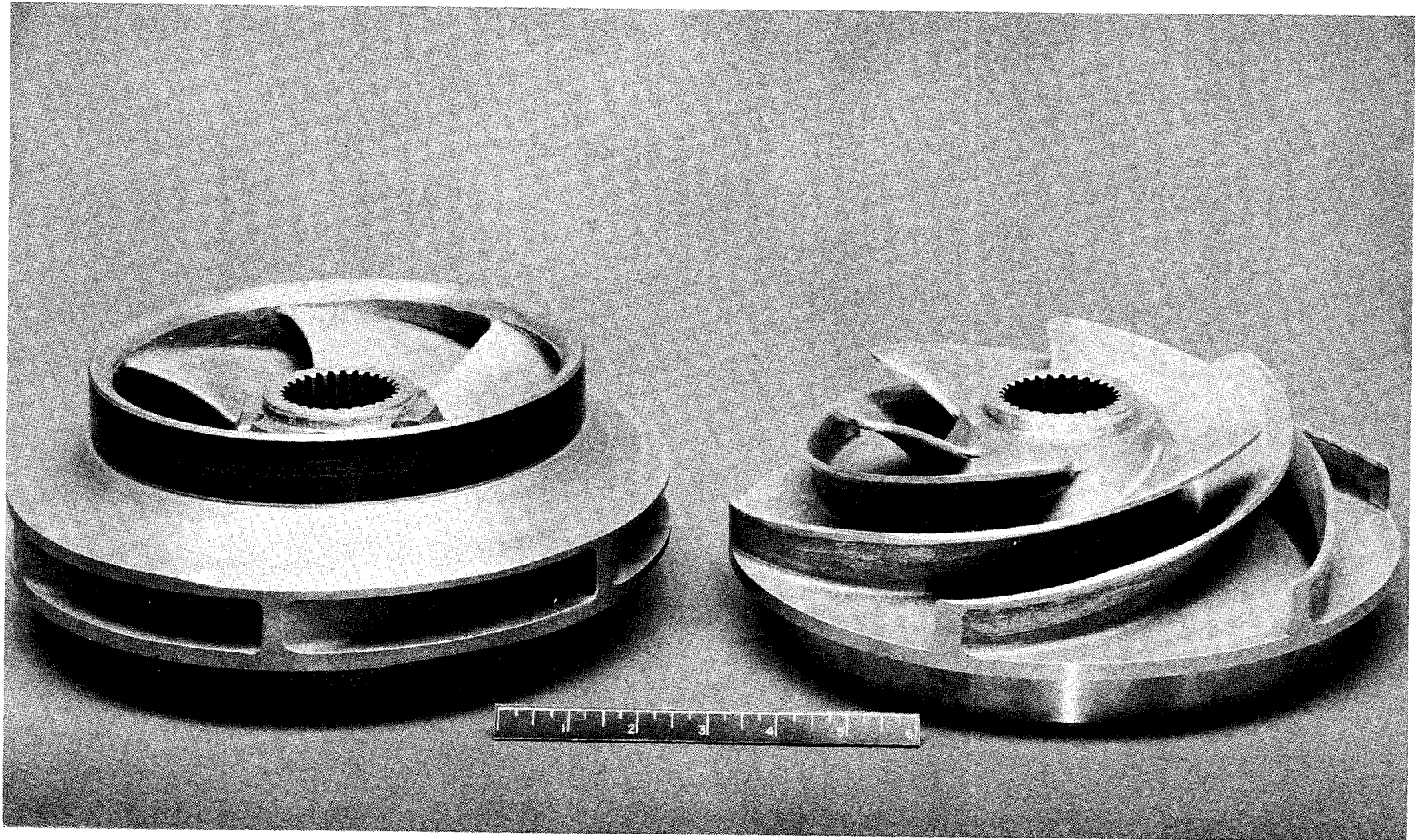


Figure 23. Shrouded and Unshrouded J-2S Oxidizer Impellers

1XY92-8/10/70-C1b

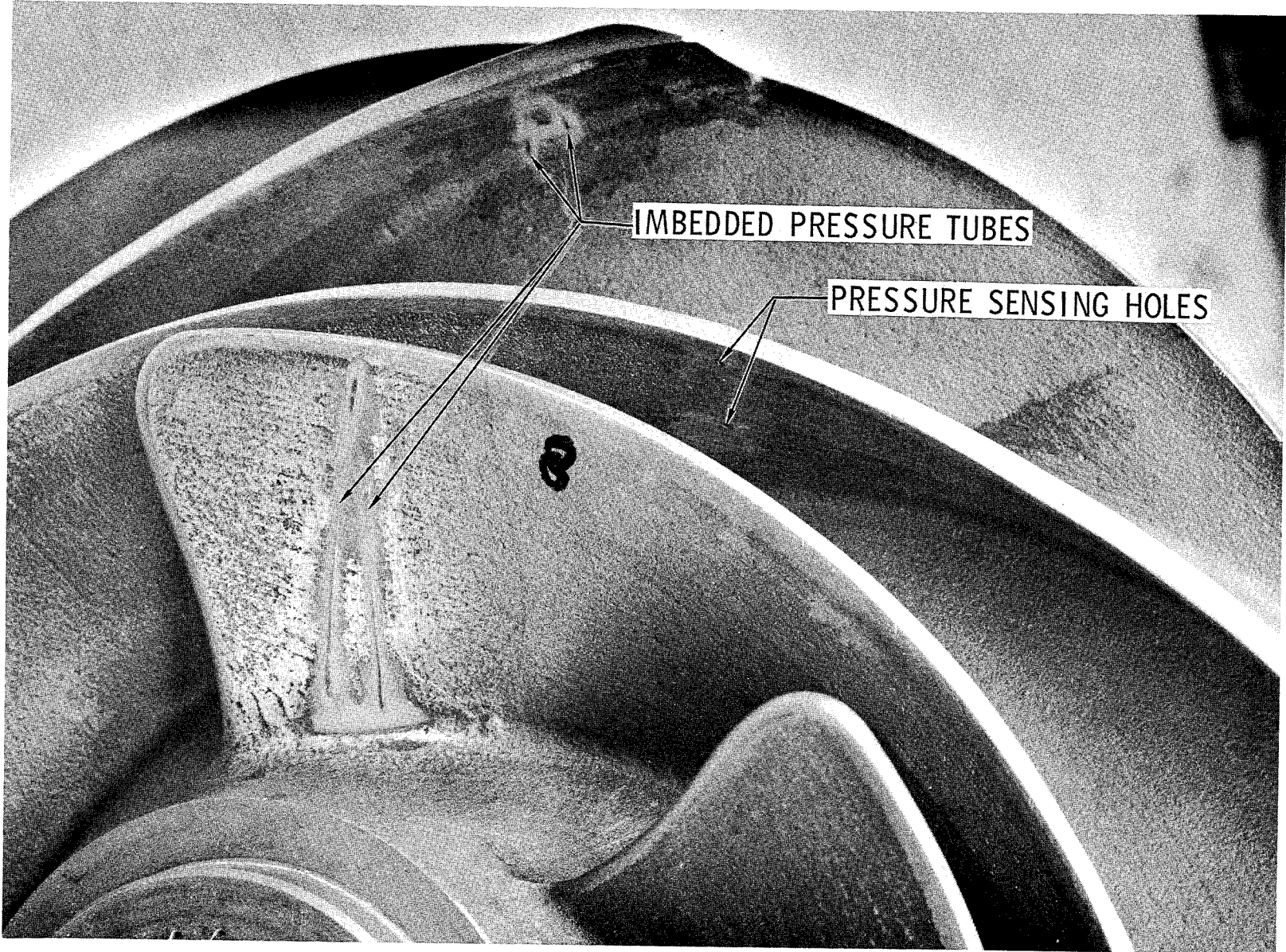


Figure 24. Impeller Pressure Tube Installation (Suction Side)

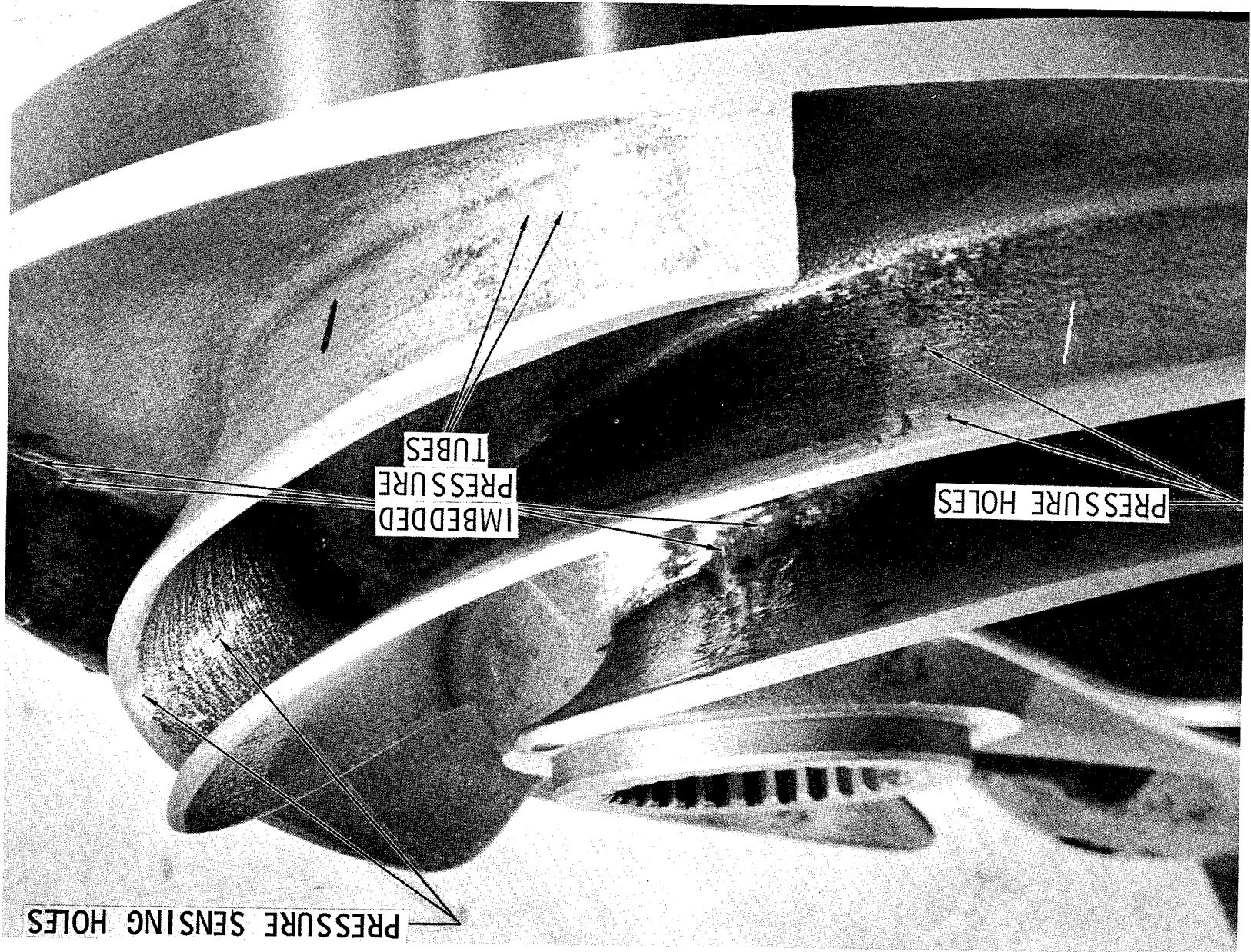
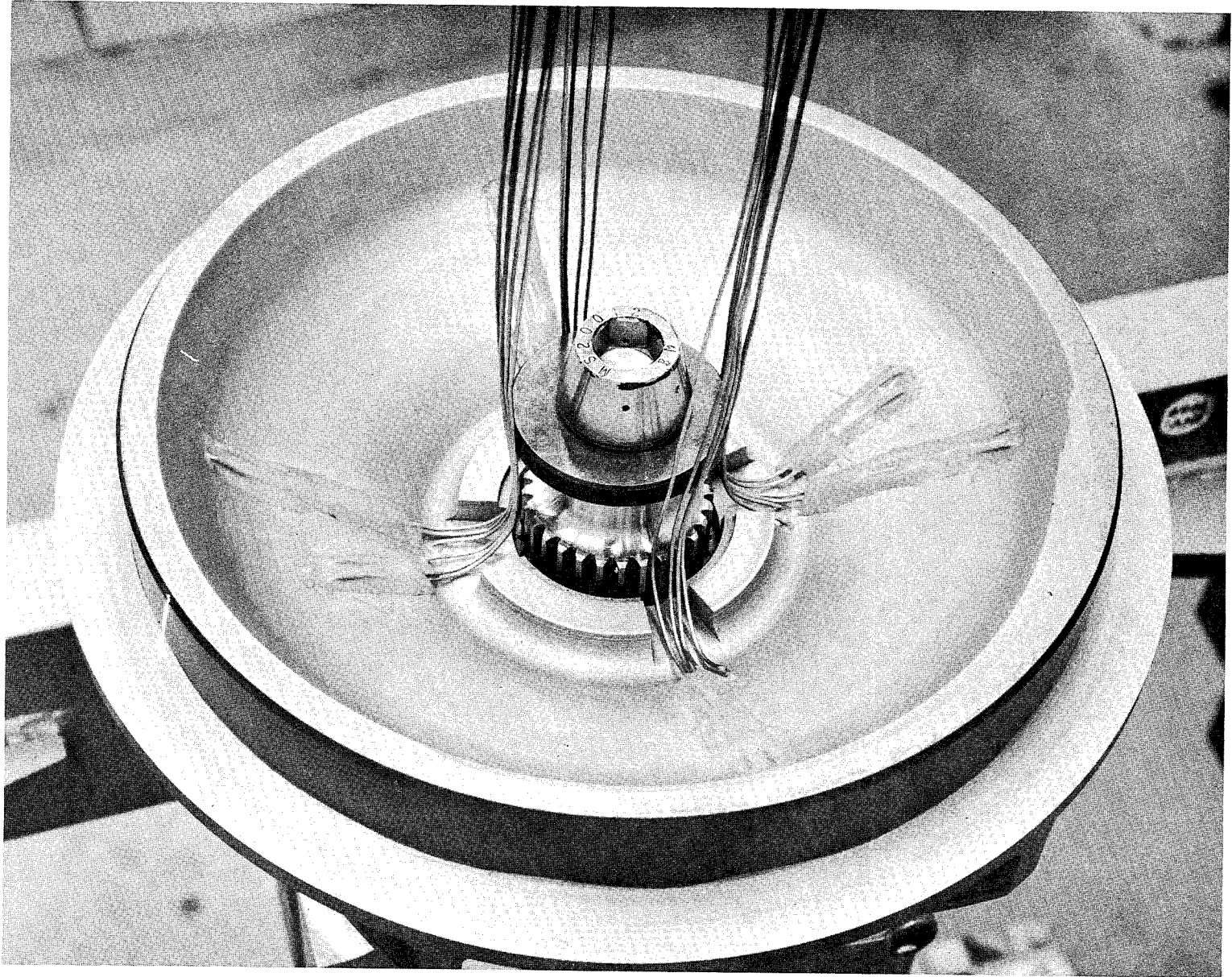


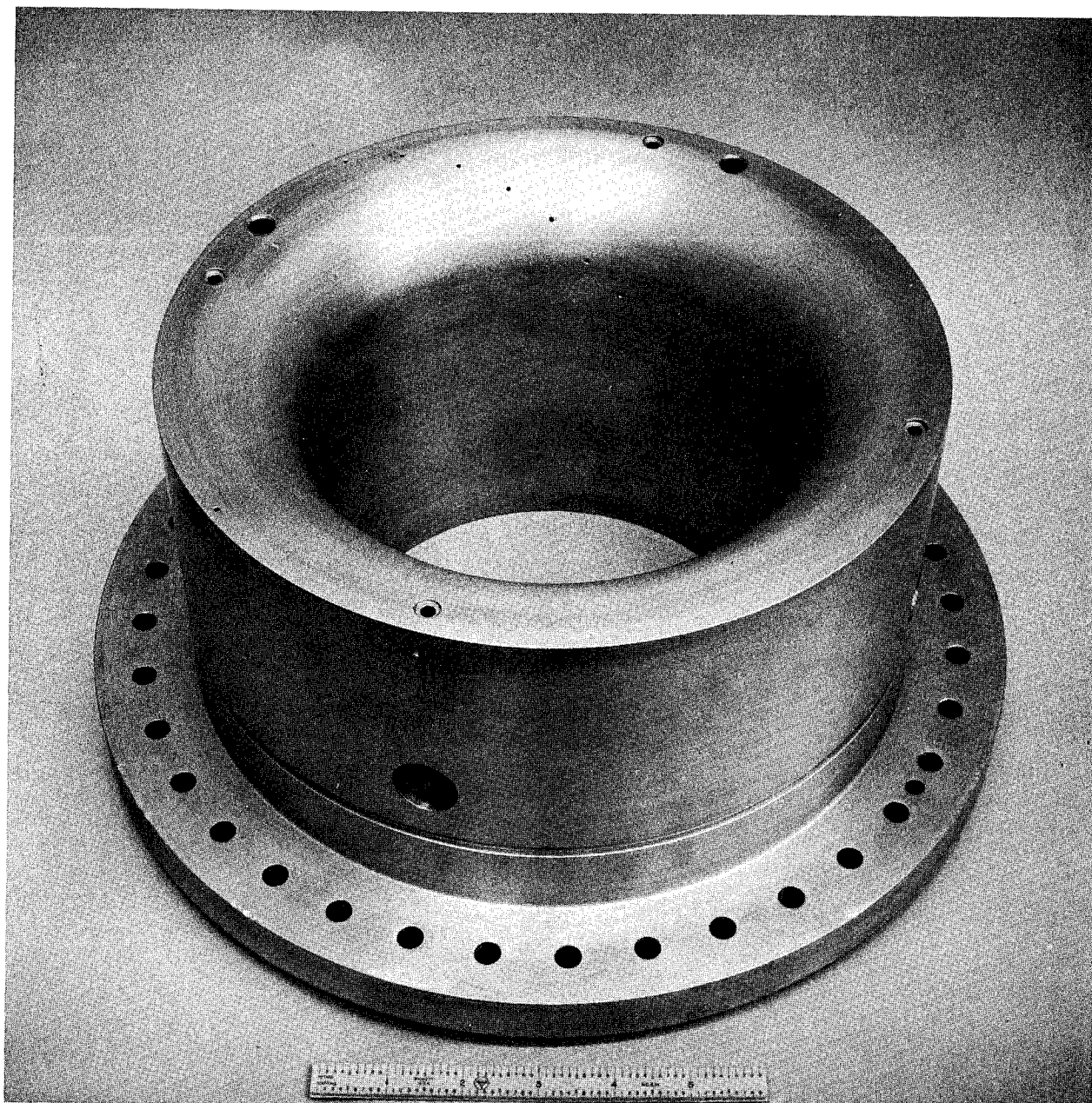
Figure 25. Impeller Pressure Tube Installation (Pressure Side)

1XYS5-11/2/70-C1C



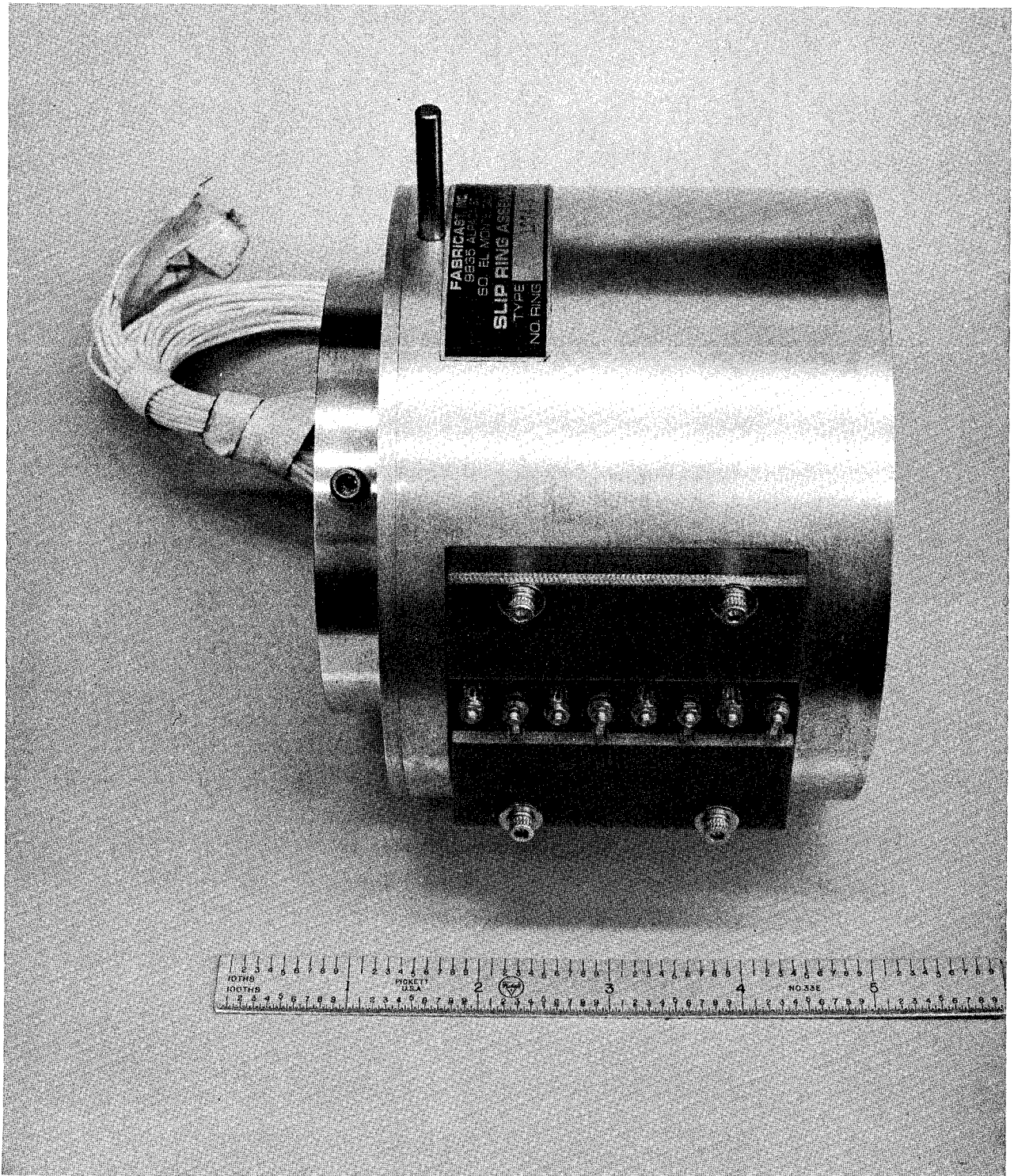
1XY55-11/2/70-C1A

Figure 26. Rear View of Impeller Showing Epoxyed Pressure Tubes (20 Each)



1XY52-12/4/70-C1B

Figure 27. Pump Inlet Assembly



1XY52-12/4/70-C1E

Figure 28. Slip-Ring Assembly

One Scanivalve assembly (Fig. 29) was obtained with the purge modification described in Task D. The assembly also shows the sleeve assembly. Installed in the assembly is the electric motor and drive train and the pressure transducer.

As existing torquemeter shaft was modified by reducing its shaft diameter from 1.394 inches (3.541 cm) to 1.196 inches (3.038 cm) to increase the operating range of the torquemeter.

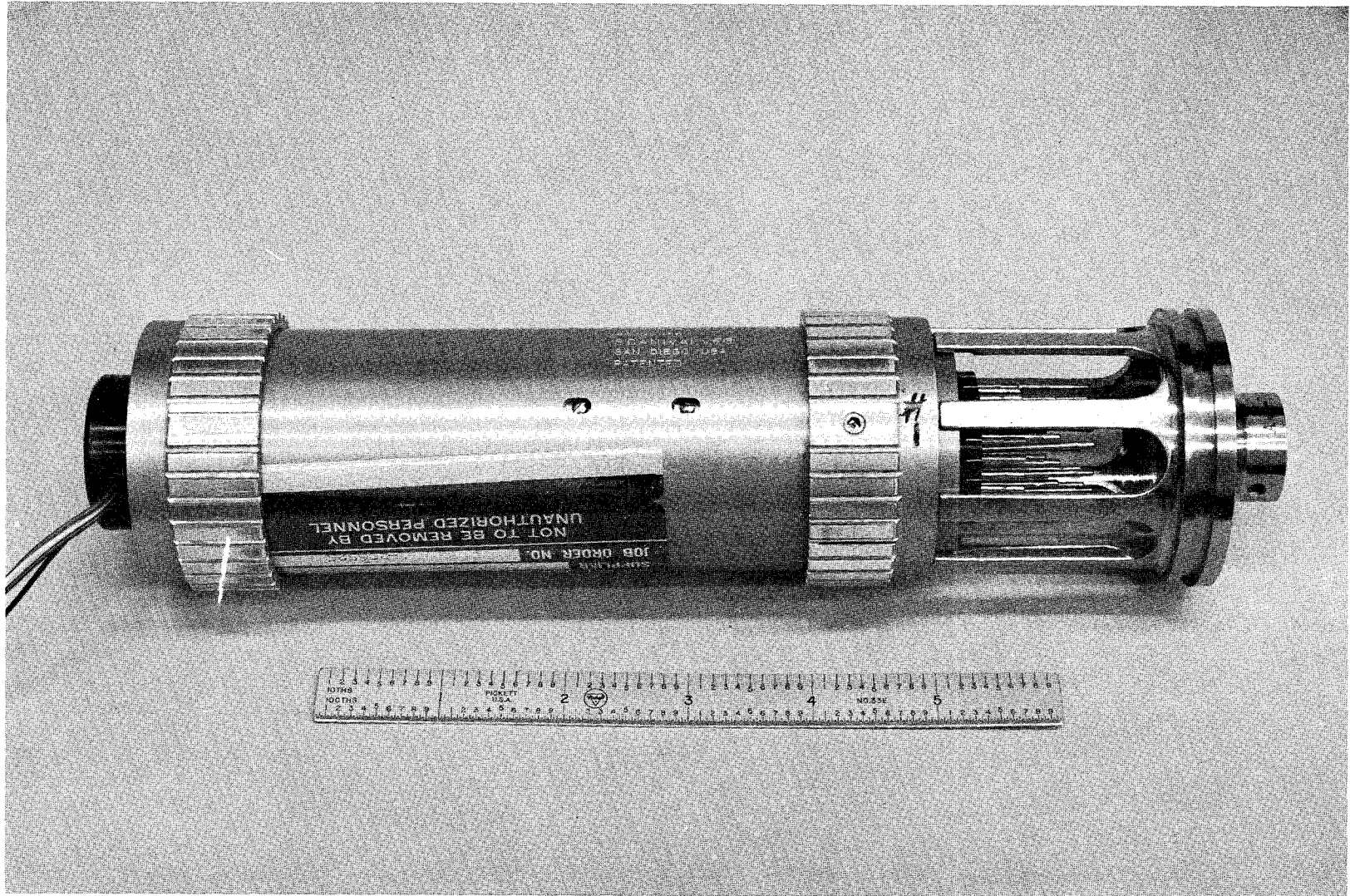
An existing pump test adaptor was obtained from the Tooling Department and modified for this program. All other parts required for the assembly were fabricated or purchased.

Buildup of Test Pump

The main shaft was installed into the pump volute and test adaptor. Installation of the instrumented impeller was accomplished by snaking the pressure tubes through the main shaft. The tube ends are shown in Fig. 30 protruding through the aft end of the main shaft.

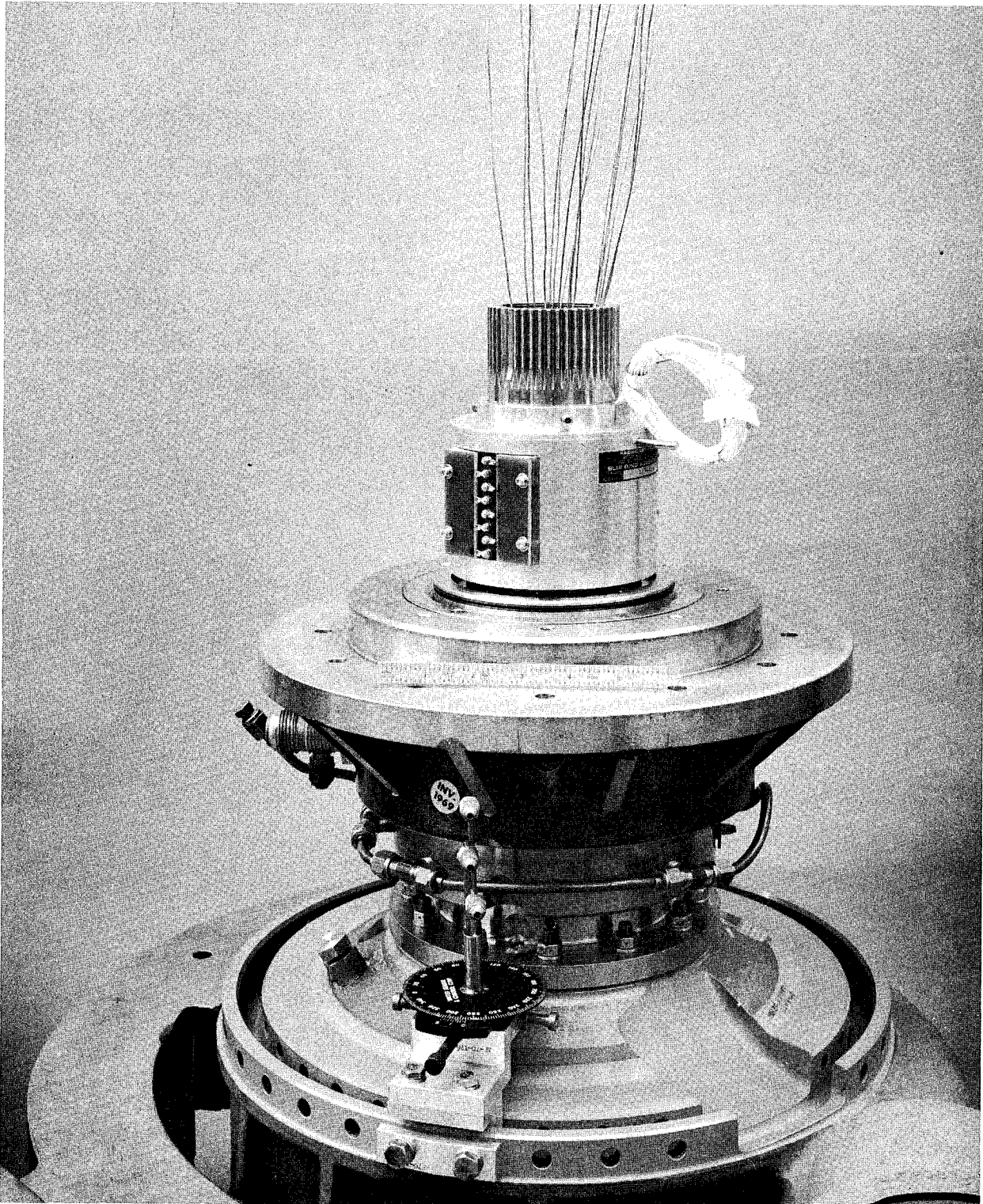
Installation of the Scanivalve assembly into the main drive shaft was then completed. The impeller blade pressure tubes were leak pressure checked prior to sealing of the aft end of the main drive shaft. Installation of the slip-ring assembly onto the main shaft was completed. The wire leads for both the Scanivalve electric motor and pressure transducer signal were also attached to the slip-ring assembly. Figures 31 and 32 show the sealed aft end of the pump test assembly. The pump inlet was pressurized and both Scanivalve electric motor and pressure transducer were successfully statically checked out.

The inducer was mounted on the drive shaft (Fig. 33), and then the pump inlet was installed onto the pump assembly with the impeller clearance set at 0.015 inch (0.0381 cm). Figure 34 shows the inlet view of the completed assembly. The pump test assembly was then shipped to the pump calibration test facility for installation and testing.



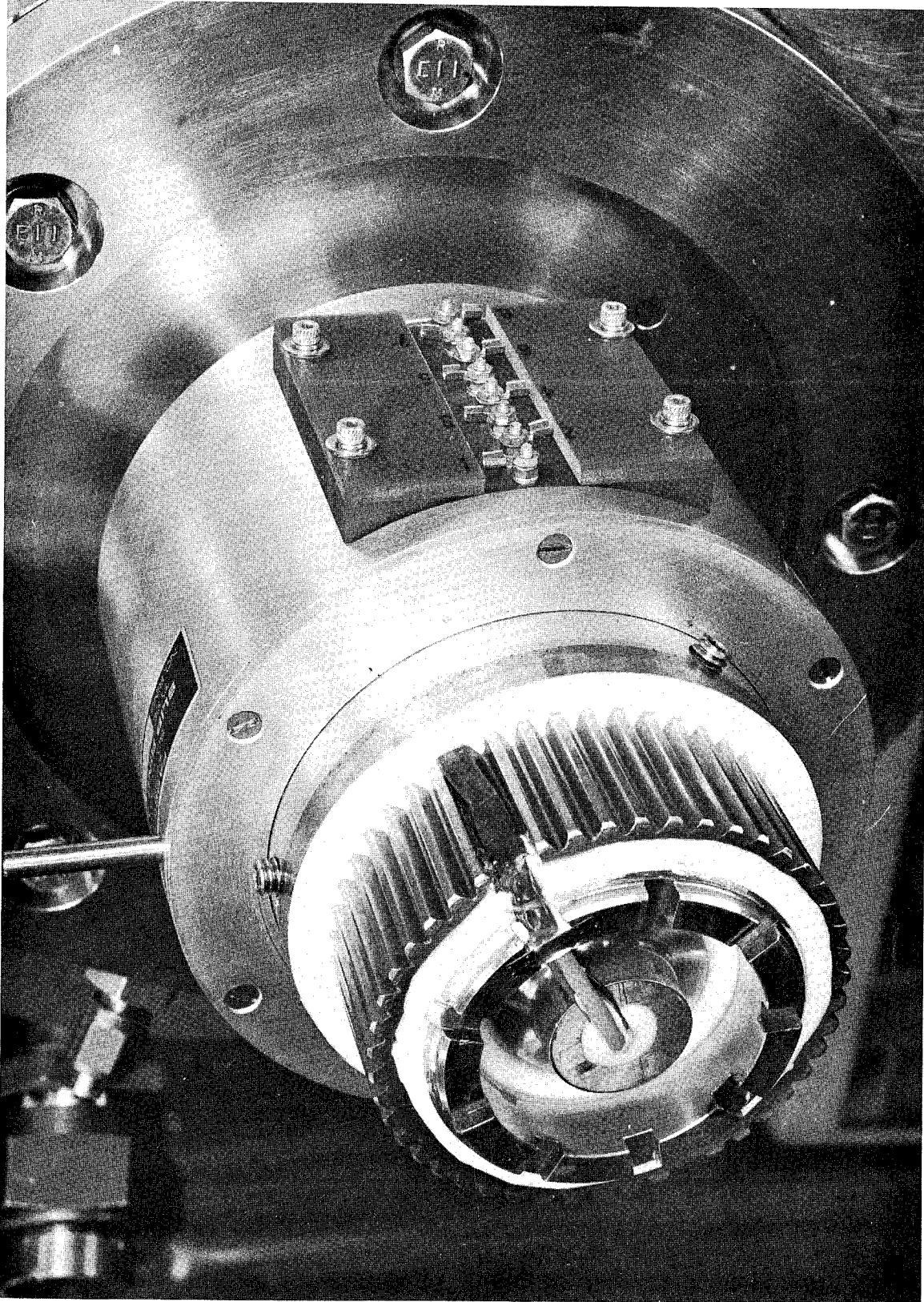
1XY52-12/4/70-C1A

Figure 29. Scanivalve Assembly



1XY52-12/4/70-C1D

Figure 30. Impeller Pressure Tubes Protruding Through
Aft End of Main Shaft

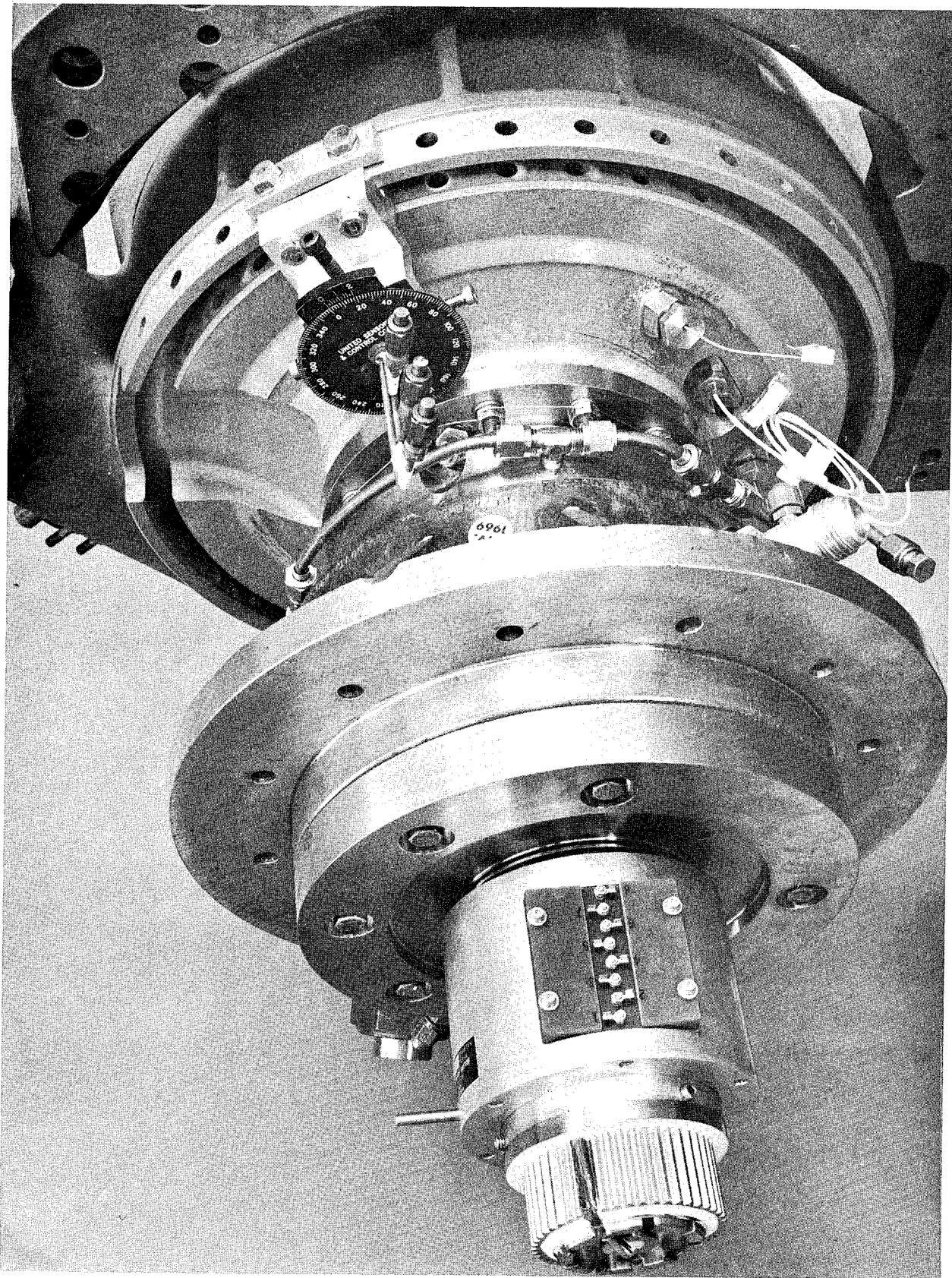


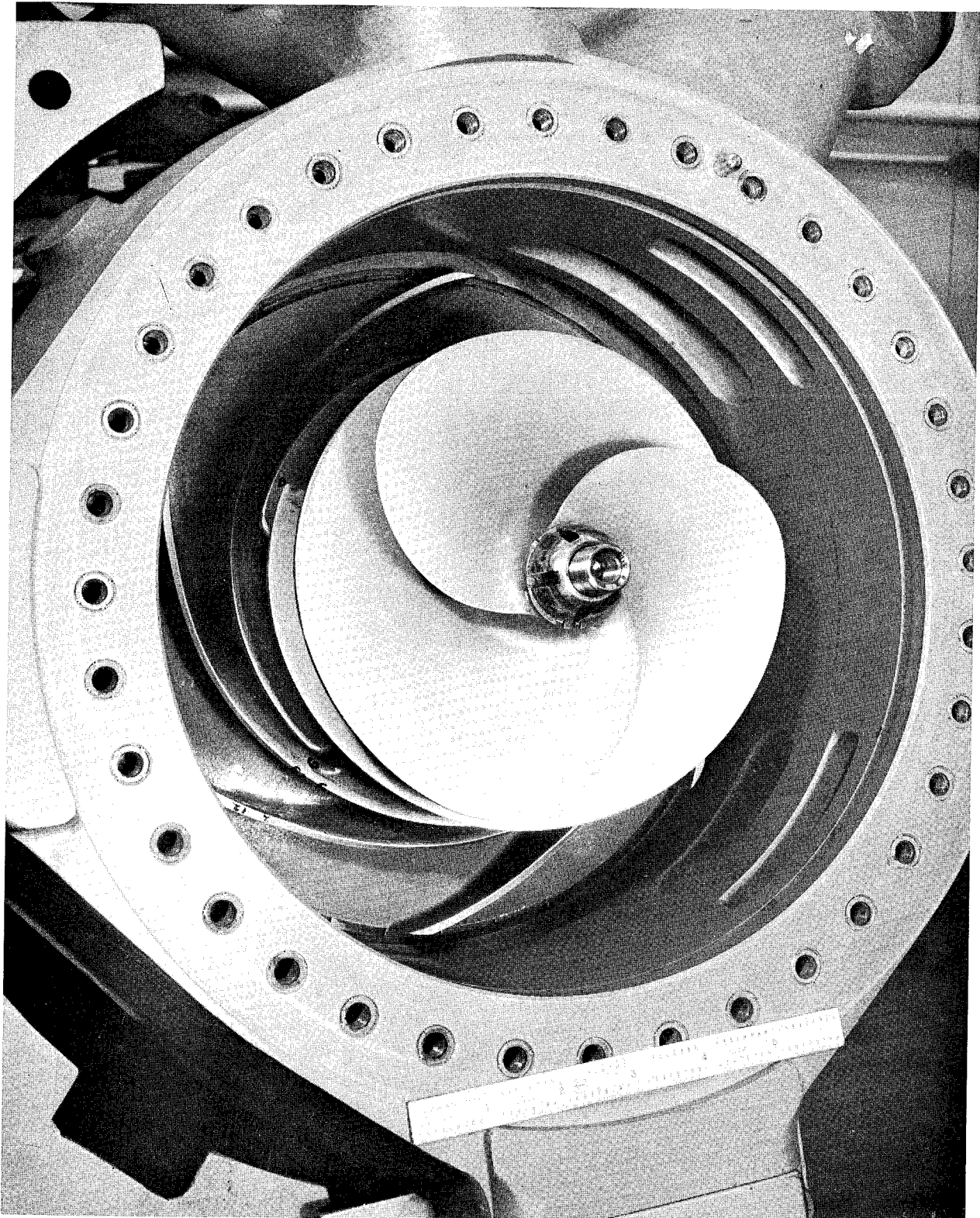
IXY62-1/25/71-C1B

Figure 31. Sealed Aft End of Main Shaft

1XY72-1/25/71-C1A

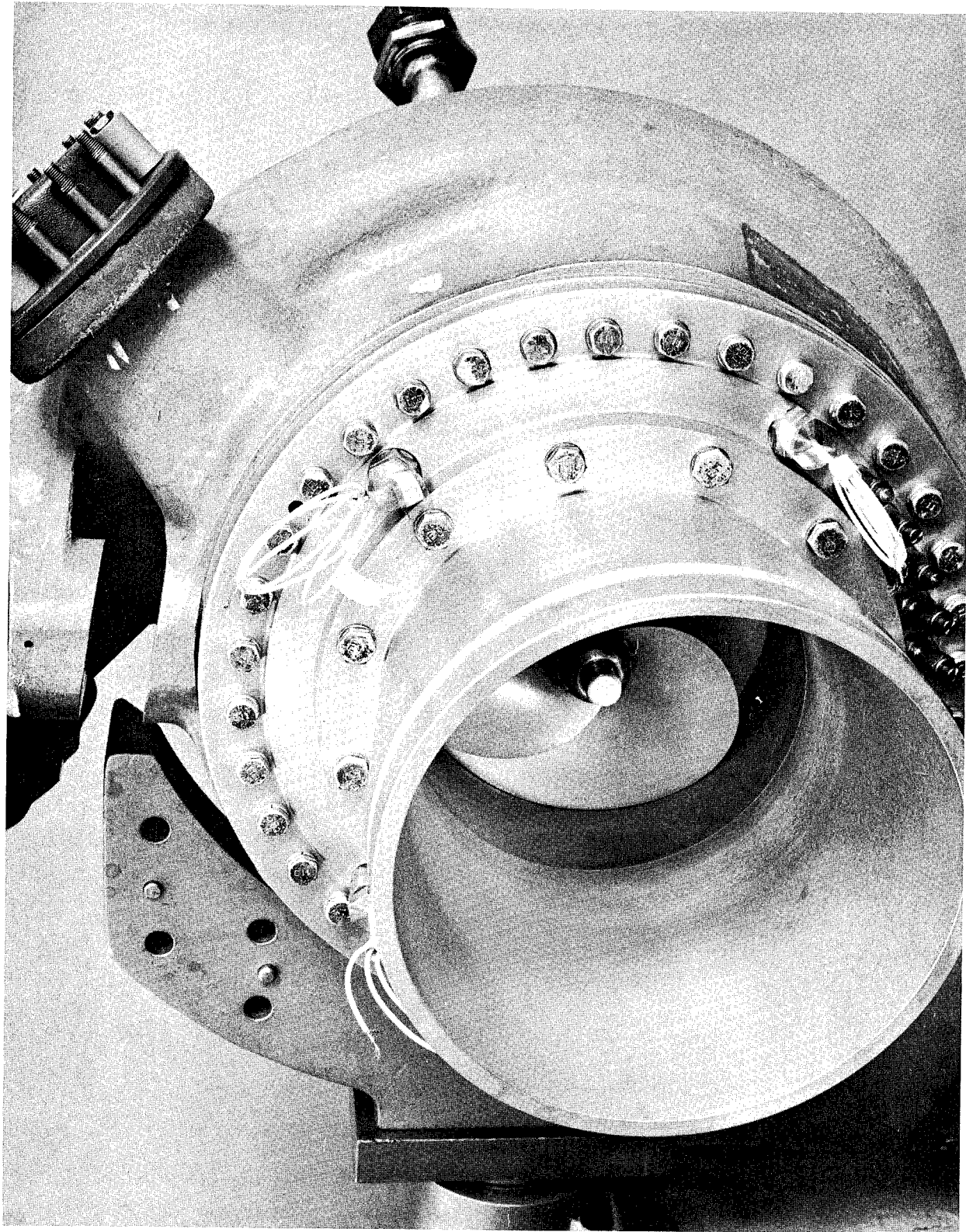
Figure 32. Assembled Aft End of Pump Assembly





1XY52-12/4/70-C1C

Figure 33. Inducer and Impeller Installed on Drive Shaft



1XY62-1/25/71-C1C

Figure 34. Inlet View of Pump Assembly

TASK F: TEST AND DATA CORRELATION

The experimental test program was conducted at the Pump Calibration Facility in Canoga Park. Four impeller clearance magnitudes were tested using a J-2 oxidizer unshrouded impeller. The test program was completed successfully, but required two rebuilds because of the pump adapter bearing failures.

Pump Calibration Facility

The experimental program was conducted at the Pump Calibration Facility located at Canoga Park, California. The pump drive consists of a 1200-rpm (125.6 rad/s) reversible, synchronous, electrical motor rated at 4000 horsepower (2984 kw). The 4000-horsepower (2984 kw) gearbox consists of two output shafts, one capable of producing speeds of 3976 rpm (416.29 rad/s) and 5038 rpm (527.49 rad/s), which was utilized for this test program. The Yee-type torquemeter (torque as a function of angular twist) is placed between the gearbox and pump mounting pedestal.

Figure 35 shows the schematic of the drive system and flow loop. Water is supplied by an 8000-gallon (30.28 m³) tank. A heat exchanger, located adjacent to the test tank, maintains a constant fluid temperature of approximately 75 F (297.04 K) during tests. The test tank is rated at 150 psi (103.42 N/cm²) and has a vacuum capability of about 28.5 inches of mercury (9.624 N/cm²) vacuum. The inlet ducting consists of 8-inch (20.32 cm) schedule-40 steel piping, and the discharge loop consists of 6-inch (15.24 cm) schedule-120 steel piping rated at 2000 psi (1378.9 N/cm²).

Pump speed is measured by a magnetic pickup of a 60-tooth gear with the data recorded on a Berkley Counter. Flow measurements are obtained by both magnetic- and turbine-type flowmeters located in series in the inlet loop. A removable, full-flow, stainless-steel, 40-micron (0.00004 m) filter is also located in the inlet duct. Torque measurements are obtained by the Yee Torque-X-Ducer system and recorded on Brown charts. Inlet and discharge pressures are obtained by direct pneumatic Foxboro and Brown Wiancko carrier systems. Fluid temperatures are obtained by Minneapolis Honeywell platinum resistance bulbs, and are recorded on Brown recorders. The facility instrumentation and control room is air conditioned and adjacent to the test cell. A separate air-conditioning unit is also located in the test cell for maintaining ambient temperatures during tests.

Pump Assembly Installation

Prior to installation of the pump assembly, the facility torquemeter with the modified torqueshaft was successfully calibrated both statically with load and then dynamically without load. The support mount and pump test assembly were then installed into the pump test facility. Both the quill shaft and main pump shaft were aligned, and the pump test assembly locked into the support mount by locking bolts and dowel pins. The torquemeter assembly was also locked in the support mount by using radial locking bolts.

Both the pump inlet and discharge ducting were installed, and the required instrumentation was installed and calibrated. Figures 36 and 37 show the completed installation of the pump test assembly in the Pump Calibration Facility.

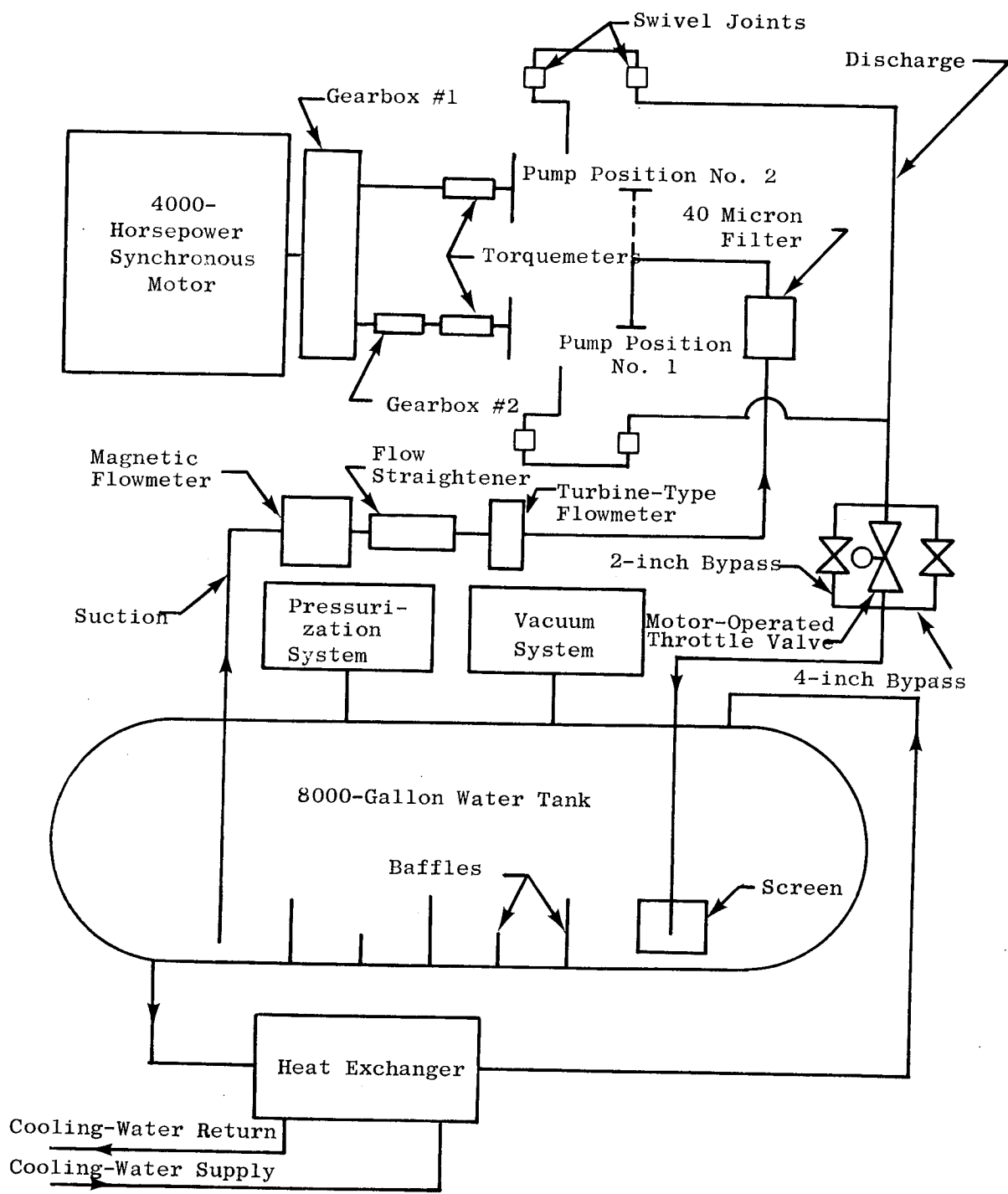
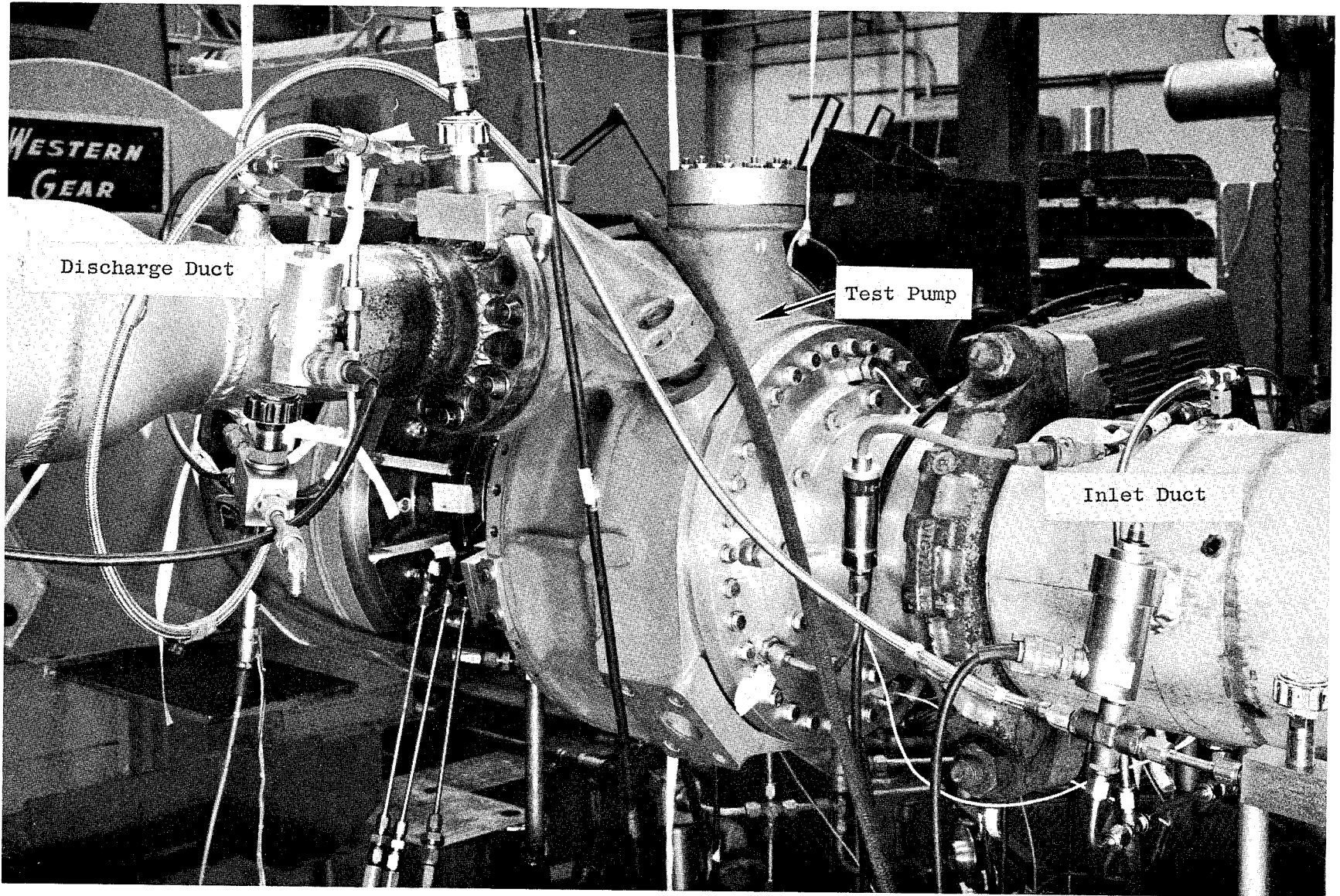
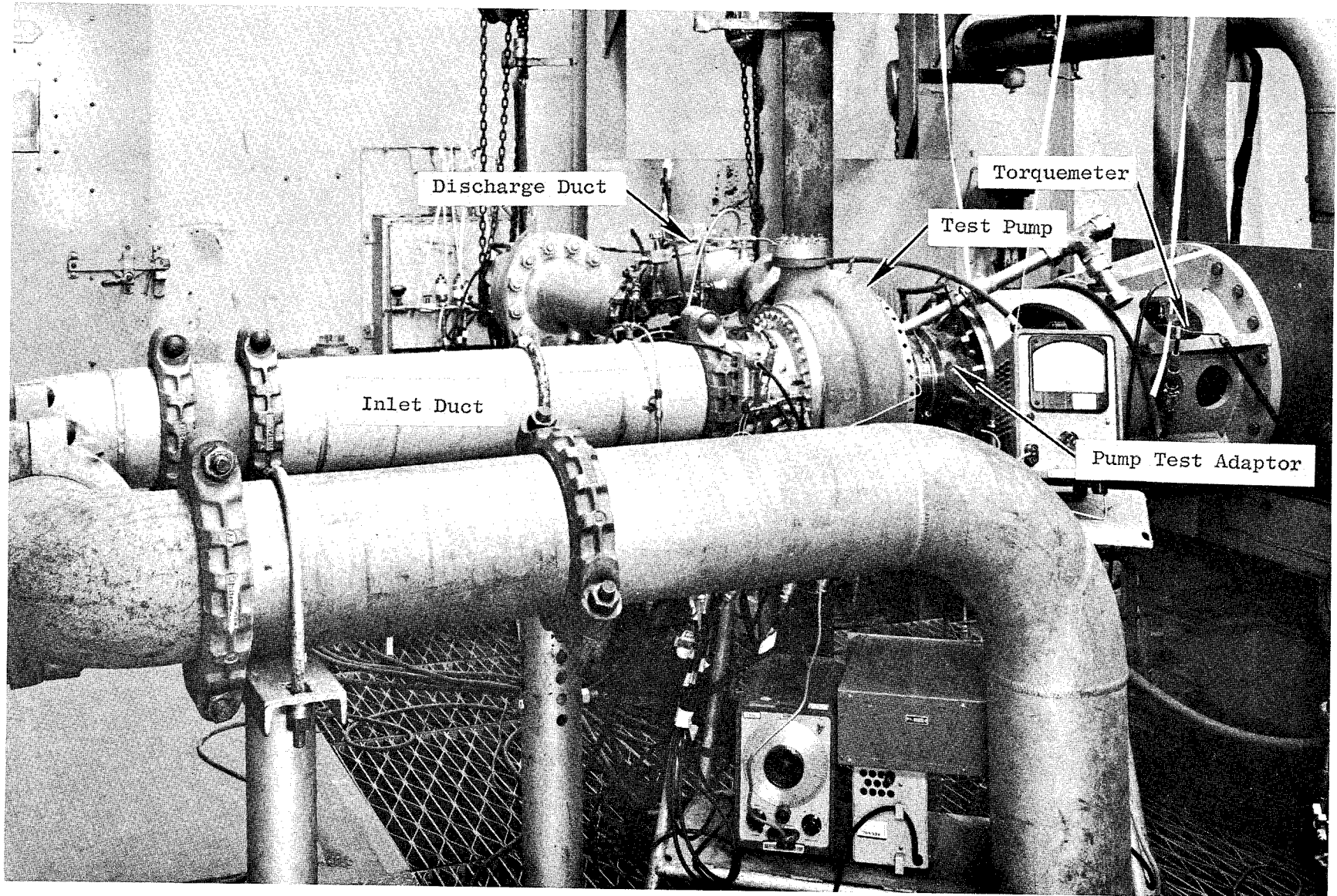


Figure 35. Schematic of the Pump Calibration Facility



1XY54-3/2/71-C1B

Figure 36. Installed Pump Test Assembly



1XY54-3/2/71-C1A

Figure 37. Pump Test Assembly in the Pump Calibration Facility

Test Program

The test results were obtained from the pump test assembly operating in water. A total of 18 tests were conducted and head-flow efficiency data, as well as cavitation performance and blade pressures from the Scanivalve were obtained. Four impeller tip clearance adjustments were tested and performance data at clearances of 0.015 inch (0.0381 cm), 0.085 inch (0.216 cm), 0.031 inch (0.0787 cm), and 0.009 inch (0.0229 cm) were obtained. Data for these clearances were taken at speeds of 3976 rpm (416.29 rad/s) and 5038 rpm (527.49 rad/s). Blade surface static pressure data were obtained at the 0.015-inch (0.0381 cm) clearance at a speed of 3976 rpm (416.29 rad/s).

Table 6 is a summary of the tests performed indicating operating conditions, duration, and the type of tests run. As the table indicates, two bearing failures occurred during the test series (test numbers 3 and 7). In both cases, the failure mode was seizure of the No. 2 bearing (inner bearing of the duplex set). A number of changes involving the slave lubrication system, test rig lubrication circuit, housing-to-bearing outer race fit, and axial thrust compensation (pressure control in the impeller back side cavity) were made before trouble-free operation was achieved. The Scanivalve data were lost on test 5 because of an electrical short in the Scanivalve drive motor. The proximity data were not obtained because of electrical shorting of the Bently transducers; erroneous discharge probe data were obtained and, therefore, are not presented.

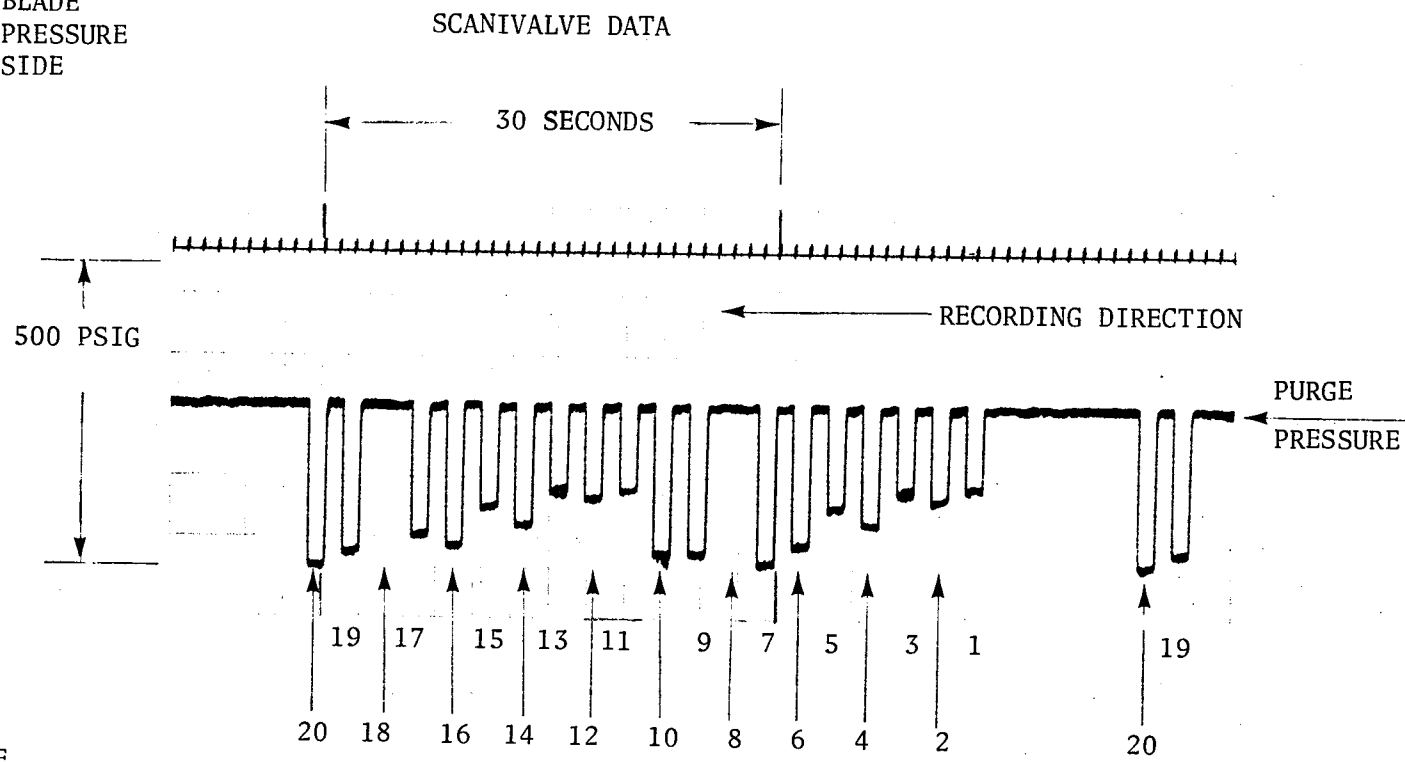
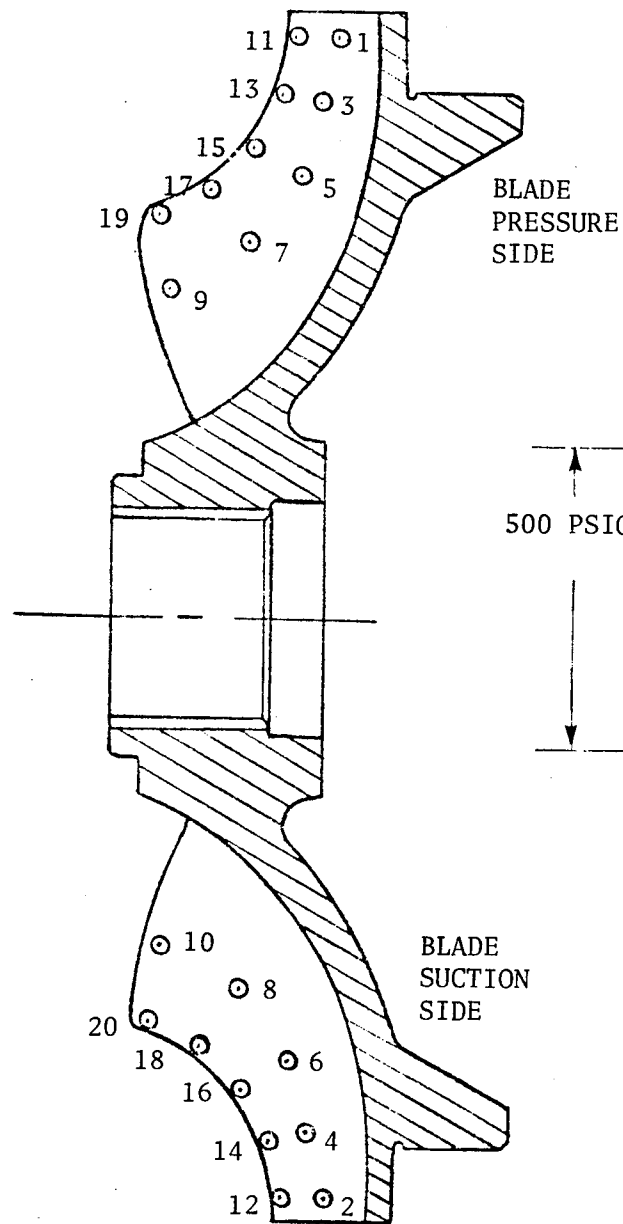
Data Reduction Technique

Scanivalve Data. Test 3 resulted in good scanivalve data. The data indicated suction-side and pressure-side static pressures on the impeller blades. The resultant data trace as recorded on the strip charts is indicated in Fig. 38. This figure also shows the locations of the pressure- and suction-side pressure taps on the meridional view. The exact locations are shown in Fig. 18. Pressure-side and suction-side taps were positioned at the same point in the meridional view, but on opposite blades. This allowed the blade pressure differential to be found simply by the difference between the two pressure readings. The tortuous path of the blade pressure tap tubing resulted in failure of the pressure tubing for stations 7, 8, and 18. All other tap locations, however, showed good calibrations and readings throughout the test. Failure of the Scanivalve was traced to the motor, which ceased to function during test 5. The replacement of the scanivalve system would have required a complete teardown and rebuild. The results of test 3 indicate that the system gave good pressure data, as was anticipated.

Static Pressure Tap Data. Static pressure taps were located along the front of the pump housing so as to read the main static pressure rise along the impeller tip. A total of eight pressure taps (designated tap No. 2 through No. 9) were located along the housing. This allowed the static pressure on the housing to be compared with the pressure rise found in the suction and pressure side of the impeller blade Scanivalve data. Two static pressure taps were located on the rear housing behind the impeller (designated tap No. 10 and No. 12), and measured pressure levels in the impeller rear shroud area and the balance cavity area, respectively (Fig. 21). These data were recorded on strip charts and were reduced by hand

TABLE 6. TEST PROGRAM LOG

Test No.	Type	Speed, rpm (rad/s)	Flow, gpm (cm ³ /s)	Test date	Duration seconds	Remarks
Nominal Clearance = 0.015 inch (0.0381 cm)						
1	Shakedown	~3000 (314.1)	~1400 (88,312)	2/25/71	10	Start-stop
2	Checkout	3976 (416.29)	1900 (119,852)	2/26/71	138	Facility, instrumentation and Scanivalve checkout test
3	Head Flow	3976 (416.29)	1514, 1264, 865 (95,503, 79,733, 54,564)	3/1/71	308	Terminated due to bearing failure
4	Checkout	3976 (416.29)	1420 (89,574)	6/22/71	130	Facility cutoff
5	Head Flow	3976 (416.29)	1510, 1245, 1023, 756, 1245 (95,251, 78,535, 64,531, 47,688, 78,535)	6/23/71	152	No Scanivalve data
6	↓	3976 (416.29)	1501, 1256, 991, 766 (94,683, 79,228, 62,512, 48,319)	7/2/71	132	Hydrodynamic test
7	↓	5038 (527.49)	2231, 1913, 1582, 1276 (140,732, 120,672, 99,793, 80,490)	7/2/71	210	Terminated due to bearing failure
Maximum Clearance = 0.085 inch (0.216 cm)						
8	Checkout	3976 (416.29)	1250, 1520, 991, 767 (78,850, 95,882, 62,512, 48,382)	8/26/71	83	OK
9	Head Flow	3976 (416.29)	1501, 1251, 983, 749 (94,683, 78,913, 62,008, 47,247)	8/27/71	150	↓
10	↓	5038 (527.49)	2230, 1897, 1598, 1279 (140,668, 119,663, 100,802, 80,679)	8/27/71	223	↓
11	Cavitation	5038 (527.49)	1592 (100,423)	8/27/71	264	↓
Intermediate Clearance = 0.031 inch (0.0787 cm)						
12	Head Flow	3976 (416.29)	1530, 1261, 1001, 756 (96,512, 79,544, 63,143, 47,688)	8/27/71	192	OK
13	↓	5038 (527.49)	2230, 1905, 1580, 1282 (140,668, 120,167, 99,666, 80,867)	8/27/71	160	↓
14	Cavitation	5038 (527.49)	1591 (100,360)	8/27/71	242	↓
Nominal Clearance = 0.015 inch (0.0381 cm)						
15	Cavitation	5038 (527.49)	1607 (101,370)	8/30/71	284	
Minimum Clearance = 0.009 inch (0.0229 cm)						
16	Head Flow	3976 (416.29)	1521, 1261, 1016, 767 (95,945, 79,544, 64,089, 48,383)	8/30/71	196	OK
17	↓	5038 (527.49)	2225, 1906, 1591, 1271 (140,353, 120,231, 100,360, 80,175)	8/30/71	172	↓
18	Cavitation	5038 (527.49)	1591 (100,360)	8/30/71	224	↓
						Test Program Complete



NOTE: READINGS 7, 8 AND 18 ARE NOT VALID BECAUSE OF FAILED PRESSURE TUBING

Figure 38. Typical Scanivalve Blade Pressure Data

for all tests. The readings were indicated as a percent of the chart pressure calibrated range and, accounting for calibration shifts, the data were reduced to units of psig (N/cm^2) at all flow levels in head-flow tests and at many levels of NPSH for the cavitation test. The volute discharge flange pressure tap readings and the inlet pressure data were reduced similarly.

Test Results

Scanivalve Data for Blade-Loading Determination. Figures 39 and 40 present the static pressures measured on the blade pressure and suction surface. The test was run at 3976 rpm (416.29 rad/s) with an impeller tip axial clearance of 0.015 inch (0.0381 cm) at three flowrates. The data are plotted as a function of meridional distance along the impeller blade. Figures 41 and 42 present the same test data plotted as a function of the pressure tap diameter. Due to the loss of data from the taps previously mentioned, several data points were interpolated from the smooth curve generated through the data.

Static Wall Tap Data. Static pressure levels were measured during all the tests to determine the mean static pressure rise along the front housing as a function of diameter at all clearance levels. These data were plotted as a function of diameter for each head-flow test at each clearance, and are presented in Fig. 43 through 53. Included in these figures are rear shroud pressures, inlet pressures, and volute discharge pressure. The static pressure data measured along the front housing of the pump in test 3 show good agreement with the Scanivalve data from test 3. The static wall tap must sense the pressure differential on the blade as the blade moves by the tap. It is expected then that the static pressure reading would indicate a mean pressure somewhere between the blade suction and pressure surface levels, which is the case for test 3. Static pressure readings also allow the axial thrust calculations to be determined with greater accuracy.

It should be noted that the pressure levels of tap locations 8 and 9 differ to a large extent. Pressure tap No. 8 is in the same quadrant of the pump as taps No. 2 through No. 7, and tends to indicate good continuity with those pressure readings. Tap location No. 9 is placed 90 degrees from tap location No. 8. The reason for the large difference is due to the stagnation pressure buildup on the volute tongue, which influences the angular pressure distribution. This effect is reduced as the radius decreases since pump rotation causes a smoothing of the pressure profile. It is not expected that angular position of the pressure taps would cause large differences in wall static pressure levels at diameters inside the impeller tip diameter.

Cavitation Test Results. Cavitation tests were conducted for nominal flow at the four clearances and at a mean water temperature of 75 F (297 K). Inlet pressures were reduced to levels which caused a minimum of 10-percent pump head loss. The tests were made at a test speed of 5038 rpm (527.5 rad/s). The reduced results of these tests are presented in Fig. 54 through 57, and show pump head rise as a function of NPSH. The cavitation characteristics indicate a stable pump head level down to the "knee" of the curve, where the pump head falls quickly into the supercavitating condition except at the lowest tip clearance where a slightly unstable condition is evident.

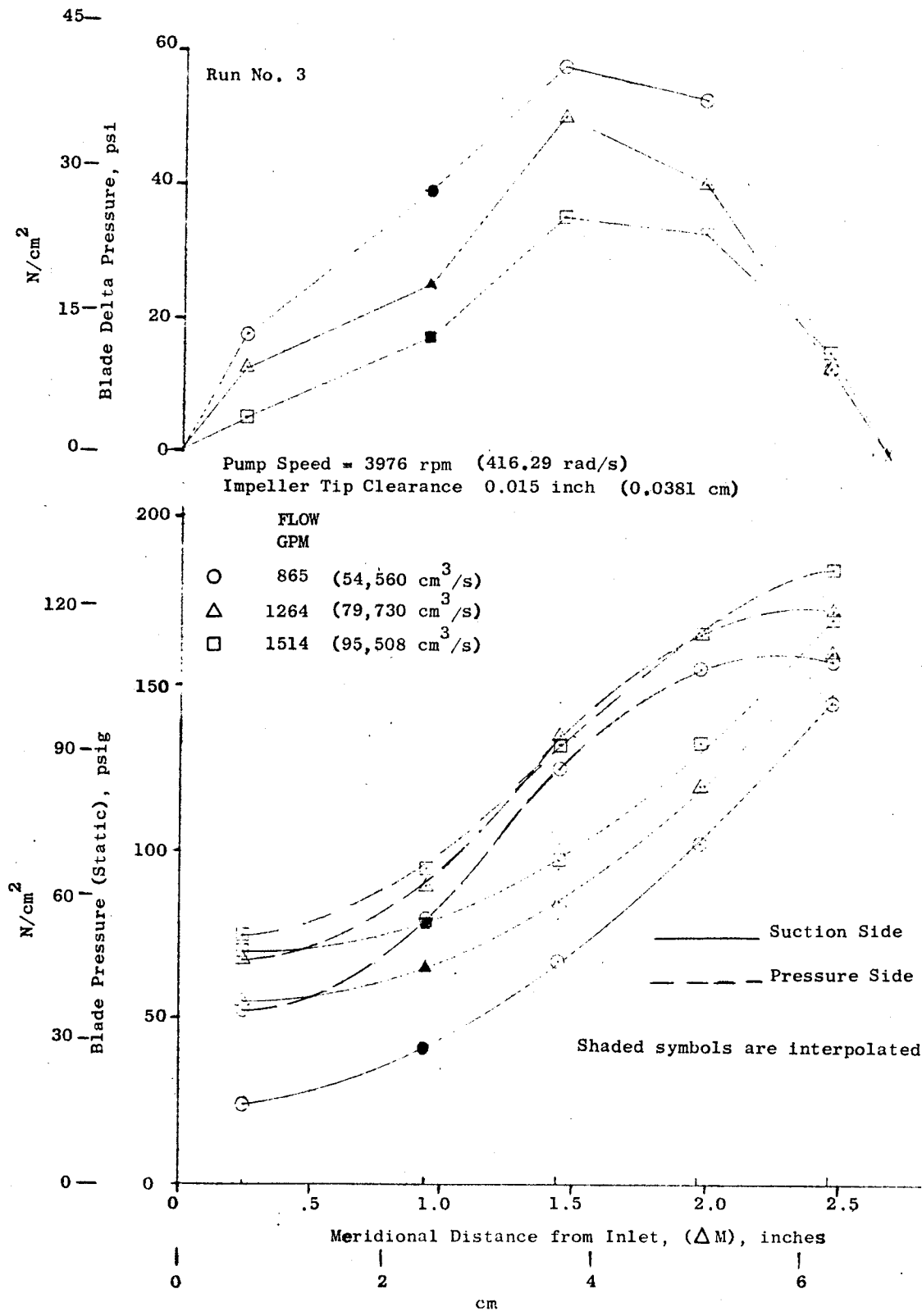


Figure 39. Blade Static Tip Streamline Pressures

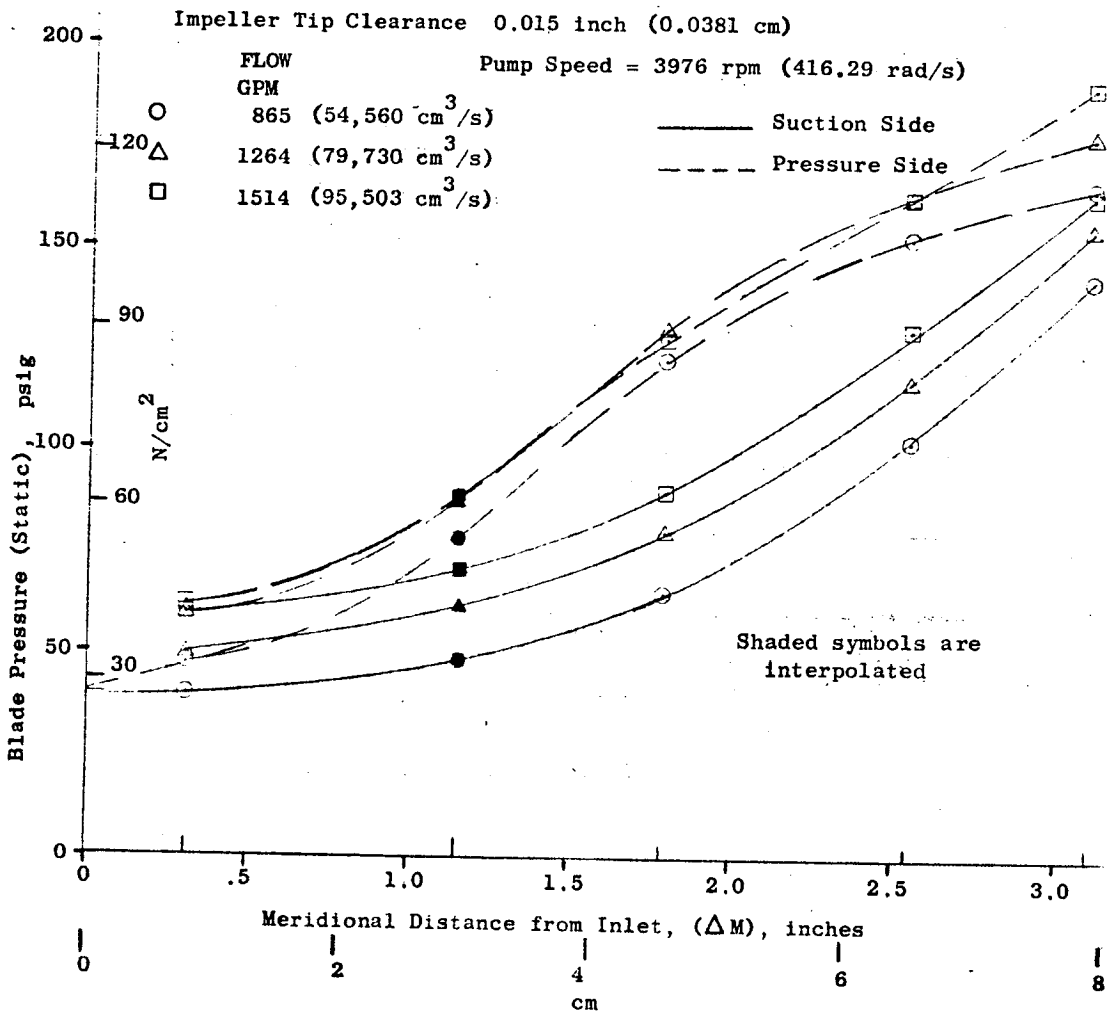
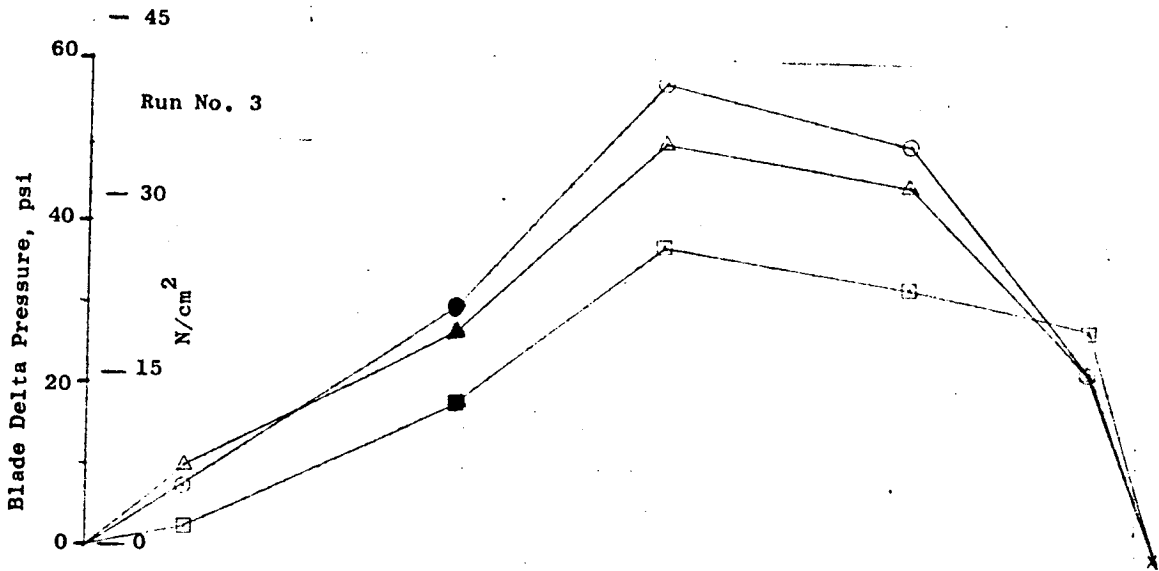


Figure 40. Blade Static Mean Streamline Pressures

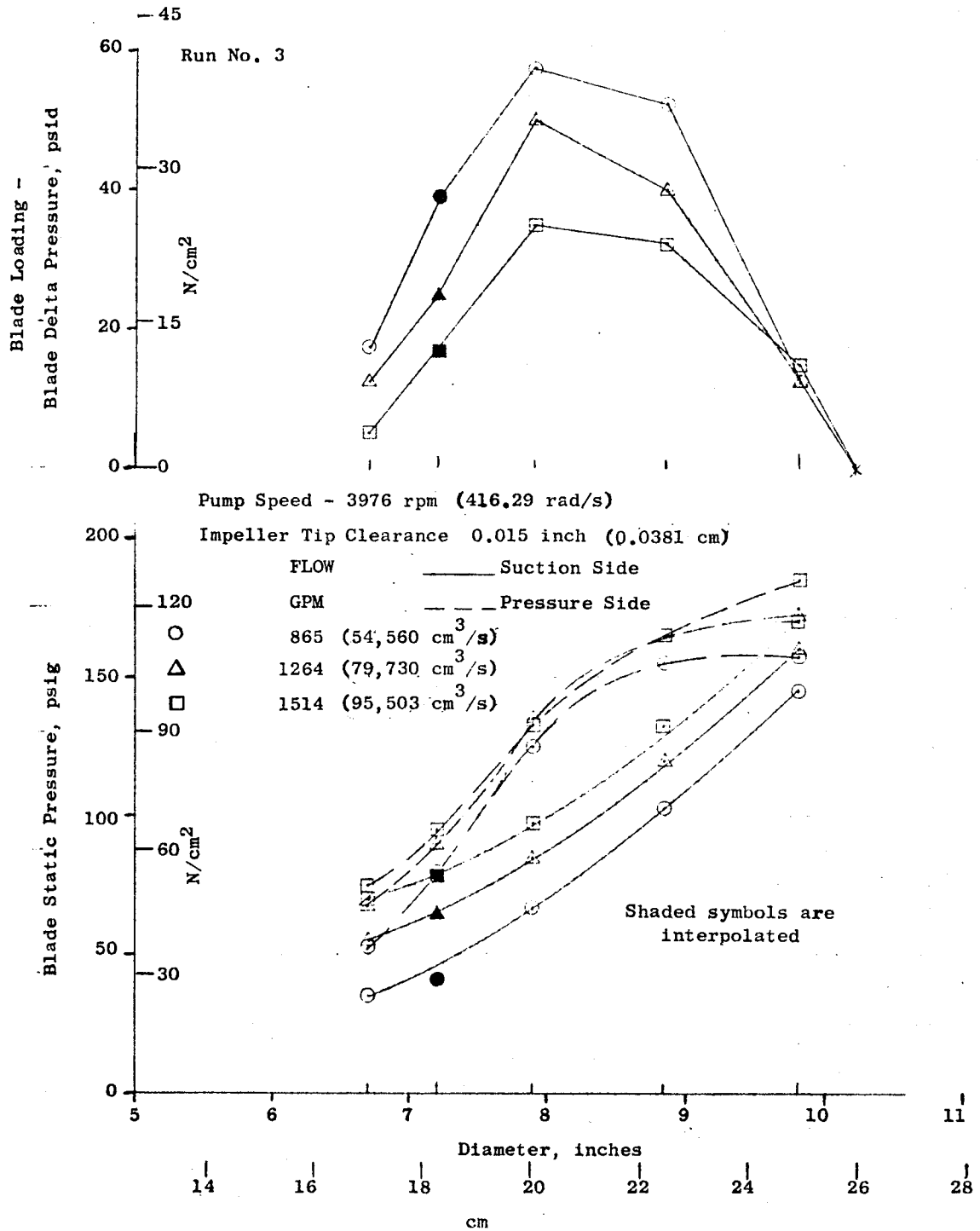


Figure 41. Blade Static Tip Streamline Pressures for Open Impeller

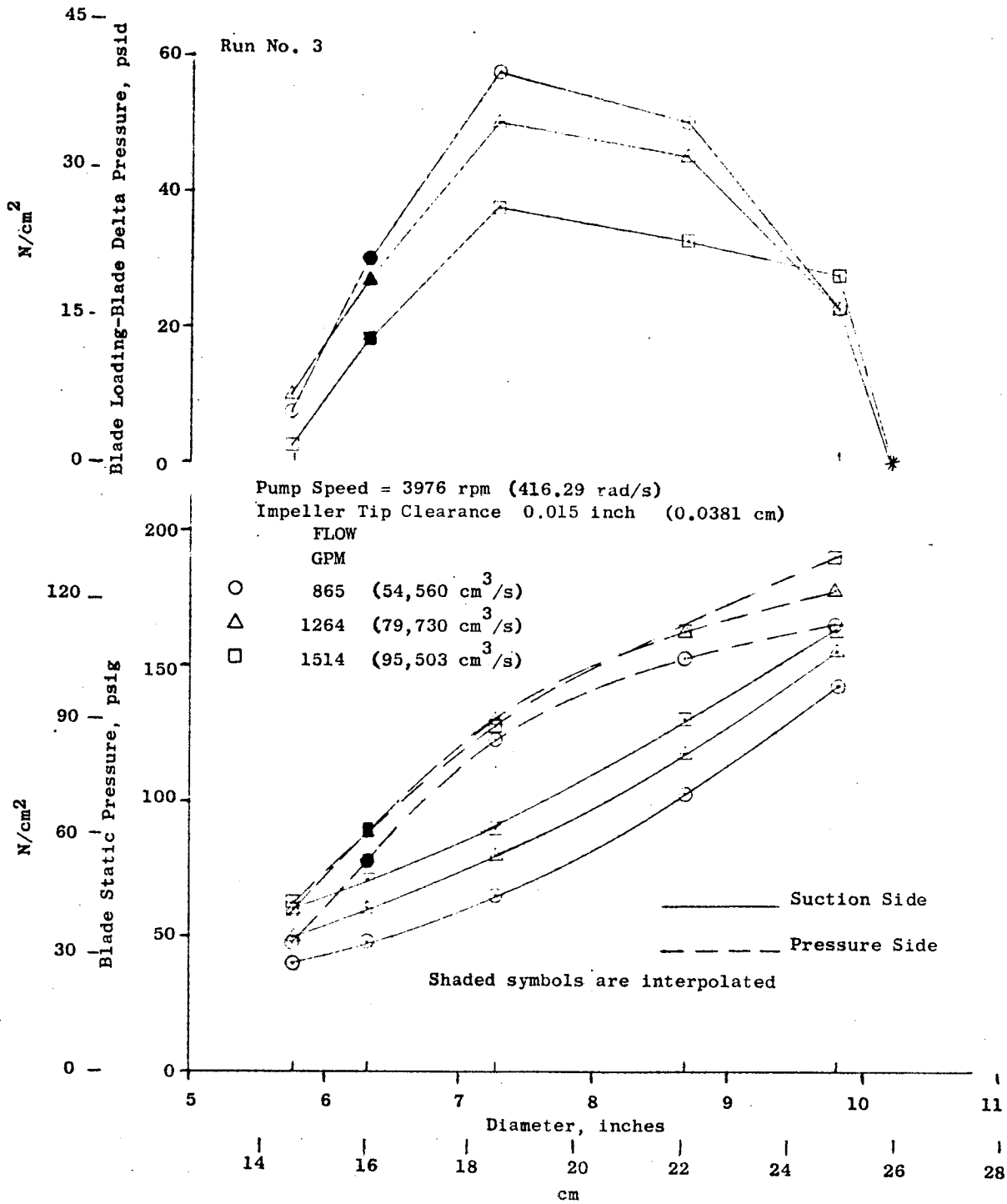


Figure 42. Blade Static Mean Streamline Pressures for Open Impeller

Run No. 3
 Curve Speed - 3976 rpm (416.29 rad/s)
 Test Speed - 3976 rpm (416.29 rad/s)
 Impeller Tip Clearance 0.015 inch (0.0381 cm)

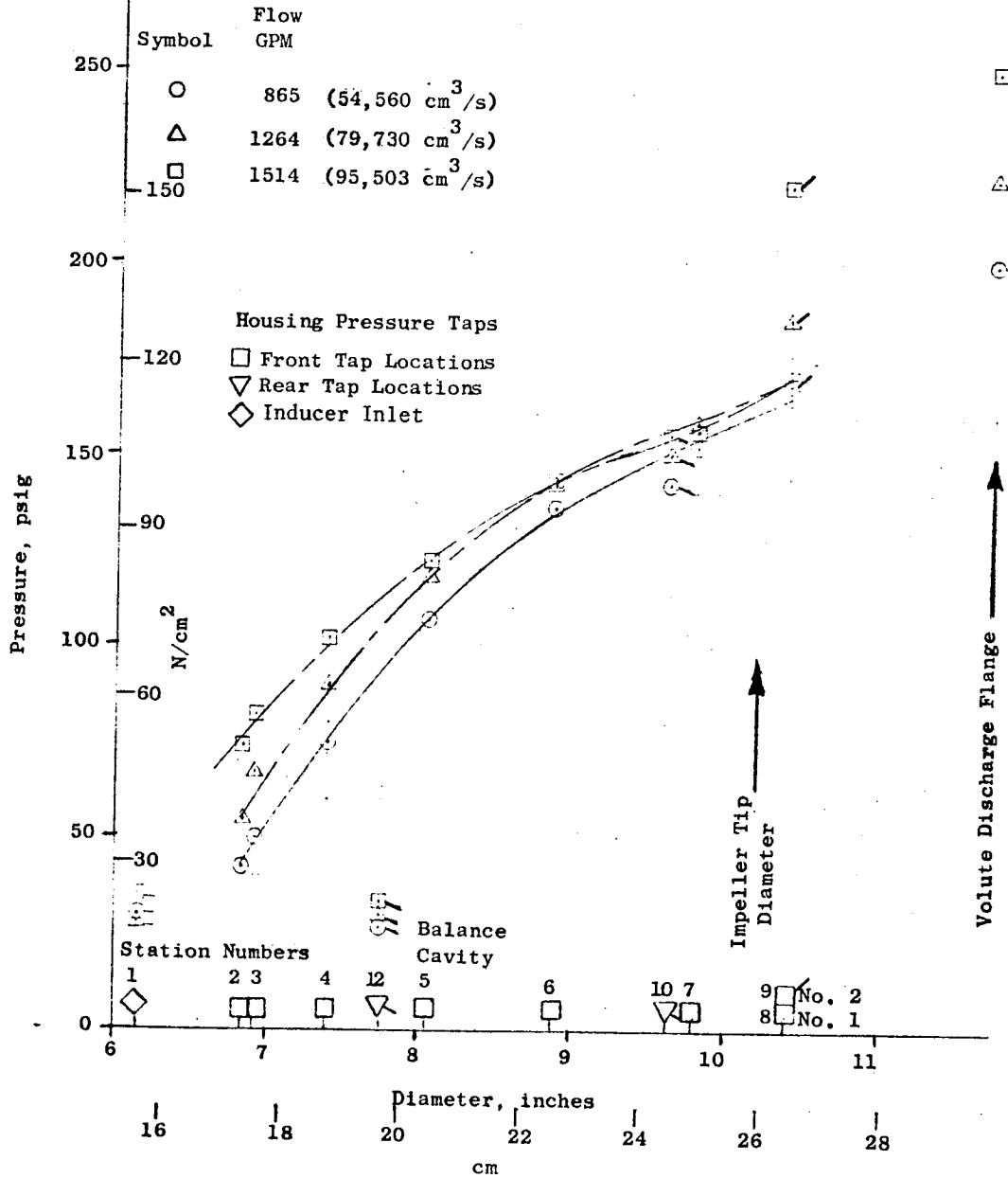


Figure 43. Wall Tap Static Pressures for Open Impeller

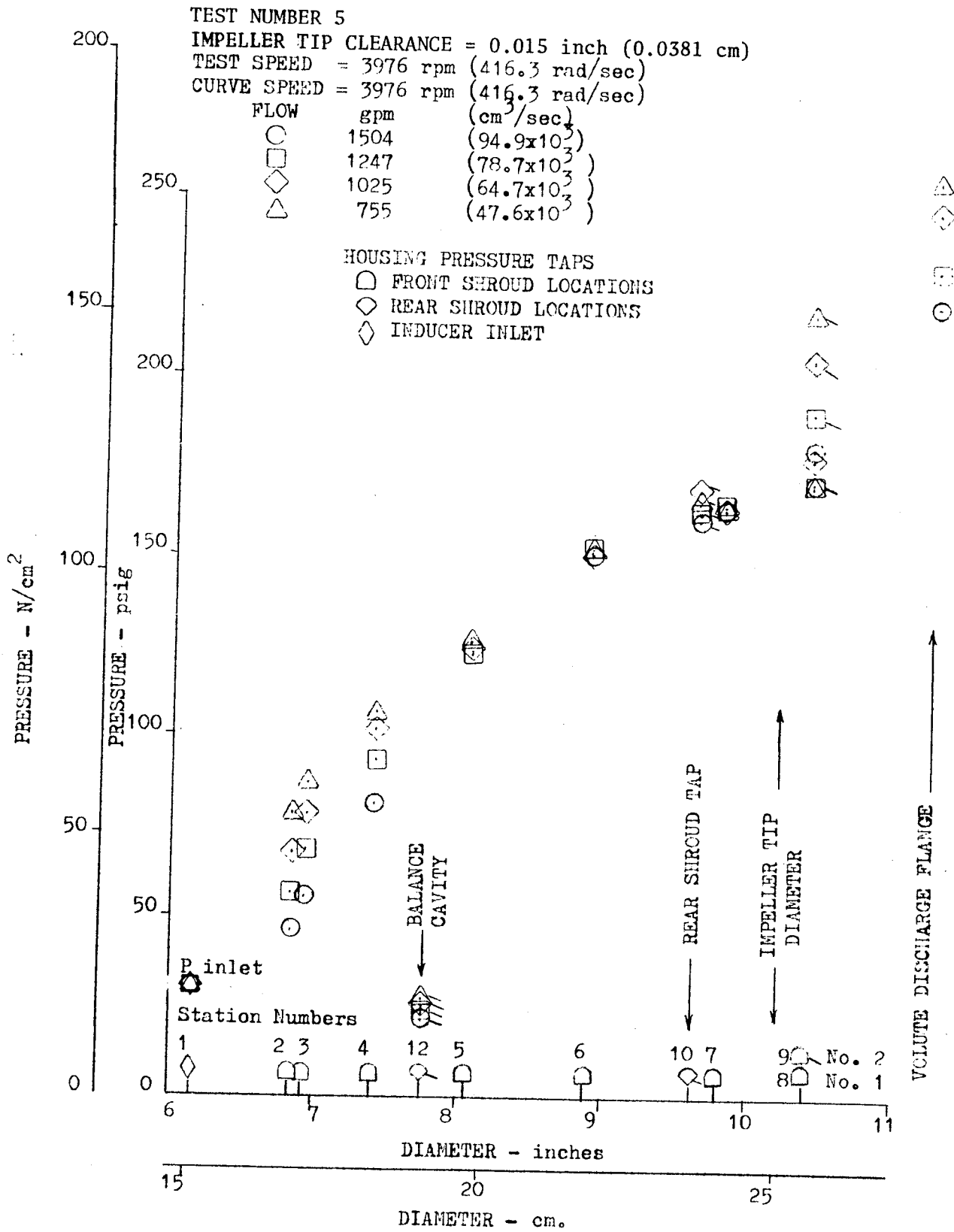


Figure 44. Modified J-2 Oxidizer Pump Wall Tap Static Pressures for Open-Faced Impeller

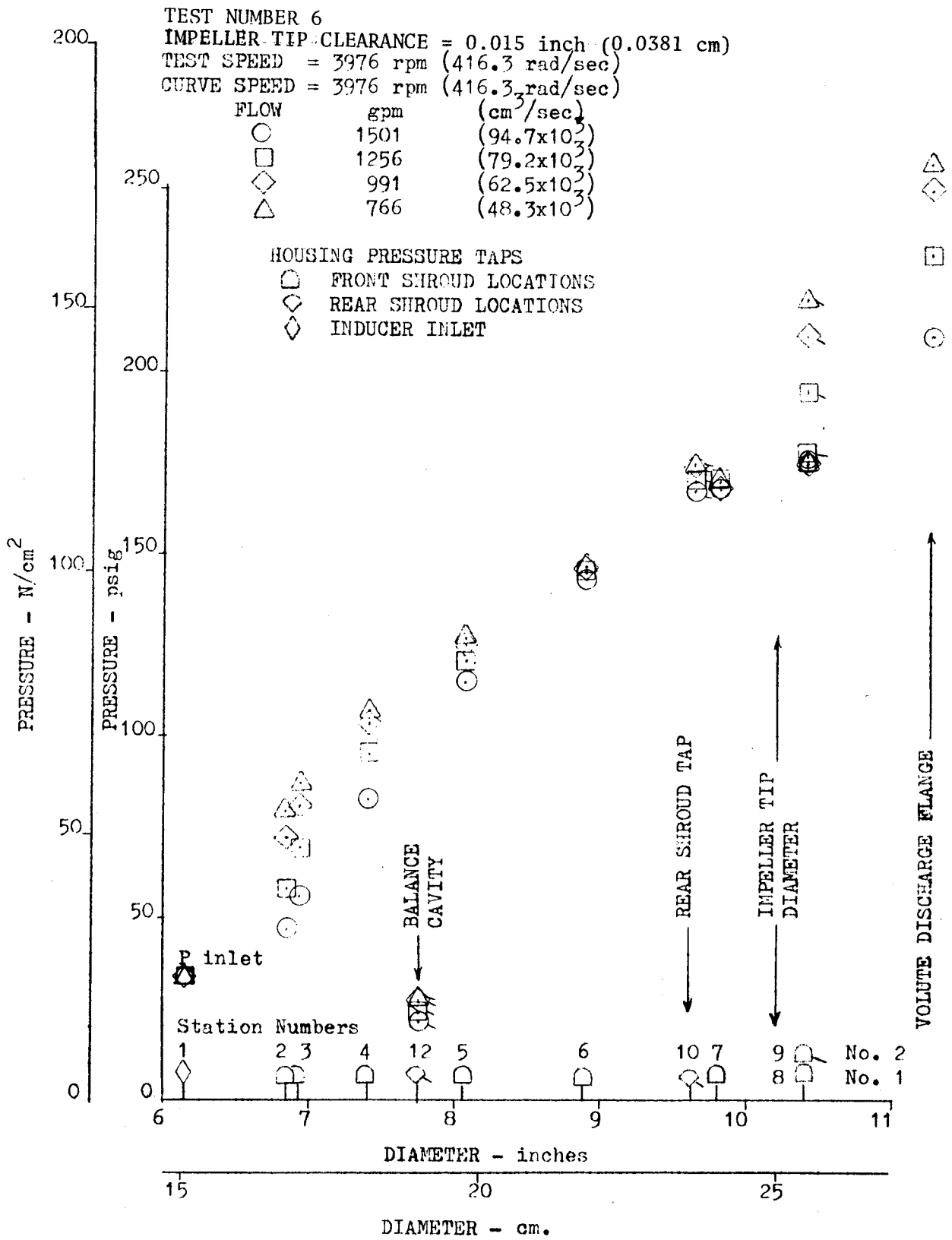


Figure 45. Modified J-2 Oxidizer Pump Wall Tap Static Pressures for Open-Faced Impeller

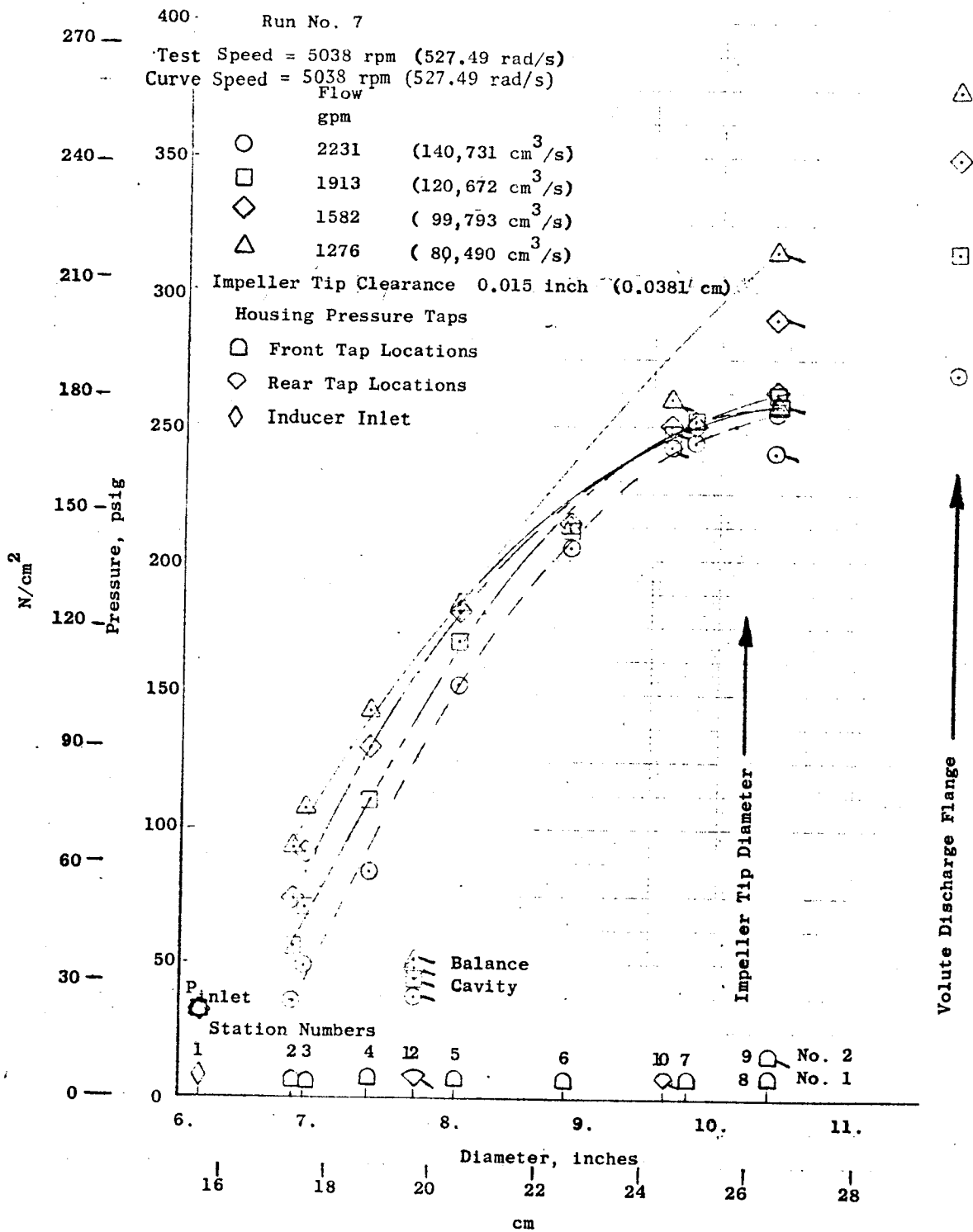


Figure 46. Wall Tap Static Pressures for Open Impeller

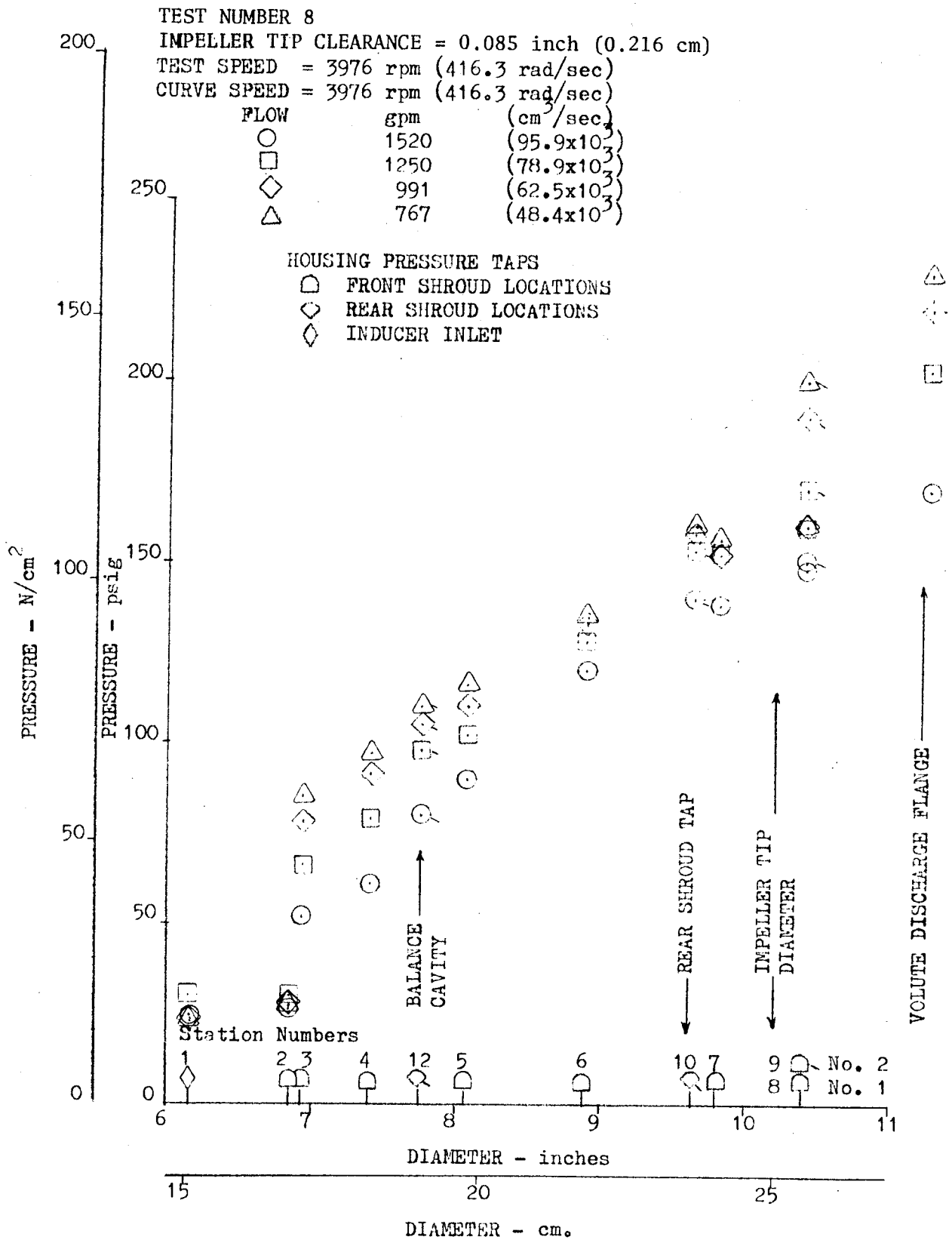


Figure 47. Modified J-2 Oxidizer Pump Wall Tap Static Pressures for Open-Faced Impeller

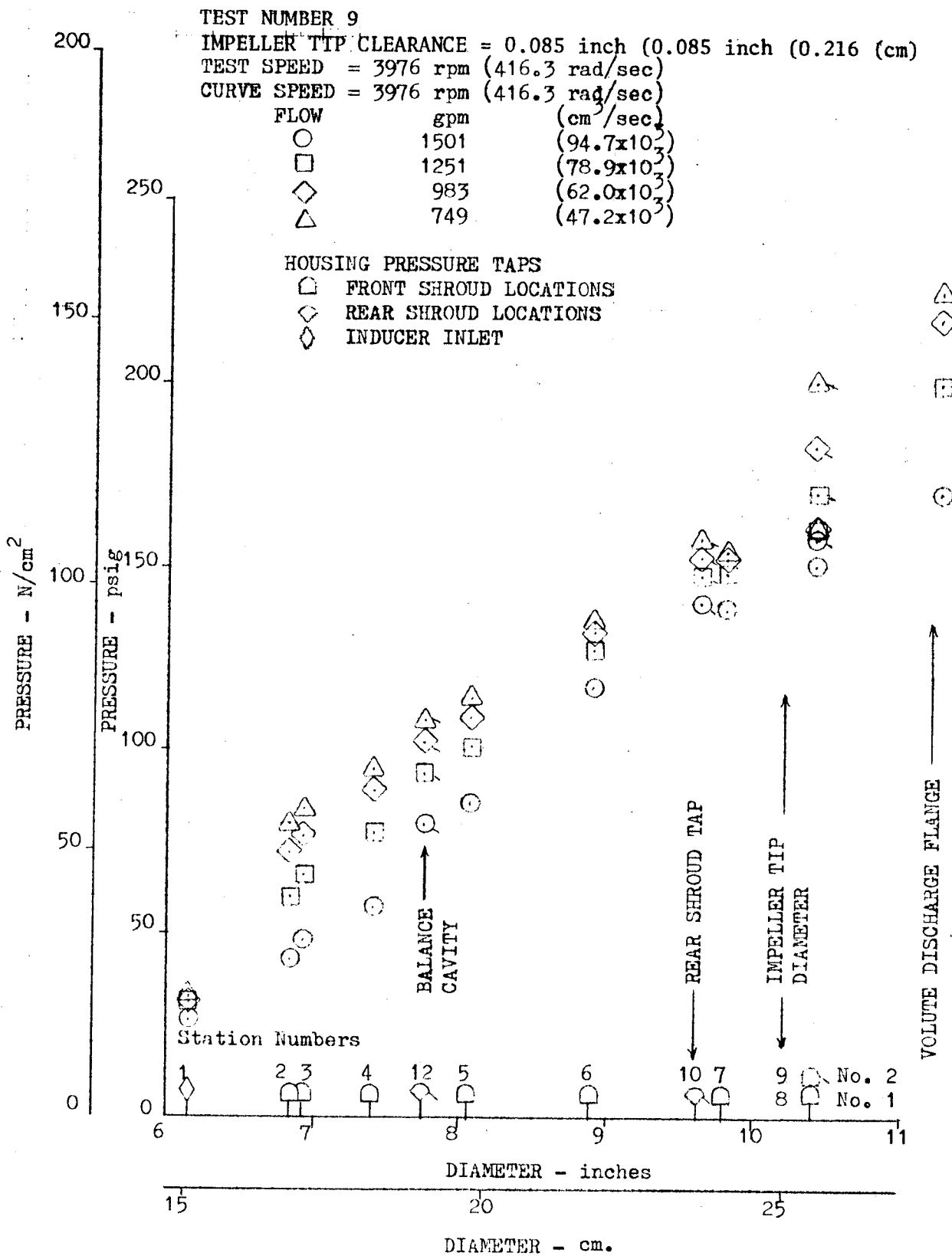


Figure 48. Modified J-2 Oxidizer Pump Wall Tap Static Pressures for Open-Faced Impeller

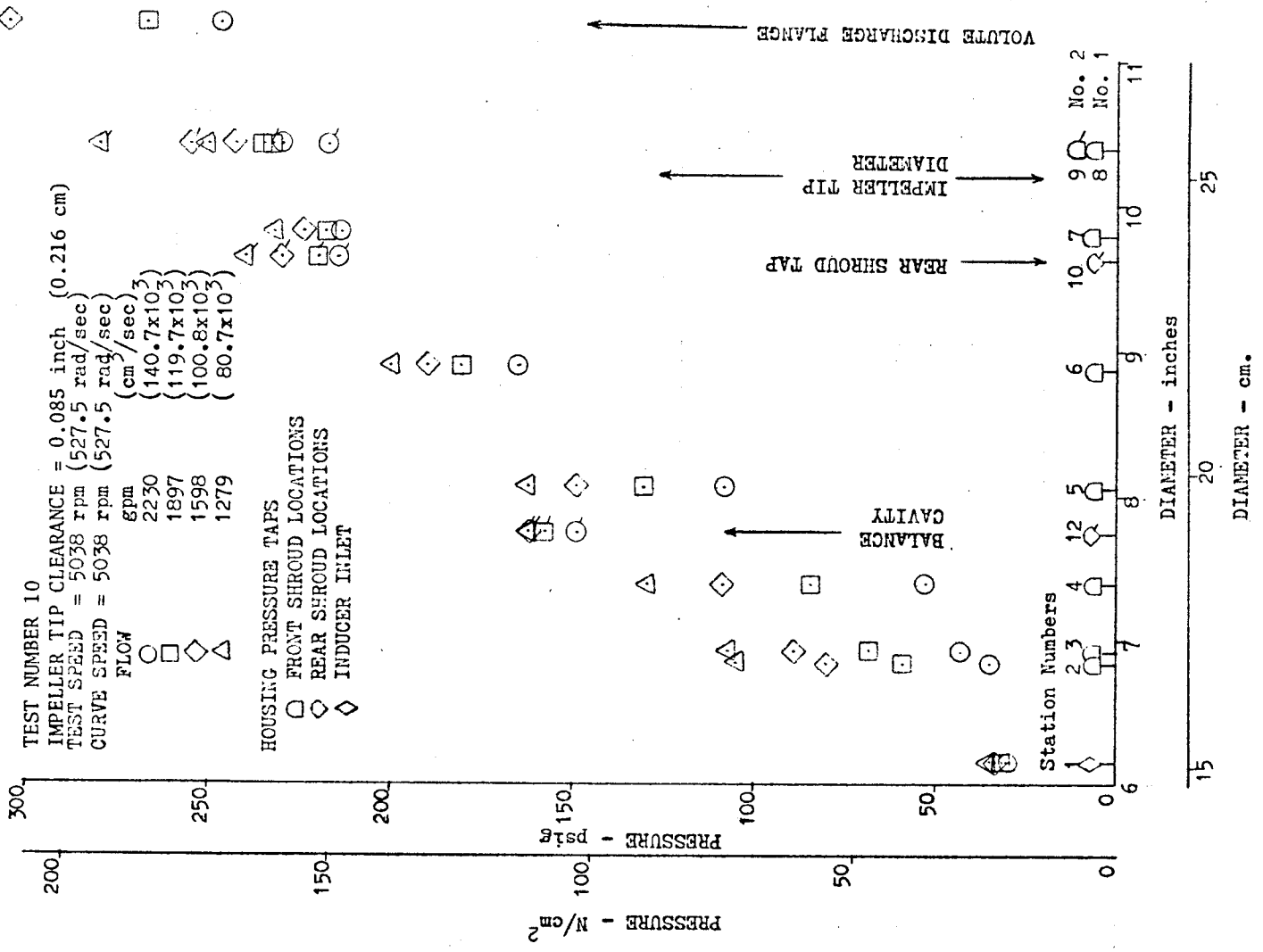


Figure 49. Modified J-2 Oxidizer Pump Wall Tap Static Pressures for Open-Faced Impeller

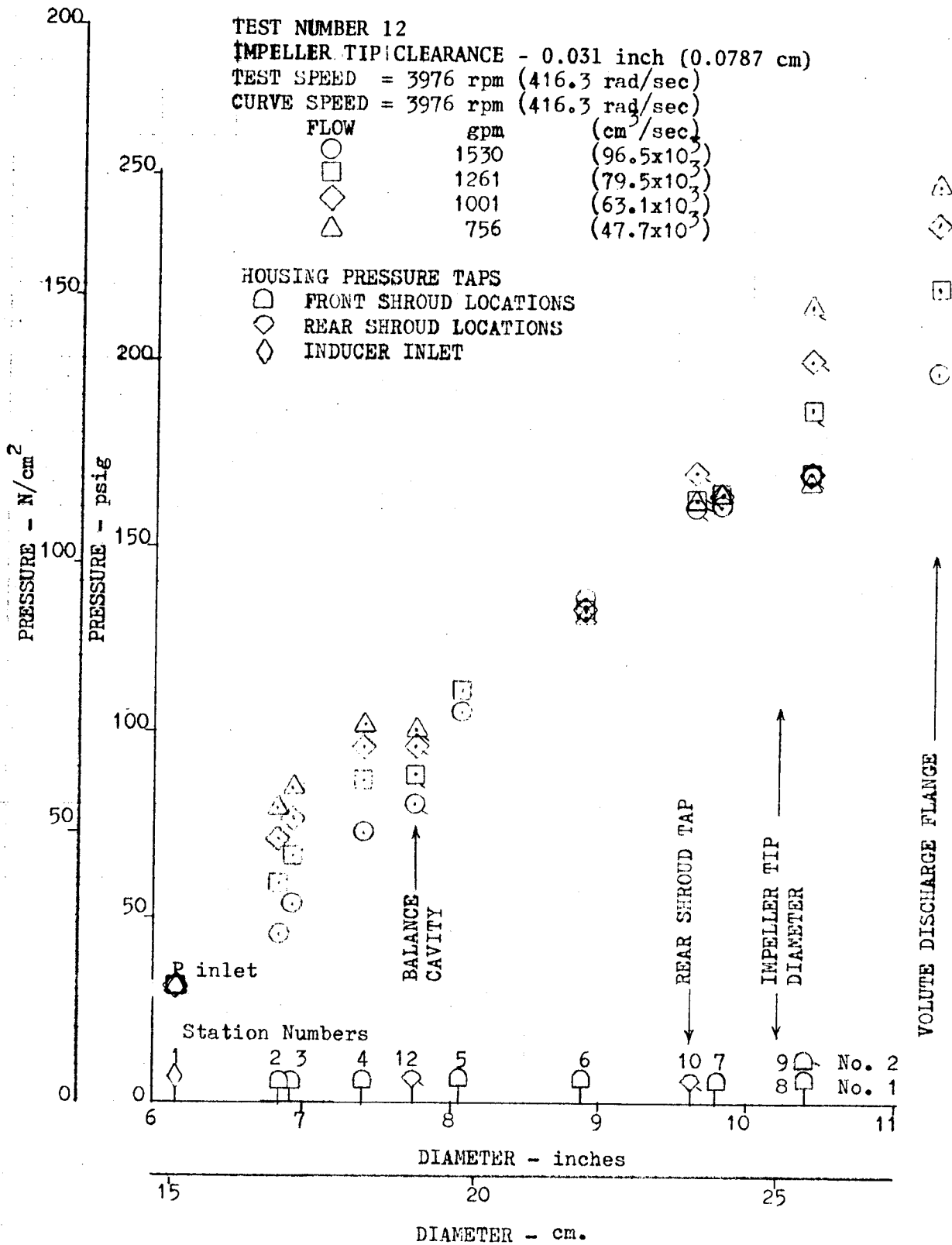


Figure 50. Modified J-2 Oxidizer Pump Wall Tap Static Pressure for Open-Faced Impeller

(362.5) \triangle \diamond

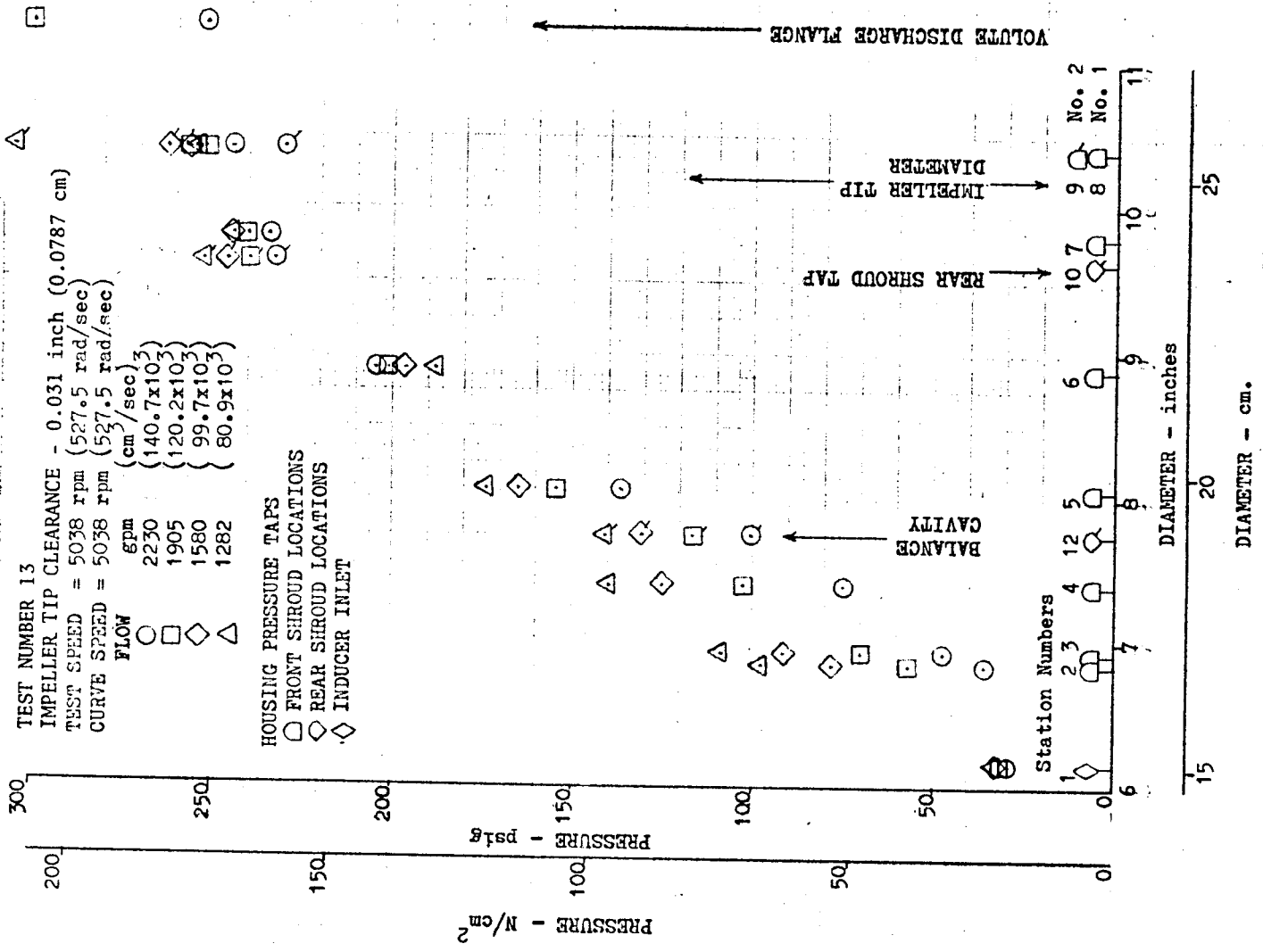


Figure 51. Modified J-2 Oxidizer Pump Wall Tap Static Pressures for Open-Faced Impeller

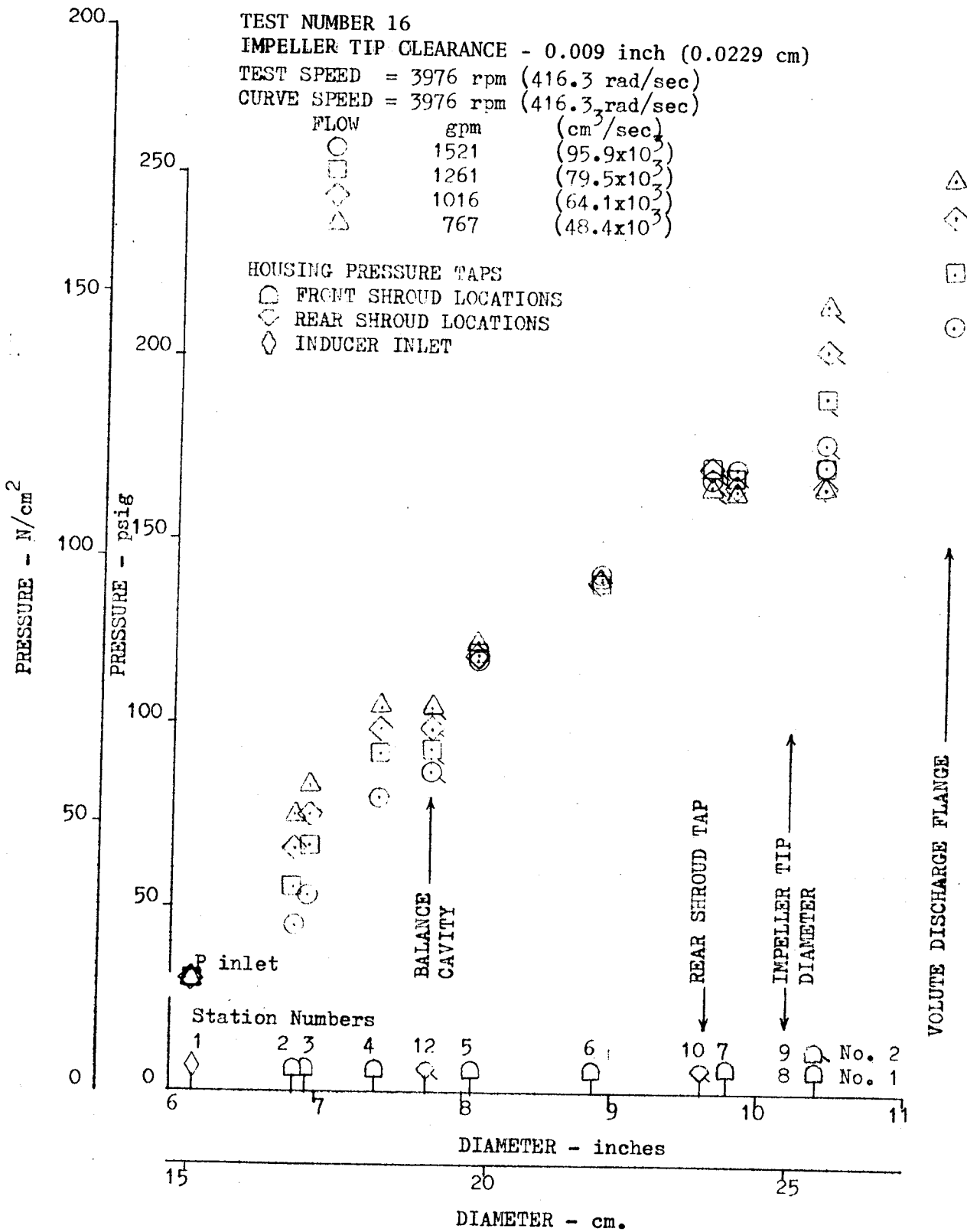


Figure 52. Modified J-2 Oxidizer Pump Wall Tap Static Pressures for Open-Faced Impeller

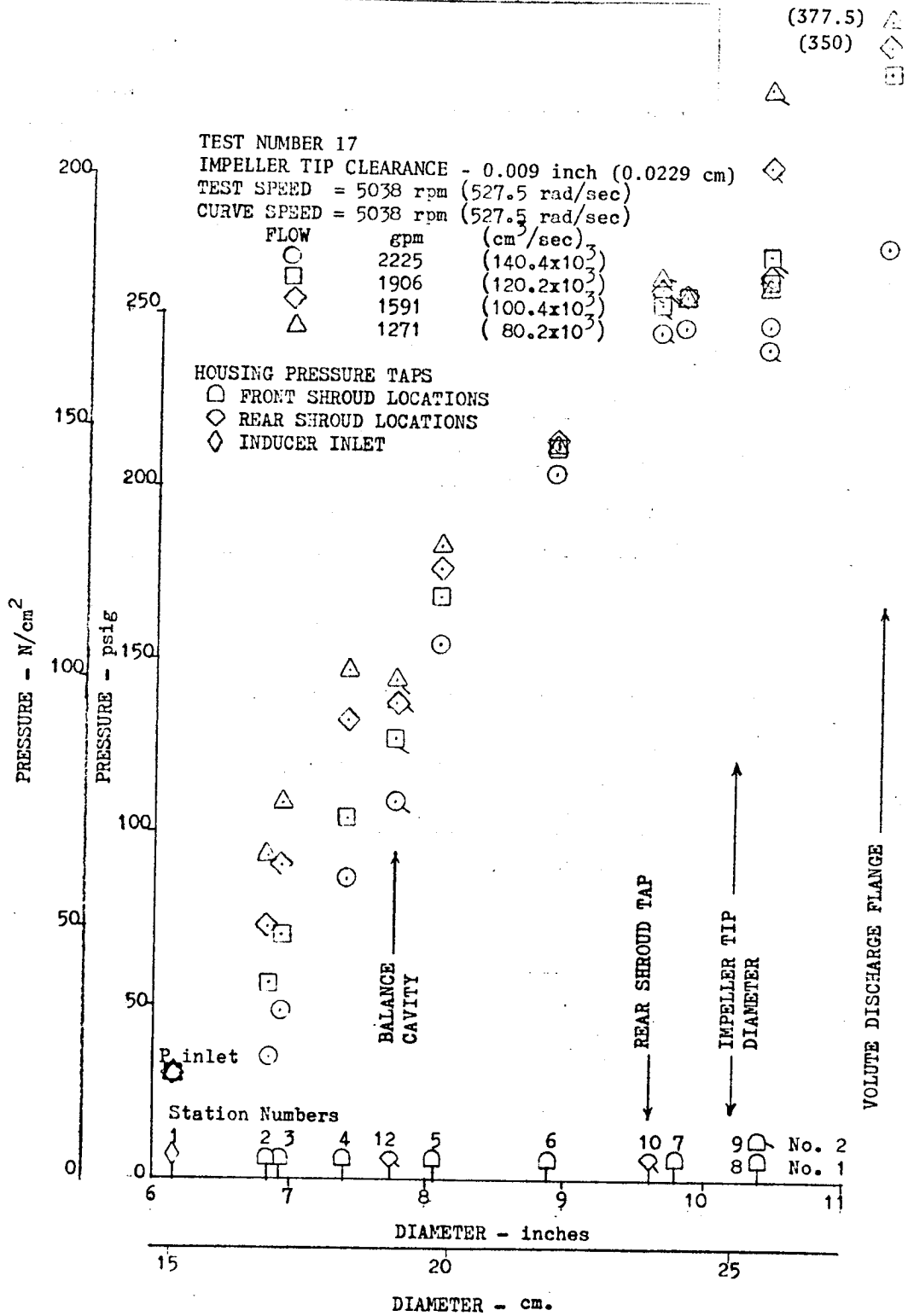


Figure 53. Modified J-2 Oxidizer Pump Wall Tap Static Pressures for Open-Faced Impeller

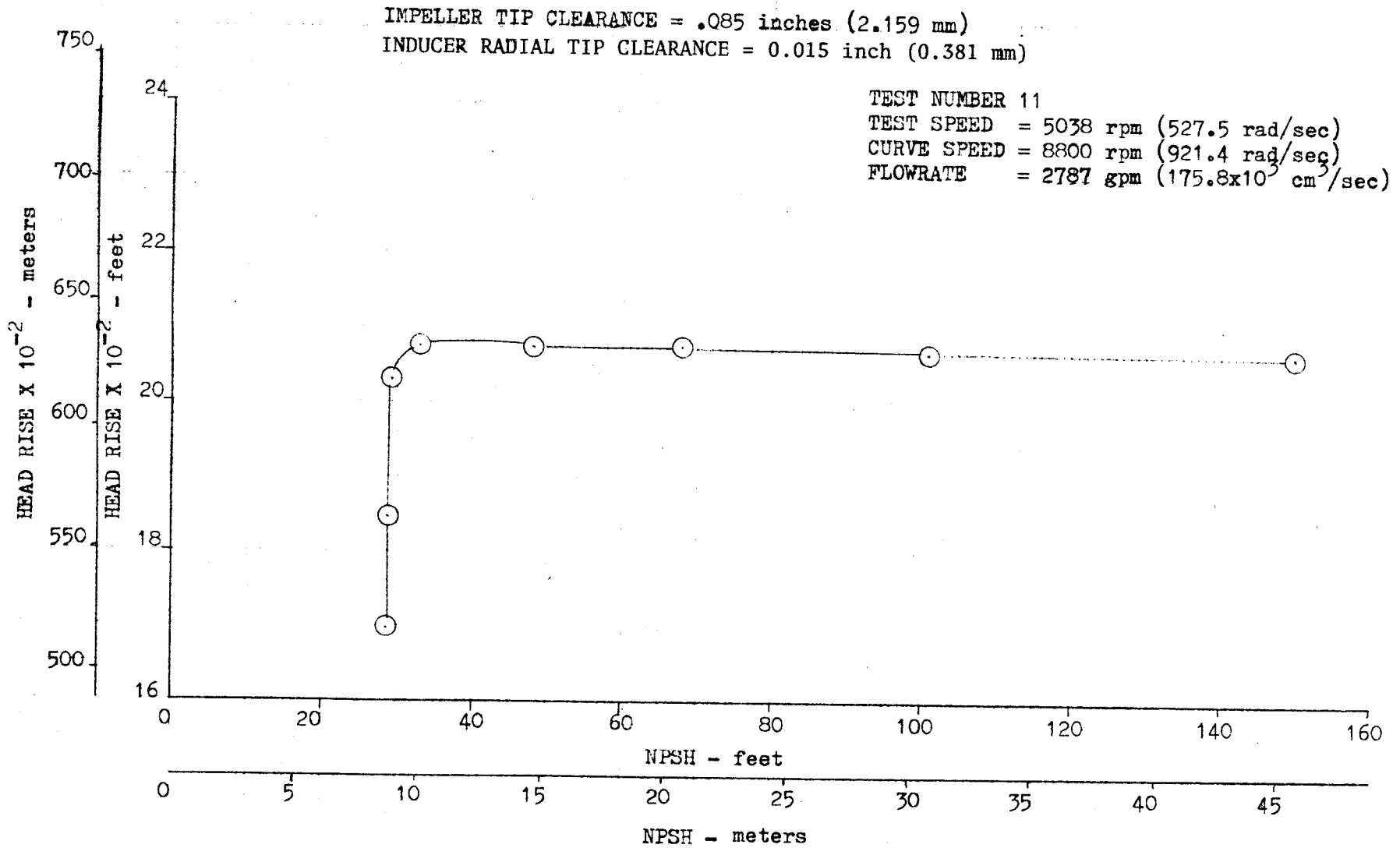


Figure 54. Modified J-2 Oxidizer Pump Suction Performance

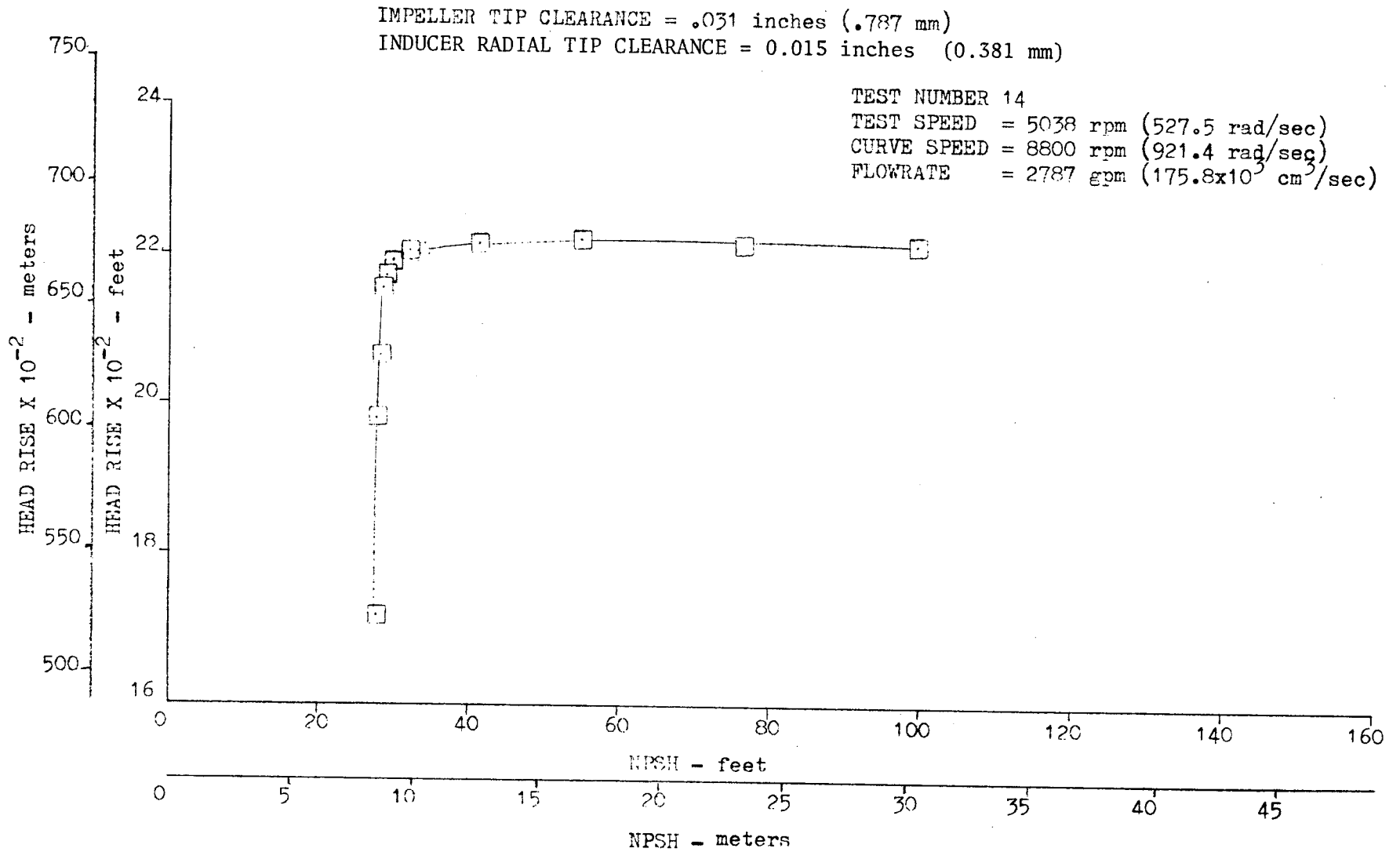


Figure 55. Modified J-2 Oxidizer Pump Suction Performance

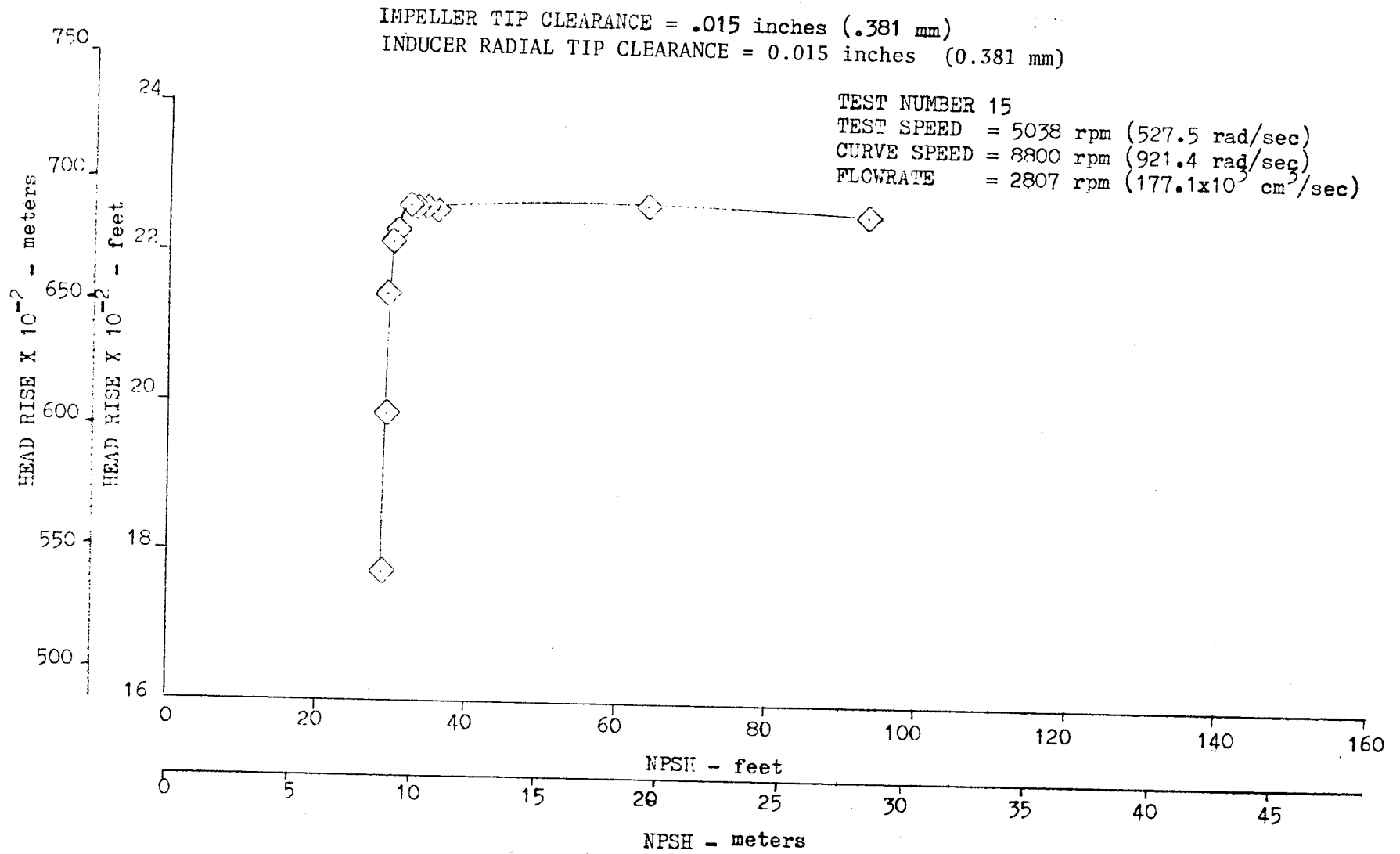


Figure 56. Modified J-2 Oxidizer Pump Suction Performance

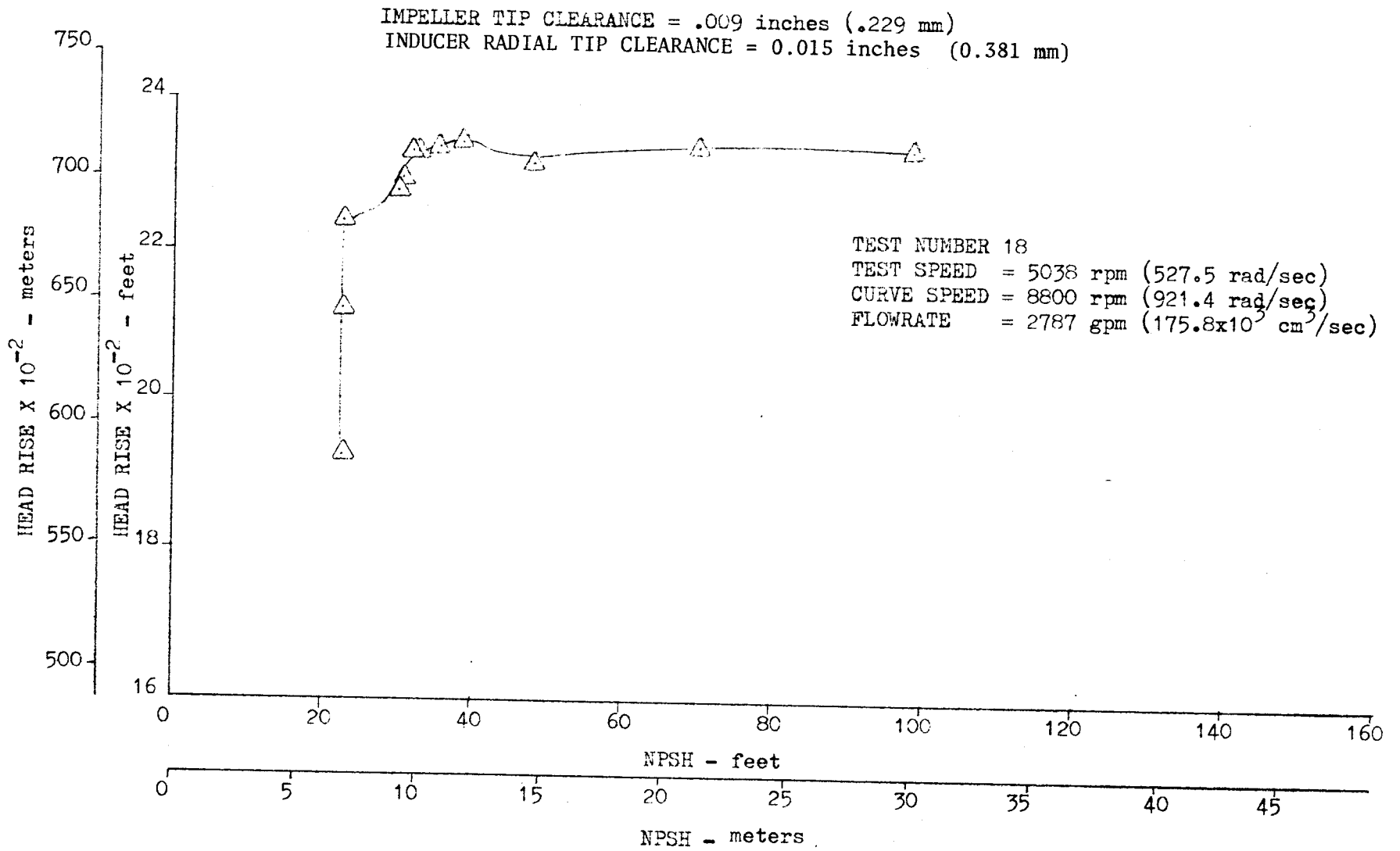


Figure 57. Modified J-2 Oxidizer Pump Suction Performance

The static wall tap data furnished pressures at the entrance to the impeller at the inducer exit. These pressures with inlet pressure indicate the inducer pressure rise, which can be plotted as a function of NPSH. Some inducers have a tendency to lose head gradually as NPSH is decreased. The reduction in head may not be seen in the pump discharge pressure, however, since the impeller head rise makes up for it. The impeller capability to make up for inducer head loss may be a function of tip clearance. The inducer pressure rise as a function of NPSH for the cavitation tests are presented in Fig. 58 through 61. These data indicate that the inducer head loss is nearly abrupt, and indicates that the impeller loses head due to cavitation whenever the inducer head supply is reduced. Impeller tip clearance has little effect on pump suction performance as indicated by the comparison of NPSH values at the head falloff points in Fig. 54 through 57 or Fig. 58 through 61. The exception to this is the lowest tip clearance which shows both a slight instability and lower critical NPSH.

Head-Flow Efficiency Results. The test data for the head-flow characteristics and the effects of tip clearance on them were made at two pump speeds. Pump head was determined from the pressure rise of the pump and the velocity head levels at pump inlet and discharge. Each head-flow test was made at four flow levels at a constant speed. Torque data were recorded from a torquemeter which supplied the pump brake horsepower level at each flow. The torque levels were reduced along with the head-flow levels to efficiency. The results of these tests are presented in Fig. 62 and 63 for pump test speeds of 3976 rpm (416.3 rad/s) and 5038 rpm (527.5 rad/s), respectively. The data of both test speeds was corrected to the J-2 production pump nominal operating speed of 8800 rpm (921.4 rad/s). The data indicate a general degradation in the head and efficiency as the impeller tip clearance is reduced. The torquemeter readings were bad during tests 3 and 8, which precluded the efficiency determination. Torque data on test No. 7 were bad except for one flowrate.

Correlation of Test Data

Blade-Loading Comparison to Model Prediction. A method for calculation of the relative fluid velocities on the blade surfaces of arbitrarily shaped blades in incompressible, nonviscous flow has been developed and is presented in Appendix B. The relative velocities are necessary to determine the static pressure distribution within an impeller passage. If the total pressure is taken as constant across an impeller passage, the relative velocities can be used to find the static pressure on the blade surfaces. Using Bernoulli's equation

$$H_{\text{total}} = H_s + \frac{W_s^2}{2g} = H_p + \frac{W_p^2}{2g}$$

where H_{total} denotes the total head, H_s and H_p denote static head on suction and pressure blade surfaces, and W_s and W_p denote fluid velocities relative to the blade suction and pressure surfaces. The resultant equation can then be given as

$$H_p - H_s = \frac{1}{2g} (W_s^2 - W_p^2)$$

INDUCER TIP RADIAL CLEARANCE = .015 inches (.381 mm)
OPEN IMPELLER TIP CLEARANCE = .085 inches (2.18 mm)

TEST NUMBER 11
TEST SPEED = 5038 rpm (527.5 rad/sec)
CURVE SPEED = 5038 rpm (527.5 rad/sec)
FLOW = 1592 gpm (100.4×10^3 cm³/sec)

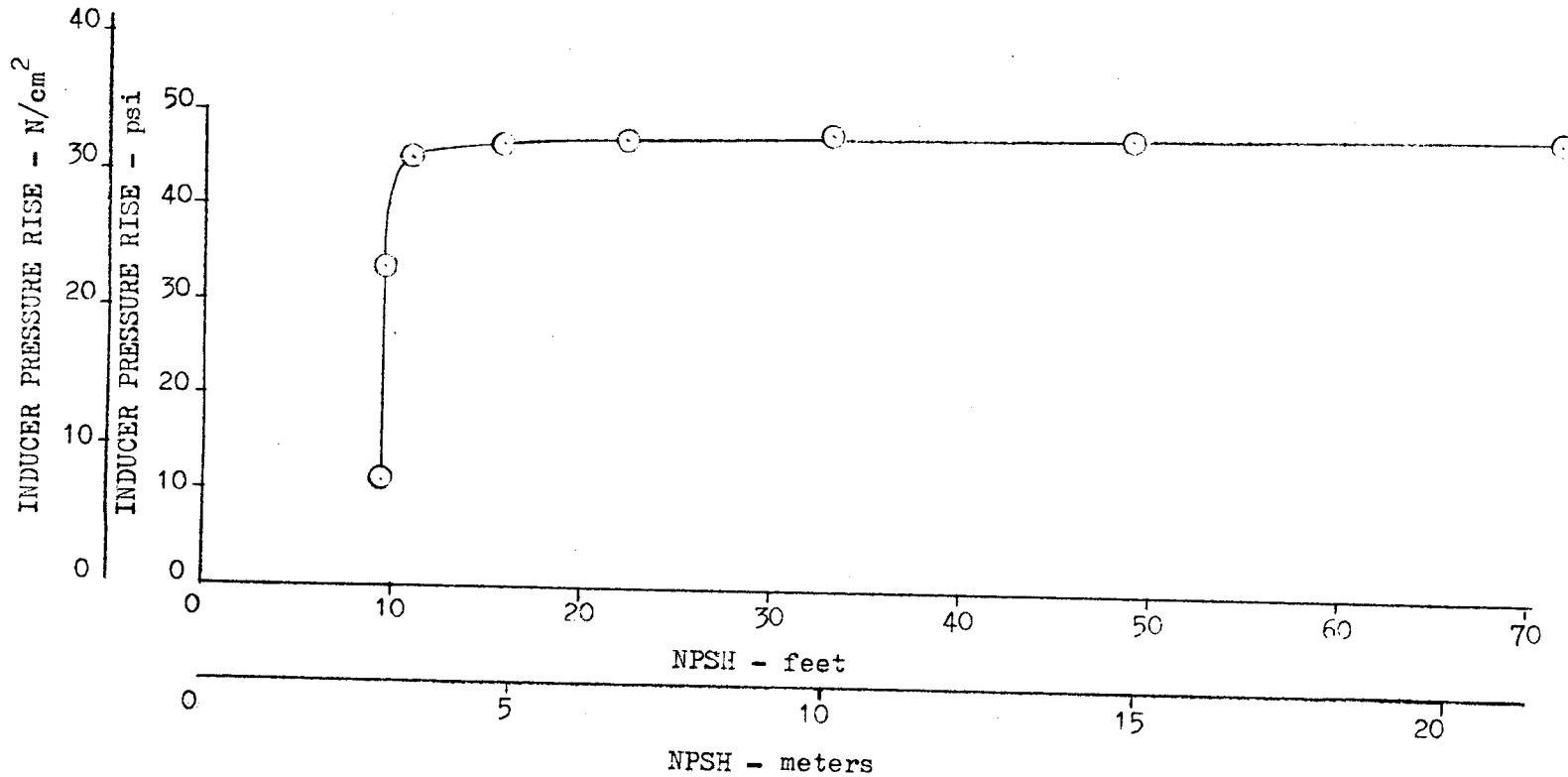


Figure 58. Modified J-2 Oxidizer Pump Suction Performance (Open-Faced Impeller)

INDUCER TIP RADIAL CLEARANCE = .015 inches (.381 mm)
 OPEN IMPELLER TIP CLEARANCE = .031 inches (.787 mm)

TEST NUMBER 14
 TEST SPEED = 5038 rpm (527.5 rad/sec)
 CURVE SPEED = 5038 rpm (527.5 rad/sec)
 FLOW = 1592 gpm ($100.4 \times 10^3 \text{ cm}^3/\text{sec}$)

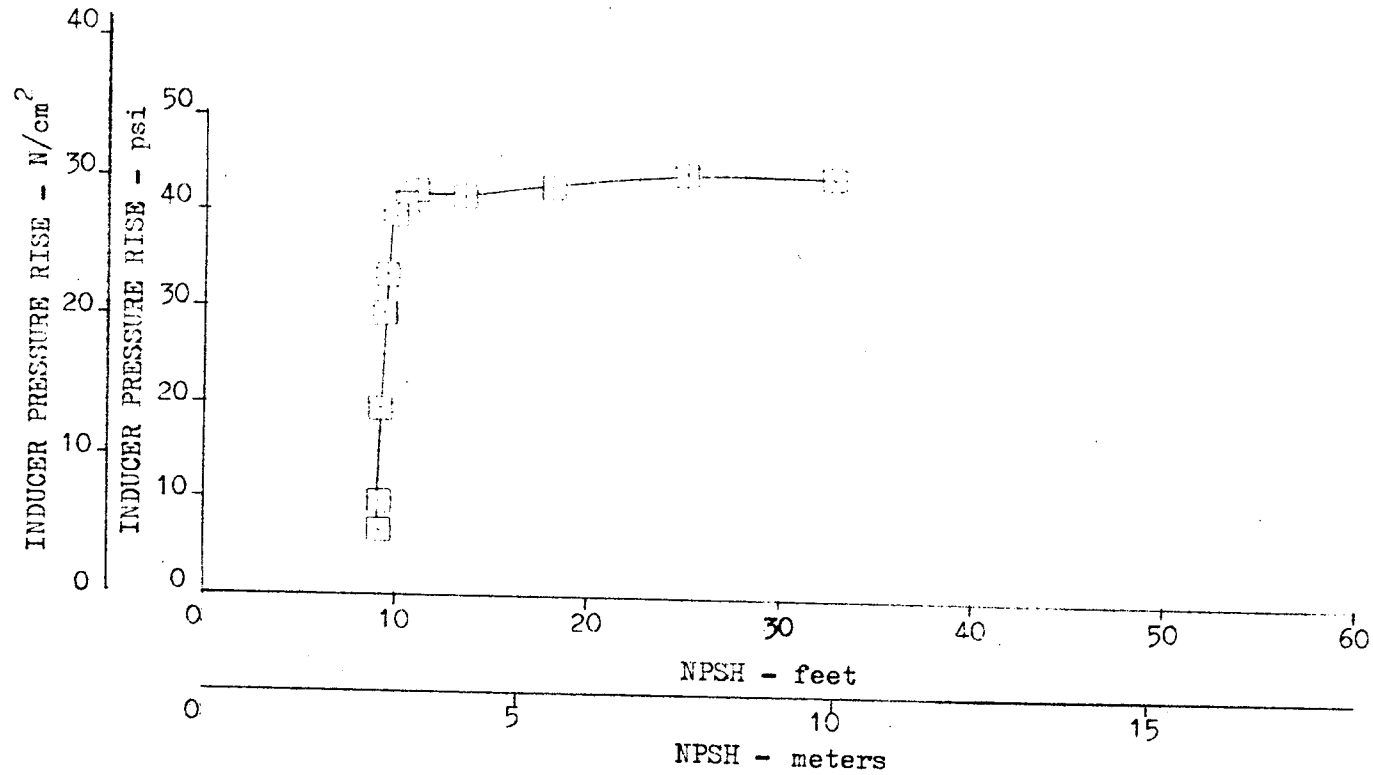


Figure 59. Modified J-2 Oxidizer Pump Suction Performance (Open-Faced Impeller)

INDUCER TIP RADIAL CLEARANCE = .015 inches (.381 mm)
OPEN IMPELLER TIP CLEARANCE = .015 inches (.381 mm)

TEST NUMBER 15
TEST SPEED = 5038 rpm (527.5 rad/sec)
CURVE SPEED = 5038 rpm (527.5 rad/sec)
FLOW = 1607 gpm (101.4×10^3 cm³/sec)

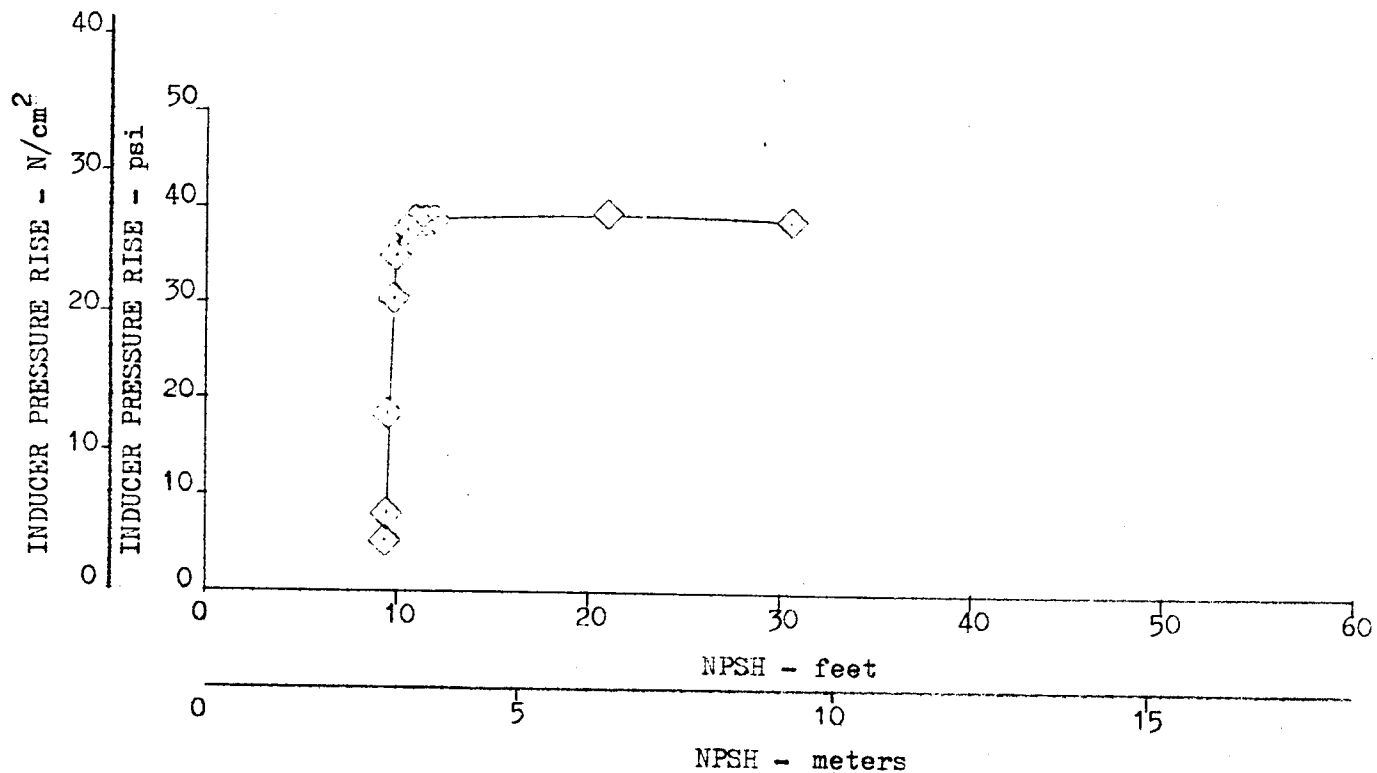


Figure 60. Modified J-2 Oxidizer Pump Suction Performance (Open-Faced Impeller)

TEST NUMBER 18
 TEST SPEED = 5038 rpm (527.5 rad/sec)
 CURVE SPEED = 5038 rpm (527.5 rad/sec)
 FLOW = 1592 gpm (100.4x10³ cm³/sec)

INDUCER TIP RADIAL CLEARANCE = .015 inches (.381 mm)
 OPEN IMPELLER TIP CLEARANCE = .009 inches (.229 mm)

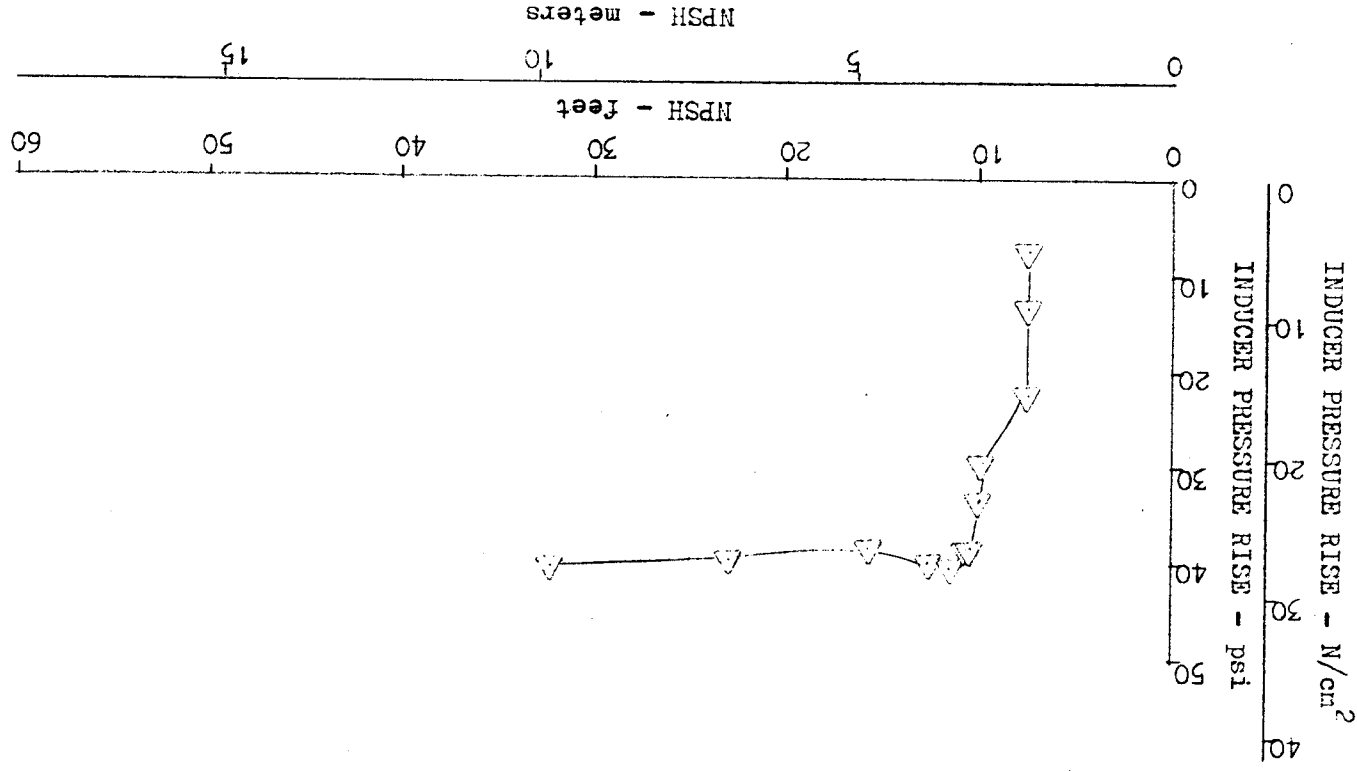


Figure 61. Modified J-2 Oxidizer Pump Suction Performance (Open-Faced Impeller)

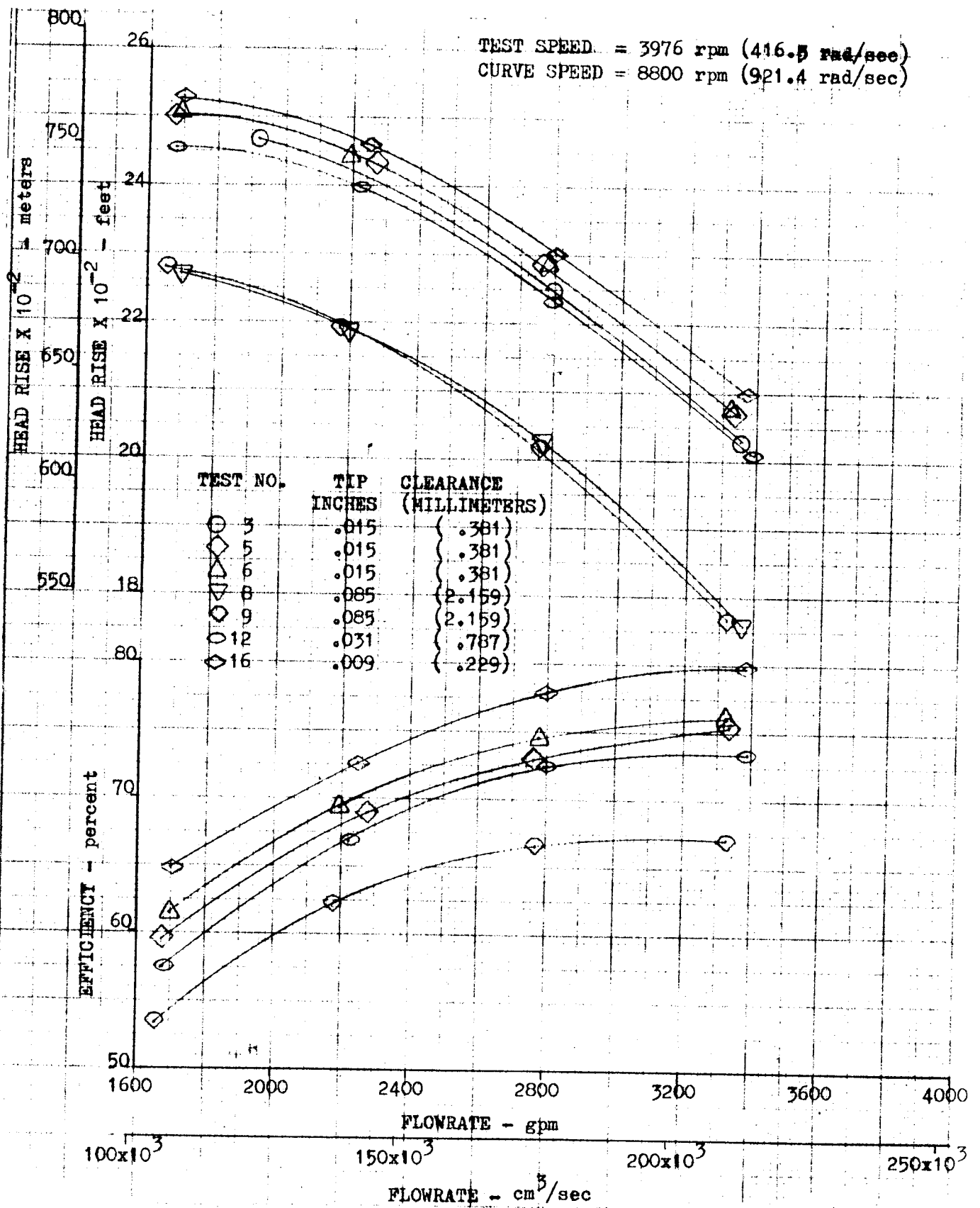


Figure 62. Modified J-2 Oxidizer Pump Tip Clearance Effect on Performance

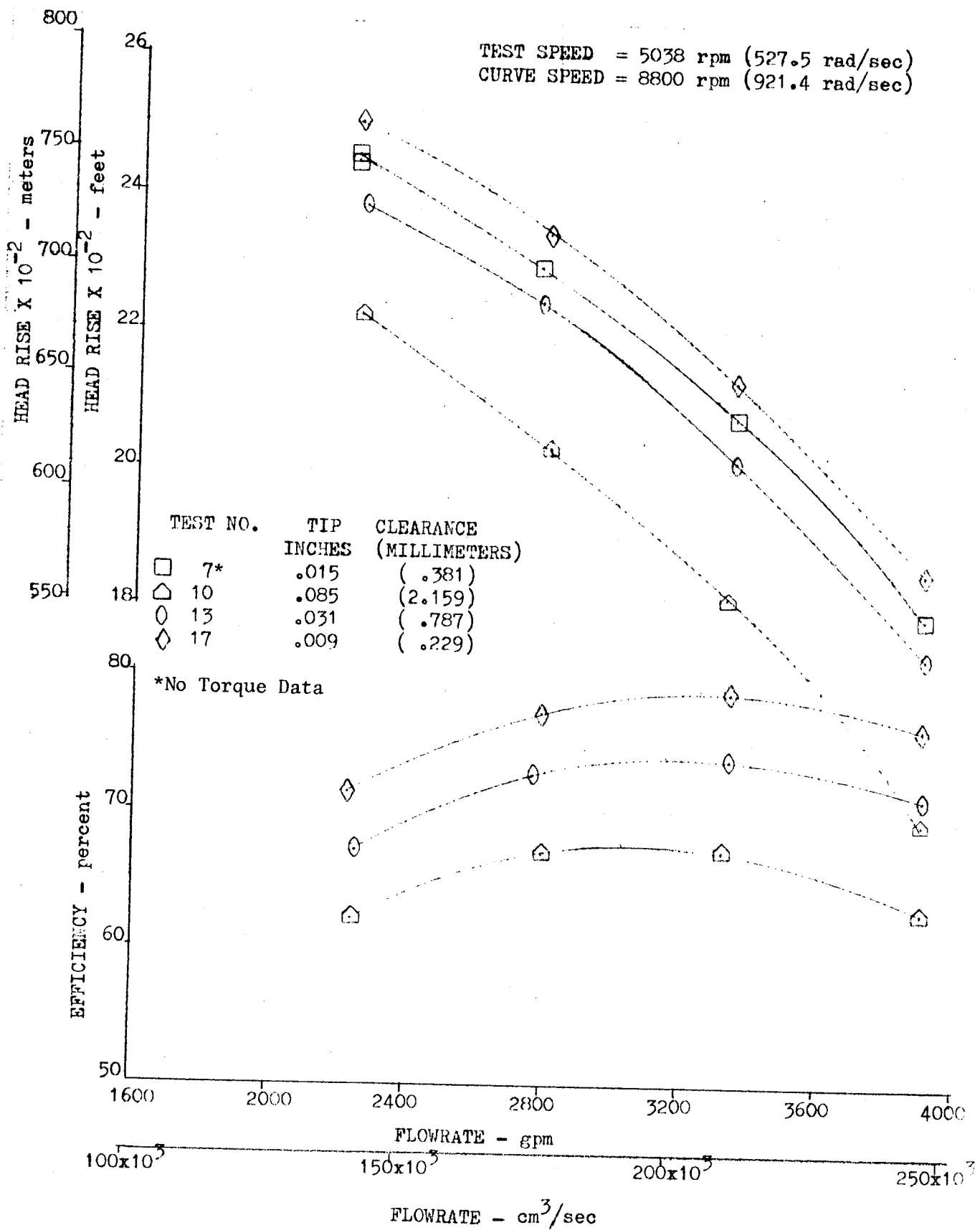


Figure 63. Modified J-2 Oxidizer Pump Tip Clearance Effect on Performance

The program input presented in Appendix B requires a detailed geometry of the impeller. The input data include front and rear shroud definition, assumption of the streamtubes within the impeller, blade angle definition along all streamlines, and blade thickness distribution and fluid angles within the impeller. The data are input at the points of intersection of the streamlines and the lines normal to the flow.

Several impellers of which a detailed geometry could be found were used, and the blade loading was determined at the nominal operating conditions. The resultant values will be presented in a later section. The blade loading for the J-2 oxidizer impeller was calculated and compared with the data from the scanivalve tests. This comparison is presented in Fig. 64. The results indicate that the calculated blade loading is higher than the measured values. The calculated values are based on a closed model or one without any flow across the blade tips. Comparison of the impeller test head with the calculated head based on the integrated blade loading also indicates the impeller head to be larger than that found in the test model. J-2 test data indicated an impeller head of 2250 feet (686 m) at 8800 rpm (921.4 rad/s) and nominal flow. The calculated pressure rise due to blade loading is found to be 3019 feet (920 m). It is interesting to note that the ratio of calculated head to test head multiplied by the test blade loading brings the blade differential pressures into much closer agreement. This indicates that the slip factors used in the program could be varied to improve the blade-loading calculation. Other losses which may be more significant than slip might also be considered.

Only five pairs of pressure taps were used along each streamline. This results in making it difficult to define exactly the blade-loading curve shape. The data of Fig. 64 indicate, however, that the maximum blade loading occurs closer to the pump inlet than calculated. The calculated blade-loading varies as the partial derivative of the blade angle β_B with respect to the meridional length m along a streamline ($\partial\beta_B/\partial m$). The hydrodynamic layouts were used to develop the blade angle distribution for the calculation, and this could have some degree of effect on the difference between this and the test piece. Also, it must be remembered that the added flow moving through an impeller due to tip clearance leakage could cause a shift in the blade loading. A flow model which considers the viscous effects of flow would be expected to provide better correlation.

Additional data would be very useful in the improvement of the blade-loading/relative velocity calculation program. The data presented are the first of their kind available, since good data must contain the detailed description of the test piece as well as the measured blade-loading results for comparison to that calculated by the model. This area of effort is very important to the designer in turbomachines of high-performance levels, since blade-loading requirements are necessary to properly design the part to withstand the stress levels in that range of operation.

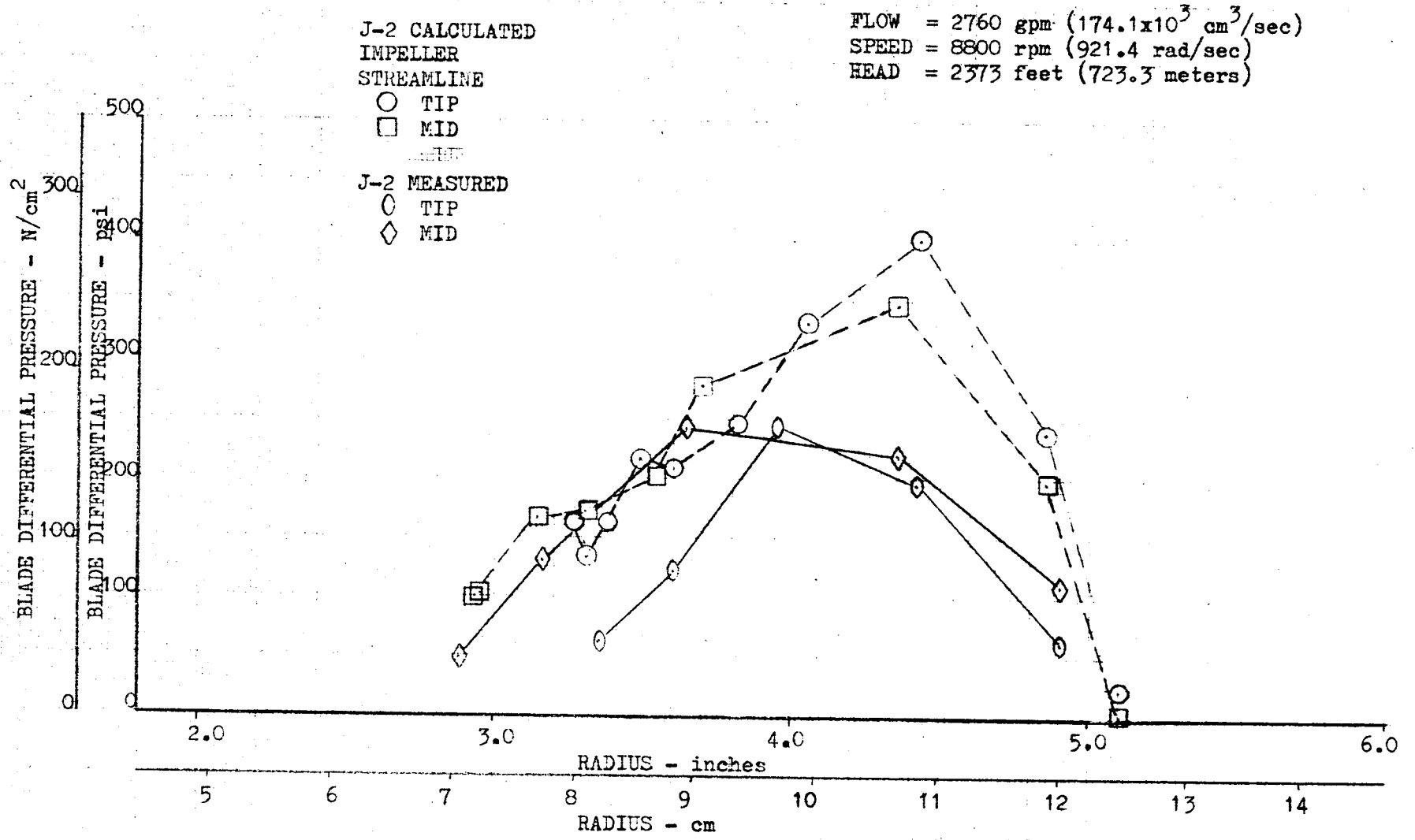


Figure 64. J-2 Oxidizer Impeller Comparison of Calculated Blade Loading Distribution to Measured

Tip Clearance Effects on Cavitation. A series of cavitation tests were made at four impeller tip clearances to determine the effects of tip clearance on pump suction performance. A summary of the tests is presented in Fig. 65. The data indicate that the suction performance is not affected up to 2-percent head fall-off within the range of tip clearances tested ($0.0113 < \lambda/b_t < 0.107$). A typical J-2 production pump is presented also to indicate suction performance is very similar. A critical NPSH curve for NPSH at 2-percent pump head falloff is presented in Fig. 66 for the nominal J-2 oxidizer pump. The nominal performance was established by averaging 10 pumps. The cavitation results of the test impeller indicate that at all clearances the critical NPSH was within 1 foot of each other, and indicates slightly better performance than the nominal J-2 oxidizer pump. The data fell well within the 2σ (standard deviation) band of the J-2 oxidizer pumps, however, and must be considered as equal.

Comparisons of cavitation curves of pump head and inducer pressure rise for this pump indicate no effect due to impeller tip clearance. Other inducer impeller combinations, however, may show that, with a decrease in inducer head rise, the pump head rise remains constant over a decreasing range of NPSH until the impeller suction performance capability is exceeded and pump head is lost. Although this impeller did not show suction performance change with tip clearance, it cannot be stated emphatically that this is always the case. Cavitation tests on impellers without inducers could be tested to determine the resultant effect of tip clearance on suction performance and the influence on incidence angle change due to tip clearance leakage back to the inlet.

Tip Clearance Effects on Pump Head Flow, and Efficiency. The pump performance with the modified J-2 oxidizer impeller was reduced considerably by increasing the impeller tip clearance. The test results of Fig. 67 and 68 indicate a continual reduction in head and efficiency as tip clearances were varied from 0.009 inch (0.229 mm) to 0.085 inch (2.16 mm). The data also indicate that performance of the shrouded J-2 oxidizer pump was comparable or slightly better than that of the modified J-2 shroudless impeller operating at the minimum tip clearance.

The head-flow-efficiency curves of Fig. 67 and 68 were used to develop comparisons of the pump headrise and efficiency at a given flow as a function of impeller tip clearance at the two test speeds. These comparisons are presented in Fig. 69 through 72. These data indicate that impeller head and efficiency improve with tip clearance reduction to the minimum tip clearance tested. The data indicate that the head change is nearly linear with the tip clearance over the interval tested. The efficiency data indicate a nearly linear effect from the clearance levels of approximately 0.015 inch (0.381 mm) to 0.085 inch (2.16 mm).

The efficiency gain with tip clearance below approximately 0.015 (0.381 mm) is greater than a linear progression. This may be due to the boundary layer scraping effect where the boundary layer thickness δ is greater than the tip clearance λ , as discussed in the Performance Analysis section. Studies have indicated that when tip clearance is much larger than the boundary layer thickness, the viscous effects seem to be negligible (Ref. 6).

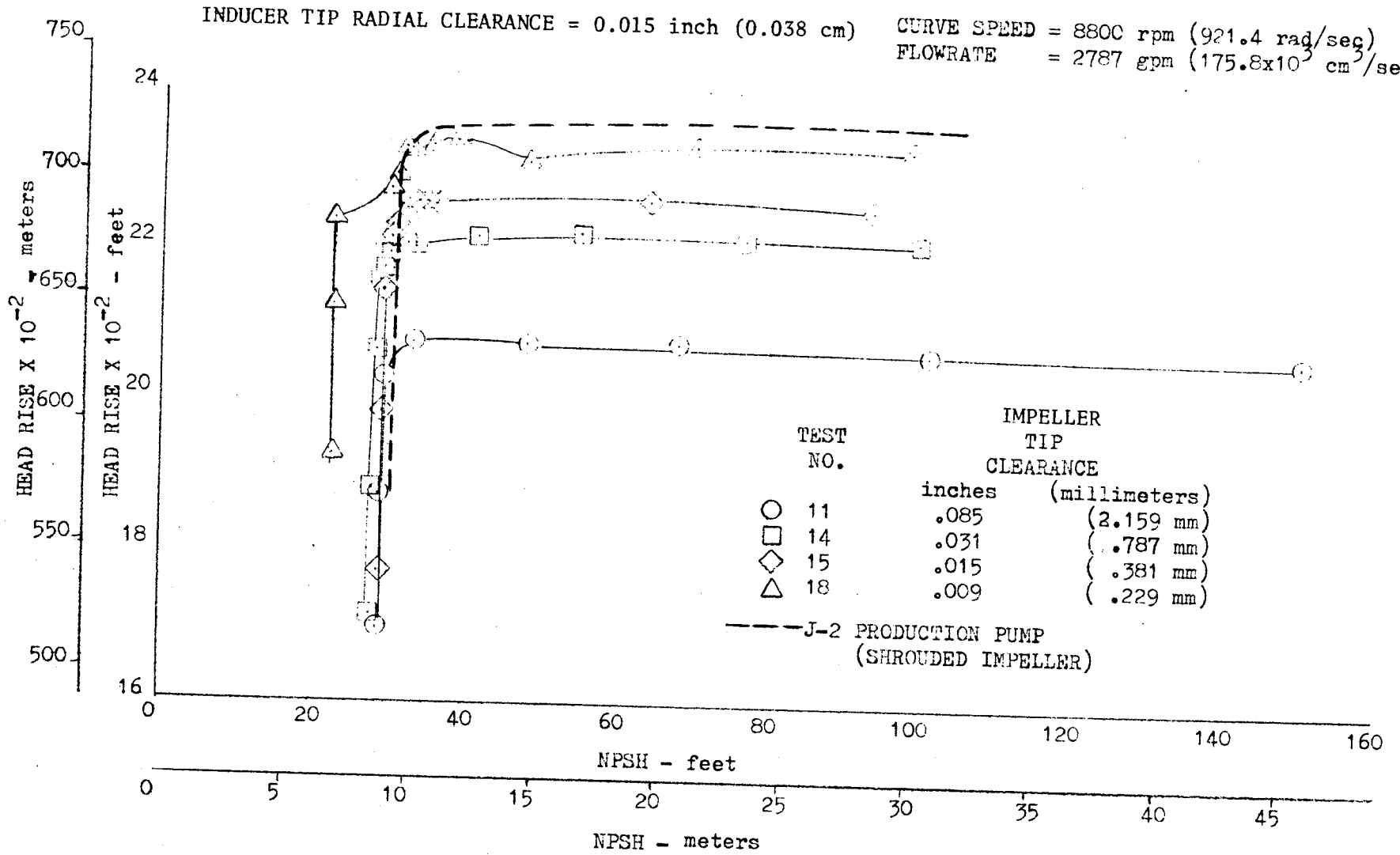


Figure 65. Modified J-2 Oxidizer Pump Suction Performance for Shrouded and Open-Faced Impellers

CURVE SPEED = 8800 rpm (921.4 rad/sec)
 FLOWRATE = 2787 gpm (175.8x10³ cm³/sec)

TEST NO.	TIP CLEARANCE	
	inches	(millimeters)
○ 11	.085	(2.159 mm)
□ 14	.031	(.787 mm)
◇ 15	.015	(.381 mm)
△ 18	.009	(.229 mm)

— NOMINAL J-2 PRODUCTION PUMP (SHROUDED IMPELLER)

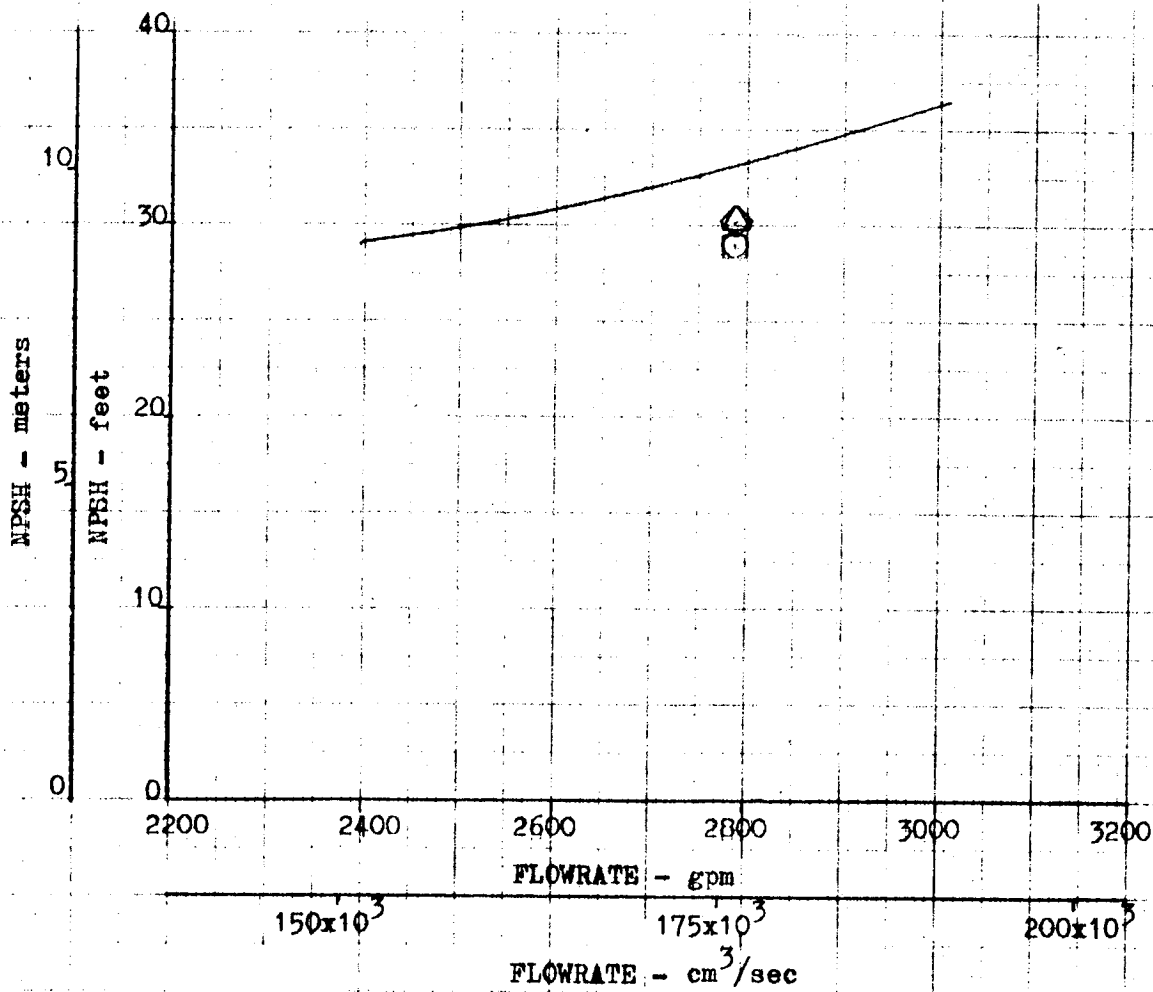


Figure 66. Modified J-2 Oxidizer Pump Suction Performance for Shrouded and Open-Faced Impellers Operating With Same Inducer

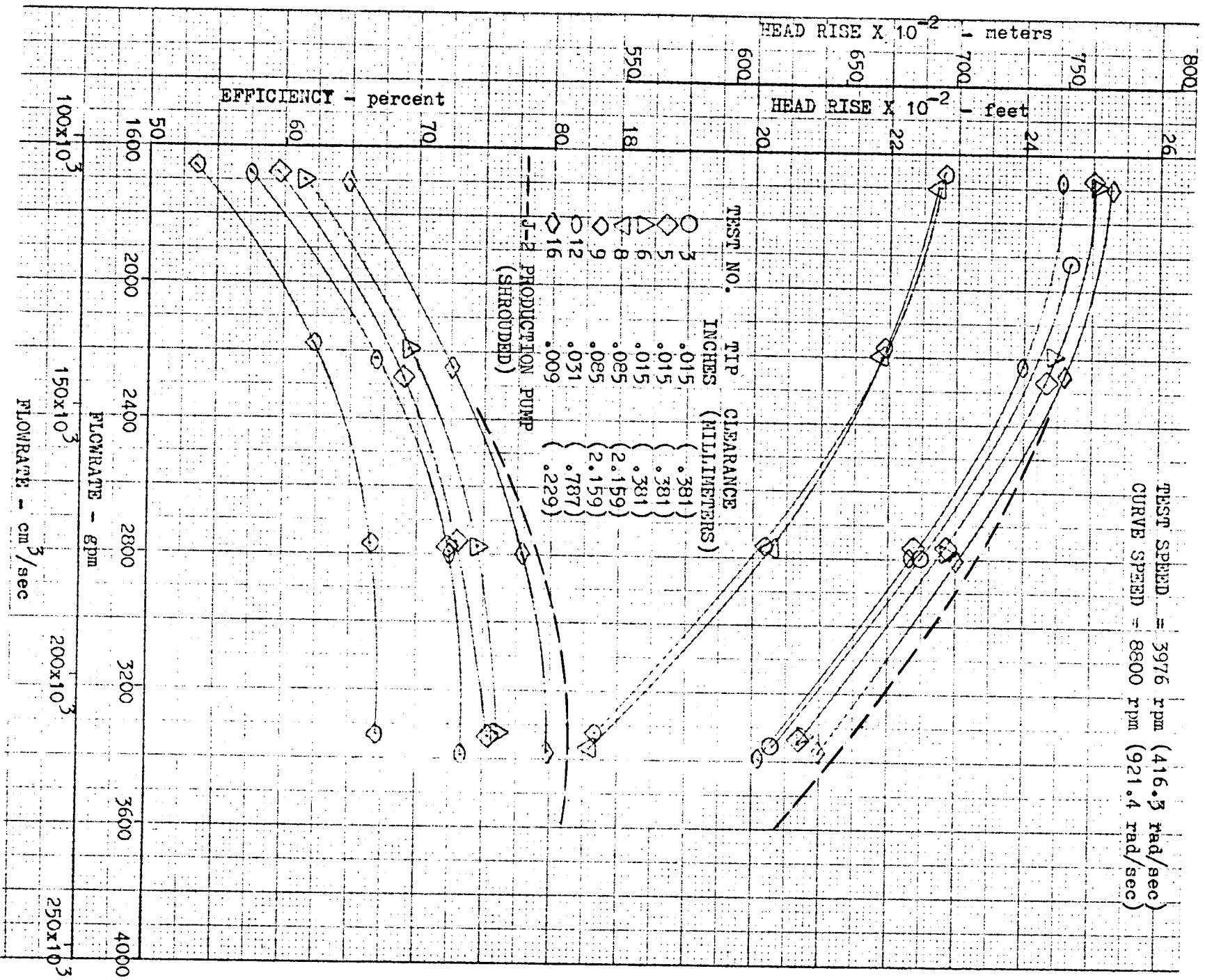


Figure 67. Modified J-2 Oxidizer Pump Tip Clearance Effect on Performance

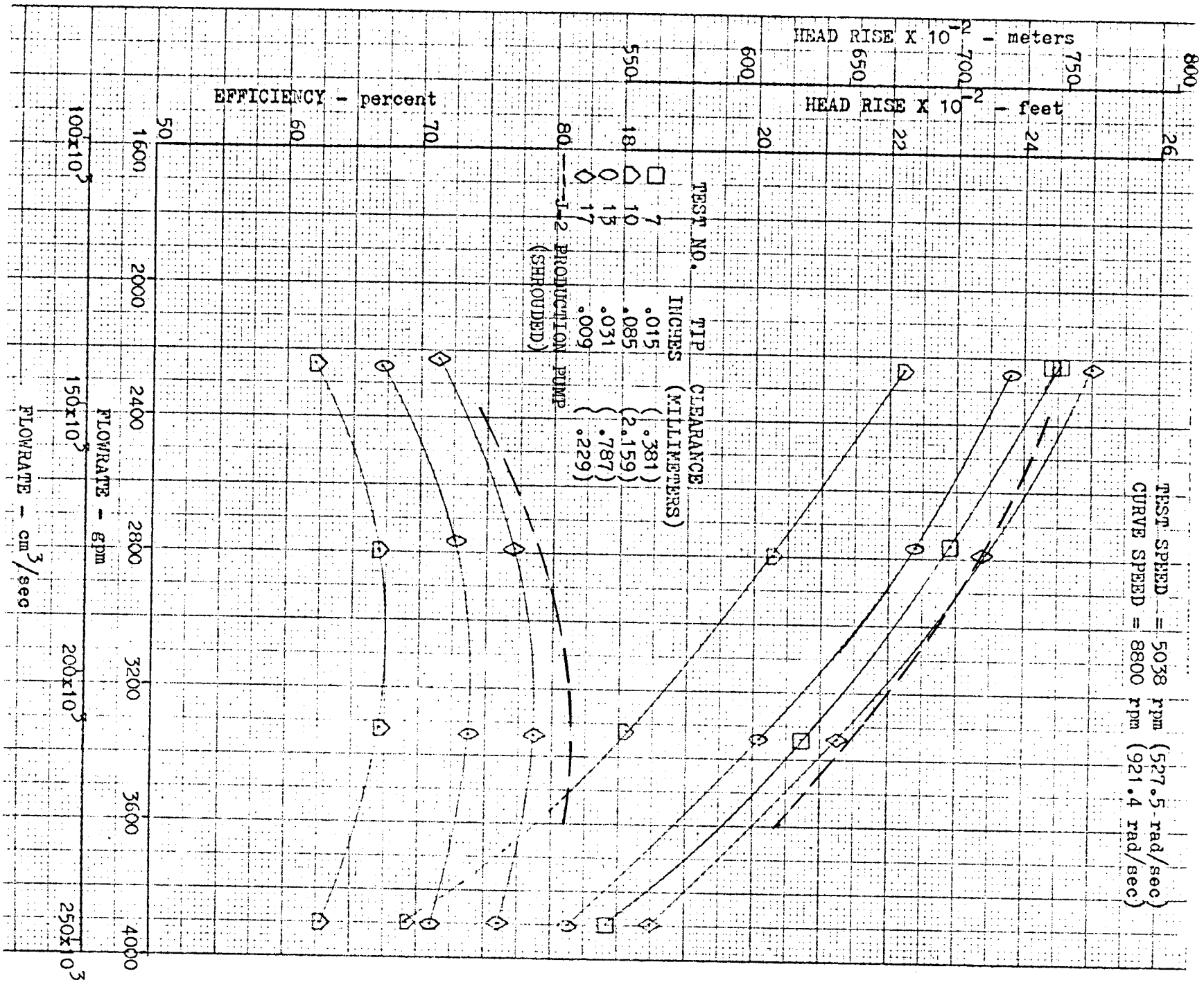


Figure 68. Modified J-2 Oxidizer Pump Tip Clearance Effect on Performance

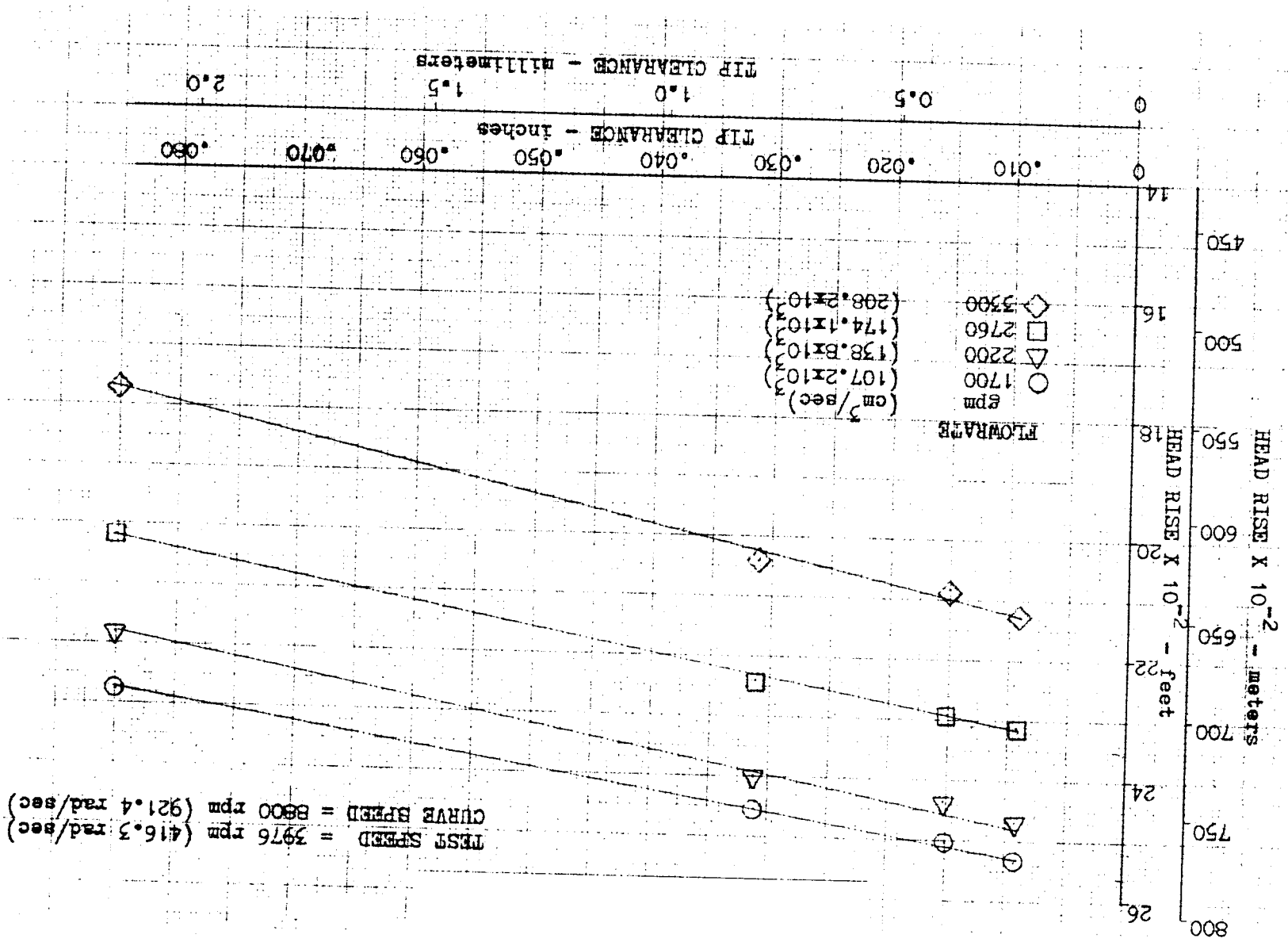


Figure 69. Modified J-2 Oxidizer Pump Tip Clearance Effect on Head Rise

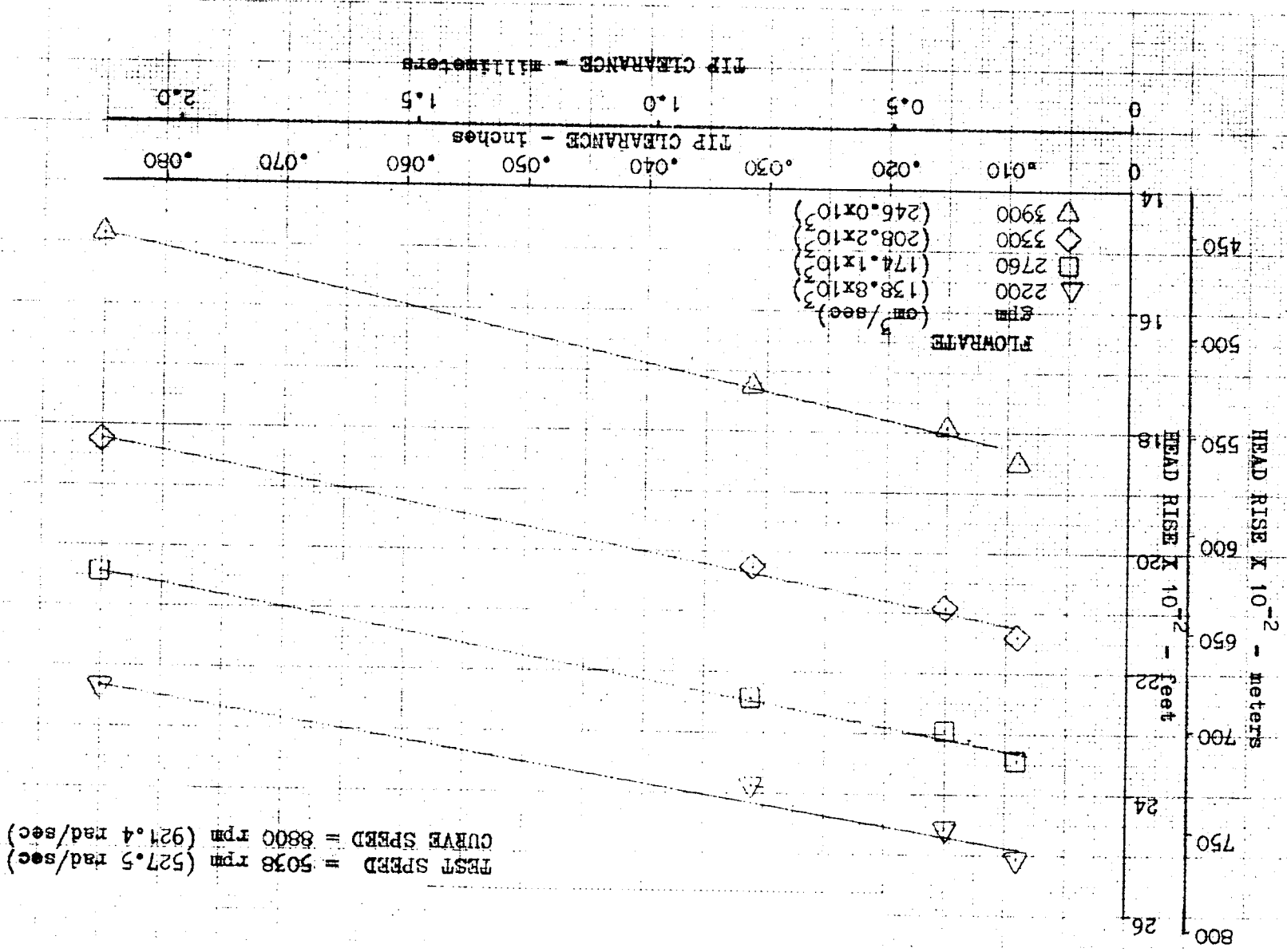


Figure 70. Modified J-2 Oxidizer Pump Tip Clearance Effect on Head Rise

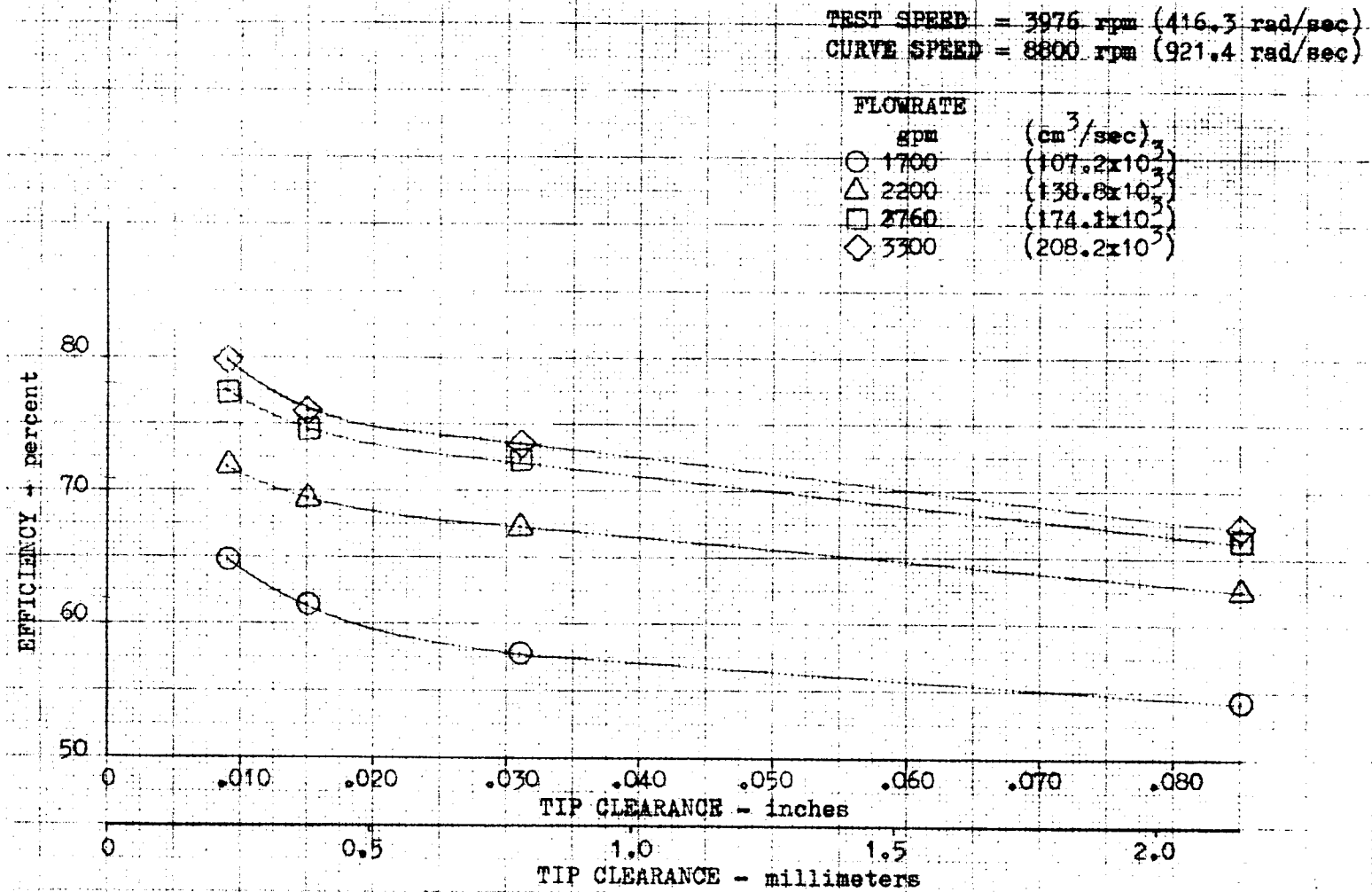


Figure 71. Modified J-2 Oxidizer Pump Tip Clearance Effect on Pump Efficiency

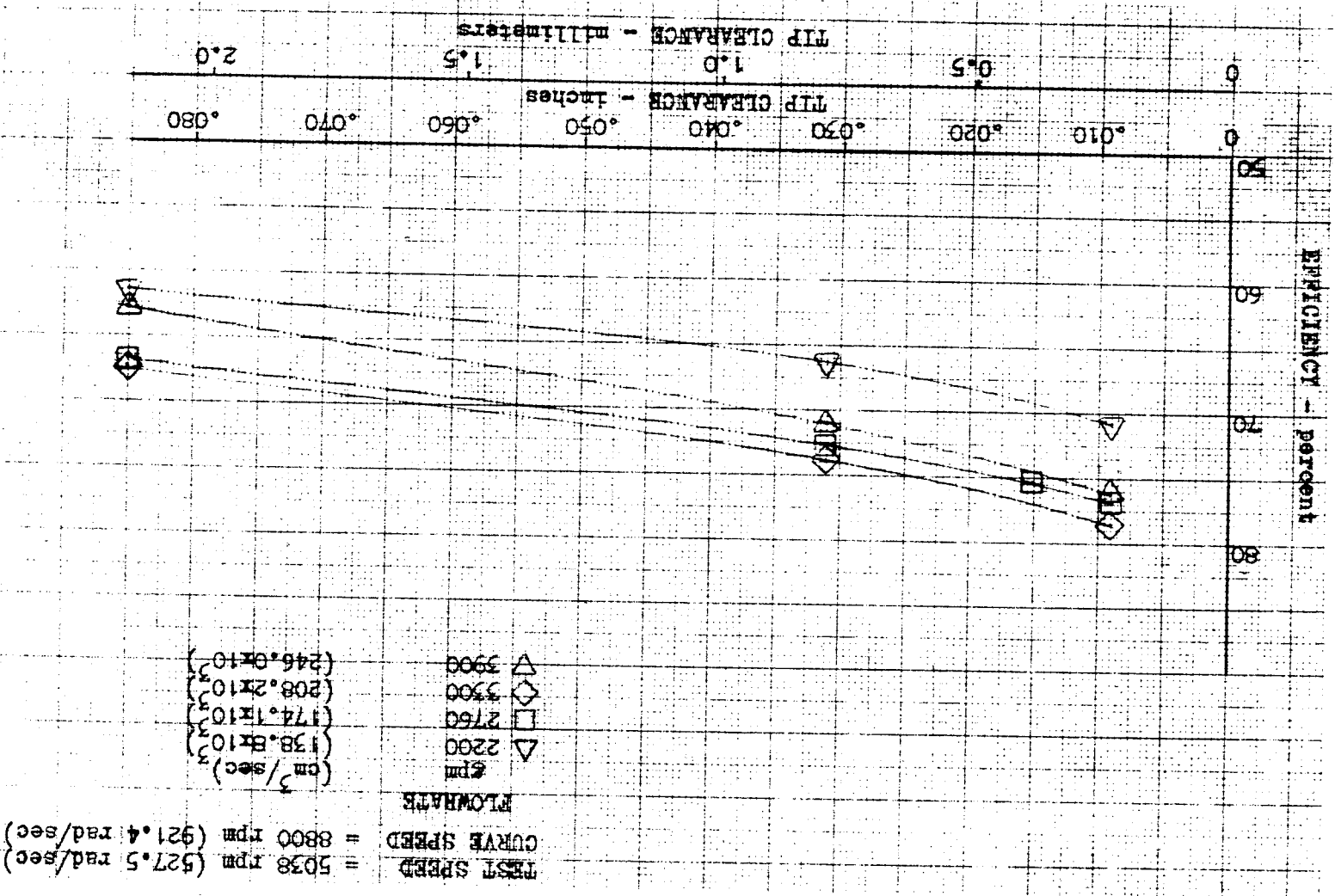


Figure 72. Modified J-2 Oxidizer Pump Tip Clearance Effect on Pump Efficiency

A summary curve was developed for the modified J-2 oxidizer pump, presenting for each flowrate the head coefficient ratio, the torque ratio, and the efficiency ratio, all referenced to an extrapolated zero-clearance reference as a function of the ratio of tip clearance to impeller discharge tip width (Fig. 73 and 74). As before, straightline variations exist in the head ratio throughout the range of clearances tested. This characteristic is the same for the efficiency except for the smallest clearance tested. It is now of interest to note that, at nominal flow, the torque did not change and the corresponding loss in head is proportional to the loss in efficiency. At lower flowrates, the torque was greater than at the zero reference clearance while, at the highest flows, the torque was much less than the reference torque. An explanation of this can be found in the pump performance characteristics curve and will be presented in the next section.

Correlation of Test Data With the Formulated Models

Development of Available Data. The literature search indicated there were very little detailed data available from which impeller performance versus tip clearance correlations could be developed. Several articles in the literature had performance characteristics of pumps operating at several tip clearances (Ref. 3, 8, and 9). These, however, did not give enough detail of the hardware tested to be able to make a close study of the type required here. The final selection was reduced to three specific pumps. Those were the S-4 oxidizer pump previously studied within Rocketdyne, the pump designated RI-15 presented in papers by Wood, Welna, and Lamers (Ref. 7 and 10), and the J-2 oxidizer test pump. Each pump tested has enough data to make a detailed study by developing blade-loading calculations and having head-flow efficiency data presented at one or more tip clearances. Blade-loading curves at the design flow were developed based on the impeller geometry specified. The S-4 impeller performance is presented in Fig. 75. The pump was tested at zero running clearance or at a slight rubbing condition, and at a clearance of 0.025 inch (0.635 mm). The shrouded impeller data are also presented and indicate a greater head rise but lower efficiency, which could be due to added disk friction and front seal leakage effects with shrouded impellers. The meridional view of the S-4 oxidizer impeller (Fig. 76) was taken from hydrodynamic blade and impeller layouts, which also gave the blade angle distribution as shown in Fig. 77. These data allowed the calculation of the tip blade-loading profile, which is presented as a function of radius and meridional length in Fig. 78.

The performance curves of the RI-15 model impeller of Wood, Welna, and Lamers (Ref. 7) gave test data at clearances of 0.008 inch (0.203 mm) and at 0.028 inch (0.711 mm). The shrouded impeller performance also is presented in Fig. 79. The references listed above also provided a definition of the impeller geometry (Fig. 80). Impeller inlet and discharge blade angles were given, and a blade angle distribution was assumed (Fig. 81) in order to calculate the tip streamline blade loading. The results are presented in Fig. 82, and indicate a smooth increase in blade loading which may be due to the assumed smooth blade angle distribution used in the calculation.

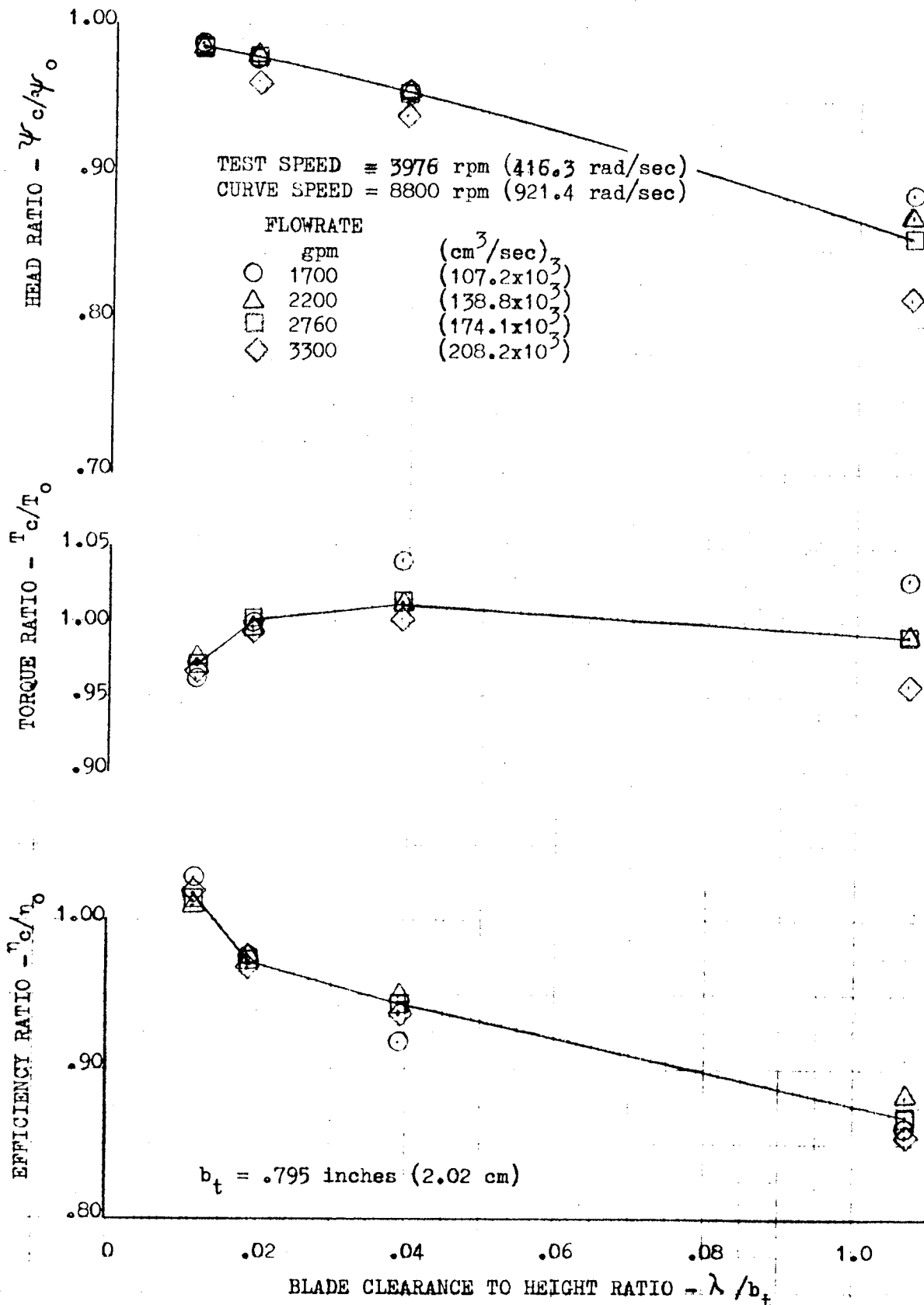


Figure 73. Modified J-2 Oxidizer Pump Tip Clearance Effects on Pump Performance (Summary)

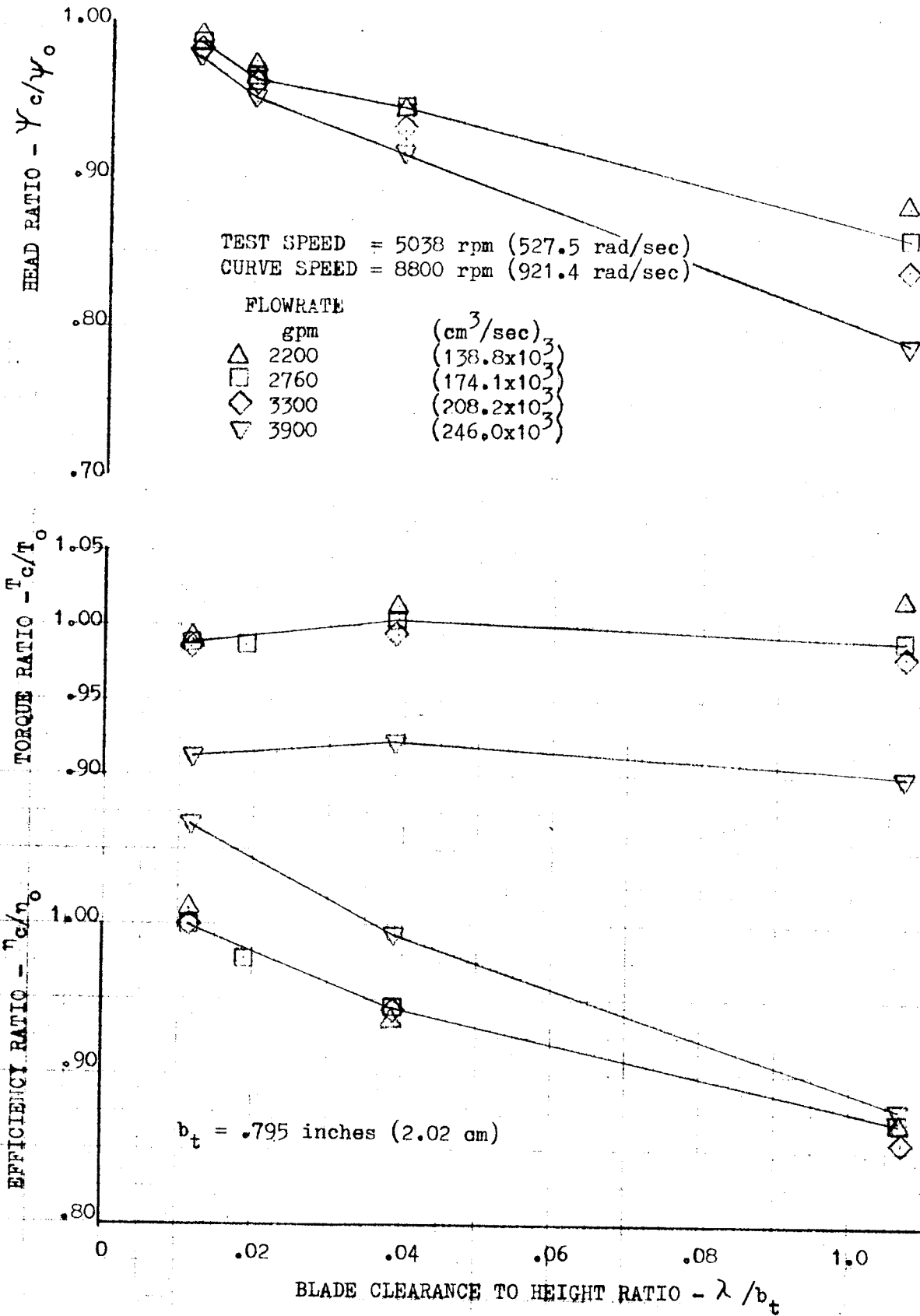


Figure 74. Modified J-2 Oxidizer Pump Tip Clearance Effects on Pump Performance (Summary)

SPEED = 10017 rpm (1049 rad/sec)
 -----SHROUDED IMPELLER
 _____FRONT SHROUD REMOVED

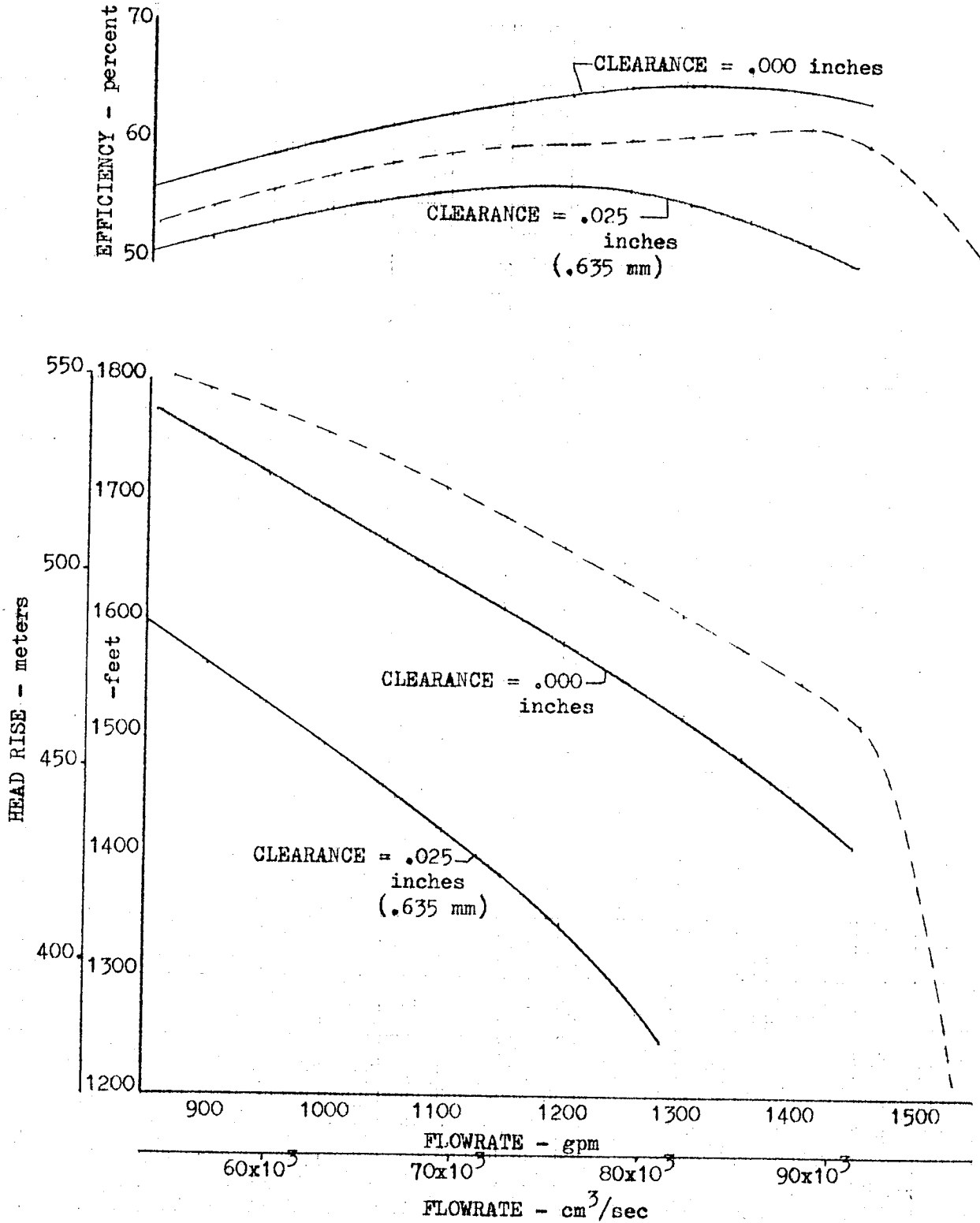


Figure 75. S-4 Oxidizer Pump Performance Comparison Shrouded and Open-Faced Impellers

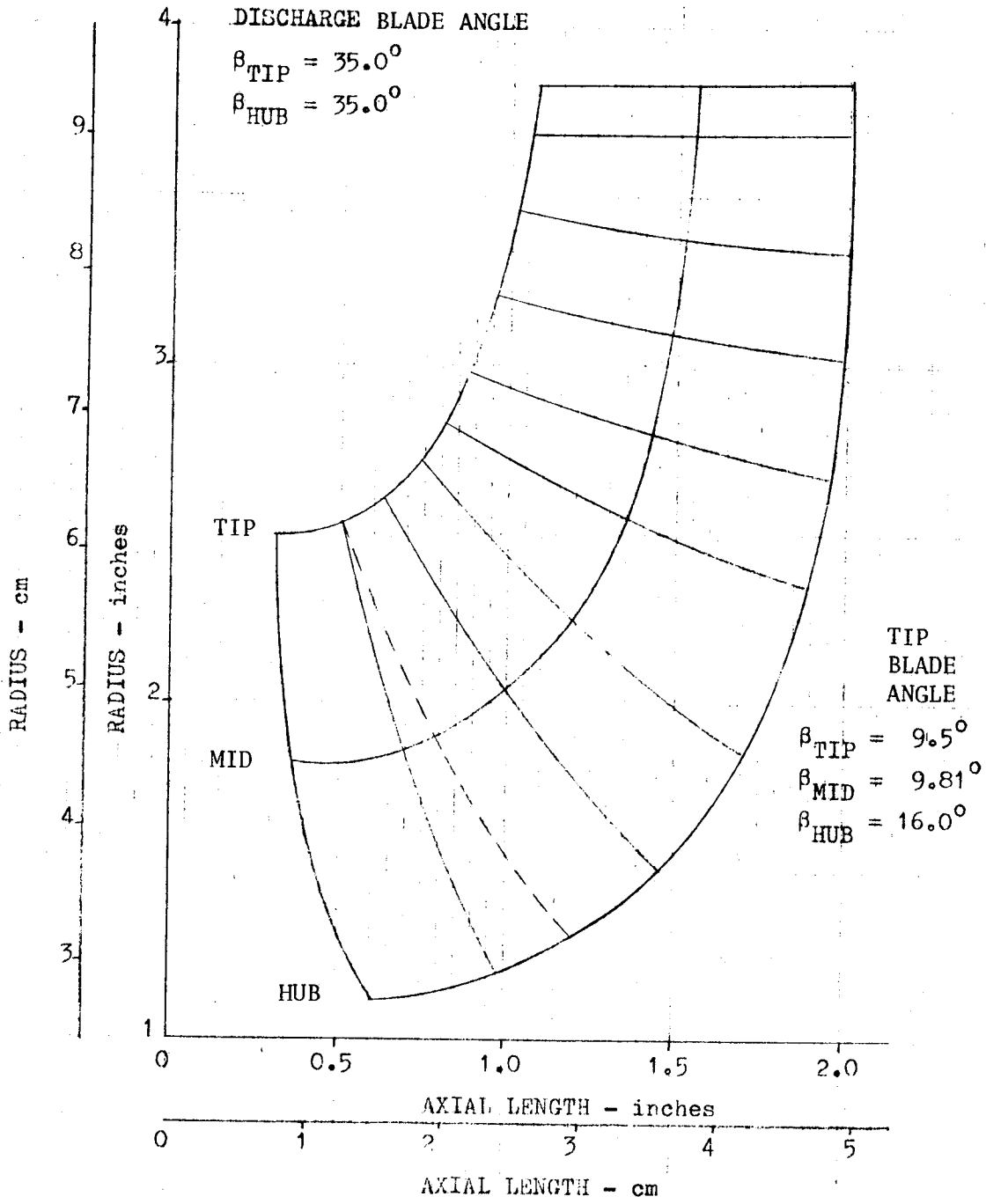


Figure 76. S-4 Oxidizer Impeller Meridional View for Calculation of Blade Loading

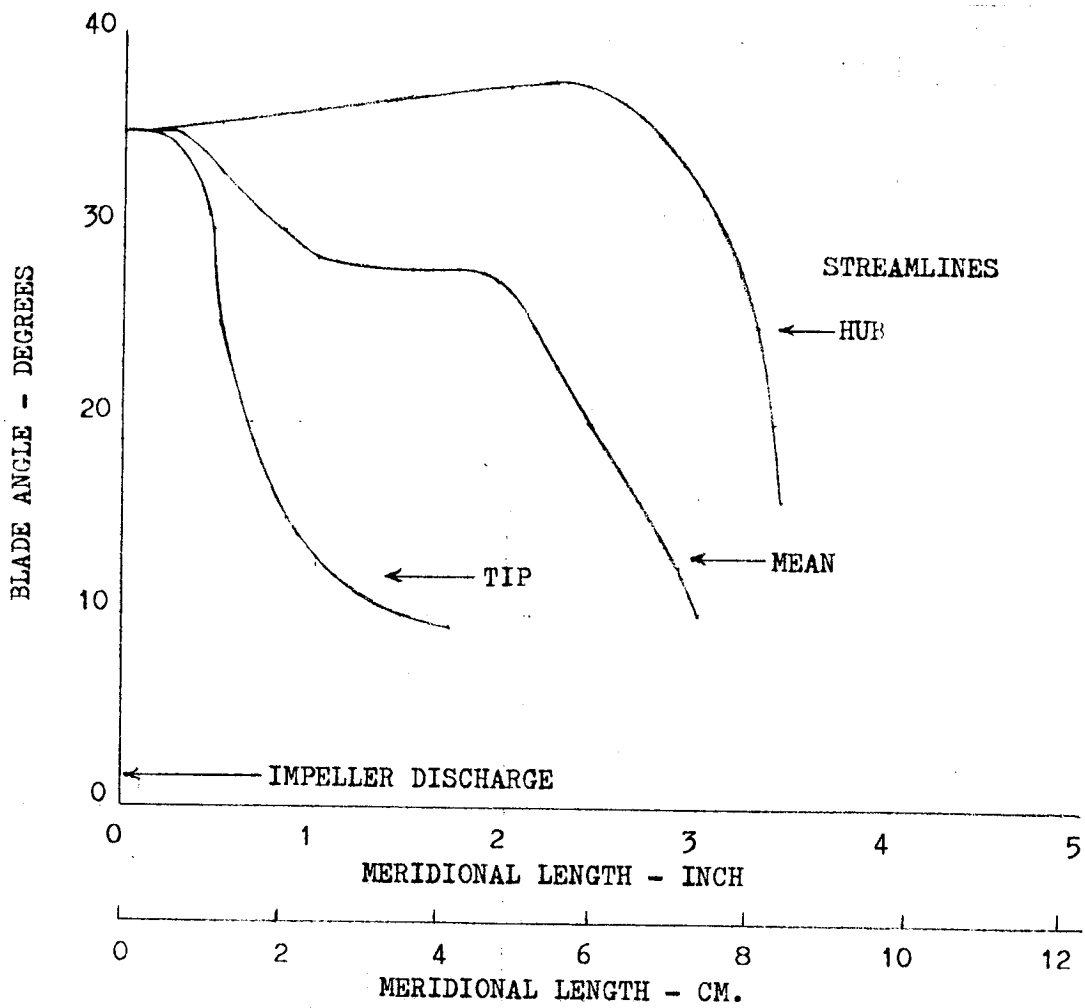


Figure 77. S-4 Oxidizer Impeller Blade Angle Distribution

FLOW = 1200 gpm ($75.7 \times 10^3 \text{ cm}^3/\text{sec}$)
 SPEED = 10017 rpm (1048.8 rad/sec)
 HEAD = 1583 feet (482.5 meters)

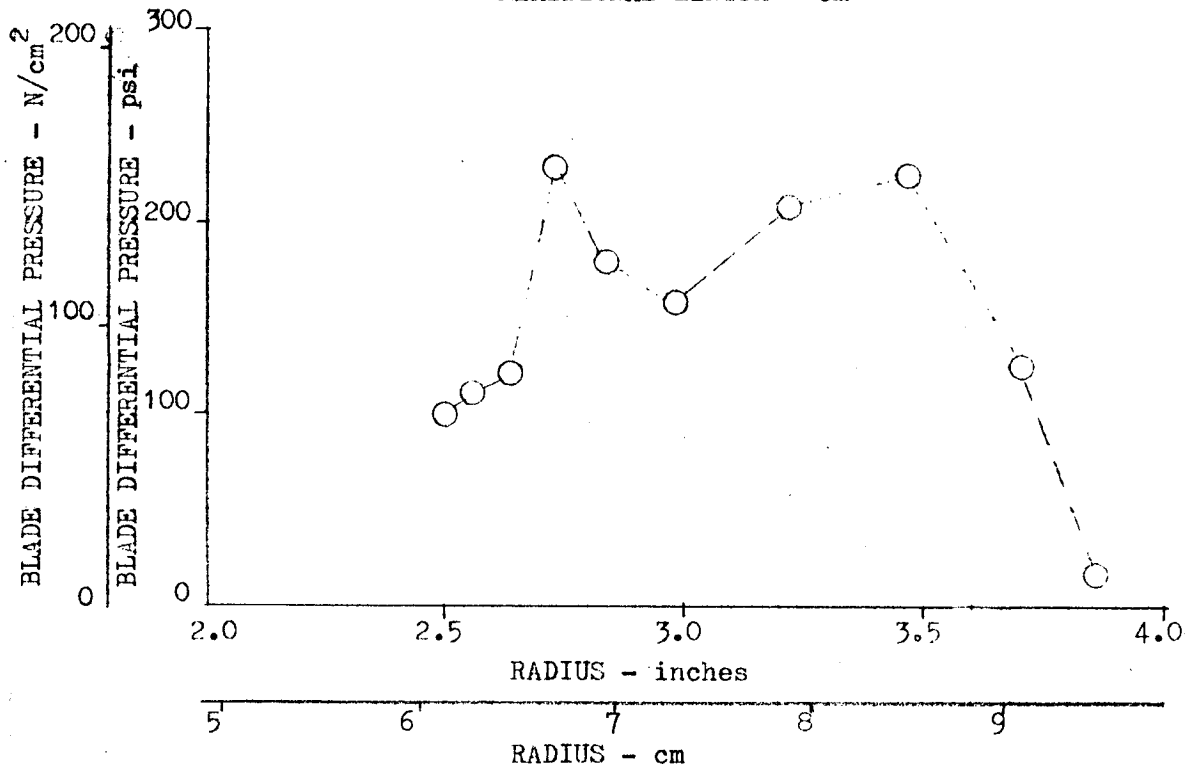
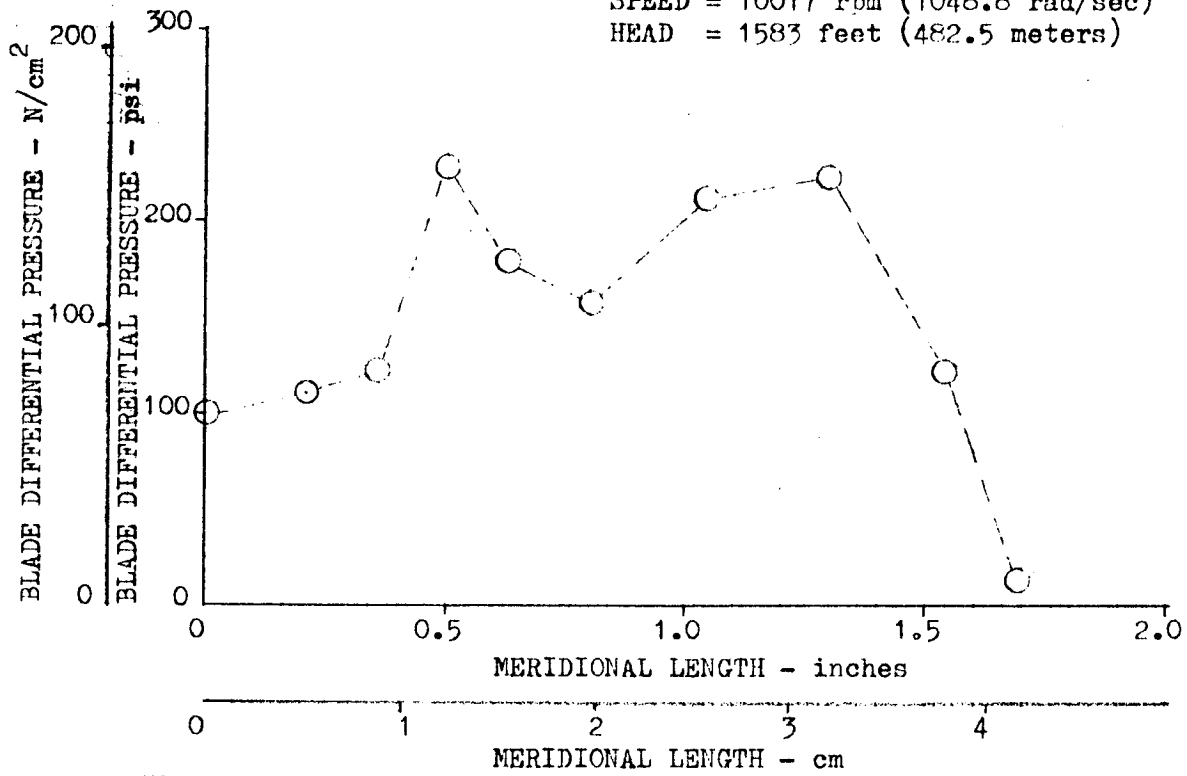


Figure 78. S-4 Oxidizer Impeller Calculated Blade Loading at Impeller Tip

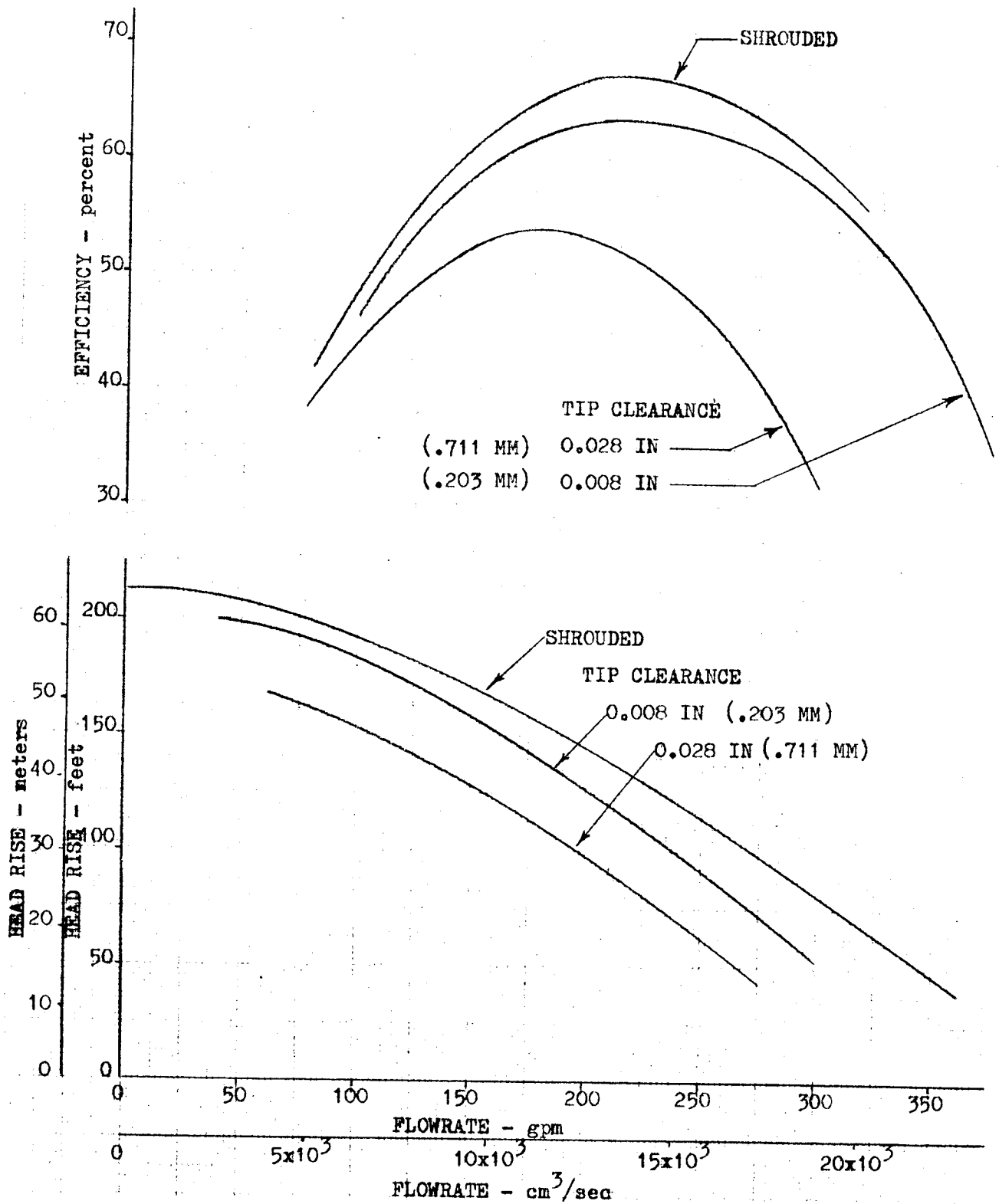


Figure 79. Hydraulic Performance of RI-15 Model Impellers
ASME Paper No. 64-WA/FE-17

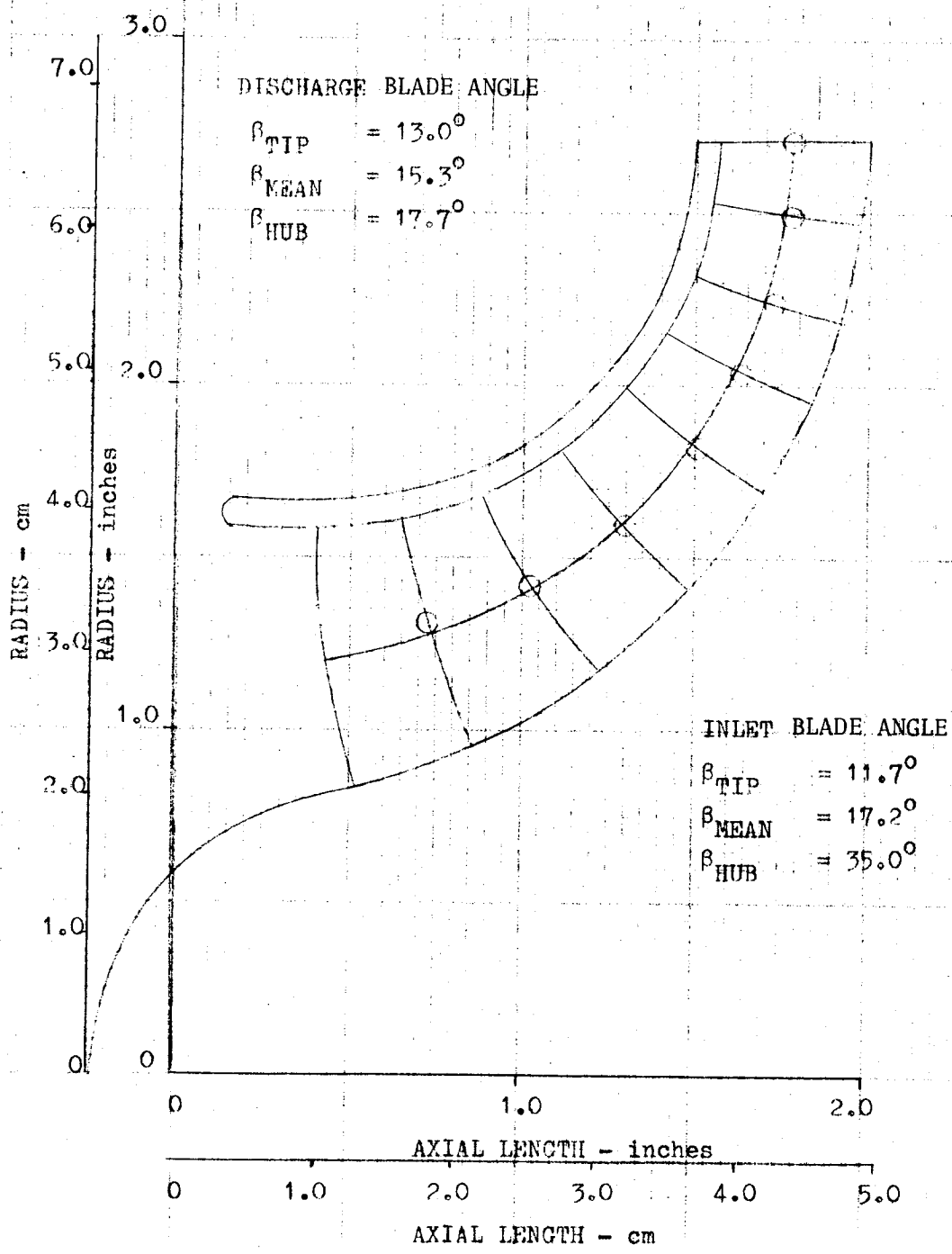


Figure 80. Wood's Impeller RI-15 Meridional View for Calculation of Blade Loading

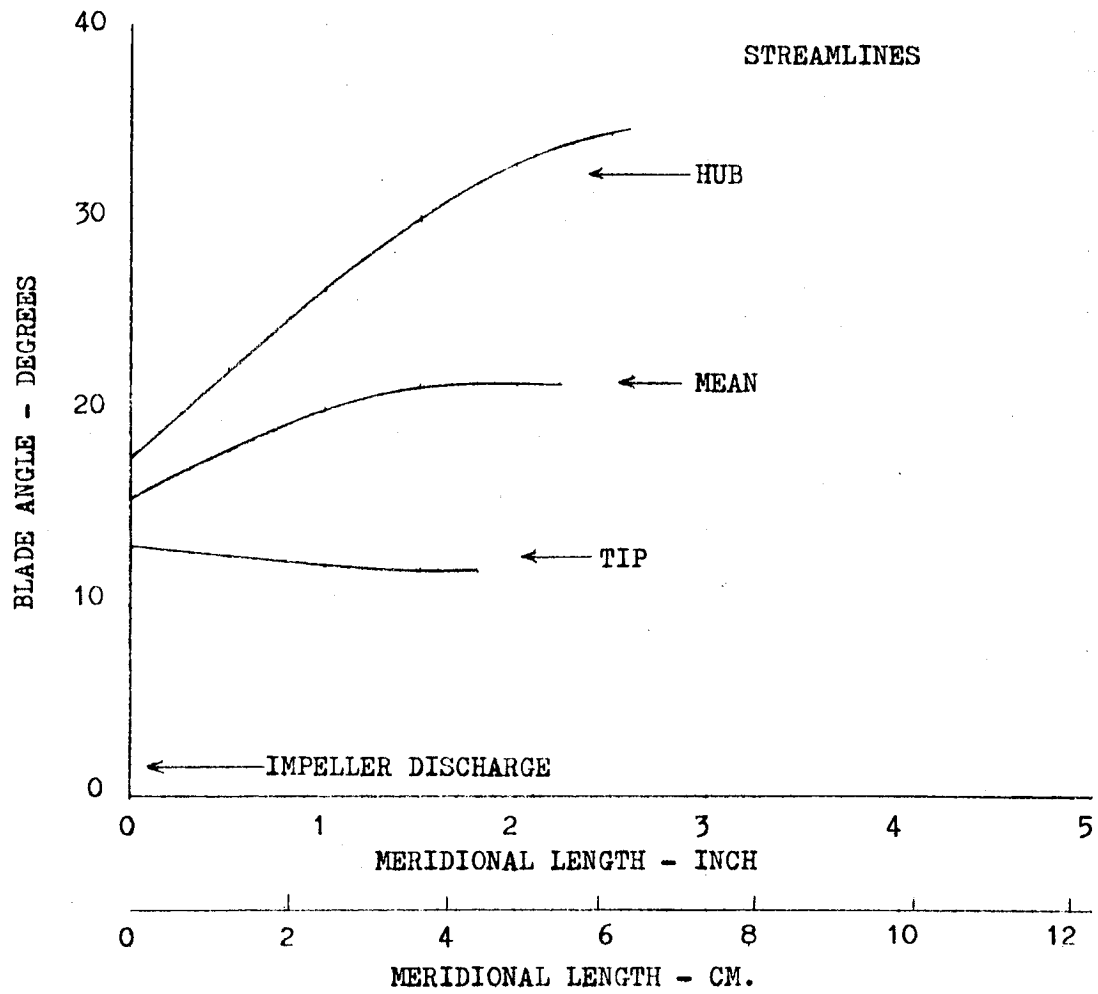


Figure 81. RI-15 Model Impeller Blade Angle Distribution

FLOW = 210 gpm ($13.25 \times 10^3 \text{ cm}^3/\text{sec}$)
 SPEED = 5000 rpm (523.5 rad/sec)
 HEAD = 132 feet (40.2 meters)

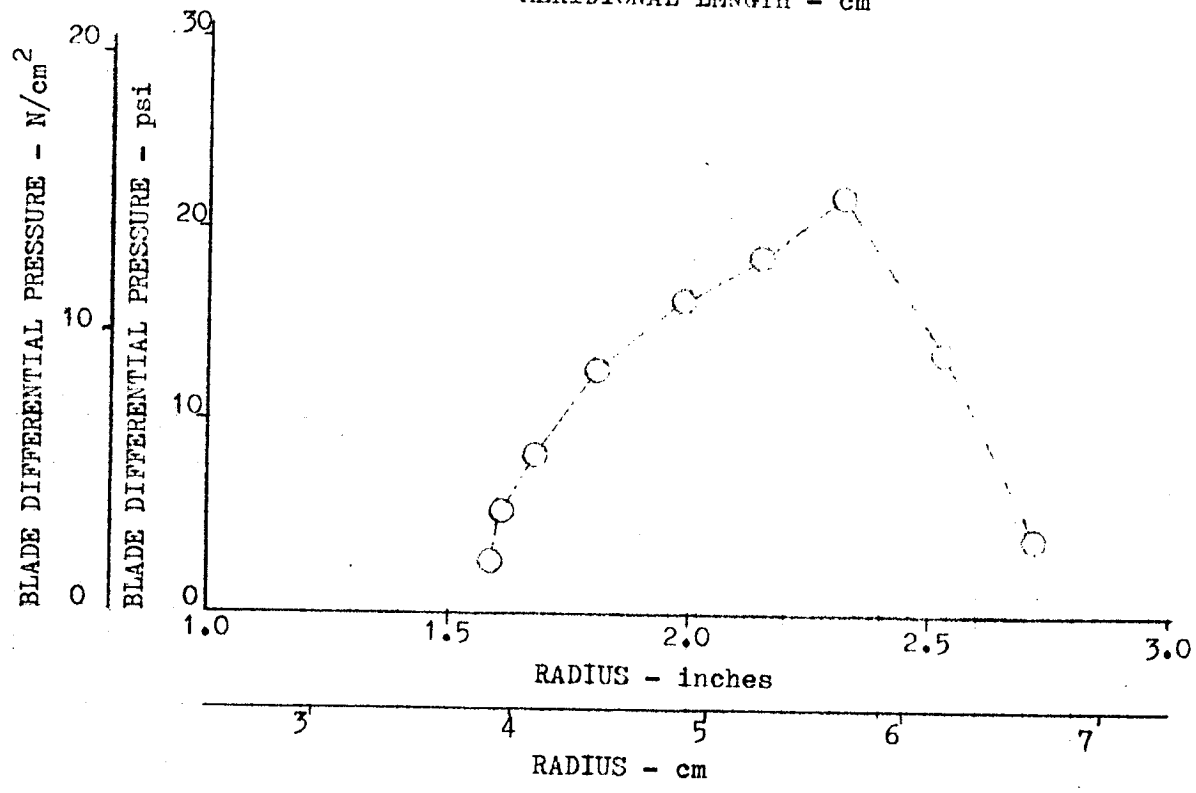
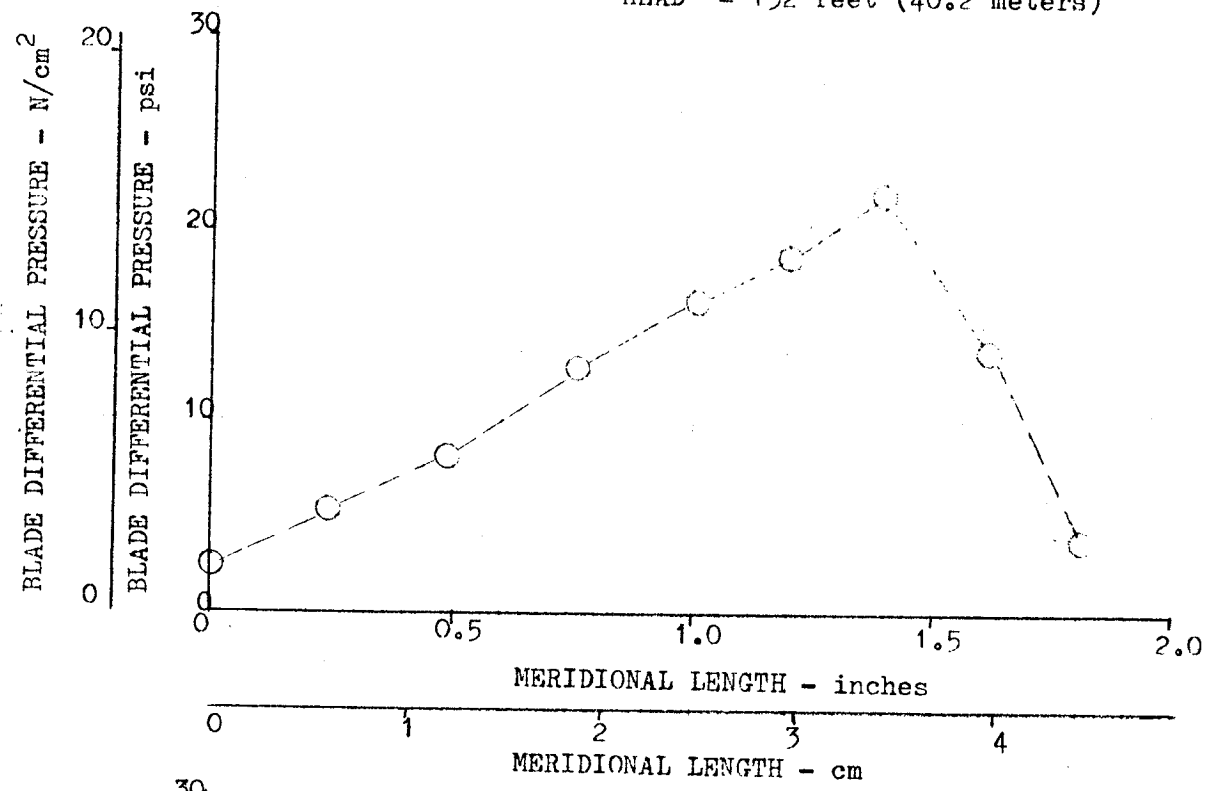


Figure 82. Wood's Impeller RI-15 Calculated Blade Loading at Impeller Tip

The meridional view of the J-2 oxidizer pump is presented in Fig. 83. The view presents the four assumed streamlines used in the J-2 blade-loading calculation. The pressure tap locations used for measuring the blade loading are also presented. Blade angle distribution is as shown in Fig. 84. The resultant blade-loading calculations for the tip streamline are given in Fig. 85, and are presented as functions of meridional length and radius.

Head Change Due to Tip Clearance. The data from the two pumps found in the literature were reduced and are presented to indicate the direct effect of tip clearance on the pump head, torque, and efficiency. These data are presented as ratios of a reference zero tip clearance flow which was formed by extrapolation of the data to a zero clearance. These data for the S-4 and RI-15 pumps are presented in Fig. 86 and 87, respectively. A similar summary of performance for the J-2 pump is found in Fig. 76 and 77.

Two models were presented in Task B for the determination of the head change due to tip clearance. Both dealt with the determination of the impeller throughflow by calculation of the leakage through the tip clearance. The resultant head shift was then accounted for by the change of impeller flow coefficient. In the first method, the net leakage flow was calculated by integration of the tip clearance flow over the blade tip meridional length with the tip clearance leakage velocity defined as a function of the blade pressure differential. The resultant equation for the leakage flow due to tip clearance was

$$Q_L = K \lambda \sqrt{\frac{2}{\rho} \Delta P_{\max}} \int_0^{m_t} \sqrt{M} \, dm$$

The integral was considered as a form factor. The head coefficient ratio was then defined as:

$$\frac{\psi_c}{\psi_o} = 1 + \frac{B \phi_D}{\psi_D} \left(\frac{K \lambda \sqrt{\Delta P_{\max}} \sqrt{2/\rho} M'}{2\pi \phi_D U_t r_t b_t} \right)$$

The available impellers with blade-loading calculations were integrated numerically to obtain the form factors, and the equation of head loss ratio was solved. The equivalent empirical constants (K) agreed closely for the J-2 pump and the RI-15, being values of 11.30 and 10.54, respectively. The S-4 pump data indicated a factor of 18.0 would be required. The blade loading of the S-4 oxidizer pump did indicate that the pump head would be much higher than was found by the test data, which would affect the leakage flow factor. The head rise predicted by the blade-loading calculation was greater on all pumps than the measured values. The form factor was corrected by the square root of the ratio of measured head to calculated head and the values of K were calculated. The constants K still closely agreed for the J-2 pump and the RI-15 pump with respective values of 12.18 and 12.45, while the required constant for the S-4 oxidizer pump was 26.29. The results, using an empirical constant (K) of 10.0, are presented in Fig. 88, and indicate good agreement for two of the three pumps that have been analyzed.

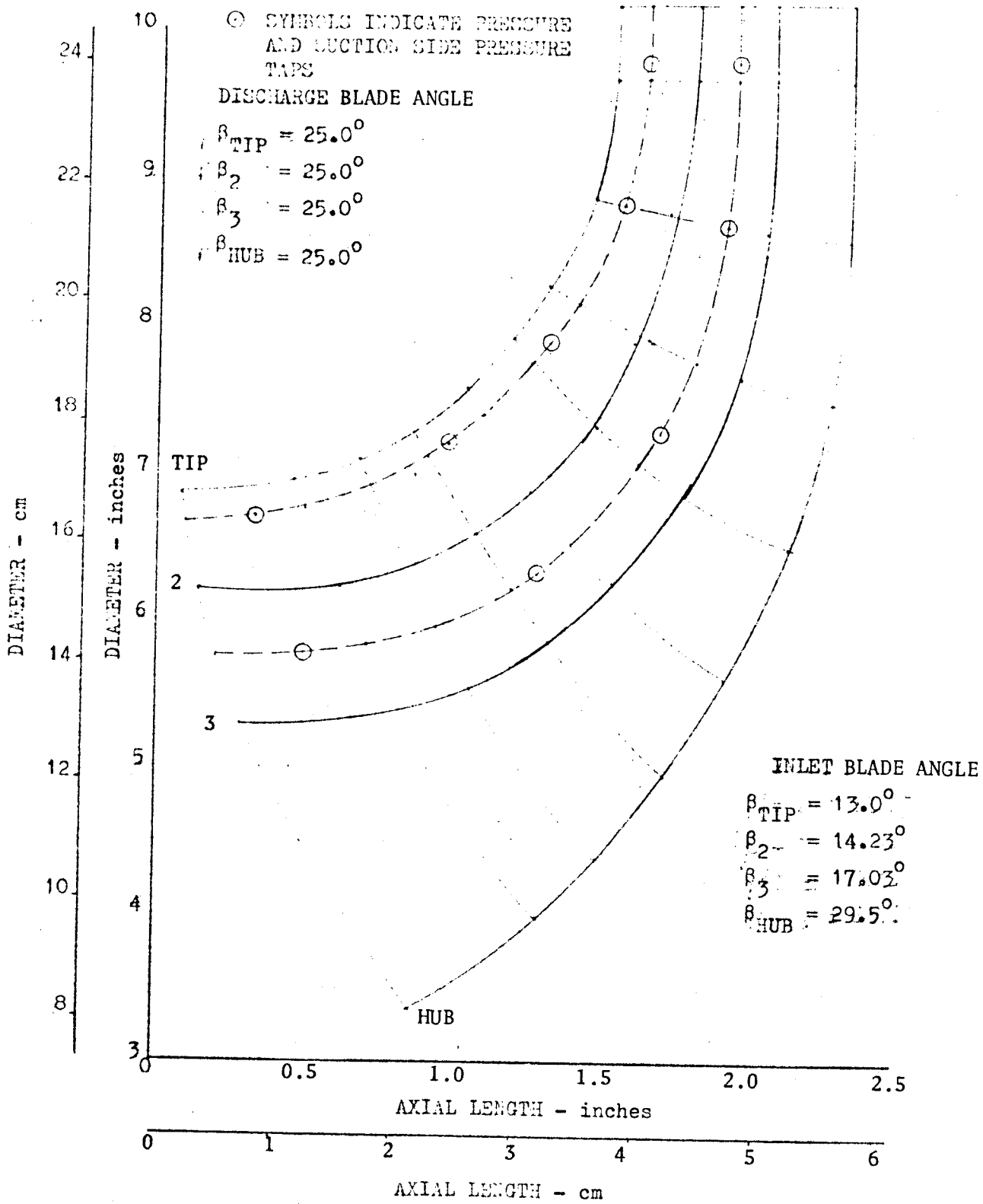


Figure 83. J-2 Oxidizer Pump Impeller Front Shroud Removed

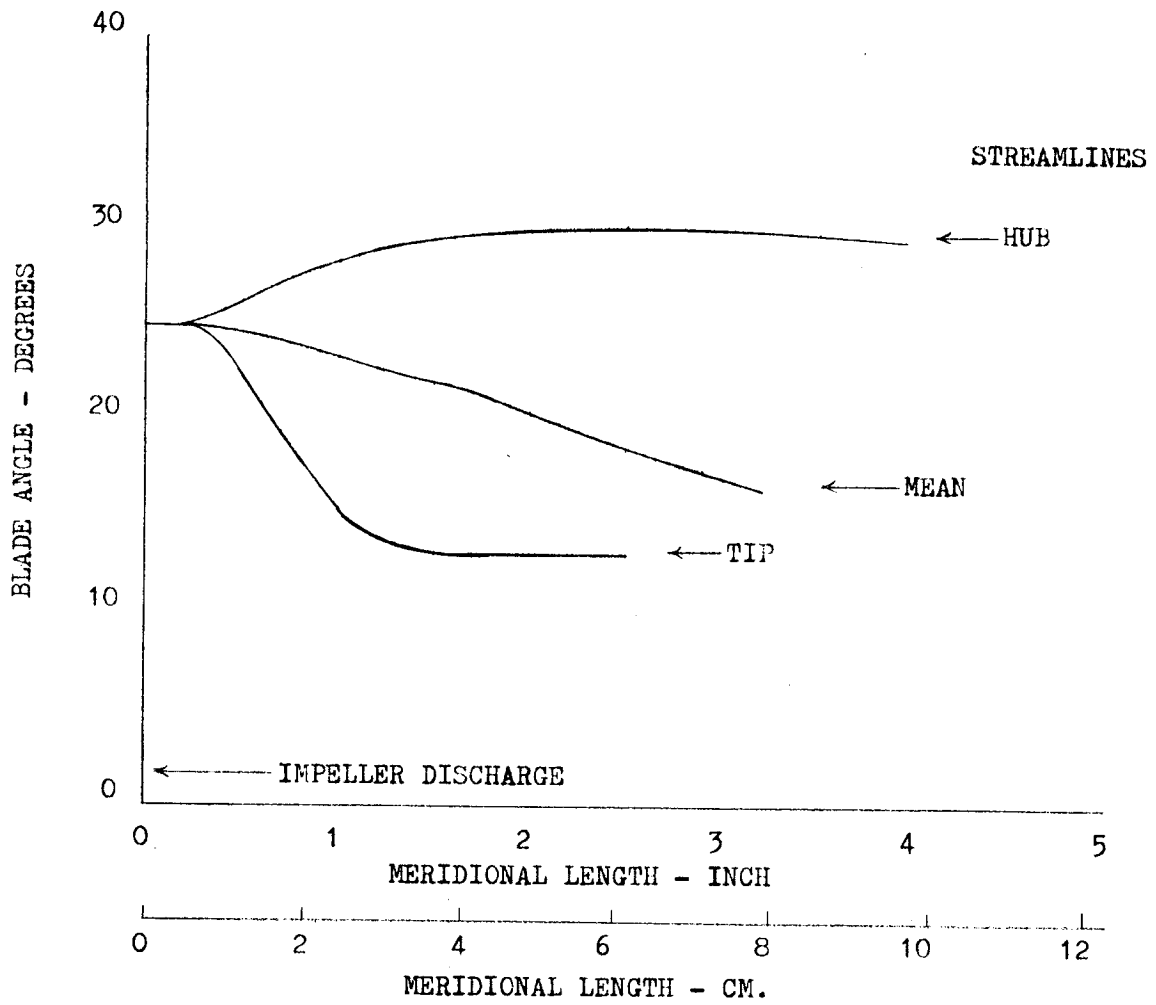


Figure 84. J-2 Modified Oxidizer Impeller (Front Shroud Removed)
Blade Angle Distribution

FLOW = 2760 gpm ($174.1 \times 10^3 \text{ cm}^3/\text{sec}$)
 SPEED = 8800 rpm (921.4 rad/sec)
 HEAD = 2373 feet (723.3 meters)

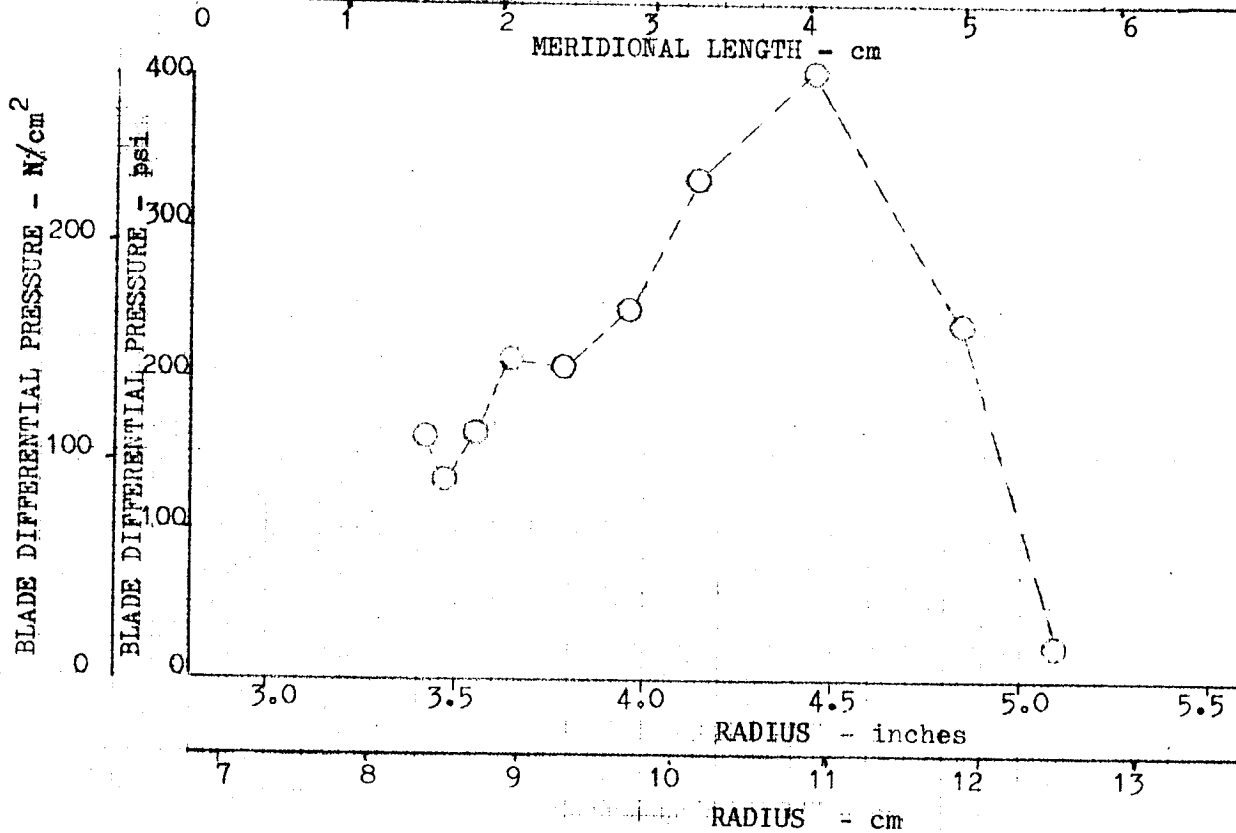
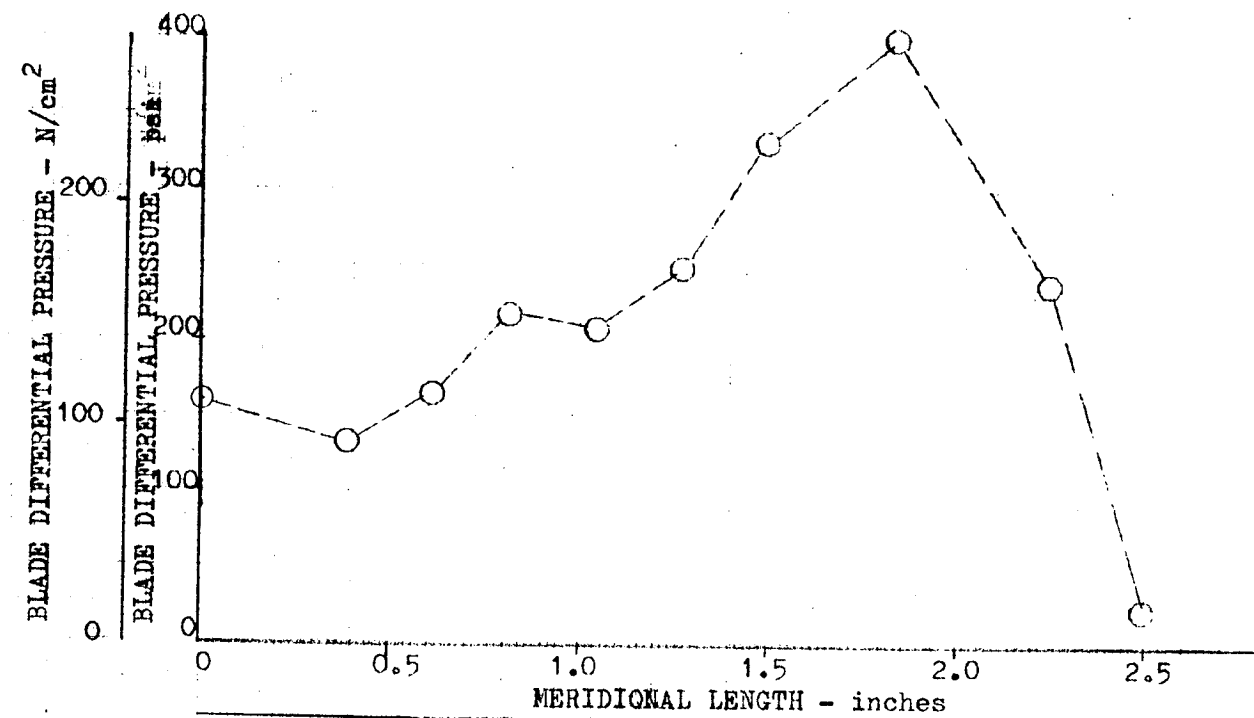


Figure 85. J-2 Oxidizer Impeller Calculated Blade Loading at Impeller Tip

SPEED = 10017 rpm (1048.8 rad/sec)

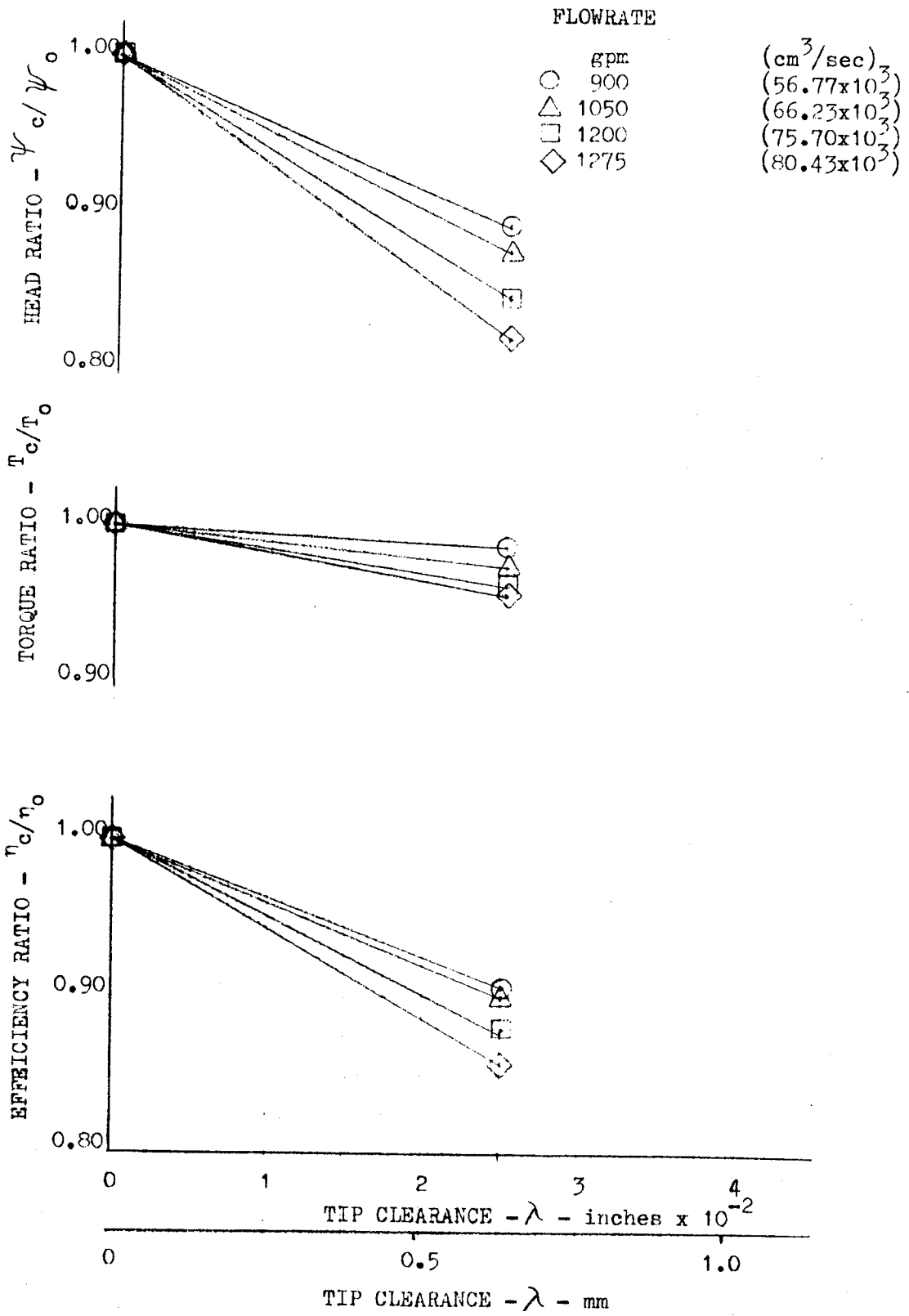


Figure 86. S-4 Oxidizer Pump Tip Clearance Effects on Pump Performance (Summary)

SPEED = 5000 rpm (523.5 rad/sec)

FLOWRATE

gpm	(cm ³ /sec)
○ 100	(6.31x10 ³)
△ 150	(9.46x10 ³)
□ 210	(13.25x10 ³)
◇ 275	(17.35x10 ³)

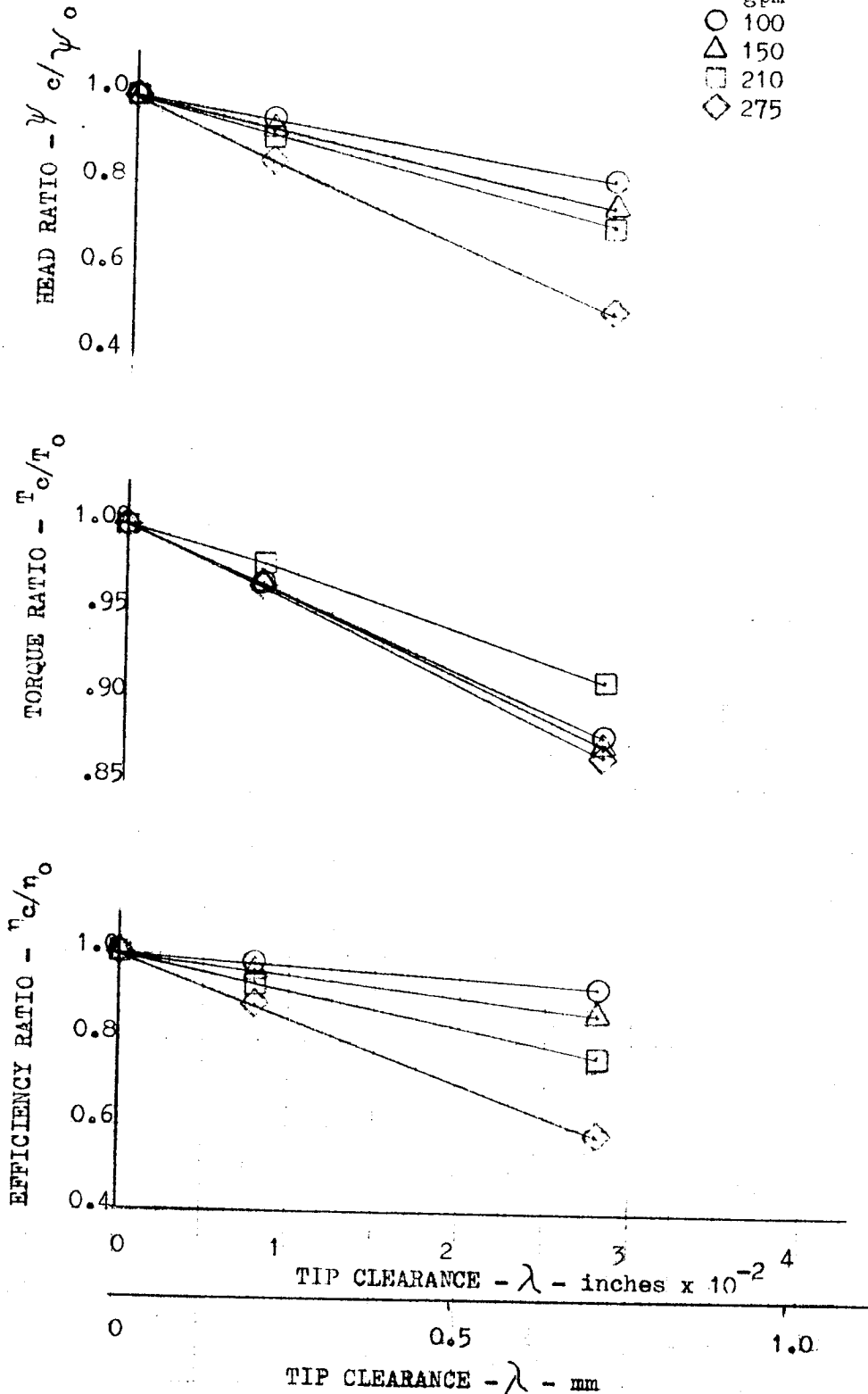


Figure 87. Wood's RI-15 Pump Tip Clearance Effects on Pump Performance (Summary)

$$\frac{\psi_c}{\psi_0} = 1 + \frac{B \phi_0}{\psi_0} \left(\frac{K \lambda \sqrt{\Delta P_{MAX}} \sqrt{2 \rho} M'}{2 \pi \phi_0 U_t r_t b_t} \right)$$

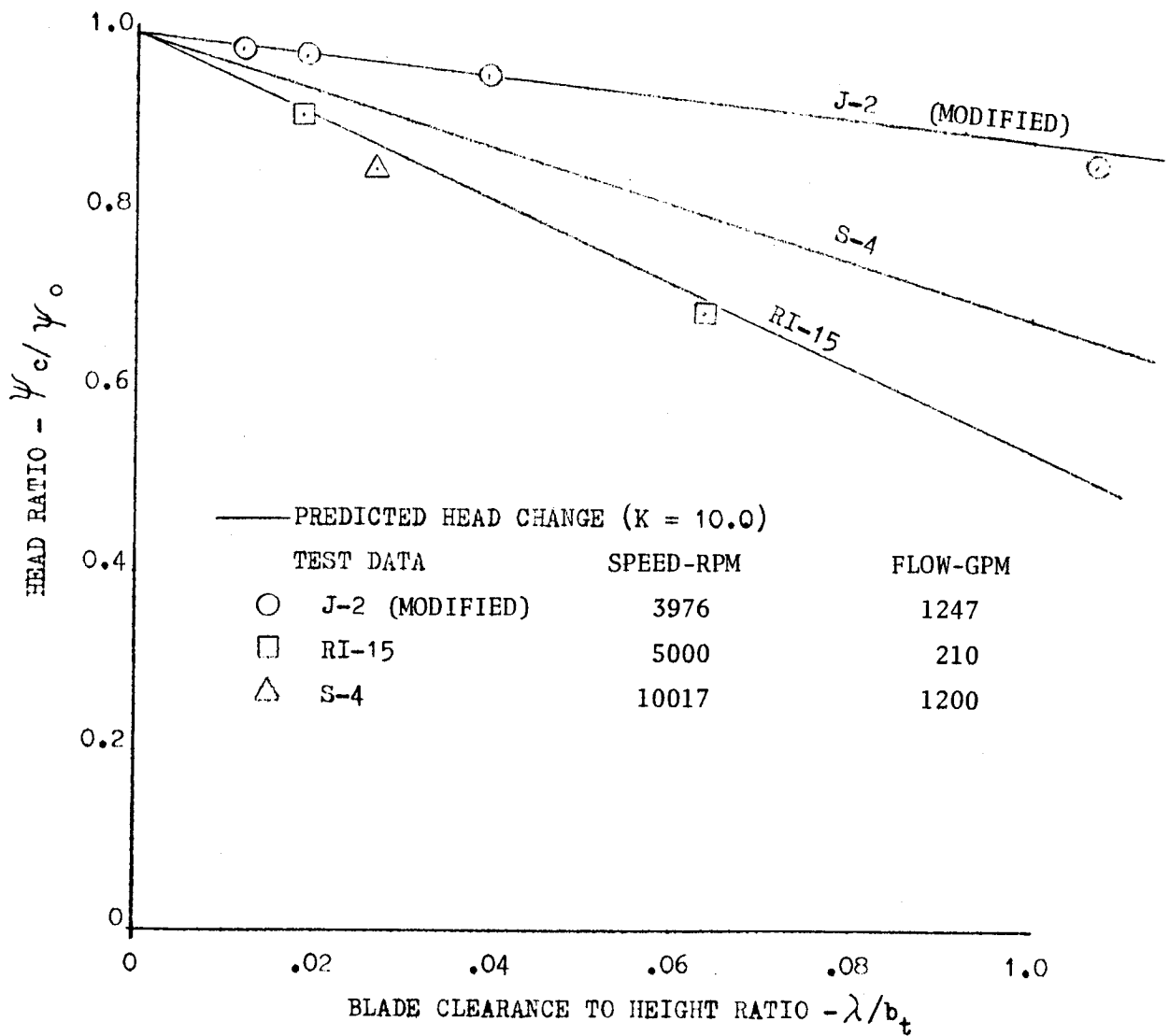


Figure 88. Head Change Due to Tip Clearance Based on Flow Change Using Blade Loading

The second method developed was to determine a flow shift in the impeller due to tip clearance leakage as a function of pump head coefficient. The leakage flow was given by the equation

$$\frac{\phi_L}{\phi_D} = K \frac{\sqrt{2\psi_D}}{\phi_D} \frac{\lambda}{b_A}$$

The head coefficient ratio was then defined as

$$\frac{\psi_c}{\psi_D} = 1 + \frac{B\lambda K}{b_A} \sqrt{\frac{2}{\psi_D}}$$

The use of this model gave good results at the design flow. The empirical constant (K) was found to be 0.74, 0.702, and 0.707 for the S-4, RI-15, and J-2 pump data, respectively. These data were developed using a 10-percent increment of flow to determine the slope (B) of the head-flow curve. Figure 89 presents the results of the data against predicted head change based on a K factor of 0.71 for all pumps at design Q/N. The data agree very well with the prediction, using the average blade height in the tip clearance ratio. When the inlet blade height is used for the prediction, only slightly less accurate results occur, as is indicated in Fig. 90. The use of a K factor of 0.88 was used with the inlet blade height. Excellent results with the three pumps are indicated.

The use of an increased flow interval of 30 to 40 percent of design flow for the slope determination caused greater variations in the constant K. The operating conditions at off design could not be predicted, nor could the tip clearance effect at design (Fig. 91). The values of head at the high flows on the head-flow curves indicate a greater loss ratio and, at lower flows, indicate a lower loss ratio due to tip clearance. Examination of the pump performance curves can possibly shed some light as to the reasons for this. All data indicate a greater head loss for a given tip clearance at the highest flows. The pump head-flow characteristics indicate a greater negative slope on all pumps at the higher flow levels. The concept of tip leakage flows explains this since the leakage flow adds to the flow through the impeller, which affects the impeller velocity triangle. The greater flow decreases the tangential flow component C_U , which results in a reduced pump head. The slope of the H-Q curve indicates a greater head reduction for the same flow increment at the higher flow, which satisfies the condition on all the test data presented.

$$\frac{\psi_c}{\psi_o} = 1 + \frac{\beta K \lambda}{b_A} \sqrt{\frac{2}{\psi_D}}$$

	PUMP	SPEED		FLOWRATE	
		RPM	(rad/sec)	GPM	(cm ³ /sec)
○	S-4	10017	(1048.8)	1200	(75.70x10 ³)
□	RI-15	5000	(523.5)	210	(13.25x10 ³)
◇	J-2	3976	(416.3)	1248	(78.72x10 ³)
△	J-2	5058	(529.6)	1588	(100.17x10 ³)

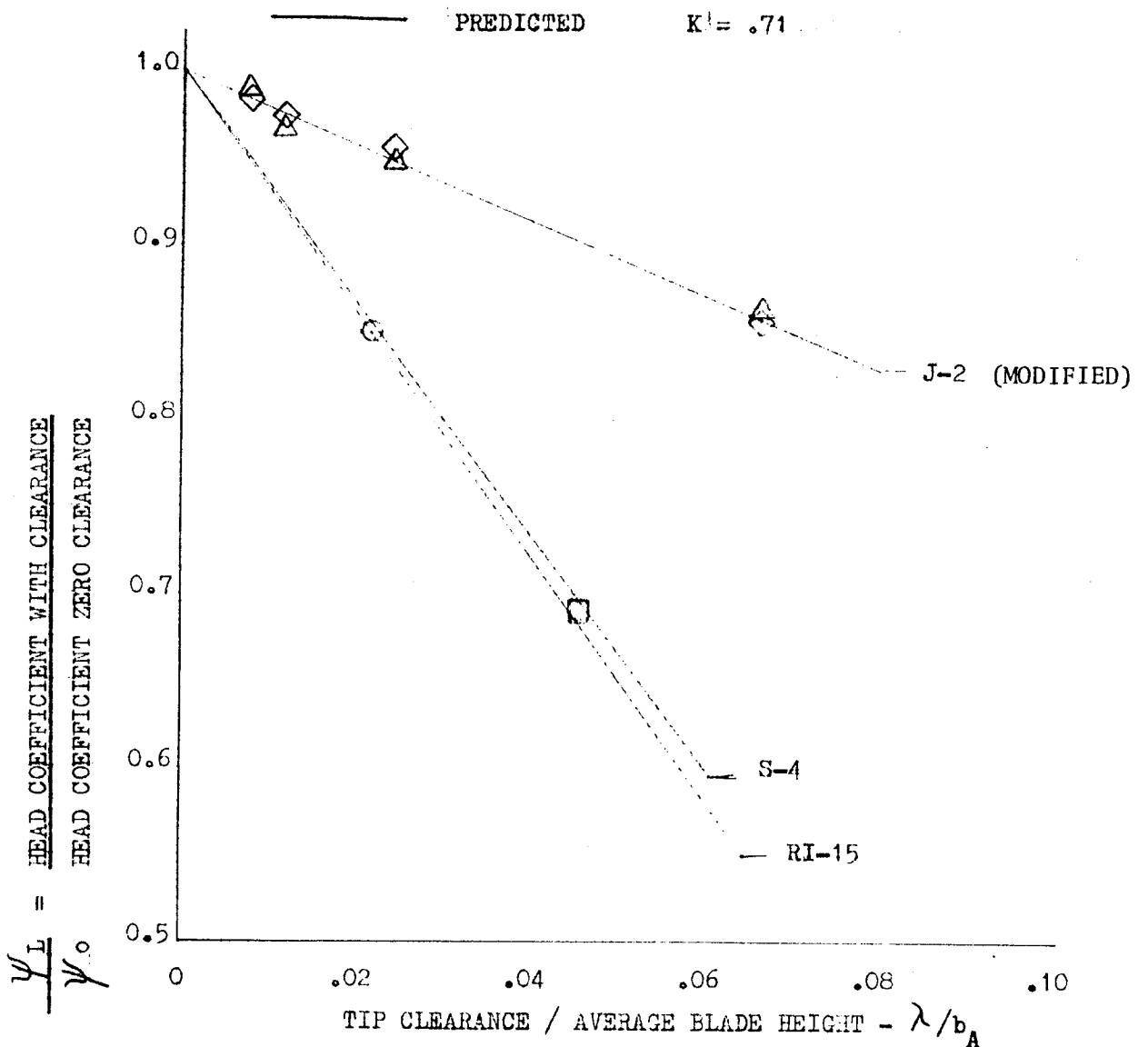


Figure 89. Head Loss Due to Tip Clearance at Design Flow

$$\frac{\psi_c}{\psi_o} = 1 + \frac{\beta K \lambda}{b_A} \sqrt{\frac{2}{\psi_o}}$$

	PUMP	RPM	(rad/sec)	GPM	(cm ³ /sec)
○	S-4	10017	(1048.8)	1200	(75.70x10 ³)
□	RI-15	5000	(523.5)	210	(13.25x10 ³)
◇	J-2	3976	(416.3)	1248	(78.72x10 ³)
△	J-2	5058	(529.6)	1588	(100.17x10 ³)
— —	PREDICTED		K = .88		

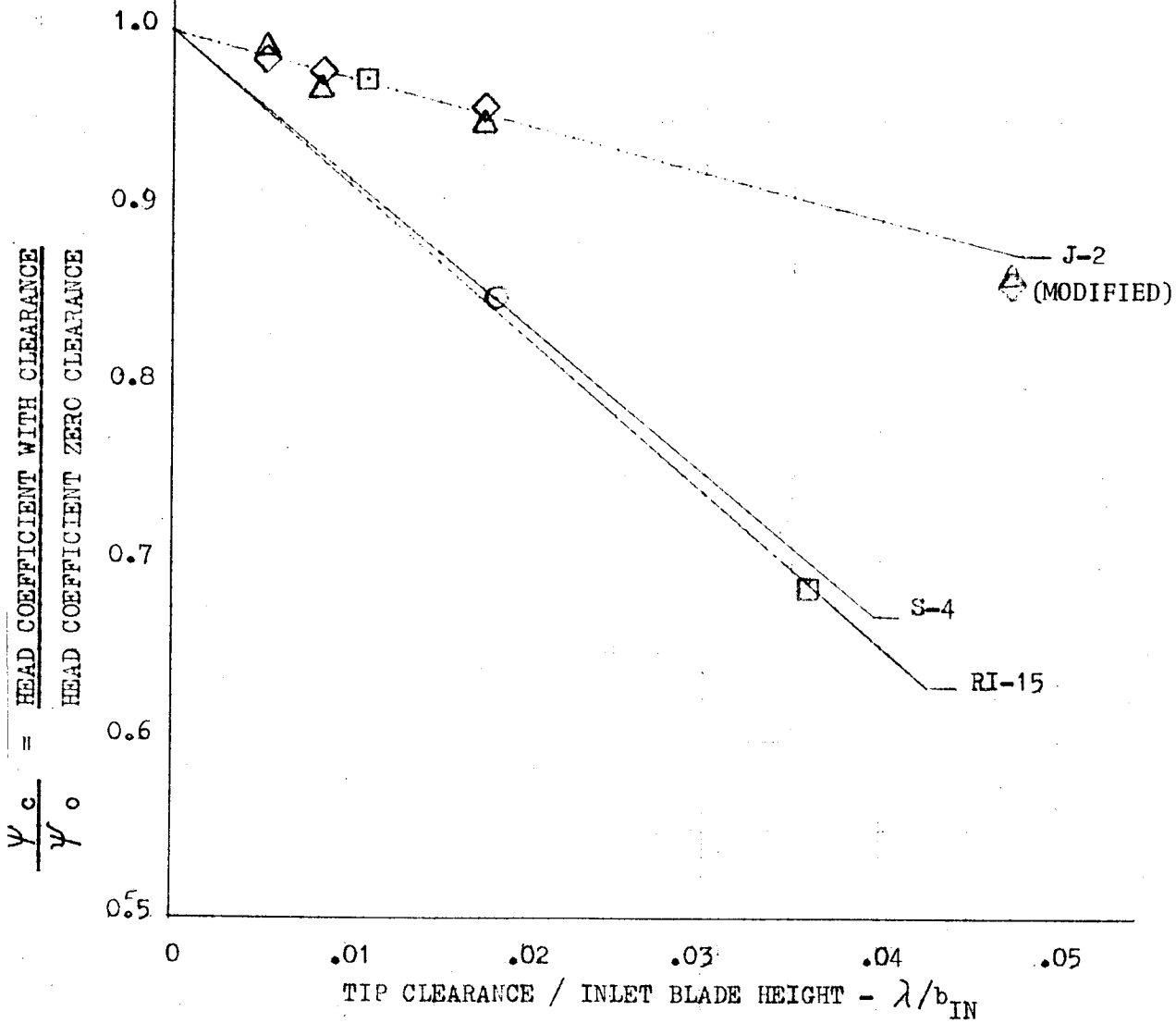


Figure 90. Head Loss Due to Tip Clearance at Design Flow

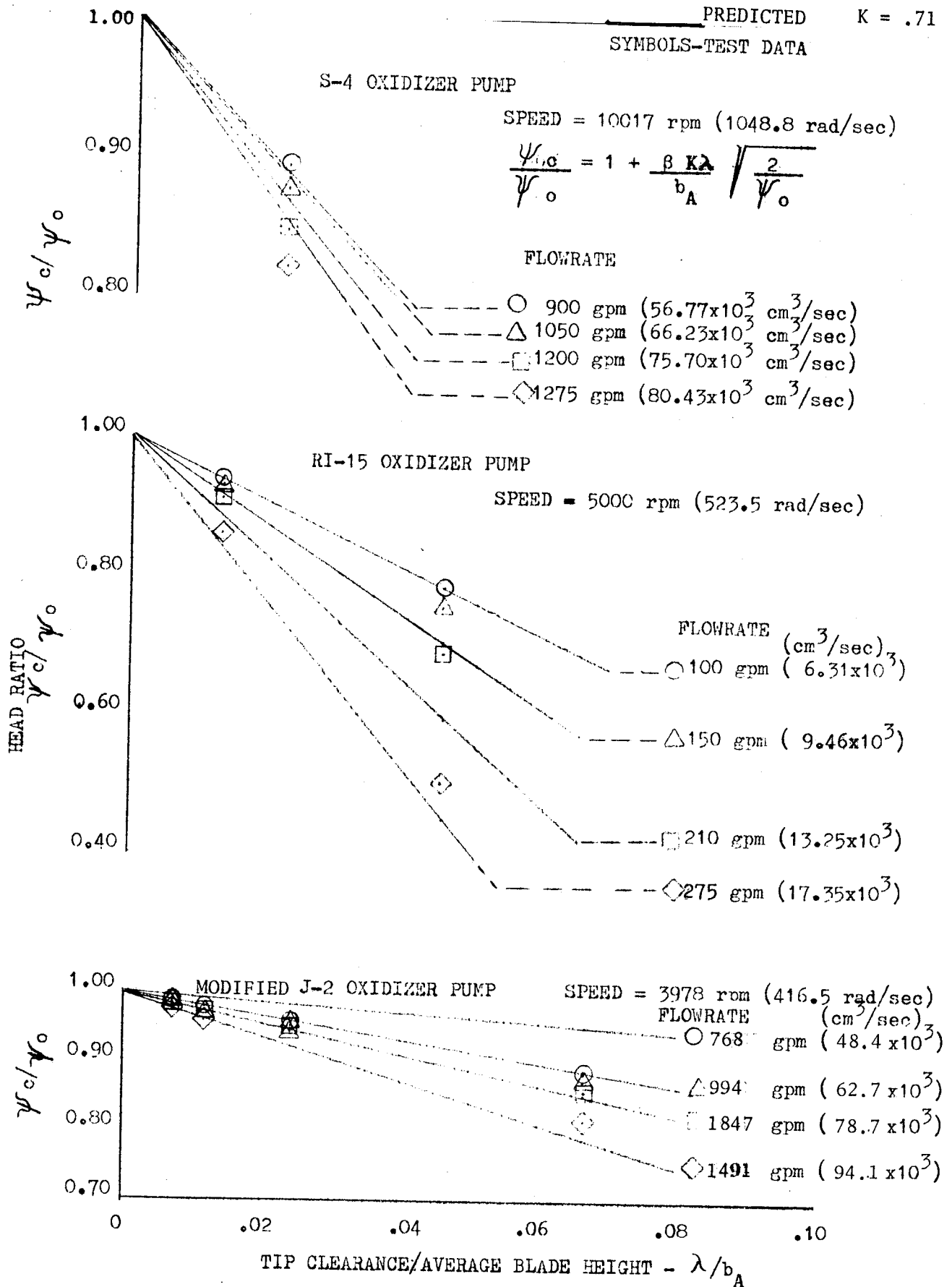


Figure 91. Head Change Due to Tip Clearance Leakage and Increased Impeller Flow 135

The results indicate a constant K used in the equation presented should be on the order of 0.71 to give good predictions of head loss due to clearance change at the design point, and the flow increment used in determining the slope B should be near the magnitude to give the resultant value of ϕ_L/ϕ_D as calculated above.

Torque Change Due to Tip Clearance. The formulated model calculates torque loss due to the leakage momentum loss of the tip clearance flow. The mass flowrate through the clearance is a function of the blade loading and is found by using an orifice equation across the blade tip. Blade-loading curves were generated for the three test pumps and are given in Fig. 78, 82, and 85 for the S-4, RI-15, and J-2 pumps, respectively. The torque loss ratio is given by

$$\frac{T_c}{T_o} = 1 - \frac{2K^2\lambda}{b_t} \left[\frac{\frac{A}{2r_t^2} \left(1 - \left(\frac{r_1}{r_t}\right)^2\right) + \frac{B}{3r_t} \left(1 - \left(\frac{r_1}{r_t}\right)^3\right) + \frac{C}{4} \left(1 - \left(\frac{r_1}{r_t}\right)^4\right) + \dots}{\frac{A}{r_t^2} \left(1 - \frac{r_1}{r_t}\right) + \frac{B}{2r_t} \left(1 - \left(\frac{r_1}{r_t}\right)^2\right) + \frac{C}{3} \left(1 - \left(\frac{r_1}{r_t}\right)^3\right) + \dots} \right]$$

where the values A, B, and C define the blade loading by $\Delta P = A + Br + Cr^2 + \dots$

The torque loss ratios at the design point were calculated for the pumps using an effective K factor of 0.90. The results are presented in Fig. 92 as a function of tip clearance ratio to the blade height at the discharge. The results indicate good agreement between the S-4 and RI-15 test pumps. The exact K factors required to obtain the test values of torque loss were 0.90 and 0.94 for the S-4 and RI-15 pumps, respectively.

It is interesting to note that the torque did not change appreciably with tip clearance change on the J-2 test pump. The data shown in Fig. 74 indicate that within the test instrumentation accuracy, the torque ratio was nearly constant at unity for all tip clearances (up to approximately 120 percent of design Q/N), which indicates the efficiency and head change were nearly equal. The torque ratio was not unity, but was at a near constant level at the highest flow (140-percent of design Q/N) for the test speed of 5038 rpm (527.5 rad/s). This characteristic is probably due to the fact that on centrifugal pumps at flow ranges greater than about 120 percent of design flow, large losses are seen and have been attributed to cavitation effects. These losses are additive to the tip clearance losses and are a result of an operating region in which the pump design cannot operate efficiently. The data indicating this loss are from three separate tests at three tip clearances and, therefore, should be considered reliable.

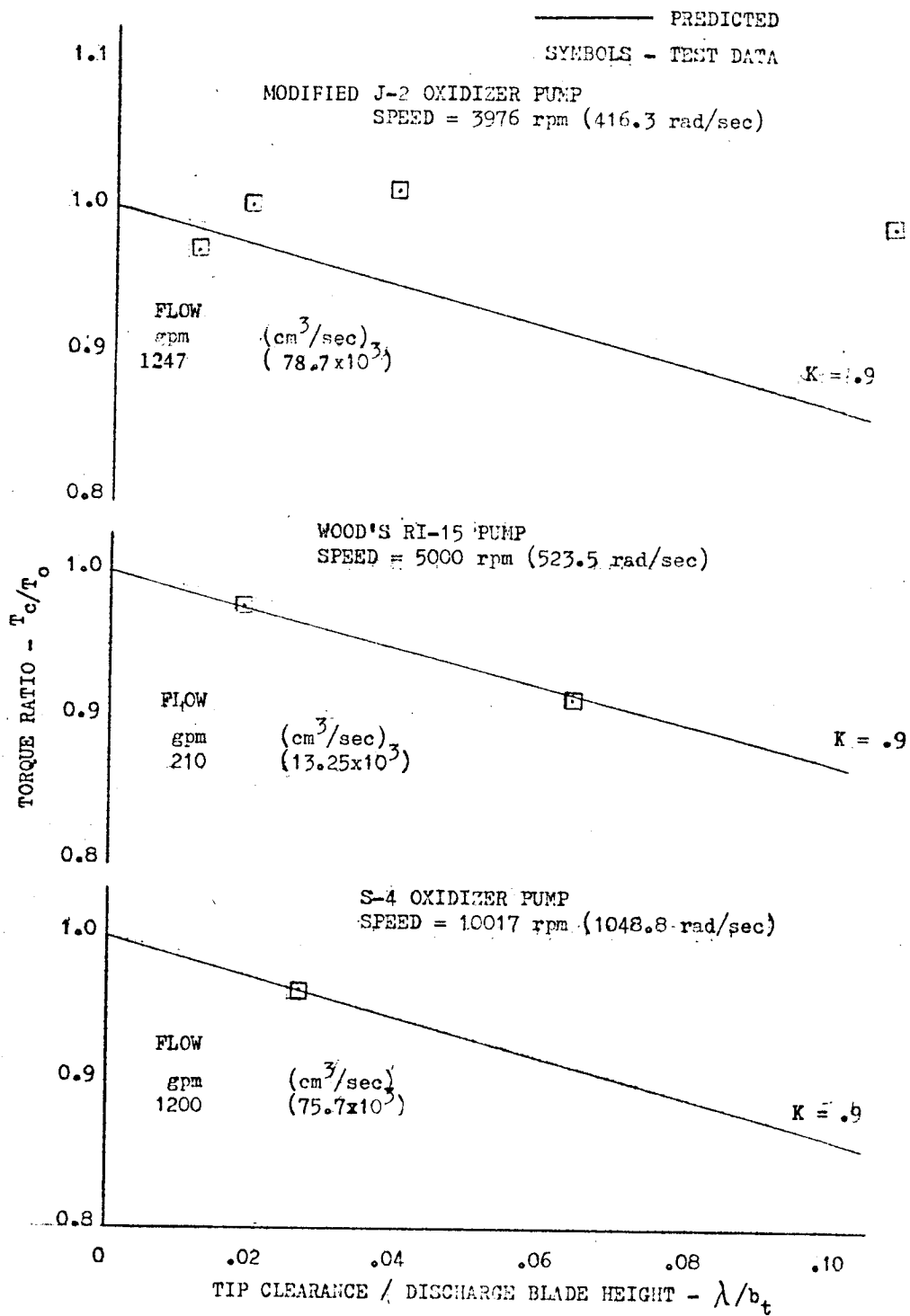


Figure 92. Torque Loss Due to Momentum Loss in the Tip Clearance Leakage Flow

CONCLUDING REMARKS

Based on the results of the analytical and experimental program described herein, the following conclusions can be drawn.

PREDICTION OF BLADE LOADING AND IMPELLER VELOCITY DISTRIBUTION

The computer program is capable of predicting the relative velocity distribution between impeller blade surfaces with an accuracy as good as can be expected considering that the method assumes a nonviscous fluid. The prediction accuracy is tied closely to the determination of the fluid slip correction which provides the relationship between the fluid angle and the blade angle at the pump discharge. The blade-loading prediction, when reduced by the ratio of the true impeller head rise to the head rise calculated from blade loading, gives values that correspond quite well to the test data. The position of maximum measured blade loading also is slightly closer to the impeller inlet than that calculated. Sufficient test data were not generated to determine the effects of tip clearance with an open impeller on the prediction of spanwise blade loading. The further development of this program can facilitate more accurate prediction of the blade loading for stress calculation purposes, as well as lead to a method of determining the spanwise pressure distribution effect of tip clearance on open-faced impellers. Further effort in this area will result in better hydrodynamic design capability for the designer of high-performance rocket engine pumps.

Test programs with open as well as shrouded impellers to determine blade pressure distribution were proved completely feasible with the test apparatus used in this study. The method of using a pressure-scanning valve located in the impeller shaft has proved to be very satisfactory. This approach has provided a long-needed technique that will allow measurement of internal local pressures on all types of rotating machinery. Further studies utilizing these methods would greatly improve the state of the art of impeller design and performance prediction.

PREDICTION OF TIP CLEARANCE EFFECT ON TORQUE, HEAD, AND EFFICIENCY

The analytical procedures and methods presented have resulted in models to predict the change in head, torque, and efficiency in an impeller due to tip clearance. The study of the effect of boundary layer scraping and its effect on the spanwise blade pressure distribution has been discussed. The test data indicate that boundary layer effects were probably not present in the test pump on most tests. However, at the smallest operating clearance of 0.009 inch (0.229 mm), the torque decreased more than 2 percentage points than would be predicted neglecting boundary layer, causing a net efficiency increase of 2 percent. A slight increase was evident in the head rise of the pump at the test speed of 5038 rpm, but was not indicated on data with test speeds of 3976 rpm.

The data from the pumps used in the study show a single inconsistency that cannot be adequately explained at this time. The torque ratio of the two pumps found in

the literature show good agreement with the model and decrease with tip clearance increase, while the torque ratio of the J-2 oxidizer pump test data remains constant for all values of tip clearance. A review of the J-2 test data indicates good accuracy, and the test data must be considered good. The prediction of head change due to tip clearance at the flow, which approximates maximum efficiency, shows good agreement, but deviates at other flowrates. This may be caused by the fact that the head used in the model is the overall pump head. At flows other than those in which maximum efficiency occurs, the difference between the true impeller head rise and the pump head rise is greater due to the increased losses at these flows. Additional effort with the current model should examine the use of the impeller head rise rather than the overall pump head rise when predicting a tip clearance leakage. The leakage can then be added to the impeller delivered flow to determine the new resultant head rise.

CLEARANCE AND COST ANALYSIS

For a given pump design, the hardware and manufacturing costs should be lower if increased tip clearance is permitted. However, in actual practice, unshrouded impeller pump designs are generally manufactured with small blade tip and housing clearances to maintain good pump performance. To obtain the desired close clearance, profiles are machined on a pattern from which the impeller housing contours are then duplicated. The design impeller tip clearance at assembly is then obtained by the use of shims. To maintain impeller tip clearance during pump operation, axial and radial thrust, thermal and pressure deflections, mechanical dynamics of the pump rotor, and shaft deflections due to cavitation-induced radial loads are some of the important factors that must be considered in a proper design.

Shrouded and unshrouded liquid oxygen pump designs were priced based on one end item. The cost analyses included fabrication, tooling, inspection, and assembly. The cost of the unshrouded and shrouded impeller configurations was found to be approximately the same.

GENERAL

The comparison of predicted performance with test data indicate the need to acquire very accurate data for a study of this type. For tip clearance ranges used during these tests, which were from 1 to over 10 percent of the impeller blade height (which covers the range used in modern rocket engine design), the head loss at design flow was from 1 to 16 percent of the reference head, with efficiency losses of the same magnitude. Instrumentation accuracies on the order of ± 1 percent are the minimum required for such tests. Such accuracy requirements should be considered for any attempt to obtain additional data such as presented herein.

APPENDIX A

LITERATURE SURVEY SUMMARY

DEAN, R. C.

Influence of Tip Clearance on Boundary Layer Characteristics in a Rectilinear Cascade

Report No. 27-3, Gas Turbine Laboratory, Massachusetts Institute of Technology, 1954

Empirical data are presented which reveal the mechanism and the influence of tip leakage in a rectilinear cascade. The influence of tip leakage is determined from measured flow patterns in the main stream and boundary layer, from pressure distributions and calculations of momentum flux, from passage and mixing loss calculations, and from calculated parameters indicating boundary layer "health." A model of the interaction of tip leakage and secondary flow in the wall boundary layer is built from the experimental data.

FOWLER, H. S.

An Investigation of the Flow Processes in a Centrifugal Compressor Impeller

National Research Council of Canada, July 1966

A program of experimentation was developed to analyze the flow patterns within a centrifugal compressor impeller. A test rig was built on which 6-1/2-foot-(1.98 m) diameter impellers could be rotated up to 70 rpm (7.33 rad/sec). An observer sitting in the middle of the impeller and rotating with it, was able to examine the flow in the channel with smoke and record it on movie film. A hot-wire anemometer was used to measure flow velocities. Wool tufts in the channel were photographed to aid in determining flow direction. The variable discussed in the report are the effect of: impeller shroud as opposed to stationary casing, various degrees of running clearance, and flow pattern in the impeller channel due to throttling the flow at the volute exit. Detailed comparisons of velocity profiles in the impeller channel are presented for various impeller clearances, and without impeller shrouds.

FOWLER, H. S.

Some Measurements of the Flow Pattern in a Centrifugal Compressor Impeller

ASME Paper 65 WA/GTP-7, 1965

Description of the test apparatus which consists of a large 6-1/2-foot (1.98 m) compressor impeller which contained a space in the hub where an observer rotating up to 70 rpm (7.33 rad/sec) with the impeller observed and recorded flow patterns, velocity profiles, etc., with the help of wool tufts, smoke, and a hot-wire anemometer. Data are presented for velocity profiles in shrouded and unshrouded impellers at various tip clearances.

FURUYA, Y, I. NAKAMURA, AND H. KAWACHI

The Experiment on the Skewed Boundary Layer On a Rotating Body

ISME Bulletin, Vol. 9, November 1966, pp 702-710

When a body of revolution rotates in an axial stream, skewed boundary layers develop on the body surface. Experiments were carried out on the skewed boundary layers over a body of revolution with a streamlined nose. Measured velocity profiles differed little from the quasicollateral condition. A velocity component perpendicular to the streamline appeared in a layer near the wall with a thickness of 0.0591 inch (1.5 mm). The magnitude of this velocity component was about 5 percent of the main stream velocity. Measured boundary layer thickness compared with two theories which used the momentum integral equations. Although there are some differences in the assumed velocity profile between the theoretical and experimental results, this agreement was fairly good.

GEARHART, W. S.

Tip Clearance Cavitation in Shrouded Underwater Propulsors

AIAA Paper No. 65-573, 14 June 1965

The problem of cavitation in the tip clearance region of a shrouded rotating blade was discussed. The tip clearance flow associated with various shaped blade ends rotating near a stationary wall was characterized and experimental results were presented. Tip clearance flow was defined as that which passes through the area between a blade and a guide wall and originates from the pressure difference across the blade tip section and the relative motion between the blade end and adjacent guide wall. "Gap" and "tip vortex" cavitation are also defined. Blade end configurations to minimize gap and tip vortex cavitation are described.

GEARHART, W. S.

Tip Clearance Flow In Turbomachines

Pennsylvania State University, Ordnance Research Laboratory, Navy Department, Bureau of Naval Weapons, Contract N0w 63-0209-c.

Experience in testing rotating blades indicated that cavitation usually occurs in the tip clearance region of the rotating blades before it occurs on the blades themselves. An investigation was initiated to study the mechanics of the tip clearance flow and its characteristics. It was assumed that cavitation in the tip clearance region was dependent on the following parameters: (1) ratio of blade tip thickness to tip clearance height, (2) ratio of the momentum thickness of the boundary layer on the wall to the tip clearance, (3) ratio of hydrodynamic tip loading to the tip speed, and (4) gap configuration or shape.

A test apparatus was built which used air as the test medium. To simulate the relative motion between a blade end and the casing wall, an endless belt was used. With this apparatus, it was possible to vary the above parameters, and pressure and velocity distribution associated with various gaps were obtained.

HAMRICK, J. T.

Some Aerodynamic Investigations in Centrifugal Impellers

ASME Transactions, Vol. 78, pp 591-602, April 1956

Results of both theoretical and experimental investigations of flow in rotating impeller passages are presented. The manner in which losses arise, their effect upon the flow within the passage, and their overall effect upon impeller performance are discussed. In addition, analysis and design methods based on isentropic flow calculations are discussed and their application to the design of mixed-flow impellers is demonstrated.

HARTMAN, M. J., G. W. LEWIS, AND E. R. TYSL

Design and Experimental Performance of a Small Centrifugal Pump for Liquid Hydrogen

NASA T.M. X-389, September 1960

A shrouded 4-inch- (10.16 cm) diameter hydrogen pump rotor was designed and tested in liquid hydrogen. The pump rotor was operated at a flow coefficient of 0.2, and a pressure coefficient of 0.585, and indicates a hydraulic efficiency of 0.65. This was a low-specific-speed rotor from which such efficiencies are expected. An unshrouded model was tested and the results indicated a large reduction in performance compared to the shrouded pump. The minimum allowable clearance for the unshrouded rotor was large compared to the height of the flow passage.

HORLOCK, J. H.

Some Recent Research in Turbomachinery

Vol. 182, Pt. 1, No. 26, Proceedings of Instrumentation Mechanical Engineers, 1967-68

Research on turbomachinery carried out at Liverpool University in the period 1958 to 1966 is reviewed. The work includes accurate determination of two-dimensional incompressible flow in cascades. The interaction of laminary and turbulent boundary layers with flows due to tip clearance is discussed.

HORLOCK, J. H., P. M. B. PERCIVAL, J. F. LOUIS, AND B. LAKSHMINARAYANA

Wall Stall in Compressor Cascades

ASME Paper 64-WA/FE-29, 1964

The effects of increased cascade deflection on development of the end-wall boundary layer, separation of the effects of secondary flow (produced by the deflection of a vorticity vector initially perpendicular to the flow at entry), skin friction at the end wall, flow visualization of the wall stall, attempts to reduce the secondary flow, and the severity of the wall stall were investigated. These attempts were made by reducing the blade chamber through the end-wall boundary layer and by optimizing the clearance between the tip of the blade and the end wall. The following conclusions were reached: (1) the end-wall boundary layer development in compressor cascades cannot be adequately described by simple secondary flow because of the separation in the corner bounded by the end wall and blade suction surface; (2) the end wall rather than the secondary flow caused the separation and high loss; (3) the severity of the wall stall increased with main stream deflection in a cascade of constant chamber, but may be reduced by reducing the chamber through the boundary layer region; (4) there was an optimum tip clearance at which the extent of the wall stall was minimized. These conclusions were limited to the case where no streamwise vorticity was present at entry.

JEFFERSON, J. L. AND R. C. TURNER

Some Shrouded and Tip Clearance Effects in Axial-Flow Compressors

Trans. N.E. Coast Inst. of Engineers and Shipbuilders, Vol. 74, 1957-1958

This paper, with a reference to the economics of blade manufacture, explains the reasons for the main series of tests carried out at the National Gas Turbine Establishment, the material being supplied by C. A. Parsons & Company, Ltd. Four series of tests are described in detail. Various combinations of shrouding and tip clearances were investigated; untwisted constant-section blading being used in the first three series. The experiments were conducted over a range of shrouding leakage clearances, and included an investigation of the boundary layer flow on the convex surface of a stator blade in the compressor. A brief review of published work on the effects of normal radial tip clearance was followed by a description of some early results obtained on a multistage compressor. It was concluded that shrouding of the type investigated should be avoided if possible, especially under certain aerodynamic conditions. If it is necessary, the clearance should be maintained at the smallest practicable value. The use of very fine radial tip clearances also may result in a loss of performance, although values in excess of 1 percent of the blade height are shown to be undesirable.

LAKSHMINARAYANA, B.

Methods of Predicting the Tip Clearance Effects in Axial-Flow Turbomachinery

ASME Paper No. 69 WA/FE-26, November 1969

An expression is derived for the decrease in stage efficiency due to tip clearance. The analysis includes all dominant flow and blade parameters that affect the flow in the clearance region. The predictions agree closely with several compressor,

fan, pump, and turbine data. The theoretical treatment of the flow predicts blade-to-blade variation in outlet angles accurately and stagnation pressure losses qualitatively. The predictions are compared with various experimental data available in the literature.

LAKSHMINARAYANA, B. AND J. H. HORLOCK

Leakage and Secondary Flows in Compressor Cascades

Reports and Memoranda No. 3483, Ministry of Technology, 1967

This paper describes the effects of leakage and secondary flows on lift, outlet angles, induced drag, and loss coefficients in a rectilinear cascade of compressor blades in which spanwise gaps simulated the clearance spaces of an axial compressor. The resultant leakage flow was studied under three different conditions: uniform inlet flow, nonuniform inlet flow near the gaps, and severely nonuniform inlet flow and an end wall within the gaps.

MELLOR, G. L. AND R. E. STRONG

End-Wall Effects in Axial Compressors

ASME Paper 67-FE-16

The end-wall blockage effect in axial compressors can be related readily to the conventional displacement thickness of boundary layer theory. With the help of an end-wall hypothesis introduced in the paper, the displacement thickness can be related to end-wall losses. An effort was made to obtain empirical information about the end-wall displacement thickness and, therefore, the blockage and loss. Only multistaged data were presented and were examined only at maximum efficiencies. A computer program was presented which calculated the annulus flow in a compressor, and determined the cascade losses, end-wall loss, and displacement thickness necessary to match experimental efficiency. The particular results indicated that end-wall displacement thickness was strongly correlated with rotor tip clearance. The results are confined to a narrow band of pressure coefficients, indicating that further work is necessary.

MILLER, M. J. AND R. F. SOLTIS

Detailed Performance of a Centrifugal Pump Impeller in Water

NASA TN-D-4613, June 1968

Shrouded and unshrouded versions of a 7.44-inch-(18.90 cm) diameter, radial-bladed centrifugal impeller were tested in room-temperature water. Detailed measurements permitted calculations of both circumferential and spanwise variations of flow and performance parameters over a wide range of flows. Flow and performance parameters at five stations were measured or calculated. Measured

stations were (1) inlet to impeller, (2) impeller outlet in vaneless space, and (3) volute periphery. Calculated stations were at leading and trailing edges of the impeller blade. The data presented primarily describe performance and flow conditions across the impeller. Results from both the shrouded and unshrouded version of impeller are presented. Average head coefficient and average efficiency as a function of average flow coefficient for shrouded and unshrouded impellers (clearance of 13 percent of blade height) were presented. Data indicated that the redistribution of the streamlines caused by tip clearance flows affected the performance of all spanwise positions. Also, as flow increased, the spanwise gradients of flow parameters did not change. The slip factor varied spanwise from hub to tip for unshrouded impellers with large clearances. The unshrouded impeller had a negative H-Q slope to $\phi = 0.21$, while the shrouded impeller had a negative H-Q slope to $\phi = 0.31$ (attributed to leakage recirculation). Data also indicated that suction performance of the unshrouded impeller was lower than the shrouded impeller.

SOLTIS, R. F. AND M. J. MILLER

Visual Observations of Flow Through a Radial-Bladed Centrifugal Impeller

NASA TN-D-4282, July 1968

A 7.44-inch-(18.90 cm) diameter, radial-bladed centrifugal impeller designed by the stream filament method was operated in water over a range of flow conditions. Flow through the blade passages was visualized by observing movement of nylon tufts glued to the impeller and by injecting dye into the fluid at the pump inlet. Photograph and film sequences of the tufts and dye in the rotating passages are presented. A comparison of the visual observation also was made with the measured performance results and with the flow conditions within the blade passages as calculated from an analytical procedure.

WOOD, G. M., J. S. MURPHY, AND J. FARQUAHR

An Experimental Study of Cavitation in a Mixed-Flow Pump Impeller

ASME Transactions, Journal of Basic Engineering, pp 929-940, December 1960

A mixed-flow impeller design was tested with six, five, and four vanes in a closed water loop to study the effects of cavitation on hydraulic performance, and the results were compared with the work of other investigators. Two idealized flow models for incipient cavitation were derived to illustrate limits of cavitation design. Data showing incidence and speed effects plus the tip static pressure profiles in cavitating and noncavitating flow are also presented.

APPENDIX B

METHOD OF COMPUTING VELOCITY DISTRIBUTIONS ON ARBITRARILY SHAPED BLADES IN INCOMPRESSIBLE FLOW

This appendix presents a method for computing quasi-three-dimensional velocities in a turbomachine with arbitrarily shaped blades. The method is general in that it is useful for either nonrotating or rotating elements. The present computer program applies to incompressible, inviscid axisymmetric, steady flow.

INITIAL PARAMETERS SPECIFIED

This method is used to perform an analysis on an existing or proposed blade design; therefore, geometry and operating conditions must be given. Specifically, the fluid density and the flow and head requirements must be known. The speed of the rotating elements and the number of blades also are required. In addition, hub and tip profiles and the blade shape must be completely defined to obtain the necessary program input. The detail methods used for defining the geometry of the blade and analysis are discussed in the following sections.

DESIGN PROCEDURE

Design of a rotating component by this method normally has been a trial-and-error procedure. Originally, hub and tip contours were set, blade angle profiles along the hub and tip were assumed, then the blade-loading analysis would be conducted. This blade-loading analysis produced design data and determined the suitability of the assumed blade angle profile and the hub and tip contour. This procedure then was repeated until satisfactory results were obtained. Pressure- and suction-side coordinates of the blades were calculated and the drawings of the complete rotating component then could be made.

The blade-angle profiles initially assumed were based on previous experience. With the blade-angle profile given, along the hub, tip, and meanline, the points on these curves at constant values of wrap angle (θ) were determined. Lines (termed traces) were drawn through these points. This process is called trace position determination. With the traces on the meridional view, it was possible to perform a one-dimensional blade-loading analysis by assuming a blade thickness distribution. Experience has shown that once satisfactory results are obtained from the one-dimensional analysis, two-dimensional axisymmetric analyses will show similar satisfactory properties. Therefore, various blade-angle profiles were assumed and the loading checked, using the one-dimensional method. This one-dimensional method was found to be simpler and much less time consuming than the two-dimensional axisymmetric analysis. Once satisfactory loading was obtained from the one-dimensional method, the blade angle and the thickness profiles were sufficiently established for a two-dimensional axisymmetric analysis to be performed.

TRACE POSITION DETERMINATION

Trace position is determined by the following: (1) an established meridional view consisting of hub, tip, and meanline contours; and (2) a blade-angle (β -M) profile (see Nomenclature for M coordinate definition and note that the meanline may be thought of as an assumed streamline). Therefore, the blade angle (β) was known as a function of M coordinate. The radius R, as a function of M coordinate, was obtained by measurement on the meridional view. The M coordinate for any desired wrap angle (θ) was found from the defining relation for the blade angle using the meridional view as reference:

$$\tan \beta = R \frac{d\theta}{dM} \quad (B-1)$$

Practically, this consisted of solving the differential equation

$$d\theta = \frac{\tan \beta \, dM}{R} \quad (B-1a)$$

where R and $\tan \beta$ were known functions of M coordinate, subject to the boundary condition that at $M = 0$, $\theta = 0$. Having found this point for the three contours (hub, tip, and meanline), a smooth curve was drawn through the points at a unique value of θ . Further, observe that when traces were determined using a finalized blade-angle profile and finalized meridional contours for the hub, tip, and meanline, finalized trace positions were the result. This was true regardless of the flexibility of assumed streamlines in the two-dimensional, axisymmetric blade-loading analysis. In brief, trace positions resulted out of purely geometric considerations and were not associated with hydrodynamic phenomenon.

TWO-DIMENSIONAL, AXISYMMETRIC BLADE-LOADING ANALYSIS

This analysis is a trial-and-error process wherein streamline locations on the meridional view were assumed in the analysis. In this process of the analysis, the location of the streamlines to fit the assumptions was calculated. This would be checked against the input location for agreement. Attainment of this agreement yields results of "converged" streamlines. Only results of converged streamlines are usually presented as design data.

In the downstream section of the rotating component, where the fluid angles will differ from the blade angles, a parabolic fluid angle distribution is used to account for this difference (Stanitz & Prian Ref. B-1). The two boundary conditions used to define the parabola uniquely are as follows: (1) the Pfleiderer deviation angle correction applied at the tip to set the fluid angle, and (2) the point of deviation defined by Eq.13 of Ref. B-1. Having located this point, the slope of the fluid angle curve on the $\sin \beta$ - M plot is matched to the blade-angle curve on the same plot. This method defines the fluid angle uniquely.

The differential equation for determining the relative velocity in the meridional plane used in the axisymmetric analysis is given by

$$\begin{aligned} \frac{\partial W_m}{\partial N} - W_m \left[\frac{\partial \beta}{\partial M} \tan \beta \tan \delta - \frac{\partial \beta}{\partial N} \tan \beta - \frac{\cos^2 \beta}{R_c} + \right. \\ \left. \frac{\sin^2 \beta}{R} (\cos \alpha + \tan \delta \sin \alpha) \right] - \left[\frac{\partial W_m}{\partial M} \sin^2 \beta \tan \delta + \right. \\ \left. 2 \omega \sin \beta \cos \beta (\cos \alpha + \tan \delta \sin \alpha) \right] = 0 \end{aligned} \quad (B-2)$$

The geometric blading relationships used to derive Eq.B-2 are shown in Fig.B-1. For simplicity, Eq.B-2 can also be expressed in the form

$$\frac{\partial W_m}{\partial N} + W_m F_1 = F_2 \quad (B-3)$$

where

$$F_1 = - \left[\frac{\partial \beta}{\partial M} \tan \beta \tan \delta - \frac{\partial \beta}{\partial N} \tan \beta - \frac{\cos^2 \beta}{R_c} + \frac{\sin^2 \beta}{R} (\cos \alpha + \tan \delta \sin \alpha) \right]$$

and

$$F_2 = \frac{\partial W_m}{\partial M} \sin^2 \beta \tan \delta + 2 \omega \sin \beta \cos \beta (\cos \alpha + \tan \delta \sin \alpha)$$

The method employed numerically integrated the above equation in steps, each step being across a single streamtube. In effect, a median value for F_1 and F_2 is found for each streamtube along each normal. F_1 and F_2 are then held constant across that streamtube. Noting that at a given point $W_m = C_m$, Eq. B-3 will then be reduced to

$$\frac{d C_m}{N} = F_2 - F_1 C_m$$

or

$$\frac{d C_m}{F_2 - F_1 C_m} = dN \quad (B-4)$$

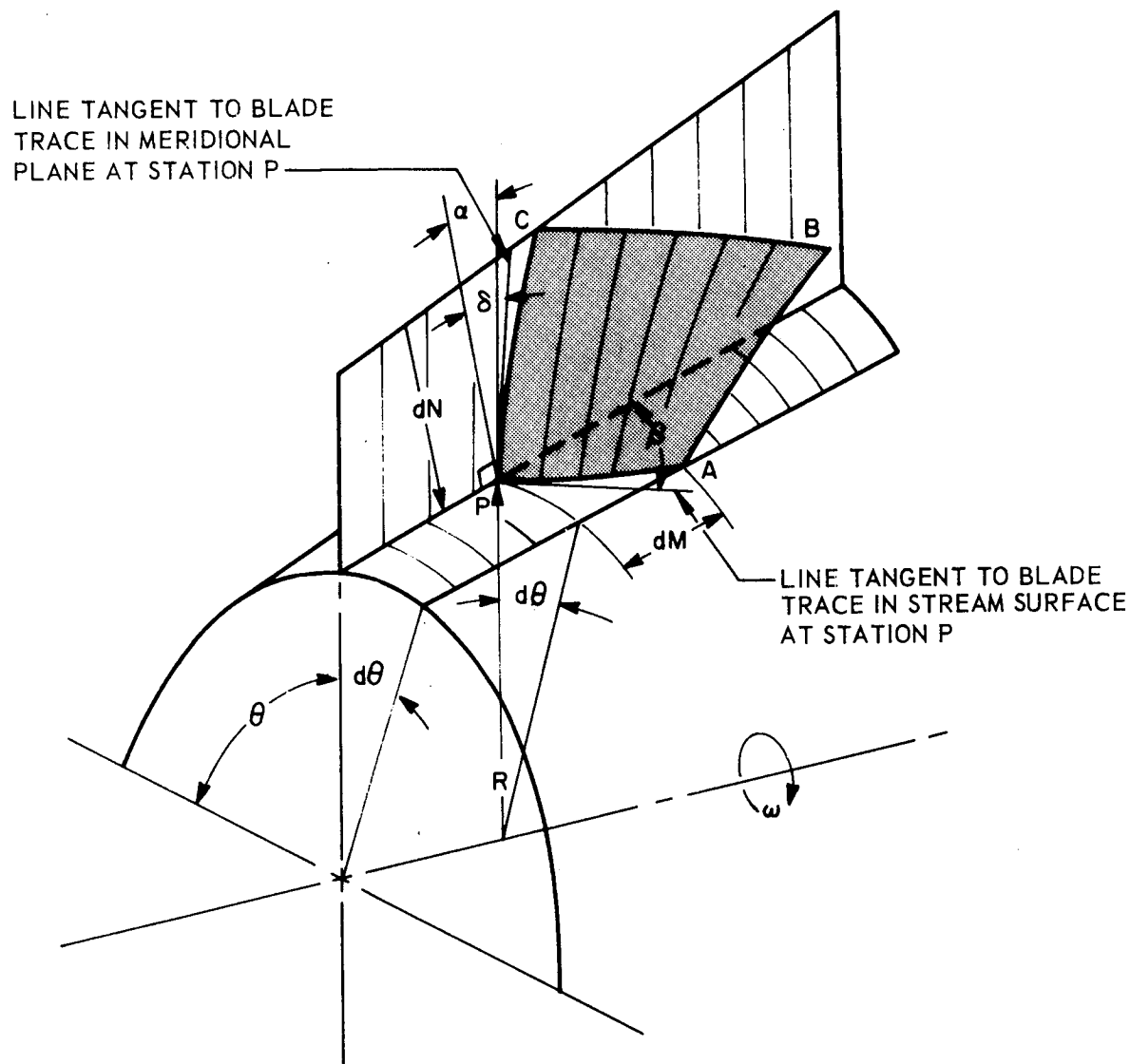


Figure B-1. Blading Geometry

Integrating across a streamtube,

$$\int_{C_{m_0}}^{C_m} \frac{1}{F_2 - F_1 C_m} d C_m = \int_0^{\Delta N} dN$$

or

$$-\frac{1}{F_1} \text{Ln} \left(F_2 - F_1 C_m \right) \Big|_{C_{m_0}}^{C_m} = \Delta N \quad (\text{B-5})$$

where C_m is the meridional velocity at the streamline corresponding to the hub contour of the streamtube, and C_{m_0} is the same parameter but at the streamline corresponding to the tip contour of the streamtube. Equation B-5 reduces to

$$-\frac{1}{F_1} \text{Ln} \left[\frac{F_2 - C_m F_1}{F_2 - C_{m_0} F_1} \right] = \Delta N$$

which, after taking antilogs, becomes

$$\frac{F_2 - C_m F_1}{F_2 - C_{m_0} F_1} = e^{-F_1 \Delta N}$$

which reduces to the expression

$$F_2 - C_m F_1 = \left(F_2 - C_{m_0} F_1 \right) e^{-F_1 \Delta N}$$

and dividing by F_1 one obtains

$$C_m = \frac{F_2}{F_1} + \left(C_{m_0} - \frac{F_2}{F_1} \right) e^{-F_1 \Delta N} \quad (\text{B-6})$$

Every parameter in this equation can be calculated except C_{m_0} . Therefore, the calculation is reiterated until a suitably accurate C_{m_0} is obtained. C_{m_0} is evaluated on the first iteration only, from the continuity condition for each streamtube, and C_{m_0} is assumed constant across the streamtube.

Accordingly,

$$C_{m_0} = \frac{Q'}{(2 \pi R_m - z t_m) \Delta N}$$

The value of C_{m_0} is systematically adjusted by iterative methods until the continuity equation is satisfied at the design flow condition within ± 0.5 percent. Therefore, it can be seen that the method used to evaluate C_{m_0} on the first iteration is of minor importance as long as C_{m_0} on the final iteration yields results that check the continuity condition with sufficient accuracy.

Equivalent results may be obtained by using equations derived along a particular characteristic line as has been done in Ref. B-1. It is also possible (at least theoretically) to solve the differential equations derived along the normal to the streamline in closed form. The method described above has been programmed for solution on an IBM 360 computer.

A relative velocity distribution that satisfies the continuity condition and the Eulerian equations of motion was found only when the streamlines converged to a unique position. Attainment of this convergence in the meridional plane permitted analysis of the flow in the blade-to-blade plane. The underlying logic was that the resulting relative or absolute velocity component found in Eq. B-6 was set equal to the like quantity at the point midway between blades in the blade-to-blade portion of the analysis (i.e., $W = W_{BR}$ or $W_m = W_{BRm}$). To proceed, it was necessary to assume some flow configuration in the blade-to-blade plane. Following Stanitz and Prian (Ref. B-1), it was assumed that the relative velocity distribution (in the blade-to-blade plane) was linear with distance (at constant radius) between the pressure side of the trailing blade and the suction side of the leading blade. The following relations were then applied:

$$W_{BR} = \frac{W_{DR} + W_{TR}}{2} \quad (B-7)$$

or rearranged

$$W_{DR} = 2 W_{BR} - W_{TR} \quad (B-7a)$$

and

$$W_{TR} = \frac{\cos \beta}{2} \left\{ \frac{2 W_{BR}}{\cos \beta} + \frac{d}{dM} \left[(U - W_{BR} \sin \beta) R \theta_{inc} \right] \right\} .$$

It could be seen that these equations were in agreement with Ref. B-1 observing that the driving and trailing surface blade angles (at constant radius) were considered equal.

DERIVATION OF EQUATIONS

Consider the flow in a plane normal to the axis of symmetry (Fig. B-2):

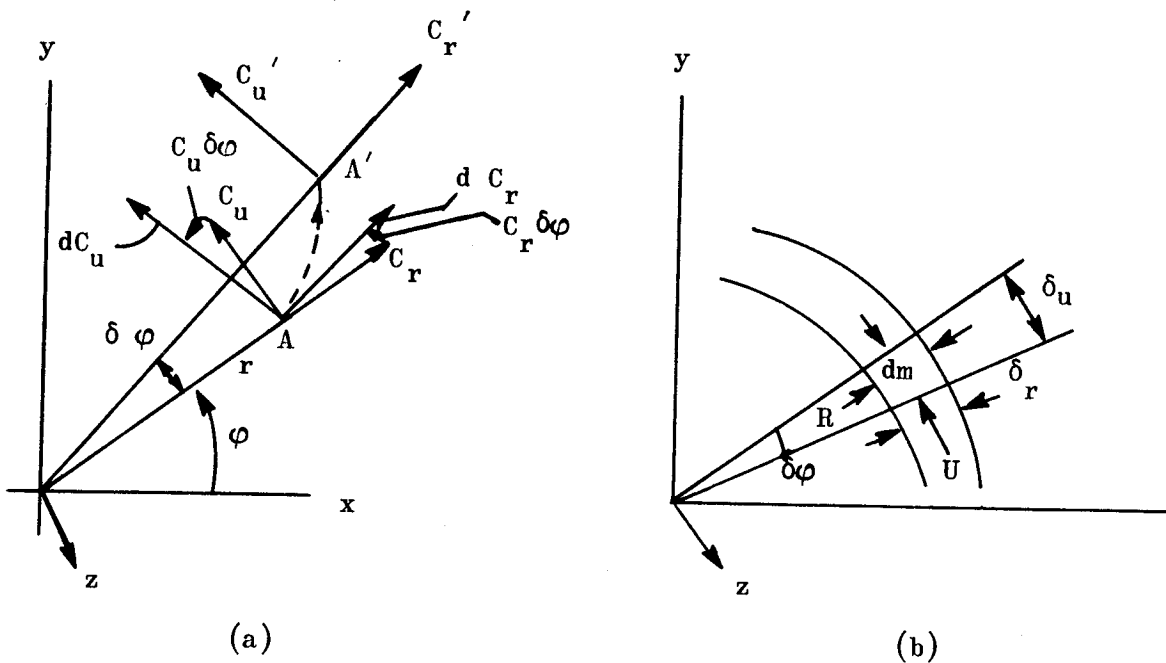


Figure B-2

where on Fig. B-2a

C_r, C_u, C_z are the velocity components at A and

C_r', C_u', C_z' are the velocity at A', a time δt later.

(A' is also shown superimposed on A)

On Fig. B-2b, the elemental volume is

$\delta_v = \delta_r \cdot \delta_u \cdot \delta_z$ and ρ is the mass per unit volume.

From Fig. B-2b the accelerating forces (forces per unit mass acting: R.U.Z.) are

$-\delta_u \delta_z \frac{\partial p_r}{\partial r} \delta r + \rho R \delta V$ in the direction of R,

$-\delta_r \delta_z \frac{\partial p_u}{\partial \phi} \delta \phi + \rho U \delta V$ in the direction of U, and

$-\delta_r \delta_u \frac{\partial p_z}{\partial z} \delta z + \rho Z \delta V$ in the direction of Z.

From Fig. B-2a (for steady flow) the accelerations are

$\frac{dC_r}{dt} - C \frac{d\phi}{dt}$ in the radial direction,

$\frac{dC_u}{dt} + C_r \frac{d\phi}{dt}$ in the tangential direction, and

$\frac{dC_z}{dt}$ in the axial direction.

Noting the angular velocity is

$$\frac{d\phi}{dt} = \frac{C_u}{r}$$

we have

$$A_{\text{radial}} = \frac{dC_r}{dt} - \frac{C_u^2}{r} ,$$

$$A_{\text{tangential}} = \frac{dC_u}{dt} + \frac{C_r C_u}{r} , \text{ and}$$

$$A_{\text{axial}} = \frac{dC_z}{dt} .$$

Now we can relate the accelerating forces to the accelerations by Newton's second law, yielding

$$\frac{dC_r}{dt} - \frac{C_u^2}{r} = -\frac{1}{\rho} \frac{\partial p_r}{\partial r} + R$$

$$\frac{dC_u}{dt} - \frac{C_r C_u}{r} = -\frac{1}{\rho} \frac{\partial p_u}{\partial \phi} + U$$

$$\frac{dC_z}{dt} = -\frac{1}{\rho} \frac{\partial p_z}{\partial z} + Z .$$

In the limit as $\delta t \rightarrow 0$, $p_r = p_u = p_z = p$, and for axially symmetric flow $\partial p_u / \partial \phi = 0$.

For relative motion in a rotor $C_u = u + W_u$, $C_r = W_r$, and $C_z = W_z$.

The above equations, therefore, can be put in terms of relative velocity components.

$$C_u^2 = u^2 + 2u W_u + W_u^2 .$$

Therefore,

$$R = \frac{1}{\rho} \frac{\partial p}{\partial r} + \frac{dW_r}{dt} - \frac{W_u^2}{r} - \omega^2 r - 2\omega W_u$$

and

$$\frac{dC_u}{dt} = \frac{du}{dt} + \frac{dW_u}{dt} = \omega W_r + \frac{dW_u}{dt}$$

So

$$U = \frac{dW_u}{dt} + \omega W_r + \frac{W_r}{r} (u + W_u) = \frac{dW_u}{dt} + 2\omega W_r + \frac{W_r W_u}{r}$$

and

$$Z = \frac{1}{\rho} \frac{\partial p}{\partial z} + \frac{dW_z}{dt}$$

or grouped;

$$R = \frac{1}{\rho} \frac{\partial p}{\partial r} + \frac{dW_r}{dt} - \frac{W_u^2}{r} = \omega^2 r - 2\omega W_u$$

$$U = \frac{dW_u}{dt} + \omega W_r + \frac{W_r}{r} (u + W_u)$$

$$Z = \frac{1}{\rho} \frac{\partial p}{\partial z} + \frac{dW_z}{dt} \quad (B-7b)$$

We now examine the relationship between angles for arbitrarily shaped blades.

NOTE: In this blading geometry section only, the angle ϕ is essentially defined negative with respect to ϕ in the rest of the deviation.

The dextral set of mutually perpendicular unit vectors along the major axes of the turbomachine component is as follows (see Fig. B-3):

\bar{i}_1 in the tangential direction

\bar{i}_2 in the axial direction

\bar{i}_3 in the radial direction.

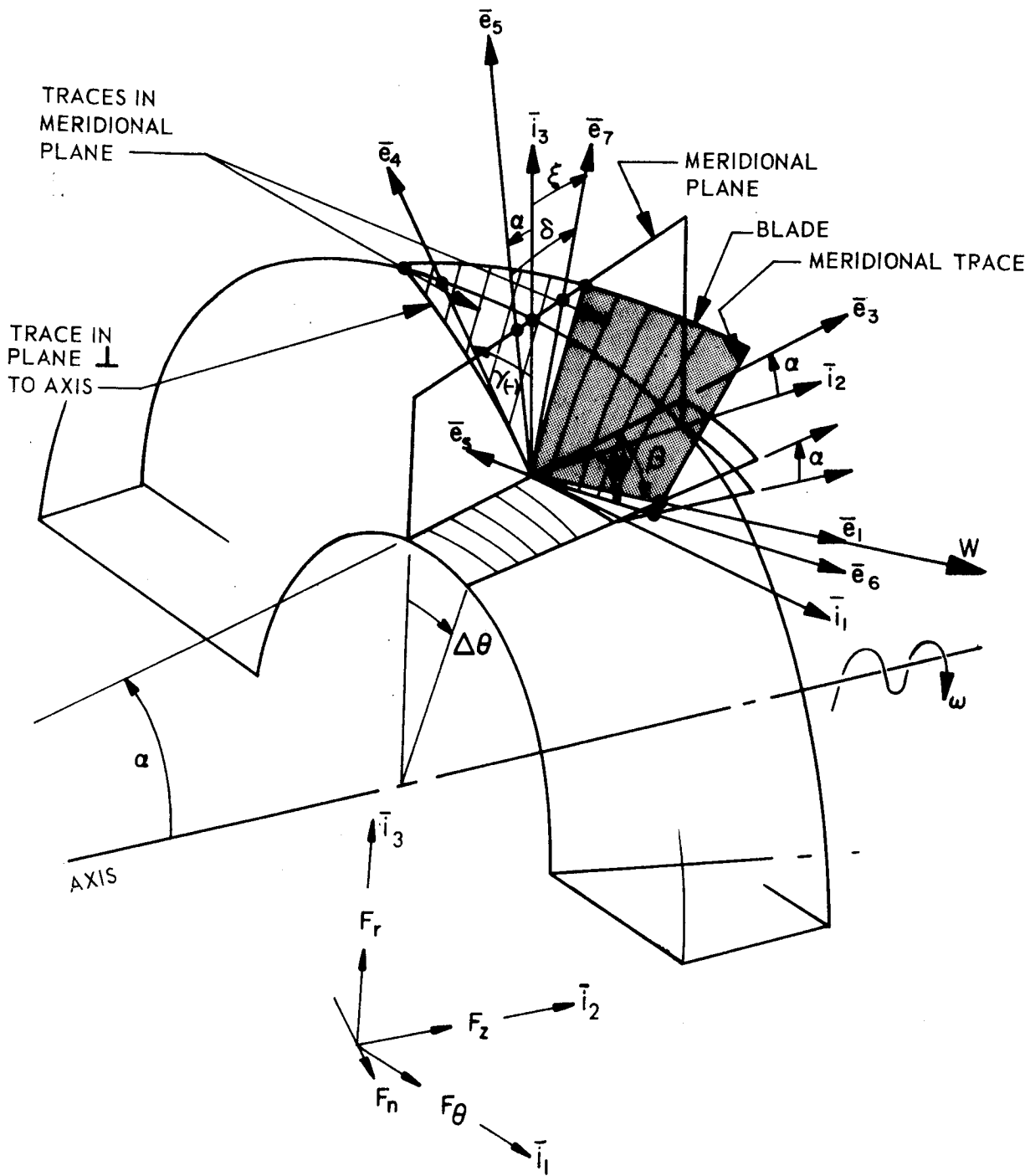


Figure B-3. General Blade Geometry in Unit Vector Notation

Unit vectors \bar{e}_3 through \bar{e}_6 are defined as follows:

\bar{e}_3 is in the direction of the intersection of the stream surface and the meridional plane.

$$\bar{e}_3 = \cos \alpha \bar{i}_2 + \sin \alpha \bar{i}_3 \text{ where } \alpha \text{ is the angle between the stream surface and the axis of rotation.}$$

\bar{e}_4 is in the direction of the intersection of the blade surface and a plane perpendicular to the axis of rotation.

$$\bar{e}_4 = \cos \gamma \bar{i}_3 - \sin \gamma \bar{i}_1 \text{ where } \gamma \text{ is the angle between a blade vector and the radial direction.}$$

\bar{e}_5 is in the direction of the intersection of the normal to the stream surface and the meridional plane.

$$\bar{e}_5 = \cos \alpha \bar{i}_3 - \sin \alpha \bar{i}_2 .$$

\bar{e}_6 is in the direction of the intersection of the blade surface and a plane in the direction of rotation.

$$\bar{e}_6 = \cos \phi \bar{i}_2 + \sin \phi \bar{i}_1 \text{ where } \phi \text{ is the angle between a blade vector and the axial direction.}$$

The vector normal to the blade surface is

$$\bar{e}_s = \bar{e}_6 \times \bar{e}_4 .$$

The vector in the direction of intersection of the blade and stream surface is \bar{e}_1 where

$$\begin{aligned} \bar{e}_1 &= \bar{e}_5 \times \bar{e}_s \\ &= \bar{e}_5 \times (\bar{e}_6 \times \bar{e}_4) = (\bar{e}_5 \cdot \bar{e}_4) \bar{e}_6 - (\bar{e}_5 \cdot \bar{e}_6) \bar{e}_4 \end{aligned}$$

by vector algebra.

Therefore,

$$\begin{aligned}\bar{e}_1 &= (\cos \alpha \cos \gamma) \bar{e}_6 - (-\sin \alpha \cos \phi) \bar{e}_4 \\ &= \bar{i}_1 (\sin \phi \cos \alpha \cos \gamma - \sin \gamma \sin \alpha \cos \phi) + \\ &\quad \bar{i}_2 (\cos \phi \cos \alpha \cos \gamma) + \bar{i}_3 (\cos \gamma \sin \alpha \cos \phi).\end{aligned}$$

The blade angle may be expressed in terms of these unit vectors as follows:

$$\tan \beta = \frac{\sin \beta}{\cos \beta} = \frac{\cos (90^\circ - \beta)}{\cos \beta} = \frac{\bar{e}_1 \cdot \bar{i}_1}{\bar{e}_1 \cdot \bar{e}_3}$$

We then obtain the relation between the angles β , ϕ , α and γ by substitution where

$$\begin{aligned}\tan \beta &= \frac{\sin \phi \cos \alpha \cos \gamma - \sin \gamma \cos \phi \sin \alpha}{\cos \phi \cos^2 \alpha \cos \gamma + \sin^2 \alpha \cos \gamma \cos \phi} \\ \tan \beta &= \frac{\sin \phi \cos \alpha \cos \gamma - \sin \gamma \sin \alpha \cos \phi}{\cos \phi \cos \gamma}\end{aligned}$$

$$\tan \beta = \tan \phi \cos \alpha - \tan \gamma \sin \alpha \quad . \quad (B-7c)$$

The force components can be related through these same angles. Since the force is in the direction of the blade normal \bar{e}_s , the force components along the major turbomachine axes are

$$F_\theta = F_s (\bar{e}_s \cdot \bar{i}_1)$$

$$F_r = F_s (\bar{e}_s \cdot \bar{i}_3)$$

$$F_z = F_s (\bar{e}_s \cdot \bar{i}_2)$$

where

$$\bar{e}_s = \bar{e}_6 \times \bar{e}_4 \text{ as before.}$$

Therefore,

$$\begin{aligned}\bar{e}_s &= \bar{e}_6 \times \bar{e}_4 = (\cos \phi \bar{i}_2 + \sin \phi \bar{i}_1) \times (\cos \gamma \bar{i}_3 - \sin \gamma \bar{i}_1) \\ &= (\cos \phi \cos \gamma) \bar{i}_1 - (\sin \phi \cos \gamma) \bar{i}_2 - (\cos \phi \sin \gamma) \bar{i}_3.\end{aligned}$$

So

$$F_\theta = F_s \cos \phi \cos \gamma$$

$$F_r = F_s \cos \phi \sin \gamma$$

$$F_z = -F_s \sin \phi \cos \gamma$$

yielding

$$F_\theta/F_r = \frac{1}{\tan \gamma}, \quad F_\theta/F_z = \frac{-1}{\tan \phi}.$$

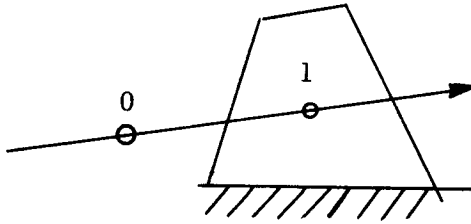
The force normal to the stream surface is F_n where

$$F_n = F_r (\bar{i}_3 \cdot \bar{e}_5) + F_z (\bar{i}_2 \cdot \bar{e}_5).$$

Then in terms of the tangential force component (F_θ)

$$F_n = F_\theta \tan \gamma \cos \alpha + F_\theta \tan \phi \sin \alpha. \quad (\text{B-8})$$

We now derive necessary relationships from the energy equation.



Relating the energy of particles at positions 0 and 1: The energy added = total energy - initial energy

$$\left(\frac{U C_u}{g}\right)_1 - \left(\frac{U C_u}{g}\right)_0 = \left(h_1 + \frac{C_u^2 + C_m^2}{2g}\right) - H_i$$

where

h_1 is static enthalpy

H_i is absolute total enthalpy.

Note that

$$\left(\frac{U C_u}{g}\right)_0 = 0$$

$$\frac{1}{g} \left[\omega r_1 (\omega r_1 + W_{u_1}) \right] = h_1 + \frac{1}{2g} \left[(\omega r_1 + W_{u_1})^2 + C_{m_1}^2 \right] - H_i$$

$$\frac{1}{g} (\omega^2 r_1^2 + \omega r_1 W_{u_1}) = h_1 + \frac{1}{2g} (\omega^2 r_1^2 + 2W_{u_1} \omega r_1 + W_{u_1}^2 + C_{m_1}^2) - H_i$$

$$h_1 - \frac{\omega^2 r_1^2}{2g} + \frac{W_{u_1}^2}{2g} + \frac{C_{m_1}^2}{2g} = H_i$$

now

$$W^2 = W_u^2 + C_m^2$$

So

$$h_1 - \frac{1}{2g} \left[(\omega r_1)^2 - W^2 \right] = H_i$$

which is the same for each streamline, and taking the differential

$$dh_1 = \frac{1}{g} \left[\omega^2 r_1 dr_1 - W dW \right].$$

For an isentropic process

$$dh_1 = \frac{1}{\rho_1 g} dp_1$$

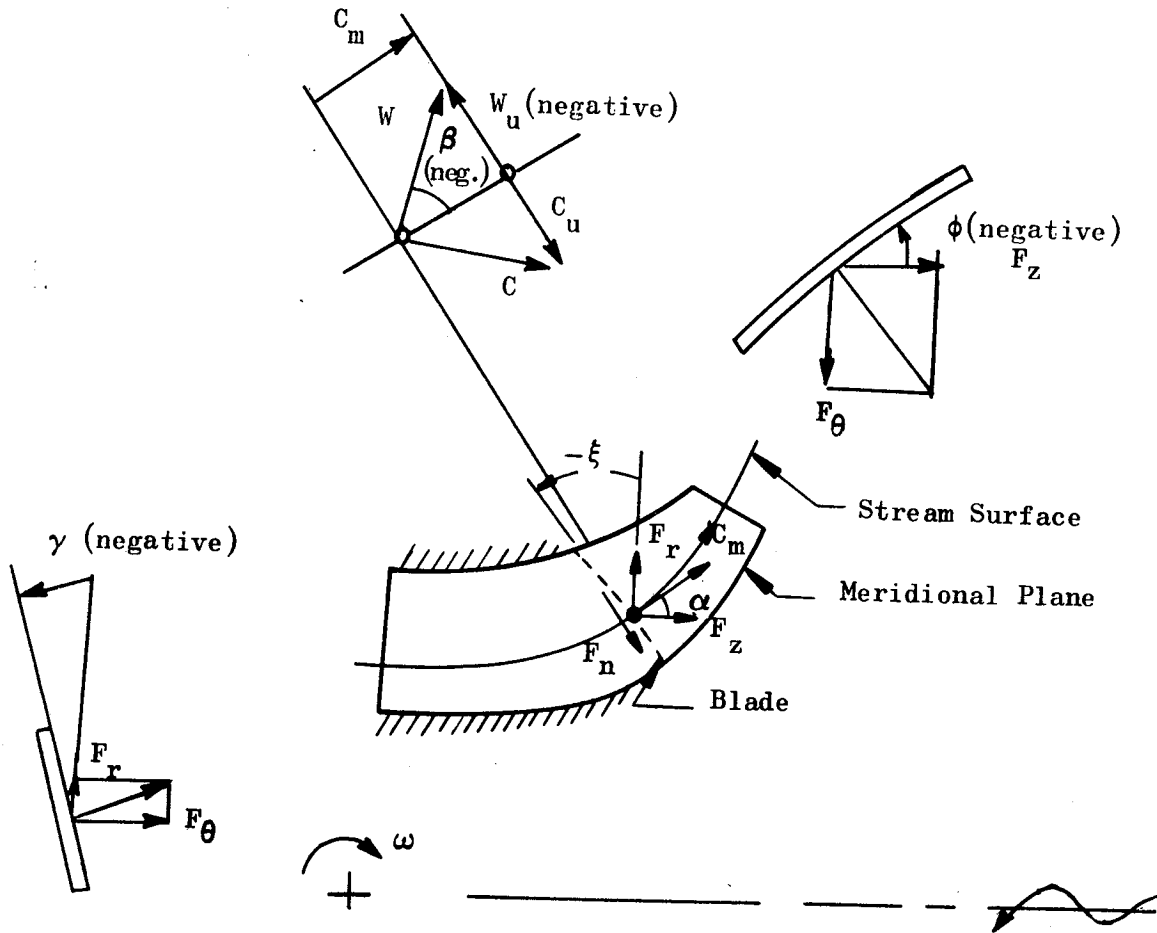
and equating we have

$$\frac{1}{\rho} dp - (\omega^2 r dr - W dW) = 0$$

and the derivative with respect to n is

$$\frac{1}{\rho} \frac{dp}{dn} = \omega^2 r \frac{dr}{dn} - W \frac{dW}{dn}.$$

The geometry of the passage is as follows:



From which,

$$F_n = F_z \sin \alpha - F_r \cos \alpha$$

Now substituting for F_z and F_r from Eq. B-7b and

$$F_n = \left(\frac{1}{\rho} \frac{\partial p}{\partial z} + \frac{dW_z}{dt} \right) \sin \alpha - \left(\frac{1}{\rho} \frac{\partial p}{\partial r} + \frac{dW_r}{dt} - \frac{W_u^2}{r} - \omega^2 r - 2 \omega W_u \right) \cos \alpha$$

or

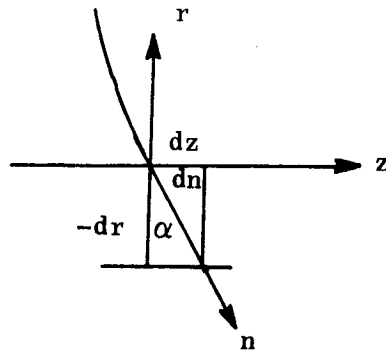
$$F_n = \frac{1}{\rho} \left(\frac{\partial p}{\partial z} \sin \alpha - \frac{\partial p}{\partial r} \cos \alpha \right) + \frac{dW_z}{dt} \sin \alpha - \frac{dW_r}{dt} \cos \alpha + \frac{W_u^2}{r} \cos \alpha + \omega^2 r \cos \alpha + 2\omega W_u \cos \alpha$$

now taking the total differential

$$\frac{dp}{dn} = \frac{\partial p}{\partial z} \frac{dz}{dn} + \frac{\partial p}{\partial r} \frac{dr}{dn}$$

where

$$\frac{dz}{dn} = \sin \alpha \text{ and } \frac{dr}{dn} = -\cos \alpha \text{ as shown below.}$$



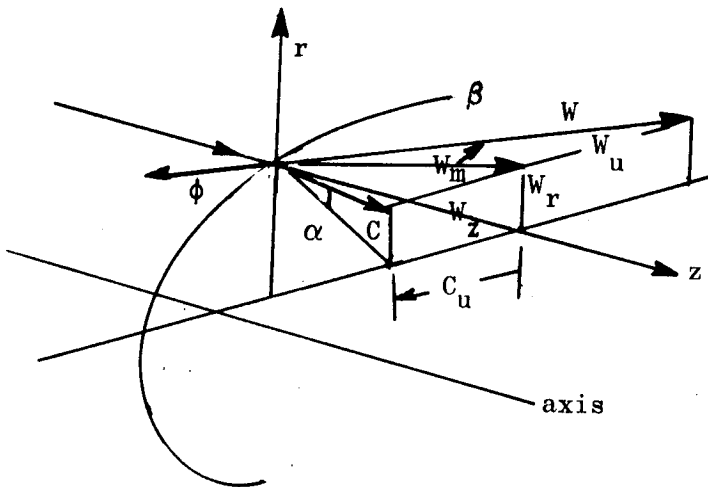
Therefore,

$$\frac{dp}{dn} = \frac{\partial p}{\partial z} \sin \alpha - \frac{\partial p}{\partial r} \cos \alpha$$

so substitution yields

$$F_n = \frac{1}{\rho} \frac{dp}{dn} + \frac{dW_z}{dt} \sin \alpha - \frac{dW_r}{dt} \cos \alpha + \frac{W_u^2}{r} \cos \alpha + \omega^2 r \cos \alpha + 2\omega W_u \cos \alpha.$$

Now putting this in terms of W_m ,



We note

$$W_z = W_m \cos \alpha$$

$$W_r = W_m \sin \alpha$$

$$W_u = W_m \tan \beta$$

and

$$\frac{dW_z}{dt} = -W_m \sin \alpha \frac{d\alpha}{dt} + \cos \alpha \frac{dW_m}{dt},$$

also

$$\frac{dW_r}{dt} = W_m \cos \alpha \frac{d\alpha}{dt} + \sin \alpha \frac{dW_m}{dt}$$

So Substituting into above equation for F_n yields

$$F_n = \frac{1}{\rho} \frac{dp}{dn} - W_m \sin^2 \alpha \frac{d\alpha}{dt} + \sin \alpha \cos \alpha \frac{dW_m}{dt} - W_m \cos^2 \alpha \frac{d\alpha}{dt} - \sin \alpha \cos \alpha \frac{dW_m}{dt} + \frac{W_u^2}{r} \cos \alpha + \omega^2 r \cos \alpha + 2 \omega W_u \cos \alpha$$

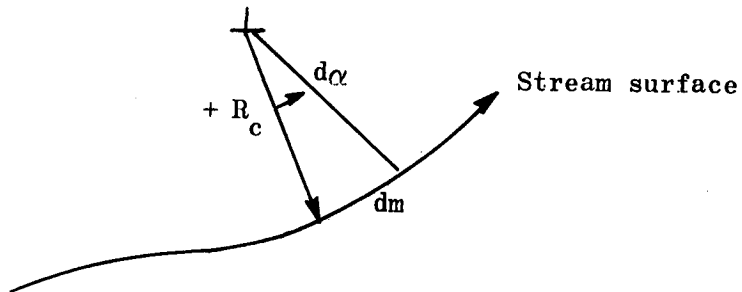
which reduced by

$$F_n = \frac{1}{\rho} \frac{dp}{dn} - W_m \frac{d\alpha}{dt} + \frac{(\omega_r + W_u)^2}{r} \cos \alpha.$$

We see that in this expression

$$\frac{d\alpha}{dt} = \frac{d\alpha}{dm} \frac{dm}{dt} = \frac{C_m}{R_c} = \frac{W_m}{R_c}$$

where R_c is the radius of curvature defined as positive when:



also from the energy equation

$$\frac{1}{\rho} \frac{dp}{dn} = \omega^2 r \frac{dr}{dn} - W \frac{dW}{dn}$$

and

$$\begin{aligned} \frac{1}{\rho} \frac{dp}{dn} &= -\omega^2 r \cos \alpha - \frac{W_m}{\cos \beta} \frac{d(W_m / \cos \beta)}{dn} \\ &= -\omega^2 r \cos \alpha - \frac{W_m}{\cos \beta} \frac{\cos \beta \frac{\partial W_m}{\partial n} - W_m \frac{\partial \cos \beta}{\partial n}}{\cos^2 \beta} \end{aligned}$$

so

$$\frac{1}{\rho} \frac{dp}{dn} = -\omega^2 r \cos \alpha - \frac{W_m}{\cos^2 \beta} \frac{\partial W_m}{\partial n} + \frac{W_m^2}{\cos^3 \beta} \frac{\partial \cos \beta}{\partial n}$$

Substituting this expression for $\frac{1}{\rho} \frac{dp}{dn}$ and the expression for $\frac{d\alpha}{dt}$ into the equation for F_n yields

$$F_n = -\omega^2 r \cos \alpha \left(-\frac{W_m}{\cos^2 \beta} \right) \frac{\partial W_m}{\partial n} + \frac{W_m^2}{\cos^3 \beta} \frac{\partial \cos \beta}{\partial n} - \frac{W_m^2}{R_c} + \frac{(\omega r + W_u)^2}{r} \cos \alpha \quad (B-9)$$

which is one expression for F_n in terms of W_m . We now seek another.

From Eq. B-7b we saw that

$$F_u = \frac{dW_u}{dt} + \omega W_r + \frac{W_r}{r} (u + W_u)$$

We again use

$$W_r = W_m \sin \alpha$$

$$W_u = W_m \tan \beta$$

We evaluate $\frac{dW_u}{dt}$ by writing the total derivative

$$\frac{dW_u}{dt} = \frac{\partial W_u}{\partial m} \frac{dm}{dt} + \frac{\partial W_u}{\partial n} \frac{dn}{dt}$$

But since n is the coordinate normal to a streamline

$$W_n = \frac{dn}{dt} = 0 \text{ and } \frac{dW_u}{dt} = \frac{\partial W_u}{\partial m} \frac{dm}{dt} = \frac{\partial W_u}{\partial m} W_m$$

Substituting for W_u we have

$$\frac{\partial W_u}{\partial t} = \left(W_m \frac{\partial \tan \beta}{\partial m} + \tan \beta \frac{\partial W_m}{\partial m} \right) W_m$$

so entering in the expression for F_u

$$F_u = W_m^2 \frac{\partial \tan \beta}{\partial m} + W_m \tan \beta \frac{\partial W_m}{\partial m} + \omega W_m \sin \alpha + \frac{W_m \sin \alpha}{r} (u + W_m \tan \beta)$$

or collecting terms we have

$$F_u = W_m \left[\frac{W_m}{r} \sin \alpha \tan \beta + \tan \beta \frac{\partial W_m}{\partial m} + 2 \omega \sin \alpha + W_m \frac{\partial \tan \beta}{\partial m} \right]$$

From Eq. B-8,

$$F_n = F_u \tan \gamma \cos \alpha - F_u \tan \phi \sin \alpha$$

NOTE: ϕ is defined with the opposite sign in the derivation here relative to that used in deriving Eq. B-8, which explains the difference in sign above. Here F_ϕ was replaced by F_u .

So by Eq. B-7 with signs on $\tan \beta$ and $\tan \phi$ changed,

$$\tan \phi = \frac{\tan \beta - \tan \gamma \sin \alpha}{\cos \alpha}$$

Substituting this expression into Eq. B-8,

$$\begin{aligned} F_n &= - F_u \tan \alpha (\tan \beta - \sin \alpha \tan \gamma) + F_u \tan \gamma \cos \alpha \\ &= F_u \left(- \tan \alpha \tan \beta + \frac{\sin^2 \alpha}{\cos \alpha} \tan \gamma + \tan \gamma \cos \alpha \right) \\ &= F_u \left(- \tan \alpha \tan \beta + \frac{\tan \gamma}{\cos \alpha} (\sin^2 \alpha + \cos^2 \alpha) \right) \end{aligned}$$

or

$$F_n = F_u \left(\frac{\tan \gamma}{\cos \alpha} - \tan \alpha \tan \beta \right)$$

which may be combined with the expression for F_u above, yielding

$$\begin{aligned} F_n &= \frac{W_m}{\cos \alpha} (\tan \gamma - \sin \alpha \tan \beta) \left[\frac{W_m}{r} \sin \alpha \tan \beta + W_m \frac{\partial \tan \beta}{\partial m} + \right. \\ &\quad \left. \tan \beta \frac{\partial W_m}{\partial m} + 2 \omega \sin \alpha \right] \end{aligned} \quad (B-10)$$

We now have two expressions for F_n , Eq. B-9 and B-10, which we equate as follows:

$$\begin{aligned}
 & -\omega^2 r \cos \alpha - \frac{W_m}{\cos^2 \beta} \frac{\partial W_m}{\partial n} + \frac{W_m^2}{\cos^3 \beta} \frac{\partial \cos \beta}{\partial n} - \frac{W_m^2}{R_c} + \frac{(\omega r + W_m \tan \beta)^2}{r} \cos \alpha \\
 & = W_m (\tan \gamma - \sin \alpha \tan \beta) \left[\frac{W_m}{r} \tan \alpha \tan \beta + \frac{W_m}{\cos \alpha} \frac{\partial \tan \beta}{\partial m} + \right. \\
 & \quad \left. \frac{\tan \beta}{\cos \alpha} \frac{\partial W_m}{\partial m} + 2 \omega \tan \alpha \right]
 \end{aligned}$$

Now expanding,

$$\begin{aligned}
 & -\omega^2 r \cos \alpha - \frac{W_m}{\cos^2 \beta} \frac{\partial W_m}{\partial n} + W_m^2 \left\{ \frac{1}{\cos^3 \beta} \frac{\partial \cos \beta}{\partial n} - \frac{1}{R_c} + \frac{\tan^2 \beta \cos \alpha}{r} - \right. \\
 & \quad \left. (\tan \gamma - \sin \alpha \tan \beta) \left(\frac{\tan \alpha \tan \beta}{r} + \frac{1}{\cos^2 \beta} \frac{\partial \beta}{\cos \alpha \partial m} \right) \right\} + \omega^2 r \cos \alpha + \\
 & \quad 2 \omega W_m \tan \beta \cos \alpha = (\tan \gamma - \sin \alpha \tan \beta) W_m \left(\frac{\tan \beta}{\cos \alpha} \frac{\partial W_m}{\partial m} + 2 \omega \tan \alpha \right)
 \end{aligned}$$

and multiplying by $\frac{-\cos^2 \beta}{W_m}$ to obtain a unit coefficient for the first term

$$\begin{aligned}
 & \frac{\partial W_m}{\partial n} - W_m \left\{ \frac{-\sin \beta}{\cos \beta} \frac{\partial \beta}{\partial n} - \frac{\cos^2 \beta}{R_c} + \frac{\sin^2 \beta \cos \alpha}{r} - (\tan \gamma - \sin \alpha \tan \beta) \right. \\
 & \quad \left. \left(\frac{\tan \alpha \sin \beta \cos \beta}{r} + \frac{1}{\cos \alpha} \frac{\partial \beta}{\partial m} \right) \right\} - 2 \omega \sin \beta \cos \beta \cos \alpha \\
 & = -(\tan \gamma - \sin \alpha \tan \beta) \left(\frac{\sin \beta \cos \beta}{\cos \alpha} \frac{\partial W_m}{\partial m} + 2 \omega \cos^2 \beta \tan \alpha \right)
 \end{aligned}$$

Gathering terms in the coefficient of W_m we have

$$-\frac{\tan \gamma \tan \alpha \sin \beta \cos \beta}{r} - \frac{\tan \gamma \partial \beta}{\cos \alpha \partial m} + \frac{\sin \alpha \tan \alpha \sin \beta \cos \beta}{r} +$$

$$\frac{\sin \alpha \tan \beta \partial \beta}{\cos \alpha \partial m} - \tan \beta \frac{\partial \beta}{\partial n} - \frac{\cos^2 \beta}{R_c} + \frac{\sin^2 \beta \cos \alpha}{r}$$

Note that the third and last term reduce as follows:

$$\frac{\sin^2 \alpha \sin^2 \beta}{\cos \alpha r} + \frac{\cos \alpha \sin^2 \beta}{r} = \frac{\sin^2 \beta}{r \cos \alpha}$$

and regrouping, the coefficient is

$$\left\{ \frac{\partial \beta}{\partial m} \left(\tan \alpha \tan \beta - \frac{\tan \gamma}{\cos \alpha} \right) - \tan \beta \frac{\partial \beta}{\partial n} - \frac{\cos^2 \beta}{R_c} + \frac{\sin^2 \beta}{r \cos \alpha} \left(1 - \frac{\tan \gamma \sin \alpha}{\tan \beta} \right) \right\}$$

and gathering terms not coefficient to W_m or $\frac{\partial W_m}{\partial m}$, we have

$$- 2 \omega \sin \beta \cos \beta \cos \alpha + \tan \gamma \cos^2 \beta \left(\frac{\tan \beta}{\cos \alpha} \frac{\partial W_m}{\partial m} + 2 \omega \tan \alpha \right) -$$

$$\tan \alpha \sin^2 \beta \frac{\partial W_m}{\partial m} - 2 \omega \sin \beta \cos \beta \frac{\sin^2 \alpha}{\cos \alpha}$$

or

$$\tan \gamma \cos^2 \beta \left(\frac{\tan \beta}{\cos \alpha} \frac{\partial W_m}{\partial m} + 2 \omega \tan \alpha \right) - \tan \alpha \sin^2 \beta \frac{\partial W_m}{\partial m} -$$

$$\frac{2 \omega \sin \beta \cos \beta}{\cos \alpha} (\sin^2 \alpha + \cos^2 \alpha)$$

Rearranging and eliminating the trigonometric identity we have

$$\frac{\partial W_m}{\partial m} \left(\frac{\tan \gamma \sin \beta \cos \beta}{\cos \alpha} - \tan \alpha \sin^2 \beta \right) - \frac{2 \omega \sin \beta \cos \beta}{\cos \alpha} + 2 \omega \tan \alpha \tan \gamma \cos^2 \beta$$

or

$$\frac{\partial W_m}{\partial m} \sin^2 \beta \tan \alpha \left(\frac{\tan \gamma}{\tan \beta \sin \alpha} - 1 \right) + 2 \omega \sin^2 \beta \tan \alpha \left(\frac{\tan \gamma}{\tan^2 \beta} - \frac{1}{\sin \alpha \tan \beta} \right)$$

Now putting all terms together, the equation is

$$\begin{aligned} \frac{\partial W_m}{\partial n} - W_m \left\{ \frac{\partial \beta}{\partial m} \left(\tan \alpha \tan \beta - \frac{\tan \gamma}{\cos \alpha} \right) - \tan \beta \frac{\partial \beta}{\partial n} - \frac{\cos^2 \beta}{R_c} + \frac{\sin^2 \beta}{r \cos \alpha} \right. \\ \left. \left(1 - \frac{\tan \gamma \sin \alpha}{\tan \beta} \right) \right\} + \left\{ \frac{\partial W_m}{\partial m} \sin^2 \beta \tan \alpha \left(\frac{\tan \gamma}{\tan \beta \sin \alpha} - 1 \right) + \right. \\ \left. 2 \omega \sin^2 \beta \tan \alpha \left(\frac{\tan \gamma}{\tan^2 \beta} - \frac{1}{\sin \alpha \tan \beta} \right) \right\} = 0 \end{aligned}$$

to compare with Eq. B-2

$$\tan \delta = \tan \alpha \left(1 - \frac{\tan \gamma}{\sin \alpha \tan \beta} \right)$$

Suction surface, midpoint and pressure surface relative velocities are plotted for the tip, meanline, and hub in Fig. B-4, B-5, and B-6, respectively.

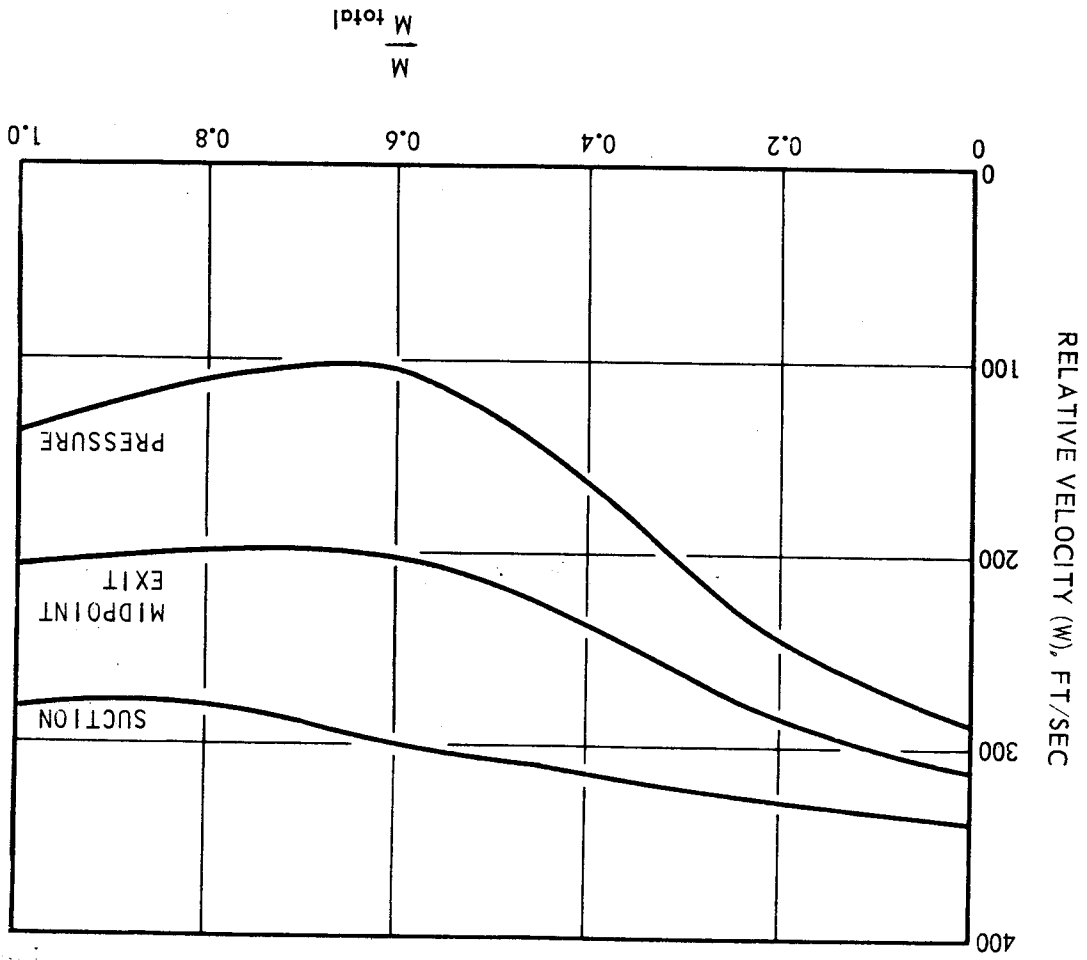


Figure B-4. Typical Relative Velocity Profile at Tip

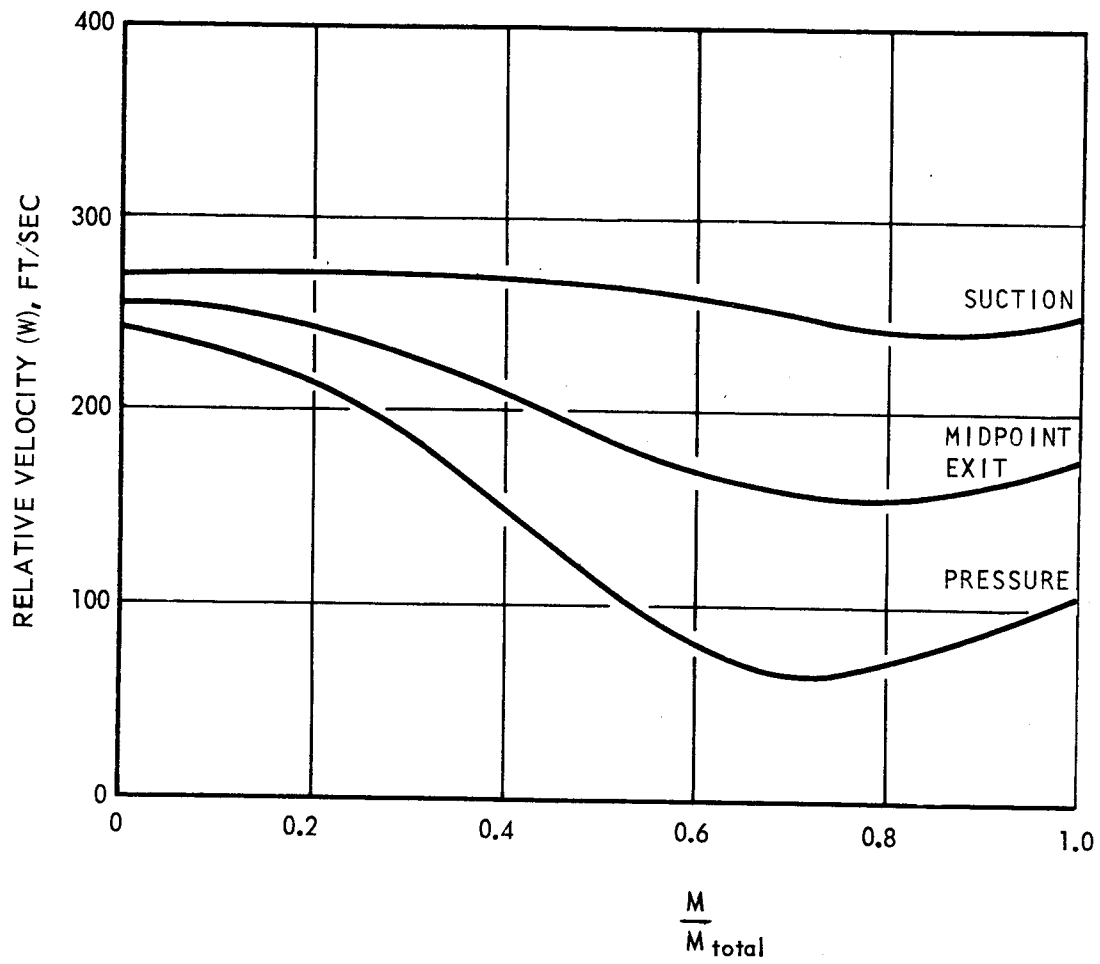


Figure B-5. Typical Relative Velocity Profile at Meanline

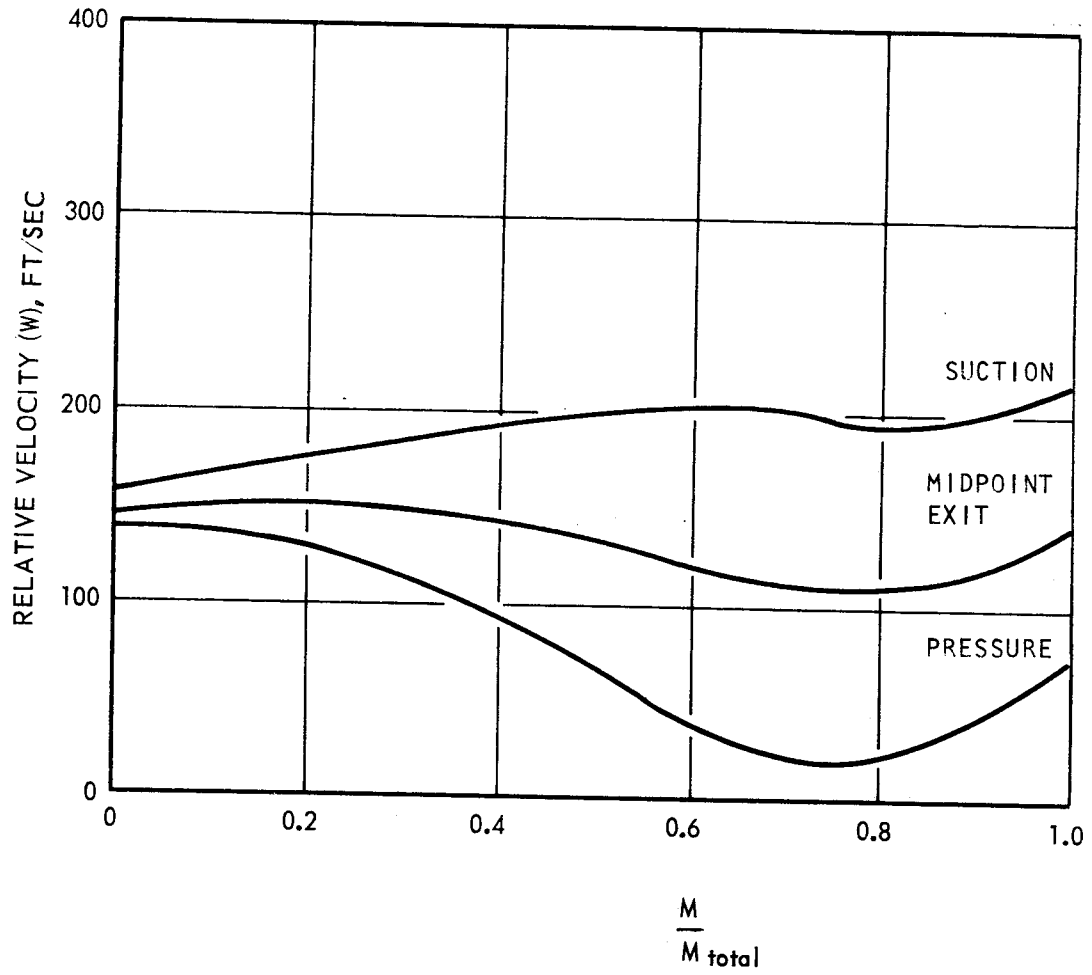


Figure B-6. Typical Relative Velocity Profile at Hub

```

C      ** VELOCITY DISTRIBUTION PROGRAM **                                00000000
C      DIMENSION G1(25),G2(25),R(25,25),Z(25,25),BETA(25,25),CHI(25,25),A00000010
C      1LFA(25,25), TRI(30),CV2(25,25),CM(25,25),DELN(25,25),DELM(25,25) ,00000020
C      2CMP(25,25),F1(25,25),F2(25,25),DCMDM(25,25),DBDM(25,25),DELNN(25,200000030
C      35),ALFBR(25,25),DBDN(25,25),DCMP(25,25),T(25,25),BBR(25,25),BBBR(200000040
C      45,25),RBR(25,25),WBR(25,25),WTR(25,25),WDR(25,25),DELP(25,25),BETB00000050
C      5(25,25),FDDP(25,25),HDMOM(25,25),UCU(25,25),B(25),TN(25),AREA(25) 00000060
C      6, CV2C(25,25)                                                    00000070
C                                                                           00000080
C      I      - INDEX OF STREAMLINES, I=1 AT TIP ,I=N AT HUB              00000090
C      J      - INDEX OF NORMALS, J=1 AT ENTRANCE, J=M AT EXIT           00000100
C      N,M    - DEFINED ABOVE                                             00000110
C      WT     - WEIGHT FLOW, LB/SEC                                       00000120
C      RG     - FLUID DENSITY, LB/FT**3                                    00000130
C      EP     - BOUNDARY LAYER FACTOR, 1.0 USED NORMALLY                 00000140
C      OMEGA  - ROT. SPEED ,RAD/SEC                                       00000150
C      R,Z    - RADIUS AND Z COORD. TO POINT I,J,Z FROM ENTRANCE END     00000160
C      BETA   - ANGLE BTWN TANG. DIRECTION AND FLOW REL. VEL. VECTOR     00000170
C      BETB   -SIMILAR BUT USING BLADE ANGLE                             00000180
C      CHI    - ANGLE BETWEEN RADIAL DIR. AND BLADE TRACE ,+ IN CCW     00000190
C             DIRECTION WHEN + Z IS TO RIGHT                             00000200
C      CV2    - CURVATURE (1/RADIUS), 1/INCHES, + IF DALFA/DM IS +       00000210
C      CV2C   - CURVATURE CALCD BY PROGRAM ,NOT USED                     00000220
C      B      - NO. OF BLADES AT J                                         00000230
C      TN     - THICKNESS NORMAL TO BLADE AT J ,ASSUMED CONST ALONG     00000240
C             NORMAL                                                       00000250
C      ***  OUTPUT ***                                                    00000260
C                                                                           00000270
C      CBCM   - DBETA/DM                                                    00000280
C      CBCN   - DBETA/DN                                                    00000290
C      F1     - COEF. TO CM IN DIFFERENTIAL EQN.                          00000300
C      F2     - THE TERM NOT INVOLVING CM IN DIFF. EQN                   00000310
C      T      - TANGENTIAL THICKNESS ,FT.                                  00000320
C      ALFBR  - ANG. BTWN STRML. AND AXIS IN MER. PLANE                   00000330
C      DELM   - DISTANCE BTWN J AND J+1 ALONG STRMLINE                    00000340
C      DELN   - DIST. BTWN I AND I+1 ALONG NORMAL                          00000350
C      2 READ INPUT TAPE 5,10,N,M,WT,RG,EP,OMEGA,((R(I,J),Z(I,J)         00000360
C      1,BETA(I,J), CHI(I,J),CV2(I,J),BETB(I,J),I=1,N),J=1,M),(B(J),J=1,M)00000370
C      2,(TN(J),J=1,M)                                                    00000380

```

		10 FORMAT (2I12,4F12.8/(6F12.8))	00000390
178	C	NEG. COMPL. OF BETA AND NEG. OF CHI USED IN PROGRAM	00000400
	C	D0 14 I=1,N	00000410
		D0 14 J=1,M	00000420
		BETA(I,J) = BETA(I,J) -90.	00000430
		BETB(I,J) = BETB(I,J) -90.	00000440
		14 CHI(I,J) = - CHI(I,J)	00000450
		PI = 3.1415926	00000460
		AN = N	00000470
		AM = M	00000480
		NM1 = N-1	00000490
		MM1 = M - 1	00000500
		D0 11 J=1,M	00000510
		11 TN(J) = TN(J)/12.	00000520
		Q = WT/(RC*EP*(AN-1.))	00000530
		D0 12 I=1,N	00000540
		D0 12 J=1,M	00000550
		R(I,J) = R(I,J)/12.	00000560
		CV2(I,J) = CV2(I,J)*12.	00000570
		12 Z(I,J) = Z(I,J)/12.	00000580
	C	CALC. ALFA AND ALFBR	00000590
		D0 40 I=1,N	00000600
		D0 39 J=1,MM1	00000610
		IF(Z(I,J+1)-Z(I,J))20,20,15	00000620
		15 ARG1 = (R(I,J+1)-R(I,J))/(Z(I,J+1)-Z(I,J))	00000630
		IF(ARG1 - 1.)25,25,20	00000640
		25 ALFA(I,J) = ATANF(ARG1)	00000650
		G0 T0 30	00000660
		20 ALFA(I,J) =90. - ATANF((Z(I,J+1)-Z(I,J))/(R(I,J+1) - R(I,J)))	00000670
		30 IF(J-1)34,34,36	00000680
		34 ALFBR(I,J) = ALFA(I,J)	00000690
		G0 T0 39	00000700
		36 ALFBR(I,J) = (ALFA(I,J-1)+ ALFA(I,J))/2.	00000710
		39 CONTINUE	00000720
		ALFA(I,M) = ALFA(I,MM1)	00000730
		40 ALFBR(I,M) = ALFA(I,M)	00000740
	C	CALC. TANGENTIAL THICKNESS	00000750
		D0 330 J=1,M	00000760
			00000770

6428

** VELOCITY DISTRIBUTION PROGRAM **

```

DO 330 I=1,N
330 T(I,J)=TN(J)*SQRTF(SINDF(BETB(I,J))**2/(COSDF(BETB(I,J))**2*COSDF
1(ALFBR(I,J)+CHI(I,J))**2) + 1.)
C
C CALC. DELTA M AND CURVATURE
DO 50 I=1,N
DO 50 J=1,MM1
50 DELM(I,J) = SQRTF((R(I,J+1)-R(I,J))**2 + (Z(I,J+1) - Z(I,J))**2)
DO 60 I=1,N
CV2C(I,1) = 0.
DELM(I,M) = 0.
60 CV2C(I,M) = 0.
DO 70 I=1,N
DO 70 J=2,MM1
80 TANA = SINDF((ALFA(I,J) - ALFA(I,J-1))/2.)/COSDF((ALFA(I,J) - ALFA
1(I,J-1))/2.)
IF(DELM(I,J) - DELM(I,J-1))100,90,90
90 CV2C(I,J) = 2.*TANA/DELM(I,J-1)
GO TO 70
100 CV2C(I,J) = 2.*TANA/DELM(I,J)
70 CONTINUE
C
C CALC. DBETA/DM
DO 130 I=1,N
DBDM(I,1) = (BETA(I,2) - BETA(I,1))*PI/(DELM(I,1)*180.)
DO 140 J=2,MM1
140 DBDM(I,J) = ((BETA(I,J) - BETA(I,J-1))*PI/(DELM(I,J-1)*180.))* (1.+
1(DELM(I,J-1)/(DELM(I,J-1)+DELM(I,J)))*PI*((BETA(I,J+1) - BETA(I,J)
2)/DELM(I,J) - (BETA(I,J) - BETA(I,J-1))/DELM(I,J-1)) / 180.)
150 DBDM(I,M) = (BETA(I,J) - BETA(I,J-1))*PI/(DELM(I,J-1)*180.)
C
C CALC. OF DBETA/DN
DO 162 J=1,M
DO 162 I=1,MM1
162 DELN(I,J) = SQRTF((R(I,J) - R(I+1,J))**2 + (Z(I,J)-Z(I+1,J))**2)
DO 160 J=1,M
DO 161 I=1,MM1
164 IF(I-1)165,165,166
165 DBDN(I,J)=(BETA(I+1,J)-BETA(I,J))*PI/(180.*DELN(I,J))
GO TO 161

```

```

00000780
00000790
00000800
00000810
00000820
00000830
00000840
00000850
00000860
00000870
00000880
00000890
00000900
00000910
00000920
00000930
00000940
00000950
00000960
00000970
00000980
00000990
00001000
00001010
00001020
00001030
00001040
00001050
00001060
00001070
00001080
00001090
00001100
00001110
00001120
00001130
00001140
00001150
00001160

```



```

178 SB2=0.
GO TO 179
177 SB2 = 1./((COSDF(ALFBR(I,J))-SINDF(ALFBR(I,J)) * SINDF(CHI(I,J)))/CG
1SCF(CHI(I,J))
176 F1(I,J) = -(SINDF(BETA(I,J)) * (DBDM(I,J)) * SB1 - DBDN(I,J)) / COSDF(BET
1A(I,J)) - COSDF(BETA(I,J)) ** 2 * CV2(I,J) + SINDF(BETA(I,J)) ** 2 * SB2
2/(R(I,J)))
180 F2(I,J) = (DCMCM(I,J) * SB1 * SINDF(BETA(I,J)) ** 2 + OMEGA * SB2 * SINDF(2.*
1BETA(I,J)))
INTEGRATION
DO 230 J=1,M
CM(1,J) = CMP(1,J)
TRI(J) = 0.
225 TRI(J) = TRI(J) + 1.
FLW = 0.
DO 220 I=2,N
RF = (F2(I,J) + F2(I-1,J)) / (F1(I,J) + F1(I-1,J))
CM(I,J) = RF + (CM(I-1,J) - RF) / EXPF(DELN(I-1,J) * (F1(I,J) + F1(I-1,J))
1/2.)
220 FLW = FLW + (P*(R(I,J) + R(I-1,J)) - B(J) * T(I-1,J)) * (CM(I,J) + CM(I-1,
J)) * DELN(I-1,J) * R0/2.
IF(ABS(FW - FLW) / FW - .005) 230, 230, 222
222 IF(TRI(J) - 25.) 223, 223, 240
223 IF(TRI(J) - 1.) 224, 224, 226
224 CMLAST = CM(1,J)
DIFL = WT - FLW
CM(1,J) = CM(1,J) * WT / FLW
GO TO 225
226 DIF = WT - FLW
CMA = CM(1,J)
CM(1,J) = CM(1,J) - DIF * (CMLAST - CM(1,J)) / (DIFL - DIF)
CMLAST = CMA
DIFL = DIF
GO TO 225
226 DIF = WT - FLW
CMA = CM(1,J)
CM(1,J) = CM(1,J) - DIF * (CMLAST - CM(1,J)) / (DIFL - DIF)
CMLAST = CMA
DIFL = DIF
GO TO 225
230 CONTINUE
RECALC. CM DISTRIB IF RUN=0.
IF(RUN-1.) 167, 232, 232
DO 141 I=1,NM1
00001560
00001570
00001580
00001590
00001600
00001610
00001620
00001630
00001640
00001650
00001660
00001670
00001680
00001690
00001700
00001710
00001720
00001730
00001740
00001750
00001760
00001770
00001780
00001790
00001800
00001810
00001820
00001830
00001840
00001850
00001860
00001870
00001880
00001890
00001900
00001910
00001920
00001930
00001940

```

	DO 141 J=1,M	00001950
	BBR(I,J)=(BETA(I,J) + BETA(I+1,J))/2.	00001960
	BBBR(I,J)=(BETB(I,J)+ BETB(I+1,J))/2.	00001970
182	RBR(I,J) =(R(I,J)+R(I+1,J))/2.	00001980
	141 WBR(I,J) =(CM(I,J)+CM(I+1,J))/(2.*COSDF(BBR(I,J)))	00001990
	DO 190 I=1,NM1	00002000
	DO 190 J=1,MM1	00002010
C	NOTE DCMP(I,J) IS USED HERE WITH DIFF. MEANING THAN AT STMT NO17300002020	00002020
	190 DCMP(I,J) = (RBR(I,J+1)*(OMEGA*RBR(I,J+1) + WBR(I,J+1)*SINDF(BBR(I	00002030
	1,J+1))) - RBR(I,J)*(OMEGA*RBR(I,J) + WBR(I,J)*SINDF(BBR(I,J)))	00002040
	1.*PI*(RBR(I,J)+RBR(I,J+1)) -2.*B(J)*T(I,J))/((RBR(I,J)+RBR(I,J+1))	00002050
	1*B(J)*DELM(I,J))	00002060
	DO 191 I=1,NM1	00002070
	WTR(I,1) =(COSDF(BBBR(I,1))/2.)*(2.*WBR(I,1)/COSDF(BBBR(I,1))+	DCM00002080
	1P(I,1))	00002090
	191 WTR(I,M) =(COSDF(BBBR(I,M))/2.)*(2.*WBR(I,M)/COSDF(BBBR(I,M))+	DCM00002100
	1P(I,MM1))	00002110
	DO 192 I=1,NM1	00002120
	DO 192 J=2,MM1	00002130
	192 WTR(I,J) =(COSDF(BBBR(I,J))/2.)*(2.*WBR(I,J)/COSDF(BBBR(I,J))+	DCM00002140
	1P(I,J-1) +DCMP(I,J))/2.)	00002150
	DO 193 I=1,NM1	00002160
	DO 193 J=1,M	00002170
	193 WDR(I,J)=2.*WBR(I,J) - WTR(I,J)	00002180
C		00002190
	DO 144 I=1,NM1	00002200
	DO 144 J=1,M	00002210
	144 CELP(I,J)=R0*(WTR(I,J)**2 - WDR(I,J)**2)/(144.*64.4)	00002220
	DO 145 I=1,NM1	00002230
	HDCP(I,1)=0.	00002240
	145 HDMOM(I,1)=0.	00002250
	DO 146 I=1,NM1	00002260
	DO 146 J=2,M	00002270
	HDCP(I,J) = HDCP(I,J-1) + OMEGA*RBR(I,J-1)*CELP(I,J-1)*DELM(I,J-1)	00002280
	1*DELN(I,J-1)*144.*B(J)*(AN-1.)/WT	00002290
	146 HDMOM(I,J) = -OMEGA*(RBR(I,1)*(OMEGA*RBR(I,1)+ (CM(I,1)+CM(I+1,	00002300
	1))*SINDF(BBR(I,1))/(2.*COSDF(BBR(I,1)))) - RBR(I,J)*(OMEGA*RBR(I,J)	00002310
	2) + (CM(I,J) + CM(I+1,J))*SINDF(BBR(I,J))/(2.*COSDF(BBR(I,J))))	00002320
	3 / 32.2	00002330

DO 148 I=1,NM1	00002340
148 UCU(I) = OMEGA*RBR(I,1)*(OMEGA*RBR(I,1) + (CM(I,1)+CM(I+1,1))*SINDF	00002350
1(BBR(I,1))/(2.*COSDF(BBR(I,1))))/32.2	00002360
DO 320 J=1,M	00002370
FL1 = 0.	00002380
I=1	00002390
K=1	00002400
CML = 1.	00002410
300 FL = (CM(I,J)+CM(I+1,J))*(PI*(R(I,J)+R(I+1,J)) - B(J)*T(I,J))*DELN	00002420
1(I,J)/2.	00002430
A=1.	00002440
301 FL2 = A*Q - FL1 - FL	00002450
FL1P = Q - FL2	00002460
IF(FL2)302,304,304	00002470
302 A = A+1.	00002480
GO TO 301	00002490
304 B2 = K	00002500
IF(FL+FL1-Q)306,308,308	00002510
308 DELNN(K,J) = (Q-FL1)*2./((CM(I,J) + CM(I+1,J))*(PI*(R(I,J) + R(I+1	00002520
1,J)) - B(J)*T(I,J))) + FL1/CML	00002530
IF(DELNN(K,J))325,325,305	00002540
305 IF(K-N+1)309,320,320	00002550
309 FL1 = 0.	00002560
313 K=K+1	00002570
KA = A+B2-2.	00002580
IF(K-KA)311,311,306	00002590
311 DELNN(K,J) = Q*2./((CM(I,J)+CM(I+1,J))*(PI*(R(I,J) +R(I+1,J)) - B(00002600
1J)*T(I,J)))	00002610
IF(DELNN(K,J))325,325,313	00002620
306 IF(I-N+1)314,315,315	00002630
315 IF(K-N+1)314,316,316	00002640
314 CML =(CM(I,J)+CM(I+1,J))*(PI*(R(I,J) +R(I+1,J)) -B(J)*T(I,J))/2.	00002650
FL1 =FL1P	00002660
I=I+1	00002670
GO TO 300	00002680
316 DELNN(K,J) =(Q-FL1)*2./((CM(I,J) + CM(I+1,J))*(PI*(R(I,J)+R(I+1,J)	00002690
1)- B(J)*T(I,J))) + FL1/CML	00002700
IF(DELNN(K,J))325,325,320	00002710
325 WRITE OUTPUT TAPE 6,326,K,J	00002720

6428

** VELOCITY DISTRIBUTION PROGRAM **

D0510	I=1,N	00003120
M5	= 1	00003130
	IF(M-9)520,520,515	00003140
515	M6 = M5 + 8	00003150
	GO TO 525	00003160
520	M6=M	00003170
525	WRITE OUTPUT TAPE 6,700,(CV2(I,J),J=M5,M6)	00003180
700	FORMAT(/8H- CV2 9F10.3)	00003190
	WRITE OUTPUT TAPE 6,723,(CV2C(I,J),J=M5,M6)	00003200
	WRITE OUTPUT TAPE 6,701,(DBDM(I,J),J=M5,M6)	00003210
701	FORMAT(8H0 DBDM 9F10.3)	00003220
725	FORMAT(8H0 CHI 9F10.3)	00003230
724	FORMAT(8H0 DELN 9F10.3)	00003240
	WRITE OUTPUT TAPE 6,702,(DBDN(I,J),J=M5,M6)	00003250
702	FORMAT(8H0 DBDN 9F10.3)	00003260
703	FORMAT(8H0 DCMDM 9F10.3)	00003270
704	FORMAT(8H0 F1 9F10.3)	00003280
705	FORMAT(8H0 F2 9F10.3)	00003290
706	FORMAT(8H0 T 9F10.3)	00003300
707	FORMAT(8H0 ALFBR 9F10.3)	00003310
708	FORMAT(8H0 BETA 9F10.3)	00003320
709	FORMAT(8H0 R 9F10.3)	00003330
710	FORMAT(8H0 Z 9F10.3)	00003340
711	FORMAT(8H0 DELNN 9F10.3)	00003350
712	FORMAT(8H0 CMP 9F10.3)	00003360
713	FORMAT(8H0 CM 9F10.3)	00003370
714	FORMAT(8H0 WTR 9F10.3)	00003380
715	FORMAT(8H0 WBR 9F10.3)	00003390
716	FORMAT(8H0 WDR 9F10.3)	00003400
717	FORMAT(8H0 DELP 9F10.3)	00003410
718	FORMAT(8H0 HDDP 9F10.3)	00003420
719	FORMAT(8H0 HDMCM 9F10.3)	00003430
721	FORMAT(8H0 B 9F10.3)	00003440
722	FORMAT(8H0 DELM 9F10.3)	00003450
723	FORMAT(8H0 CV2C 9F10.3)	00003460
	WRITE OUTPUT TAPE 6,703,(DCMDM(I,J),J=M5,M6)	00003470
	WRITE OUTPUT TAPE 6,704,(F1(I,J),J=M5,M6)	00003480
	WRITE OUTPUT TAPE 6,713,(CM(I,J),J=M5,M6)	00003490
	WRITE OUTPUT TAPE 6,705,(F2(I,J),J=M5,M6)	00003500

```

WRITE OUTPUT TAPE 6,706,(T1,J),J=M5,M6)
WRITE OUTPUT TAPE 6,707,(ALFBR(I,J),J=M5,M6)
WRITE OUTPUT TAPE 6,708,(BETA(I,J),J=M5,M6)
WRITE OUTPUT TAPE 6,709,(R(I,J),J=M5,M6)
WRITE OUTPUT TAPE 6,710,(Z(I,J),J=M5,M6)
WRITE OUTPUT TAPE 6,721,(B(J),J=M5,M6)
WRITE OUTPUT TAPE 6,725,(CHI(I,J),J=M5,M6)
WRITE OUTPUT TAPE 6,722,(DELM(I,J),J=M5,M6)
IF(I-NM1)522,522,523
WRITE OUTPUT TAPE 6,724,(DELN(I,J),J=M5,M6)
WRITE OUTPUT TAPE 6,711,(DELNN(I,J),J=M5,M6)
WRITE OUTPUT TAPE 6,712,(CMP(I,J),J=M5,M6)
WRITE OUTPUT TAPE 6,714,(MTR(I,J),J=M5,M6)
WRITE OUTPUT TAPE 6,715,(WBR(I,J),J=M5,M6)
WRITE OUTPUT TAPE 6,716,(WDR(I,J),J=M5,M6)
WRITE OUTPUT TAPE 6,717,(DELP(I,J),J=M5,M6)
WRITE OUTPUT TAPE 6,718,(HDDP(I,J),J=M5,M6)
WRITE OUTPUT TAPE 6,719,(HDMGM(I,J),J=M5,M6)
523 IF(M-M6-9)550,560,555
560 M5 = M6+1
M6 = M
GO TO 525
555 M5 = M6+1
M6 = M6+9
GO TO 525
550 IF(M-M6)510,510,560
510 CONTINUE
WRITE OUTPUT TAPE 6,720
FORMAT(/1H-,40X,6HTRI(J),12X,5HTN(J),12X,7HAREA(J))
DO 610 J=1,M
WRITE OUTPUT TAPE 6,445,TRI(J),TN(J),AREA(J)
728 FORMAT(/1H-,30X,6HUCU(I))
DO 730 I=1,NM1
730 WRITE OUTPUT TAPE 6,446,UCU(I)
446 FORMAT(1H0/28X,F10.4)
445 FORMAT(1H0,30X,F12.3,8X,F12.3,EX,F12.3)
537 FORMAT(1H010F10.3)
538 FORMAT(1H-10F10.3)
00003510
00003520
00003530
00003540
00003550
00003560
00003570
00003580
00003590
00003600
00003610
00003620
00003630
00003640
00003650
00003660
00003670
00003680
00003690
00003700
00003710
00003720
00003730
00003740
00003750
00003760
00003770
00003780
00003790
00003800
00003810
00003820
00003830
00003840
00003850
00003860
00003870
00003880
00003890

```

6428 ** VELOCITY DISTRIBUTION PROGRAM **
 600 GO TO 2
 END(1,0,0,0,0,0,1,0,0,1,0,0,0,0,0)

00003900

NOMENCLATURE

b	=	blade blockage factor
c or C	=	absolute velocity
c_p or c_v	=	specific heat
n	=	enthalpy
m or M	=	M coordinate; curvilinear distance along any assumed streamline in the meridional plane
M	=	Mach number
M_{total}	=	M coordinate at component exit normal minus M coordinate at component inlet normal
n or N	=	N coordinate; curvilinear distance along a line everywhere normal to a set of assumed streamlines in the meridional plane
p or P	=	pressure
Q'	=	Volume flow through a streamtube defined by two adjacent streamlines
r or R	=	Radius or radial coordinate
R	=	gas constant
R_C	=	Radius of curvature
R_m	=	Radius to midpoint of line normal to two adjacent streamlines
s	=	entropy
t	=	Circumferential blade thickness
t_m	=	Circumferential blade thickness at midpoint of line normal to two adjacent streamlines
T	=	absolute temperature
u or U	=	Component tangential velocity at radius R
v	=	specific volume
w or W	=	relative velocity
W_{BR}	=	relative velocity midway between two adjacent blades assuming linear relative velocity distribution in blade-to-blade plane
W_{DR}	=	relative velocity at driving surface of trailing blade synonymous with blade pressure side relative velocity
W_m	=	meridional relative velocity component

W_{m_0}	= meridional component of relative velocity at the tip ($N=0$)
W_{TR}	= relative velocity at trailing surface of preceeding blade, synonymous with blade suction side relative velocity
z	= number of blades; or axial coordinate
α	= angle in meridional plane between a tangent to a normal and the radial direction
β	= blade angle in stream surface with reference to meridional plane ($\beta = \beta' - 90^\circ$)
β'	= blade angle in stream surface with reference to tangential direction ($\beta' = \beta + 90^\circ$)
Γ	= circulation
δ	= angle in meridional plane between a tangent to a normal and a tangent to the blade trace
δ	= deviation angle
Σ	= angle between stream line and axial direction
ζ	= loss coefficient
η_e	= polytropic expansion efficiency
φ or θ	= wrap angle or angular coordinate in plane normal to axis of rotation
θ_{inc}	= wrap angle between driving face of trailing blade and trailing face of preceeding blade
μ	= flux, or specific mass flow
ψ	= stream function
ω	= angular velocity of impeller

APPENDIX B REFERENCES

- B-1. Stanitz, J. D. and V. D. Prian: A Rapid Approximate Method for Determining Velocity Distribution on Impeller Blades of Centrifugal Compressors, TN 2421, National Advisory Committee for Aeronautics, Washington, D.C., 1951.
- B-2. Vavra, M. H.: Aero-Thermodynamics and Flow in Turbomachines, John Wiley and Sons, Inc., New York, London, 1960.

APPENDIX C

PARTS REQUIREMENTS LIST FOR AP70-126 TEST INSTALLATION

Existing Parts

456205 Inducer 1 Required

Make From Existing Parts

AP70-126-26 Volute Assembly 1 Required
(make from 458161 volute and
from 458425 seal assembly)

AP70-126-33 Impeller 1 Required
(make from 460422-3 casting)

AP70-126-25 Housing Assembly 1 Required
(make from T-5029142-201)

Existing Parts Available From T-5029142
(To be used on AP70-126 Test Installation)

T5029143-501 Nose 1 Required
T5029143-406 Nut (mating ring) 1 Required
T5029143-405 Mating Ring 1 Required
T5029143-402 Nut (internal) 1 Required
T5029143-301 Retainer 1 Required
T5029143-606 No. 3-3-50-02-BO-40 Sealol Seal 1 Required
T5029143-607 No. 3-6-50-02-BO-40 Sealol Seal 1 Required
T5029143-407 Sleeve 1 Required
T5029143-404 Mating Ring 1 Required
T5029143-603 ND Q-30314 No. 5A Bearing 1 Required
T5029143-113 ND No. 110 Spring Washer (wavy) 1 Required
T5029143-304 Deflector, Oil 1 Required

T5029143-118 AN6230-8 O-Ring 1 Required
T5029143-115 AN6230-21 O-Ring 2 Required
T5029143-114 AN6230-7 O-Ring 2 Required
T5029143-116 MS9021-035 O-Ring 1 Required
T5029143-111 AN6230-17 O-Ring 2 Required
T5029143-112 AN6230-33 O-Ring 1 Required

New Parts (To Be Made)

AP70-126-2 Calibration Adapter Mount 1 Required
-003 Flange (C1020 H.R. steel plate 1.50 stock) 1 Required
-005 Body (C1020 H.R. steel plate .75 stock)
(or pipe (16.00 schedule 120) 1.218 wall) 1 Required
(seals A-106B)
-007 Flange (C1020 H.R. steel plate 1.00 stock) 1 Required
-009 Gusset (C1020 H.R. steel plate 1.00 stock) 5 Required

New Parts (To Be Made - Continued)

AP70-126-3 Torque Shaft (4340 alloy steel bar) (Similar to 126017-M3)	1 Required
AP70-126-4 Quill Shaft (4340 alloy steel bar) (Similar to 127017-M6)	1 Required
AP70-126-5 Main Shaft (Inconel-X bar) (Similar to T5029142-602)	1 Required
AP70-126-6 Sleeve, Serrated Scanivalve (6061 T6 aluminum)	2 Required
AP70-126-7 Spacer, Scanivalve End (A286 CRES)	1 Required
AP70-126-8 Nut, End Spacer (internal) (A286 CRES)	1 Required
AP70-126-9 Sleeve, End Spacer (321 CRES)	1 Required
AP70-126-10 Washer, Scanivalve Thrust (Neoprene)	1 Required
AP70-126-11 Probe, Main Shaft (serrated) (321 CRES)	1 Required
AP70-126-12 Stop, Probe (321 CRES)	1 Required
AP70-126-13 Mating Ring (440C CRES) (each side of AP70-126-35 seal assembly)	2 Required
AP70-126-14 Set Screw (make from AN565A428-16) (for slip ring assembly to main shaft)	3 Required
AP70-126-15 Nut (internal) (holds AP70-126-16 retainer in AP70-126-25 housing)	1 Required
AP70-126-16 Retainer (321 CRES) (retains rear bearings and 3-3-64 sealol seal)	1 Required
[AP70-126-17 Number Not Used]	
AP70-126-18 Mating Ring (440C CRES) (retains 3-3-64 sealol seal)	1 Required
[AP70-126-19 Number Not Used]	
AP70-126-20 Spacer Set (416 CRES) (separate rear bearings for lubrication)	1 Required
AP70-126-21 Nut, Mating Ring (A286 CRES) (rear bearing)	1 Required
AP70-126-22 Lock, Mating Ring Nut (302 CRES) (rear bearing)	1 Required
[AP70-126-23 Number Not Used]	
AP70-126024 Washer, Tab Cock (302 CRES) (to secure AP70-126-18 nut)	1 Required
AP70-126-27 Adapter (6061 T6 aluminum) (used with AP70-126-40 and -41)	1 Required
[AP70-126-28 Number Not Used]	

New Parts (To Be Made - Continued)

AP70-126-29 Adapter (Bently Prox.) (321 CRES)	2 Required
AP70-126-30-3 Shim (.320) (321 CRES)	1 Required
-5 Shim (.335) } Use between	1 Required
-7 Shim (.365) } Volute and	1 Required
-9 Shim (.385) } Pump Inlet	1 Required
AP70-126-31 Body, Pump Inlet (6061 T6 aluminum)	1 Required
AP70-126-32 Flange, Assembly of (321 CRES) (impeller cavity drain)	1 Required
AP70-126-34 Button, Pump Inlet (nylon)	4 Required
AP70-126-35 Seal Assembly (scanivalve vent)	1 Required
AP70-126-36 Nose, Assembly of	2 Required
AP70-126-37 Spring, Assembly of	2 Required
AP70-126-38 Housing	1 Required
AP70-126-39 Pin	2 Required
AP70-126-40 Tube Retainer (321 CRES) (part of AP70-126-27)	1 Required
AP70-126-41 Guide, Sleeve (321 CRES) (part of AP70-126-27)	1 Required
AP70-126-42 Probe, Retainer	1 Required
AP70-126-43 Adapter, Probe Retainer (321 CRES)	1 Required

New Parts (To Be Purchased)

Bearings	
ND QH20217DT5A or MCR7217DU-ABEC5	2 Required
Seals	
No. 3-3-B0-02-B0-64 Sealol Seal	1 Required

<u>O-Rings</u>	<u>Part No.</u>	<u>Where Used</u>	<u>Quantity</u>
	MS29513-003	AP70-126-27 Adapter	1
	-010	-43 Adapter	1
	-011	-27 Adapter	1
	-012	-29 Adapter	
		and Bently Prox.	6
	-013	-29 Adapter	2
		-43 Adapter	1
	-041	-35 Seal Assembly	2
	-042	-35 Seal Assembly	2
	-121	-32 Flange	1
	-138	-7 Spacer	1
	-159	-16 Retainer	1
	-162	-16 Retainer	1
	-275	-31 Pump Inlet	1
	-442	-31 Pump Inlet	1
Bolt	AN101321	} Cylinder to Pump Inlet	51
Washer (flat)	AN960-616		51

New Parts (To Be Purchased - Continued)

			<u>Quantity</u>
Nut	RD114-1002-0005	} Volute to Housing Flange	12
Washer (flat)	LD153-0010-0012		12
Washer (lock)	MS35338-140		12
Bolt	AN104030	} Housing to Mount	12
Nut	RD114-1002-0006		12
Washer (flat)	LD153-0010-0014		12
Washer (lock)	MS35338-141		12
Bolt	AN101219	} -35 Seal Assembly to Housing	7
Washer (flat)	LD153-0010-0012		7
Washer (lock)	MS35338-140		7
Bolt	AN148559	} -29 Adapter and Bently Prox.	4
Nut, Jam	AN316-6		6
Bolt	AN101010	} -32 Flange Impeller Cavity Drain	4
Washer (flat)	LD153-0010-0007		4
Washer (lock)	MS35338-138		4
Setscrews			
	AN565-1032-2	} To Secure -6 Sleeve	2
	AN565-1032-5		1
	AN565-1032-5 (to secure -16 retainer)		1
Pipe Plug			
	AN932D2 (use in -26 volute)		1
Plug			
	NAS1081C6A6 (use in -5 main shaft)		1

APPENDIX D

REFERENCES

1. Ellis, G. O.: "A Study of Induced Vorticity in Centrifugal Compressors." ASME Trans., Journal of Engineering For Power, pp. 63-76, January 1964.
2. Lakshminarayana, B. and G. F. Wislicenus: Investigations and Analysis of Flow Phenomena of Secondary Motions in Axial Flow Inducers, NASA-CR-67129, 1965.
3. Hamrick, J. T.: Some Aerodynamic Investigations in Centrifugal Impellers, ASME Transactions, Vol. 78, pp.591-602, April 1956.
4. Horlock, J. H.: Some Recent Research in Turbomachinery, Vol. 182, Pt. 1, No. 26, Proceedings of Instrumentation Mechanical Engineers, 1967-68.
5. Lakshminarayana, B. and J. H. Horlock: Leakage and Secondary Flows in Compressor Cascades, Reports and Memoranda No. 3483, Ministry of Technology, 1967.
6. Rains, D. A.: Tip Clearance Flows in Axial Flow Compressors and Pumps, Calif. Inst. of Tech., Mechanical Engineering Laboratory Report 5, 1954.
7. Wood, G. M., H. Welna, and R. P. Lamers: Tip-Clearance Effects in Centrifugal Pumps, ASME paper 64-WA/FE-17, December 1965.
8. Schmidt-Theuner, P., and J. Mattern: "The Effect of Reynolds Number and Clearance in the Centrifugal Compressor of a Turbocharger," Brown Boveri Review, Vol. 55, No. 8, pp. 453-456, 6 August 1968.
9. Hartman, M. J., G. W. Lewis, and E. R. Tysl: Design and Experimental Performance of a Small Centrifugal Pump for Liquid Hydrogen, NASA T. M. X-389, September 1960
10. Wood, G. M.: "Visual Cavitation Studies of Mixed Flow Pump Impellers," ASME Transactions Journal of Basic Engineering, pp. 17-28, March 1963.

APPENDIX E

BIBLIOGRAPHY LIST

- Ainley, D. G., and G. C. R. Mathieson: Examination of the Flow and Pressure Losses In Blade Rows of Axial-Flow Turbines, Aeronautical Research Reports and Memoranda No. 2891, March 1951.
- Altieri, J. V., and R. S. Kulp: Cavitation Damage of Mechanical Pump Impellers Operating in Liquid Metal Space Power Loops, NASA C. R.-165, July 1965.
- Balje, O. E. and R. L. Binsley: Turbine Performance Prediction-Optimization using Fluid Dynamic Criteria, R-6805, Rocketdyne, a division of North American Rockwell, Canoga Park, California, 1 December 1966.
- Boyce, M. P.: A Practical Three-Dimensional Flow Visualization Approach to the Complex Flow in a Centrifugal Impeller, ASME paper 66 GT-83.
- Brunner, J.: Analysis and Experimental Verification of Axial Thrust on the M-1 Liquid Oxygen Turbopump, Aerojet-General Corp., Report AGC 8800-51, NASA C. R. 54817, April 1966.
- Crouse, J. E., and D. M. Sandercock: Blade-Element Performance of A 0.7 Hub-Tip Radius Ratio Axial-Flow-Pump Rotor with Tip Diffusion Factor of 0.43, NASA Report TN D-2481.
- Csanady, G. T.: Theory of Turbomachines, Mechanical Engineering Series, McGraw-Hill Book Co., New York-San Francisco-Toronto-London, 1964.
- Eckert, B.: Axial Kompressoren Und Radialkompressoren, Springer, Berlin, 1961.
- Ellis, G. O.: "A Study of Induced Vorticity in Centrifugal Compressors." ASME Trans., Journal of Engineering For Power, pp. 63-76, January 1964.
- Folsom, R. G.: "Some Performance Characteristics of Deep-Well Turbine Pumps." ASME Trans. Vol. 63, pp. 245-250, April 1941.
- Fujie, K.: "A Study of the Flow Through the Rotor of an Axial Compressor," Bulletin Japan Society of Mechanical Engineers, Vol. 5, No. 18, 1962.
- Furuya, Y., and I. Nakamura: The Experiment on the Skewed Boundary Layer on a Rotating Body, November 1966.
- Futral, S. M., and D. E. Holeski: Effect of Rotor Tip Clearance on the Performance of A 5-Inch Single Stage Axial Flow Turbine. NASA TMX, March 1969.
- Galistskiy, N. F.: On Friction and Leakage Lo-ses in the Working Blade-Rings of Radial-Flow Turbines in Helicopter and Transport Gas-Turbine Units, NASA-TT-F-447, January 1967.
- Groh, F. G., G. M. Wood, R. S. Kulp, and D. P. Kenny: Evaluation of a High Hub/Tip Ratio Centrifugal Compressor, ASME paper No. 09-WA/FE-28, 1969.

- Hanley, W. T.: A Correlation of End Wall Losses in Plane Compressor Cascades, ASME Paper No. 68-GT-15, March 1968.
- Hansen, A. G., and H. Z. Herzig: "Secondary Flows and Three-Dimensional Boundary-Layer Effects," Aerodynamic Design of Axial-Flow Compressors, NASA SP-36, 1965.
- Hartmann, M. J., G. W. Lewis, and E. R. Tysl: Design and Experimental Performance of a Small Centrifugal Pump For Liquid Hydrogen, NASA TMX-388, September 1960.
- Hawthorne, W. R.: "The Applicability of Secondary Flow Analysis to the Solution of Internal Flow Problems", article in Fluid Mechanics of Internal Flow, edited by Gino Sovrano, Elsevier Publishing Co., Amsterdam-London-New York, 1967.
- Herzig, H. Z, A. G. Hansen, and G. R. Costello: A Visualization Study of Secondary Flows in Cascades, NACA Report 1163, 1954.
- Horlock, J. H.: Axial Flow Turbines, Butterworth & Co., England-U.S.A.-Canada, 1966.
- Hutton, S. P.: "Three-Dimensional Motion in Axial-Flow Impellers," Proc. I Mech. E., pp. 863-873, 1956.
- Kofskey, M. G., and H. E. Rohlik: Secondary Flow Phenomena in Stator and Rotor Blade Rows and Their Effect on Turbine Performance, ASME Paper No. 63-AHGT-72, 1963.
- Krylov, Ye. P., and Y. A. Spunde: "About the Influence of the Clearance Between the Working Blades and Housing of A Radial Turbine on Its Exponent," (translated from Russian), News of Institute of Higher Learning, No. 7. 1965 pp. 66-73 Foreign Tech. Div., FTD-MT-67-15 Wright Patterson AFB, Ohio.
- Lakshminarayana, B., and G. F. Wislicenus: Investigations and Analysis of Flow Phenomena of Secondary Motions in Axial Flow Inducers, NASA-CR-67129, 1965.
- Lakshminarayana, B., and J. H. Horlock: "Review: Secondary Flows and Losses in Cascades and Axial-Flow Turbomachines," Int. J. Mech. Sci., Pergamon Press, LTD., 1963, Vol. 5 pp. 287-307.
- Louis, J. F.: Secondary Flow and Losses in a Compressor Cascade, Aeronautical Research Council R&M 3136, March 1958.
- Maksutova, M. K.: Calculation of Losses Arising from the Radial Clearance of a turbine Rotor, (in Russian), 1965.
- Marshall, R., and C. Rogo: Experimental Investigation of Low Aspect Ratio and Tip Clearance on Turbine Performance and Aerodynamic Design, USAAVLABS Technical Report 67-80, May 1968.

- McNair, R. E.: Tip Clearance Effects on Stalling Pressure Rise in Axial Flow Compressors, ASME Symposium on Compressor Stall, Surge, and System Response, March 1960.
- Odivanov, L. N.: A Study of the Radial-Axial-Flow Turbine with Low Blade Heights and Large Clearances, NASA-TT-F-10441, December 1966.
- Proskuryakov, G. V.: Selection of the Optimal Degree of Reaction of the Stages of a Gas Turbine with Unshrouded Blades, Foreign Technology Division, Wright Patterson AFB, Ohio, FTD-TT-65-1721, 1965, (translated from Energomashinostroyeniye No. 5., 1965 pp. 14-17).
- Rains, D. A.: Tip Clearance Flows in Axial Flow Compressors and Pumps, Calif. Inst. of Tech., Mechanical Engineering Laboratory Report 5, 1954.
- Riley, M. W.: The Effect of Axial Clearance on the Performance of a Dual Discharge Radial Turbine, Naval Post Graduate School, Monterey, California, December 1960.
- Schmidt-Theuner, P., and J. Mattern: "The Effect of Reynolds Number and Clearance in the Centrifugal Compressor of a Turbocharger," Brown Boveri Review, Vol. 55, No. 8, pp. 453-456, 6 August 1968.
- Scholz, N.: "Secondary Flow Losses in Turbine Cascades," Journal of the Aeronautical Sciences, Vol. 21 pp 707-708, 1954.
- Schlichting, H., and A. Das: "Recent Research on Cascade Flow Problems." Transactions of ASME Vol. 88 Journal of Basic Engineering, March 1966.
- Sedille, M.: "Influence of Radial Clearance in Compressors," Academie de Sciences, p. 418 and 1789, 1939.
- Shaw, R.: "Efficiency Predictions for Axial-Flow Turbines," Int. J. Mech Sci., Pergamon Press, Ltd., 1966, Vol. 8 pp. 171-192.
- Spencer, E. A.: "The Performance of an Axial-Flow Pump," Proc. I Mech. E., pp. 874-808, 1956.
- Vavra, M. H.: Aerothermodynamics and Flow in Turbomachines, John Wiley & Sons, Inc., New York-London, 1960.
- Wood, G. M., H. Welna, and R. P. Lamers: Tip-Clearance Effects in Centrifugal Pumps, ASME paper 64-WA/FE-17, December 1965.
- Wood, G. M.: "Visual Cavitation Studies of Mixed Flow Pump Impellers," ASME Transactions Journal of Basic Engineering, pp. 17-28, March 1963.
- Wu, Chung Hua, and Wen Wu: Analysis of Tip-Clearance Flow in Turbomachines, Polytechnic Institute of Brooklyn Gas Turbine Laboratory Technical Report No. 1, July 1954.

Wu, Chung, Hua: Survey of Available Information on Internal Flow Losses through Axial Turbomachines, NACA Research Memo, RME50J13, January 1951.

Zayankin, A. Ye, and M. F. Zatsepin: Effect of the Clearance Between the Casing and the Wheel Upon the Efficiency of the Centripetal Gas Turbine, pp. 33-35, NASA TT-F-10450, 1964.

APPENDIX F

DISTRIBUTION LIST (CONTRACT NAS3-13311)

	<u>Copies</u>
National Aeronautics and Space Administration Lewis Research Center 21000 Brookpark Road Cleveland, Ohio 44135	
Attn: E. J. Kolman Mail Stop 500-313	1
Technical Report Control Office Mail Stop 5-5	1
Technology Utilization Office Mail Stop 3-16	1
AFSC Liaison Office Mail Stop 501-3	2
Library Mail Stop 60-3	1
M. J. Hartmann Mail Stop 5-9	1
W. R. Britsch Mail Stop 5-9	1
W. A. Rostafinski Mail Stop 5-9	1
R. E. Connelly Mail Stop 500-116	1
D. D. Scheer Mail Stop 500-204	6
National Technical Information Service Springfield, Virginia 22151	40
National Aeronautics and Space Administration Washington, D. C. 20546	
Attn: Code RPX	2
RPL	1

	<u>Copies</u>
Scientific and Technical Information Facility P. O. Box 33 College Park, Maryland 20740	
Attn: NASA Representative Code CRT	6
National Aeronautics and Space Administration Ames Research Center Moffett Field, California 94035	
Attn: Library	1
National Aeronautics and Space Administration Flight Research Center P. O. Box 273 Edwards, California 93523	
Attn: Library	1
National Aeronautics and Space Administration Goddard Space Flight Center Greenbelt, Maryland 20771	
Attn: Library	1
National Aeronautics and Space Administration John F. Kennedy Space Center Kennedy Space Center, Florida 32899	
Attn: Library	1
National Aeronautics and Space Administration Langley Research Center Langley Station Hampton, Virginia 23365	
Attn: Library	1
National Aeronautics and Space Administration Manned Spacecraft Center Houston, Texas 77058	
Attn: Library	1

	<u>Copies</u>
National Aeronautics and Space Administration George C. Marshall Space Flight Center Marshall Space Flight Center, Alabama 35812	
Attn: Library	1
Keith Chandler	1
Loren Gross	1
Jet Propulsion Laboratory 4800 Oak Grove Drive Pasadena, California 91103	
Attn: Library	1
U. S. Atomic Energy Commission AEC-NASA Space Nuclear Systems Office Washington, D. C. 20546	
Attn: F. C. Schwenk	1
Chemical Propulsion Info. Agency Applied Physics Laboratory 8621 Georgia Avenue Silver Springs, Maryland 20910	1
Defense Documentation Center Cameron Station Alexandria, Virginia 22314	1
Office of the Director of Defense Research and Engineering Washington, D. C. 20301	1
Advanced Research Projects Agency Washington, D. C. 20525	
Attn: D. E. Mock	1
Research and Technology Division Air Force Systems Command Bolling Air Force Base Washington, D. C. 20332	
Attn: RTD (RTNP)	1

	<u>Copies</u>
Arnold Engineering Development Center Air Force Systems Command Tullahoma, Tennessee 37389	
Attn: AEOIM	1
Air Force Aero Propulsion Laboratory Research and Technology Division Air Force Systems Command United States Air Force Wright Patterson AFB, Ohio 45433	
Attn: APRP	1
Aeronautical Systems Division Air Force Systems Command Wright Patterson Air Force Base Dayton, Ohio 45433	
Attn: Library	1
Air Force Missile Test Center Patrick Air Force Base, Florida 32925	
Attn: L. J. Ullian	1
Air Force Systems Command Andrews Air Force Base Washington, D. C. 20332	
Attn: SCLT	1
Air Force Rocket Propulsion Laboratory (RPR) Edwards Air Force Base, California 93523	1
Air Force Office of Scientific Research Washington, D. C. 20333	
Attn: SREP, Dr. J. F. Masi	1
Office of Research Analyses (OAR) Holloman Air Force Base, New Mexico 88330	
Attn: Library	1

	<u>Copies</u>
Commanding Officer U. S. Army Research Office (Durham) Box CM, Duke Station Durham, North Carolina 27706	1
U. S. Army Missile Command Redstone Scientific Information Center Redstone Arsenal, Alabama 35808	
Attn: Chief, Document Section	1
Bureau of Naval Weapons Department of the Navy Washington, D. C. 20306	
Attn: J. Kay, Code RTMS-41	1
Commander U. S. Naval Missile Center Point Mugu, California 93041	
Attn: Technical Library	1
Commanding Officer Office of Naval Research 1030 E. Green Street Pasadena, California 91101	1
Director (Code 6180) U. S. Naval Research Laboratory Washington, D. C. 20390	
Attn: H. W. Carhart	1
Picatinny Arsenal Dover, New Jersey 07801	
Attn: Chief, Liquid Propulsion Laboratory	1
Airesearch Manufacturing Co. of Arizona 402 South 36th Street Phoenix, Arizona 85034	
Attn: Library	1

	<u>Copies</u>
Aerojet-General Corporation P. O. Box 296 Azusa, California 91703	
Attn: Librarian	1
Aerojet-General Corporation 11711 South Woodruff Avenue Downey, California 90241	
Attn: F. M. West, Chief Librarian	1
Aerojet-General Corporation P. O. Box 1947 Sacramento, California 95809	
Attn: Tech. Library 2484-2015A	1
K. R. Collins	1
R. Jones	1
Aerospace Corporation P. O. Box 95085 Los Angeles, California 90045	
Attn: Library-Documents	1
Allis Chalmers Mfg. Co. Box 512 Milwaukee, Wisconsin 53201	1
Battelle Memorial Institute 505 King Avenue Columbus, Ohio 43201	
Attn: Report Library Room 6A	1
Bell Aerospace Company Box 1 Buffalo, New York 14240	
Attn: Technical Library	1
M. Messina	1

Copies

The Boeing Company
Aero Space Division
P. O. Box 3707
Seattle, Washington 98124

Attn: Ruth E. Peerenboom, Library
Processes Sup. (1190)

1

Brown Engineering Co., Inc.
Research Park
Huntsville, Alabama 35807

Attn: Library

1

Chrysler Corporation
Space Division
New Orleans, Louisiana 70150

Attn: Library

1

Curtiss-Wright Corporation
Weight Aeronautical Division
Woodridge, New Jersey 07075

Attn: Library

1

Fairchild Stratos Corporation
Aircraft Missiles Division
Hagerstown, Maryland 20740

Attn: Library

1

The Franklin Institute Research Laboratories
Benjamin Franklin Parkway
Philadelphia, Pennsylvania 19103

Attn: Library

1

The Garrett Corporation
AiResearch/Los Angeles
9851 Sepulveda Blvd.
Los Angeles, California 90009

Attn: Library

1

Copies

General Dynamics/Astronautics
P. O. Box 1128
San Diego, California 92112

Attn: Library and Information
Services (128-00)

1

General Electric Company
Flight Propulsion Laboratory Dept.
Cincinnati, Ohio 45215

Attn: D. Suichu

1

P. R. Gliebe

1

General Motors Corporation
Allison Division
P. O. Box 24013
Indianapolis, Indiana 46206

Attn: Library

1

Grumman Aircraft
Bethpage Long Island
New York 11714

Attn: Library

1

Hydronautics, Incorporated
Pindell School Road
Laurel, Maryland

1

IIT Research Institute
Technology Center
Chicago, Illinois 60616

Attn: Library

1

Lockheed Missiles & Space Company
Propulsion Engineering Division (D. 55-11)
111 Lockheed Way
Sunnyvale, California 94087

1

Copies

Lockheed Propulsion Company P. O. Box 111 Redlands, California 92374	
Attn: Library	1
Marquardt Corporation 16555 Saticoy Street Box 2013 - South Annex Van Nuys, California 91404	
Attn: Library	1
McDonnell Douglass Astronautics Co. Western Division 5301 Bolsa Avenue Huntington Beach, California 92647	
Attn: Library	1
Pesco Products Division of Borg-Warner Corp. 24700 N. Miles Road Bedford, Ohio 44146	1
Rocketdyne, A Division of North American Rockwell Corporation 6633 Canoga Avenue Canoga Park, California 91304	
Attn: Library, Dept. 596-306	1
J. Hale	1
Rocket Research Corporation 520 South Portland Street Seattle, Washington 98108	1
Scanivalve Co. P. O. Box 20,005 San Diego, California 92120	
Attn: J. C. Pemberton	1
Sundstrand Corporation Hydraulics Division Rockford, Illinois 61101	1

	<u>Copies</u>
Sundstrand-Denver Industrial Products Group 2480 W. 70th Street Denver, Colorado 80221	1
TRW Systems One Space Park Redondo Beach, California 90278	
Attn: STL Tech. Lib. Doc. Acquisitions	1
United Aircraft Corporation Corporation Library 400 Main Street East Hartford, Connecticut 06118	
Attn: Library	1
United Aircraft Corporation Pratt & Whitney Fla. Res. Development Center P. O. Box 2691 W. Palm Beach, Florida 33402	
Attn: Library	1
J. Hill	1
United Aircraft Corporation United Technology Center P. O. Box 358 Sunnyvale, California 94088	
Attn: Library	1
Worthington Corp. Advanced Products Division Harrison & Worthington Avenues Harrison, New Jersey 07029	1
Dr. George F. Wislicenus 4641 E. Coronado Drive Tucson, Arizona 85718	1
California Institute of Technology Pasadena, California	
Attn: Dr. A. Acosta	1

Copies

Iowa State University
Ames, Iowa

Attn: Dr. George Serovy

1

Pennsylvania State University
State College, Pennsylvania

Attn: Dr. B. Lakshminarayana

1

